2010

Crystal engineering of organic and metal-organic solids: design, structure and properties

Dejan-Kresimir Bucar
University of Iowa

CRYSTAL ENGINEERING OF ORGANIC AND METAL-ORGANIC SOLIDS: DESIGN, STRUCTURE AND PROPERTIES

by

Dejan-Krešimir Bučar

An Abstract

Of a thesis submitted in partial fulfillment
of the requirements for the Doctor of
Philosophy degree in Chemistry
in the Graduate College of
The University of Iowa

December 2010

Thesis Supervisor: Professor Leonard R. MacGillivray

ABSTRACT

Crystal engineering has recently emerged as a method of choice for the design and the construction of both organic and metal-organic functional materials. Solid-state synthesis, of the most commonly studied aspects of crystal engineering, has been shown to provide access to molecular targets that are hardly obtainable using principles of conventional (*i.e.* solution-based) organic synthesis. Reactions in the solid state, however, are not routinely used in organic synthetic chemistry. The scarce use of solid-state reactions can be attributed to the difficulty of predicting molecular arrangements in the solid state, as well as to the lack of methodologies to control crystal packing. Template-directed solid-state synthesis is a recently developed modus operandi that enables control over reactivity within multi-component crystals. This thesis is partially focused on the application of template-directed solid-state approach to [2+2] photocycloaddition reactions in the solid state, as well as on the understanding of intermolecular interactions in crystals. Synthetic templates have been utilized to construct cocrystals that enable a class of hitherto underdeveloped organic solid-state reactions, namely [2+2] cross-photoaddition reactions. In addition, products derived form templated solid state reactions, namely tetrapyridylcyclobutanes, have been utilized to generate exceptional materials, such as thixothropic hydrogels based on nano-dimensional metal-organic particles. The utility of crystal engineering has also been expanded to the nano-science and the development of nanomaterials. A crystallization method for the preparation of nano-dimensional cocrystals has been developed. The method has been shown to enable single-crystal-to-single-crystal [2+2] photodimerizations of olefins. In addition, nano-dimensional cocrystals have been shown to exhibit distinctive mechanical properties upon single-crystal-to-single-crystal transformations.

In addition to solid-state reactions and materials derived therefrom, we systematically studied hierarchies of supramolecular synthons in pharmaceutical

cocrystals comprised of multi-functional molecules. Pharmaceutical cocrystals have been recently shown to exhibit physical properties superior to those of parent drugs. Our studies involved xanthine alkaloids as pharmaceutical agents and a series of hydroxylated benzoic acids as cocrystal formers. Synthon hierarchies have been established for three xanthine alkaloids. We also discovered pharmaceutical salts that formed where cocrystallization was expected to occur. Reasons contributing to such unexpected salt formation were investigated using X-ray crystallography and computational methods. The established synthon hierarchies are expected to contribute to a better understanding of self-assembly processes in cocrystals that is crucial for the development of state-of-art drugs, and the design of organic reactions in the solid state.

Abstract Approved: _____
Thesis Supervisor

_____
Title and Department

_____
Date

CRYSTAL ENGINEERING OF ORGANIC AND METAL-ORGANIC SOLIDS: DESIGN, STRUCTURE AND PROPERTIES

by

Dejan-Krešimir Bučar

A thesis submitted in partial fulfillment
of the requirements for the Doctor of
Philosophy degree in Chemistry
in the Graduate College of
The University of Iowa

December 2010

Thesis Supervisor: Professor Leonard R. MacGillivray

Graduate College
The University of Iowa
Iowa City, Iowa

CERTIFICATE OF APPROVAL

_____

PH.D. THESIS

_____

This is to certify that the Ph.D. thesis of

Dejan-Krešimir Bučar

has been approved by the Examining Committee
for the thesis requirement for the Doctor of Philosophy
degree in Chemistry at the December 2010 graduation.

Thesis Committee: _____
Leonard R. MacGillivray, Thesis Supervisor

_____
Amnon Kohen

_____
Ned B. Bowden

_____
F. Christopher Pigge

_____
Geoff G. Z. Zhang

To Stjepan and Vito

…while it's tempting to play it safe, the more we're willing to risk, the more alive we are. In the end, what we regret most are the chances we never took.

Christopher Lloyd & Joe Keenan
("Frasier")

ACKNOWLEDGMENTS

The contents of this thesis would have been absolutely impossible to acheive without the help and support of many people. I would, therefore, like to take the opportunity to express my sincere gratitude to every one of them.

First of all, I am most grateful to my mentor, Professor Leonard R. MacGillivray, for passing on to me a great deal of his knowledge and experience. For tremendous support, encouragement and patience. For each and every provided opportunity. For nurturing both my curiosity and enthusiasm.

I am especially thankful to Dr. Dale C. Swenson for all his assistance in the crystallographic aspect of my studies. Each advice and every discussion was very helpful and is deeply appreciated.

I am also indebted to Dr. Geoff G. Z. Zhang and Rodger F. Henry who significantly contributed to this thesis: mostly, but surely not only, by providing different perspectives.

Assistant Professor Ernest Meštrović and Assistant Professor Nenad Judaš are thanked for preparing me for my graduate studies. Dr. Tomislav Friščić for "jump-starting" me in the lab, for all the help and advice, and for the good times outside the lab.

I also express gratitude to both the Tivanski research group and my colleagues for the great professional collaboration. Thank you, Tony, Tamara, Ivan, Manza, Qianli, Jonas, Poonam, Saikat, Joe, Phuong, Beth, John, Ryan and Jelena!

Tomislav K., Ana, Riddhi, John, Lindsay, Claude, Adam, Željko, Ivan, Juda, Tomislav F., Krcko, Mislav, Aco, Pivina and Vedran – thank you for keeping up the spirits.

Lastly, I want to thank my family – Mijo, Neda, Sandra, Stjepan, Anka and Arun for being with me and being there for me. Without them, I would not be.

ABSTRACT

Crystal engineering has recently emerged as a method of choice for the design and the construction of both organic and metal-organic functional materials. Solid-state synthesis, of the most commonly studied aspects of crystal engineering, has been shown to provide access to molecular targets that are hardly obtainable using principles of conventional (i.e. solution-based) organic synthesis. Reactions in the solid state are, however, not routinely used in organic synthetic chemistry. The scarce use of solid-state reactions can be attributed to the difficulty of predicting molecular arrangements in the solid state, as well as to the lack of methodologies to control crystal packing. Template-directed solid-state synthesis is a recently developed modus operandi that enables control over reactivity within multi-component crystals. This thesis is focused on the application of template-directed solid-state approach to [2+2] photocycloaddition reactions in the solid state, as well as on the understanding of intermolecular interactions in crystals. Synthetic templates have been utilized to construct cocrystals that enable a class of hitherto underdeveloped organic solid-state reactions, namely [2+2] cross-photoaddition reactions. In addition, products derived form templated solid state reactions, namely tetrapyridylcyclobutanes, have been utilized to generate exceptional materials, such as thixothropic hydrogels based on nano-dimensional metal-organic particles. The utility of crystal engineering has also been expanded to the nano-science and the development of nanomaterials. A crystallization method for the preparation of nano-dimensional cocrystals has been developed. The method has been shown to enable single-crystal-to-single-crystal [2+2] photodimerizations of olefins. In addition, nano-dimensional cocrystals have been shown to exhibit distinctive mechanical properties upon single-crystal-to-single-crystal transformations.

In addition to solid-state reactions and materials derived therefrom, we systematically studied hierarchies of supramolecular synthons in pharmaceutical cocrystals comprised of multi-functional molecules. Pharmaceutical cocrystals have been

recently shown to exhibit physical properties superior to those of parent drugs. Our studies involved xanthine alkaloids as pharmaceutical agents and a series of hydroxylated benzoic acids as cocrystal formers. Synthon hierarchies have been established for three xanthine alkaloids. We also discovered pharmaceutical salts that formed where cocrystallization was expected to occur. Reasons contributing to such unexpected salt formation were investigated using X-ray crystallography and computational methods. The established synthon hierarchies are expected to contribute to a better understanding of self-assembly processes in cocrystals that is crucial for the development of state-of-art drugs, and the design of organic reactions in the solid state.

TABLE OF CONTENT

LIST OF TABLES xii

LIST OF FIGURES xiv

CHAPTER 1: INTRODUCTION 1

1.1. Supramolecular chemistry and crystal engineering 1
1.1.1. Supramolecular chemistry 1
1.1.2. Crystal engineering 2
1.1.3. Supramolecular synthesis 3
1.1.4. Crystal engineering: Where from and where to? 4
1.2. Template-directed [2+2] photodimerization reactions in the solid state: principles and applications 6
1.2.1. Introduction 6
1.2.2. Template-controlled photodimerizations using organic molecules 9
1.2.3. Template-controlled photodimerization using metal ions 11
1.2.4. Applications of the products 17
1.2.4.1. 1D MOFs 18
1.2.4.2. 2D MOFs 19
1.2.4.3. Metal-organic polygons and polyhedra 22
1.2.4.4. Outlook 27
1.3. Pharmaceutical cocrystals 28
1.3.1. A brief overview 28
1.3.2. Cocrystal-screening methods 30
1.3.2.1. Mechanochemical cocrystal screening 30
1.3.2.2. Screening *via* solution-mediated phase transformation 30
1.4. Nanotechnology and crystal engineering 32
1.5. Dissertation scope and overview 33

CHAPTER 2: SUPRAMOLECULAR CONTROL OF REACTIVITY IN MOLECULAR COCRYSTALS AND MATERIALS ARRISING FROM TEMPLATE-DIRECTED SOLID STATE REACTIONS 35

2.1. Introduction 35
2.2. A Template-directed Asymmetric [2+2] Cross-photoaddition of olefins in the solid state 36
2.2.1. Introduction 36
2.2.2. Materials 41
2.2.3. Experimental 42
2.2.3.1. Synthesis of **MePE** 42
2.2.3.1. Synthesis of **ClPE** 42
2.2.3.2. Crystal growth 43
2.2.3.3. Photoreactivity studies 44
2.2.3.3. X-ray diffraction experiments 44
2.2.3.4. NMR spectroscopy 44
2.2.4. Results and discussion 44
22.2.5. Conclusion 53
2.3. A thixotropic hydrogel derived from an organic solid-state synthesis: Properties and measured densities of individual metal-organic nanoparticles 54

2.3. A thixotropic hydrogel derived from an organic solid-state synthesis: Properties and measured densities of individual metal-organic nanoparticles 54
2.3.1. Introduction 54
2.3.2. Experimental section 57
2.3.2.1. Materials 57
2.3.2.2. Synthesis of the hydrogel 57
2.3.2.3. Single-crystal X-ray diffraction. 58
2.3.2.4. Rheology measurements 58
2.3.2.5. Transmission-electron microscopy 59
2.3.2.6. AFM studies 59
2.3.2.7. STXM studies 60
2.3.3. Results and discussion 61
2.3.4. Conclusion 70

CHAPTER 3: PREPARATION AND PROPERTIES OF ORGANIC NANO-COCRYSTALS 72

3.1. Introduction 72
3.2. Preparation and reactivity of nanocrystalline cocrystals formed *via* sonocrystallization 72
3.2.1 Introduction 72
3.2.2. Materials 75
3.2.3. Experimental procedures 75
3.2.3.1. Crystallization experiments 75
3.2.3.2. Photoreactivity studies 76
3.2.3.3. X-ray diffraction studies 76
3.2.3.4. NMR spectroscopy 76
3.2.3.5. Scanning-electron microscopy 76
3.2.4. Results and discussion 77
3.2.5. Conclusion 81
3.3. Size-dependent softening and hardening of macro- and nano-sized organic cocrystals in a single-crystal transformation 82
3.3.1. Introduction 82
3.3.2. Materials 83
3.3.3. Experimental section 83
3.3.3.1. Synthesis of macro- and nano-sized cocrystals 83
3.3.3.2. AFM measurements 84
3.3.3.3. AFM nanoindentation measurements 85
3.3.3.4. SEM experiments 87
3.3.3.5. Single-crystal X-ray diffraction measurements 88
3.3.3.6. Powder X-ray diffraction measurements 88
3.3.3.7. NMR spectroscopy 88
3.3.4. Results and discussion 88
3.3.5. Conclusion 102

CHAPTER 4: SYNTHON HIERARCHIES IN PHARMACEUTICAL COCRYSTALS BASED ON XANTHINE ALKALOIDS 104

4.1 Introduction 104
4.2. Cocrystals of caffeine and (di)hydroxybenzoic acids: Structural characterization and synthon hierarchies 109
4.2.1. Introduction 109
4.2.2. Experimental section 113

4.2.2.1. Materials....113
4.2.2.2. Survey of the Cambridge Structural Database....113
4.2.2.3. Hydrogen-bond pattern analysis....114
4.2.2.3. Cocrystal screening....114
4.2.2.4. Single crystal preparation of (di)hydroxybenzoic acid cocrystals....115
4.2.2.5. Infrared (IR) spectroscopy....115
4.2.2.6. Powder X-ray diffraction measurements....115
4.2.2.7. Single crystal X-ray diffraction analyses....116
4.2.3. Results....116
4.2.3.1. Cocrystal (**caf**)·(**2HBA**)....120
4.2.3.2. Cocrystal (**caf**)·(**3HBA**)....121
4.2.3.3. Cocrystal (**caf**)·2(**4HBA**)....122
4.2.3.4. Cocrystal 2(**caf**)·(**4HBA**)....123
4.2.3.5. Cocrystal (**caf**)·(**23DBA**)·(H_2O)....125
4.2.3.6 Cocrystal (**caf**)·(**24DBA**)·(H_2O)....126
4.2.3.7. Cocrystal (**caf**)·(**25DBA**)....127
4.2.3.8. Cocrystal (**caf**)·(**35DBA**)·(H_2O)....128
4.2.3.9. Hydrogen-bond parameters....130
4.2.4. Discussion....130
4.2.5. Conclusion....139
4.3. Cocrystals of theophylline and (di)hydroxybenzoic acids: Structural characterization and synthon hierarchies....140
4.3.1 Introduction....140
4.3.2. Experimental section....145
4.3.2.1. Materials....145
4.3.2.2. Survey of the Cambridge Structural Database....145
4.3.2.3. Hydrogen-bond pattern analysis....145
4.3.2.4. Cocrystal screening....146
4.3.2.5. Single crystal growth....146
4.3.2.6. IR spectroscopy....147
4.3.2.7. Powder X-ray diffractometery....147
4.3.2.8. Single-crystal X-ray diffraction....147
4.3.3. Results....148
4.3.3.1. Cocrystal (**theo**)·(**2HBA**)....150
4.3.3.2. Cocrystal (**theo**)·(**3HBA**)....151
4.3.3.3. Cocrystal (**theo**)·(**4HBA**)....153
4.3.3.4. Cocrystal (**theo**)·(**4HBA**)....154
4.3.3.5. Cocrystal (**theo**)·(**24DBA**)....155
4.3.3.6. Cocrystal (**theo**)·(**25DBA**)....156
4.3.3.7. (H-**theo**)$^+$·(**26DBA**)$^-$·(H_2O) salt....157
4.3.3.8 Cocrystal (**theo**)·(**34DBA**)....158
4.3.3.9. Cocrystal (**theo**)·(**35DBA**)....160
4.3.4. Discussion....162
4.3.5. Conclusion....167
4.4. Cocrystals of theobromine and (di)hydroxybenzoic acids: Structural characterization and synthon hierarchies....169
4.4.1. Introduction....169
4.4.2. Experimental section....174
4.4.2.1. Materials....174
4.4.2.2. Survey of the Cambridge Structural Database....174
4.4.2.3. Cocrystal screening....175
4.4.2.4. Single crystal preparation....175
4.4.2.5. Infrared (IR) spectroscopy....176

4.4.2.6. Powder X-ray diffraction studies 176
4.4.2.7. Single crystal X-ray diffraction studies....176
4.4.2.8 Analysis of hydrogen-bond pattern....177
4.4.3. Results....177
4.4.3.1. Cocrystal (**theb**)·(**2HBA**)....179
4.4.3.2. Cocrystal (**theb**)·(**3HBA**)....180
4.4.3.3. Cocrystal (**theb**)·2(**4HBA**)·(H_2O)....181
4.4.3.4. Cocrystal (**theb**)·(**23HBA**)·(H_2O)....183
4.4.3.5. Cocrystal (**theb**)·(**24DBA**)....184
4.4.3.6. Cocrystal (**theb**)·(**25DBA**)....185
4.4.3.7. (H-**theb**)$^+$·(**26DBA**)$^-$ salt....186
4.4.3.8. Cocrystal (**theb**)·(**34DBA**)....187
4.4.3.9. Cocrystal (**theb**)·(**35DBA**)....189
4.4.4. Discussion....191
4.4.5. Conclusion....197
4.5. Unexpected salt formation at a negative pK_a value: The case of caffeine 2,6-dihydroxybenzoate....199
4.5.1 Introduction....199
4.5.2. Experimental section....201
4.5.2.1. Materials....201
4.5.2.2. Cocrystal screening....202
4.5.2.2. Single crystal preparation....202
4.5.2.3. Infrared (IR) spectroscopy....203
4.5.2.4. Powder X-ray diffraction studies....203
4.5.2.5. Single crystal X-ray diffraction studies....203
4.5.2.6. Quantum-chemical calculations....204
4.5.3. Results and discussion....205
4.5.3.1. (H-**caf**)$^+$·(**26DBA**)$^-$ salt....205
4.5.4. Conclusion....212
4.6. Towards the establishment of synthon hierarchies in related cocrystal systems: Preliminary results and outlook....213
4.6.1. Introduction....213
4.6.2. Preliminary results....214
4.6.3 Summary and outlook....216

CHAPTER 5. CONCLUSIONS....218

REFERENCES....221

APPENDIX A. GENERAL AND CRYSTALLOGRAPHIC DATA RETRIEVED FROM SINGLE-CRYSTAL X-RAY DIFFRACTION STUDIES....242

APPENDIX B. ^{1}H NMR SPECTRA....256

APPENDIX C. ESI-MASS SPECTRA AND HPLC CHROMATOGRAMS....261

APPENDIX D. A COPY OF AN ARTICLE PUBLISHED IN MOLECULAR PHARMACEUTICS IN 2007....262

APPENDIX E. A COPY OF A COMMUNICATION PUBLISHED IN NEW JOURNAL OF CHEMISTRY IN 2008....270

APPENDIX F. A COPY OF A COMMUNICATION PUBLISHED IN NEW JOURNAL OF CHEMISTRY IN 2010 (JOINT FIRST AUTHOR)....273

APPENDIX G. A COPY OF A COMMUNICATION PUBLISHED IN CHEMICAL COMMUNICATIONS IN 2010 (JOINT FIRST AUTHOR). 276

LIST OF TABLES

Table 1 X-ray crystallographic data and Young's moduli for unreacted and reacted cocrystals of 2(**5-CN-res**)·2(**4,4'-bpe**).....91

Table 2 Young's moduli for both unreacted and reacted cocrystals of 2(**5-CN-res**)·2(**4,4'-bpe**).....97

Table 3 Carbon-oxygen bond distances of the carboxylic groups of the acids.....120

Table 4 Selected hydrogen-bond parameters of the studied cocrystals (with estimated standard deviations except for fixed and riding hydrogen atoms).....129

Table 5 Twist angles θ_1 and θ_2.....132

Table 6 Overview of structural features in caffeine cocrystals involving (di)hydroxybenzoic acids.....135

Table 7 Carbon-oxygen bond distances of the carboxylic groups of the acids.....150

Table 8 Selected hydrogen-bond parameters of in **theo** cocrystals (with estimated standard deviations except for fixed and riding hydrogen atoms).....161

Table 9 Overview of structural features in the **theo** cocrystals. 165

Table 10 Carbon-oxygen bond distances of the carboxylic groups of the CCF acids 179

Table 11 Selected hydrogen-bond parameters of the **theb** solids (with estimated standard deviations except for fixed and riding hydrogen atoms).....190

Table 12 Overview of structural features in the **theb** cocrystals. 194

Table 13 Experimental and calculated pK_a values for **caf** and **26DBA** extracted from the literature.....201

Table 14 Carbon-oxygen bond distances of the carboxylic groups of the CCF acids 206

Table 15 Summary of cocrystal screening results involving xanthine derivatives and (di)hydroxybenzoic acids 215

Table A1 General and crystallographic for **MePE**, **ClPE**, and solid solution **2** (Chapter 2). 242

Table A2 General and crystallographic data for solid solution **3** and $[Cu_2(hfac)_4(\mathbf{3,4'\text{-}tpcb})]_\infty \cdot 1.6H_2O \cdot CH_3CN \cdot CHCl_3$ (Chapter 2). 243

Table A3 General and crystallographica data for 2(**5-CN-res**)·2(**4,4'-bpe**) and 2(**5-CN-res**)·(**4,4'-tpcb**) (Chapter 3).....244

Table A4 General and crystallographic data for **caf1**, **caf2** and **caf3** (Chapter 4) 245

Table A5 General and crystallographic data for **caf4**, **caf5** and **caf6** (Chapter 4). 246

Table A6 General and crystallographic data for **caf7** and **caf8** (Chapter 4)..... 247

Table A7 General and crystallographic data for **theo2**, **theo3** and **theo4** (Chapter 4). 248

Table A8 General and crystallographic data for **theo5**, **theo6** and **theo7** (Chapter 4). 249

Table A9 General and crystallographic data for **theo8**, **theo9** and **theb1** (Chapter 4). 250

Table A10 General and crystallographic data for **theb2**, **theb3** and **theb4** (Chapter 4). 251

Table A11 General and crystallographic data for **theb5**, **theb6** and **theb7** (Chapter 4). 252

Table A12 General and crystallographic data for **theb8**, **theb9** and **cafs**(RT) (Chapter 4). 253

Table A13 General and crystallographic data for **cafs** (100 K, 150 K, 200 K) (Chapter 4). 254

Table A14 General and crystallographic data related to Chapter 4: **dyp1** (Chapter 4). 255

LIST OF FIGURES

Figure 1 Supramolecular synthesis compared to conventional covalent synthesis. 1

Figure 2 Examples of supramolecular homo- and heterosynthons commonly utilized in supramolecular chemistry and crystal engineering. 3

Figure 3 Number of publications published related to crystal engineering and supramolecular chemistry as determined *via* a SciFinder survey (the number of hits relates to number of entries found as entered; duplicates could only be removed in the survey on crystal engineering) 5

Figure 4 Solid-state reactivity of *o*-ethoxy-*trans*-cinnamic acid: (a) α-, (b) β- and (c) γ-polymorphs. 8

Figure 5 Solid-state synthesis of **4,4'-tpcb** using resorcinol as a template. 10

Figure 6 Solid-state synthesis of: (a) [2.2]-paracyclophane, (b) [3]-ladderane and (c) [5]-ladderane 10

Figure 7 Crystal structures of the photoactive: (a) **dba**-UO_2Cl_2 complex and (b) ethyl-cinnamate-$SnCl_4$ complex. Reactive alkene groups highlighted using a ball and stick model (color scheme: C-gray, O-red, U-orange, Sn-blue, Cl-green). 12

Figure 8 Schematic representation of: (a) the dinuclear template first reported by Robson and Okawa, and the wireframe models of: (b) a discrete photoactive assembly and (c) a photoactive linear polymer (color scheme: C-grey, N-blue, O-red, Zn-orange)/ 13

Figure 9 Photocontrolled fluorescence in single-crystalline $[Zn_4\mathbf{L}_2(OH)_2(\mathbf{4,4'\text{-}tpcb})](ClO_4)_4 \cdot 4H_2O$ (color scheme: C-grey, N-blue, O-red, Zn-brown). 14

Figure 10 Alignment of **4-stilbz** molecules within the dinuclear complex $[Ag_2(\mathbf{4\text{-}stilbz})_4]^{2+}$. 16

Figure 11 SCSC conversion of discrete $[Ag_2(\mathbf{4\text{-}stilbz})_4]^{2+}$ assemblies to 1D $[Ag_2(\mathbf{4\text{-}py\text{-}ph\text{-}cb})_2]^{2+}{}_\infty$ polymers (color scheme: C-grey, N-blue, O-red, Ag-pink, F-yellow). 16

Figure 12 X-ray crystal structures of: (a) 1D polymer $[Cu_2(\mu_2\text{-}SO_4)_2(\mu\text{-}\mathbf{2,2'\text{-}tpcb})(H_2O)_2]_\infty$ and (b) dinuclear complex $[Cu_2(NO_3)_4(\mu\text{-}\mathbf{2,2'\text{-}tpcb})]$ and (b) space-filling of the stacking of two layers (color scheme: C-grey, N-blue, O-red, Cu-orange). 18

Figure 13 X-ray crystal structure of $[Cu_4(O_2CCH_3)_8(\mathbf{4,4'\text{-}tpcb})]_\infty$: (a) ball-and-stick model (color scheme: C-grey, N-blue, O-red, Cu-orange) and (b) space-filling of the stacking of two layers. 20

Figure 14 Perspective view of $[Co(O_2CCH_3)_2(\mathbf{4,4'\text{-}tpcb})]_\infty$ that illustrates the different cavities of the 2D MOF (color scheme: C-grey, N-blue, O-red, Co-pink). 21

Figure 15 Perspective view of $[Co(O_2CCH_3)_2(\mathbf{4,4'\text{-}tppcp})]_\infty$: (a) different cavities of the 2D framework and (b) space-filling of the included solvent molecules (color scheme: C-grey, N-blue, O-red, Co-pink). 22

Figure 16 Schematic represenatation of (a) the polyfunctional ligand **2,4'-tpcb** and the perspective view of $[Cu_6(\mathbf{2,4\text{-}tpcb})_6(H_2O)_6]^{12+}$: (b) two encapsulated ClO_4^- ions in and (c) the trigonal antiprism formed by Cu(II) ions (color scheme: C-grey, N-blue, O-red, Cl-green, Cu-orange). 23

Figure 17 Supramolecular decoration of $\{[Cu_6(\mathbf{2,4\text{-}tpcb})_6(H_2O)_6](ClO_4^-)_2\}^{10+}$ and X-ray crystal structure of $\{[Cu_6(\mathbf{2,4\text{-}tpcb})_6((+)\text{-}CPS)_6](ClO_4)_2\}^{10+}$. 24

Figure 18 Perspective view of $[Cu_4(\mathbf{2,3'\text{-}tpcb})_4(H_2O)_4]^{8+}$: (a) space-filling of the encapsulated NO_3^- ion and (b) the tetrahedron topology ions (color scheme: C-grey, N-blue, O-red, Cu-orange)....25

Figure 19 The chemical structures of polydentate **2,3'-tpcb** and **2,4'-tpcb** ligands (θ - angle of the coordination vector). 26

Figure 20 Perspective views of: (a) $[Cu_4(\mathbf{2,4\text{-}tpcb})_2(hfacac)_8]$, and (b) $[Cu_2(\mathbf{4\text{-}py\text{-}4\text{-}Cl\text{-}p\text{-}cb})_2(hfacac)_4]$ (inset: schematic representation of **4-py-4-Cl-p-cb)**. 26

Figure 21 X-ray crystal structure of: a) 2(fluox·HCl)·(succinic acid) and b) (acetaminophen)·(phenazine). Whereas the cocrystal shown in a) exhibits a superior aqueous solubility compared fluoxetine HCl, the cocrystal depicted in b) displays superior mechanical properties as compared to neat crystalline acetaminophen. 29

Figure 22 Physical stability phase diagrams of (a) cocrystals with respect to the activity of the drug, and (b) cocrystals with respect to the activity of the cocrystal former. 31

Figure 23 Examples of CPRs in solid solutions using: a) cinnamic acids, and b) 1,3-butadiene derivatives. 36

Figure 24 Absolute asymmetric synthesis involving bis[1,2,5]thiadiazolotetracyanoquinodimethane and *o*-divinylbenzene as reactants, as reported by Miyashi *et al* Hydrogen atoms are omitted for clarity. 37

Figure 25 Photoreacitiy properties of solid solutions. 38

Figure 26 Enhancement of photoreactivity properties of solid solutions using synthetic templates. 39

Figure 27 Asymmetric [2+2] cross photoaddition in a self-assembled Pd-based M_6L_4 capsule with remote chiral auxiliaries. Hydrogen atoms are omitted for clarity. 40

Figure 28 Structures of **res**, **ClPE** and **MePE**. 40

Figure 29 Template-directed synthesis in solid solutions. 41

Figure 30 Template-directed solid state synthesis of *rctt*-1,2-bis(4-pyridyl)-3,4-bis(4'-chlorophenyl)cyclobutane (a) and its X-ray crystal structure. 45

Figure 31 Chloro atoms and methyl groups being similar in shape and size (a) and benzylbenzylidenecyclopentanones used by Jones and Desiraju to engineer photoreactive solid solutions. 45

Figure 32 The crystal structure of the photostable **ClPE** polymorph obtained from acetonitrile (viewed along the crystallographic axes (1 0 -2) and (4 -1 0)). 46

Figure 33 X-ray crystal structure of **MePE**: a) juxtaposed **MePE** molecules viewed along the crystallographic *b* axies, and b) layered stacks of MePEs viewed along the crystallographic (0 1 0) and (1 0 3) planes. 47

Figure 34 X-ray diffractograms of **MePE**, solid solution **1** and **ClPE** (color scheme: red-**MePE**, black - **2**, blue – **ClPE**). 48

Figure 35 X-ray diffractograms of (**res**)·(**MePE**) (red), (**res**)·(**ClPE**) (black) and **2** (blue). 49

Figure 36 X-ray structures of: a) (**res**)·(**ClPE**)·(**MePE**), (**res**)·(**ClPE**)$_2$, (**res**)·(**MePE**)$_2$. 49

Figure 37 Crystal packing of solid solution **2** (only the **res**/**ClPE**/**MePE** component is shown for clarity). 50

Figure 38 Template-directed CPR between **ClPE** and **MePE**. 52

Figure 39 Synthesis of the 3,4'-tpcb-based hydrogel. 55

Figure 40 Metallogels upon combining $Cu(BF_4)_2{\cdot}H_2O$ and **3,4'-tpcb**: (a) acetonitrile and (b) water (T.D. Hamilton, PhD thesis, University of Iowa, 2005; reproduced with permission of the author)[153] 62

Figure 41 X-ray crystal structure of 1D $[Cu_2(hfac)_4(\mathbf{3,4'\text{-}tpcb})]_\infty$: a) crystallographic *a*-axis, b) crystal packing showing solvent-inclusion along *b*-axis, and c) packing showing solvent along *c*-axis. Solvent-occupied areas in red (color scheme: C = gray, N = blue, O = red, F = yellow, Cu = orange). 63

Figure 42 TEM micrographs of hydrogel: a) fresh gel upon standing (> 4 h), b) sol after shaking (5 min), c) transition of NMOPs of reformed gel into "pearl-necklace" structures (in red) (3-6 weeks), d) pearl-necklace nanostructures (red rectangle) and 1D nanobundles (red arrow) (6-12 weeks), e) nanobundles and nanospheres (6-12 weeks), and f) nanobundles in aged gels (about a year). 65

Figure 43 AFM height images showing main particle morphologies of the hydrogel: a) free nanoparticles with base sizes of approximately 300 nm and b) nanoparticles within the films with typical heights of 4 to 5 nm and base size of approximately 40 nm. 66

Figure 44 Shear stress versus shear rate graph for the 2% w/w thixotropic hydrogel based on $Cu(BF_4)_2$ and **3,4'-tpcb** showing a yield stress value of 8.33 Pa (indicated by arrow). A stress ramp up and down producing shear rates from about 0 to 100 sec^{-1} was used to elucidate the thixotropy of the hydrogel....67

Figure 45 STXM data: a) single energy (320 eV, 5μm x 5 μm) STXM image of NMOPs within the hydrogel and b) single particle C (•) and N (▲) atomic density *versus* particle diameter. Symbols are the data and solid lines correspond to the averaged density. 69

Figure 46 SCSC reactivity of nanodimensional crystals of: a) *p*-phenylenediacrylate and b) 2,5-distyrylpyrazine (SEM micrographs adopted from Nakanishi *et al.*[ref] and used with permission of the American Chemical Society). 73

Figure 47 Templated-directed conversion of **4,4'-bpe** into **4,4'-tpcb**. 74

Figure 48 Crystallization methods used to synthesize nano-dimensional cocrystals....75

Figure 49 SEM micrographs of macro-sized cocrystals of **1**: a) before, and b) after UV-irradiation. 77

Figure 50 X-ray powder patterns of 2(resorcinol)·2(4,4'-bpe): 1) calculated, 2) macro co-crystals (before UV-irradiation), 3) nanostructured co-crystals (before UV-irradiation), and 2(resorcinol)·(4,4'-tpcb): 4) macro co-crystals (after UV-irradiation), 5) nanostructured co-crystals (after UV-irradiation)....78

Figure 51 SEM micrographs of co-crystals of **1** grown *via* the reprecipitation method: (a) before and (b) after photoreaction. 79

Figure 52 SEM micrographs of crystals of **1** grown *via* sonocrystallization: (a) before and (b) after UV irradiation. 80

Figure 53 Typical force to the 2/3 power *versus* the tip-sample separation nanoindentation plot for unreacted (crosses) and photoreacted (triangles) nano-cocrystal. Solid lines represent linear fits and the fitted slopes were used to calculate the Young's modulus. A clear difference in slopes between the unreacted (504.5 MPa) and photoreacted (701.6 MPa) nano-cocrystals indicate different elastic properties of the two systems. The inset shows a typical force curve obtained for a single measurement on a nano-cocrystal. 87

Figure 54 Size-dependent softening and hardening of macro- and nano-sized organic cocrystals in a single-crystal transformation.....89

Figure 55 X-ray crystal structure of 2(**5-CN-res**)·2(**4,4'-bpe**): a) an assembly before UV-irradiation, b) crystal packing, c) an assembly after UV-irradiation. 90

Figure 56 Crystal packing of 2(**5-CN-res**)·2(**4,4'-bpe**): a) before and b) after a quantitative [2+2] photodimerization in the solid state (viewed along the crystallographic *a*, *b* and *c* axes). 92

Figure 57 SCSC reactivity x of 2(**5-CN-res**)·2**(4,4'-bpe**) to form 2(**5-CN-res**)·(**4,4'-tpcb**). The depicted layers are parallel to the (0 1 0) crystallographic plane of the cocrystal. 93

Figure 58 View of 2(**5-CN-res**)·2(**4,4'-bpe**) showing the crystallographic planes (010), (0 1 1) and (0 -1 1) displayed in red, blue and green, respectively (color scheme: C, grey; H, white; O, red; N, blue).....94

Figure 59 AFM height images millimeter-sized 2**(5-CN-res**)·2(**4,4'-bpe**) before and after photoreaction. (a) unreacted (0 1 1) crystal surface showing terraces and spiral pyramids and (b) unreacted (0 -1 1) face displaying uniform layer-type morphology. Photoreacted (0 1 1) (c) and (0 -1 1) (d) surfaces of the same crystal show the crystal morphology remained largely intact after reaction. 95

Figure 60 Representative AFM height images displaying the cleavage planes for (a) unreacted (0 1 1) crystal surface, (b) unreacted (0 -1 1) face, (c) photoreacted (0 1 1) face, and (d) photoreacted (0 -1 1) face. 96

Figure 61 Young's modulus distributions of measured on crystal faces (0 1 1) and (0 -1 1) before and after a photoreaction. Face (0 1 1) showed a 42% decrease in stiffness upon reaction, whereas the (0 -1 1) face displayed an 18% decrease in stiffness. Black lines shown in represent Gaussian fits. Dotted lines represent Gaussian fits for the corresponding faces in unreacted cocrystals. 98

Figure 62 SEM and AFM images and histograms of Young's modulus values for 2(**5-CN-res**)·2(**4,4'-bpe**) nano-cocrystals before, during, and after the photoreaction. SEM images of the: a) unreacted and b) photoreacted nano-cocrystals showing prism-like shapes. AFM height images (1 μm x 1 μm) of two nano-cocrystals showing approximately the same height: c) unreacted and d) reacted nano-cocrystals.....100

Figure 63 Distributions of Young's modulus values before and after a photoreaction showing a 40% increase in stiffness. Black lines represent Gaussian fits. 101

Figure 64 *In situ* AFM measurements performed during a [2+2] photoreaction of 2(**5-CN-res**)·2(**4,4'-bpe**): AFM height image of the nanocrystal before (a) and after (b) the UV exposure for a total 60 sec; (c) increase in the Young's modulus of the nanocrystal *versus* UV exposure time. Crosses are averaged moduli and error bars represent the standard deviation of the mean. 102

Figure 65. Synthon hierarchies determined by Zaworotko and coworkers. 105

Figure 66. Synthons based on O-H(hydroxy) and O^-(carboxy) groups observed in the CSD. 106

Figure 67 Chemical structures of xanthine alkaloids used to study synthon hierarchies in cocrystals involving (di)hydroxybenzoic and (di)hydroxynaphthoic acids. 107

Figure 68 Chemical structures of both benzoic and naphthoic acid derivatives used as CCFs in the described study: 2-hydroxy- (**2HBA**), 3-hydroxy- (**3HBA**), 4-hydroxy- (**4HBA**), 2,3-dihydroxy- (**23DBA**), 2,4-dihydroxy- (**24DBA**), 2,5-dihydroxy- (**25DBA**), 2,6-dihydroxy- (**26DBA**),3,4-dihydroxy- (**34DBA**), 3,5-dihydroxybenzoic acid (**35DBA**), and 1-hydroxy-2- (**1H2NA**), 2-hydroxy-1- (**2H1NA**), 3-hydroxy-2- (**3H2NA**), 6-hydroxy-2- (**6H1NA**), 1,4-dihydroxy-2- (**14D2NA**), 3,5-dihydroxy-2- (**35D2NA**), 3,7-dihydroxy-2-naphthoic acid (**37D2NA**)....108

Figure 69 Caffeine and its substructures: the imidazole (green), urea (blue) and amide (red) acceptor site. 110

Figure 70 Perspective views of: a,b) the most common imidazole-acid heterosynthon observed in caffeine-carboxylic-acid cocrystals (*i.e.* $R_2^2(7)$ and $R_3^3(11)$ motifs, respectively), c) crystal structure of caffeine and C-(n-propyl)calix(4)-resorcinarene, d) methyl-3,4,5-trihydroxybenzoate, and e) caffeine being involved in three supramolecular heterosynthons. 111

Figure 71 The crystal structure of the 1:1 **caf**:**6H2NA**. 112

Figure 72 Crystal structures of two caffeine polymorphs: a) form 1, b) form 2 (C–H···O and C–H···N interactions are highlighted in orange) 113

Figure 73 PXRD patterns of solids recovered from the screening experiments. Top/bottom: a) **caf**-hydrate/anhydrate; b) **caf-2HBA**/**2HBA**; c) **caf-3HBA**/**3HBA**; d) **caf-4HBA**/**4HBA**; e) **caf-23DBA**/**23DBA**; f) **caf-24DBA**/**24DBA**; g) **caf-25DBA**/**25DBA**; h) **caf-34DBA**/**34DBA**; i) **caf-35DBA**/**35DBA** 118

Figure 74 The carbonyl-stretching region in the FT-IR spectra of the obtained cocrystals (red) in comparison with caffeine (black) and the cocrystal former (blue). a) **2HBA**; b) **3HBA**; c) **4HBA** 1:2; d) **4HBA** 2:1; e) **23DBA**; f) **24DBA**; g) **25DBA**; h) **34DBA**; i) **35DBA**. 119

Figure 75 Perspective views: a) two-component complex of caffeine and **2HBA** defined by a $R_2^2(7)$ hydrogen-bond pattern, b) caffeine:**2HBA** complexes stacked in a "head-to-head" manner, c) stacks of caffeine:**2HBA** complexes linked via C–H···O interactions and d) adjacent sheets of caffeine:**2HBA** assemblies in (**caf**)·(**2HBA**).....121

Figure 76 Perspective views: a) four-component discrete assembly of caffeine and **3HBA** defined by a $R_2^2(7)$ hydrogen-bond pattern, b) molecular tape composed of caffeine:**3HBA** assemblies, c) molecular tapes of caffeine:**3HBA** assemblies stacked in a offset manner and d) adjacent stacks of caffeine:**3HBA** tapes linked *via* C–H···O hydrogen bonds.....122

Figure 77 Perspective views: a) **caf** involved in hydrogen-bonding with all three acceptor groups, b) molecular sheet composed of **caf** and **4HBA,** and c) sheets stacked in an offset manner being stabilized by face-to-face π-forces. 123

Figure 78 Perspective views: a) three-component discrete 2:1 assembly of caffeine and **4HBA** (only one orientation of the disordered caffeine molecule is shown for clarity), b) "zipper" motif within caffeine:**4HBA** ribbons and c) layers of caffeine:**4HBA** ribbons stacked *via* π(caffeine)···π(**4HBA**) interactions. 124

Figure 79 Perspective views: a) polymeric ribbon containing caffeine, 23DBA and water cross-linked *via* O–H(water)···N(imidazole), O−H(carboxy)···N(imidazole) and O–H(water)···O(hydroxy) hydrogen bonds, b) molecular sheet formed by molecular ribbons *via* C–H(benzene)···O(urea) interactions and c) offset stacked molecular sheets stabilized *via* π(caffeine)···π(**23DBA**) interactions. 125

Figure 80 Perspective views: a) 2D network involving caffeine, **24DBA** and water sustained by O−H(water)···O(carbonyl) and O−H(hydroxy)···O(water) hydrogen bonds, and b) caffeine-**24DBA**-water networks stacked in an ABAB manner. 126

Figure 81 Perspective views: a) wave-like 1D polymer based on caffeine and **25DBA**, b) stack of the 1D caffeine:**25DBA** polymers, and c) stacked caffeine:**25DBA** polymers sustained by weak C−H···O hydrogen bonds. 127

Figure 82 Perspective views: (a) four-component **caf**:**35DBA** assembly, (b) molecular tape consisting of caffeine, **35DBA** and water and (c) a fragment of the 3D network being based on caffeine:**35DBA** tapes that are cross-linked by water molecules 128

Figure 83 Chemical structure of caffeine with highlighted hydrogen-bond accepting functional groups. 131

Figure 84 Structural fragments investigated to determine the occurrence of O-H···O(amide) and O-H···O(urea) hydrogen bonds in the CSD. 132

Figure 85 Structural fragments investigated to determine the robustness of the O-H(hydroxy)···N(imidazole) heterosynthons in structures deposited in the CSD. 133

Figure 86 Simulated X-ray diffractogram of cocrystals (**caf**)·2(**4HBA**) and 2(**caf**)·(**4HBA**) in comparison to the diffractogram of the solid obtained from a screening experiment involving caffeine and 4-hydroxybenzoic acid. To overlay the powder patterns of (**caf**)·2(**4HBA**) and 2(**caf**)·(**4HBA**), a two-phase Rietveld refinement was performed to improve the fit of the experimental and calculated patterns. This was particularly necessary in the case of the 1:2 4-hydroxybenzoic acid/caffeine cocrystal, which appears to be more strongly effected by the temperature difference between the single-crystal and powder data collections. Color scheme: green = 2(**caf**)·(**4HBA**), red = (**caf**)·2(**4HBA**), black = physical mixture of (**caf**)·2(**4HBA**) and 2(**caf**)·(**4HBA**)) 134

Figure 87 Perspective view of: (a,b) the two positions of the disordered **caf** molecule within the 2(**caf**)·(**4HBA**) assembly, and (c) disordered **caf** molecules belonging to two neighboring "zipper"-like ribbons. 137

Figure 88 The global minimum (a) and the second ranked structure (b) of the 1:1 **caf**/**4HBA** crystal energy landscape, as determined by Price and coworkers.[259] Reproduced with permission of the American Chemical Society 139

Figure 89 Synthon hierarchy: 1º O-H(carboxy)···N(imidazole), 2º O-H(hydroxy)···O(urea) and 3º O-H(hydroxy)···O(amide) 139

Figure 90 Theophylline and its substructures: imidazole (green), urea (blue) and amide (red) hydrogen-bond accepting sites. 141

Figure 91 a) Supramolecular landscapes of **caf** and **theo** (red: hydrogen-bond acceptor, blue: hydrogen-bond donor, green: structural moiety compatible to molecular fragments that act both as donors and accptors); b) two most likely binding modes of **theo** and a carboxylic acid. 142

Figure 92 Structural fragments Hydrogen bond accepting and donating sites of **theo** (green – imidazole, red – amide, blue – urea) (a), and supramolecular synthons formed between **theo** and hydroxylated carboxylic acids. 143

Figure 93 Interactions among **theo** molecules found in cocrystals based on theo and hydroxylated carboxylic acids (a-c), as well as between **theo** molecules in the crystal structure of **theo** (d). 144

Figure 94 Perspective views: (a) a molecular ribbon based on **theo** and **2HBA** being held together by O-H(carboxy)···N(imidazole), N-H(imidazole)···O=C(amide) and bifuracated O-H(hydroxy)···O(carboxy)··· O-H(hydroxy) hydrogen bonds, (b) a 2D sheet composed of **theo**:**2HBA** ribbons, and (c) stacks of **theo**:**2HBA** sheets sustained by π(**theo**)···π(**2HBA**) interactions viewed along the (-2 0 1) and (0 1 0) crystallographic planes, d) PXRD of the **theo**/**2HBA** slurry sample compared to simulated PXRD of the **theo**:**2HBA** cocrystal. 151

Figure 95 Perspective views: (a) four-component assemblies of **theo** and **3HBA** forming a "wavy" 1D polymer, (b) molecular sheet composed 1D polymers held together by π(**theo**)···π(**25DBA**) and C-H···O interactions (viewed along the crystallographic planes (100) and (001)), (c) 3D structure composed of the stacked 2D sheets held together by π(**theo**)···π(**25DBA**) interactions and C–H···O hydrogen bonds (viewed along the crystallographic planes (1-10) and (001)).....152

Figure 96 Perspective views: (a) hydrogen-bonded "zig-zag" chains involving **theo** and **4HBA**, (b) stacks of **theo**:**4HBA** chains viewed along the crystallographic planes (2 1 0) and (0 0 1), (c) intercalated stacks of **theo**:**4HBA** held together by face-to-face π-forces viewed along the crystallographic planes (2 1 0) and (0 0 1), and the crystallographic axis *a* (inset). 153

Figure 97 Perspective views: (a) helical **theo**:**23DBA** assemblies, (b) interdigitated helices sustained *via* π(**theo**)···π(**4HBA**) interactions viewed along the crystallographic *a* axis (the red and blue helices are of opposite handedness), c) 2D sheets of **theo**:**23DHBA** helices interlinked via C–H···N and C–H···O interactions viewed along the crystallographic planes (1 0 1) and (2 -1 1) (the green and yellow molecular aggregates represent neighboring. 154

Figure 98 Perspective views of a molecular bilayer composed of hydrogen-bonded 1D **theo**:**24DBA** polymers viewed along the crystallographic *c* axis (the inset depicts a close-up view a structural fragment of the bilayer highlighting the hydrogen-bond patterns occurring within and among 1D polymers in the bilayer) (a), intercalated bilayer held together by π···π forces, viewed along the crystallographic *c* axis (b), and the crystallographic planes (1 1 0) and (0 0 1) (c). 156

Figure 99 Perspective views: (a) 2D **theo**:**25DBA** network involving **theo** and **25DBA** sustained by hydrogen bonds, and (b) stacked **theo**:**24DBA** networks held together by π···π interactions (viewed along the crystallographic (2 1 0) and (0 0 1) planes). 157

Figure 100 Perspective views: (a) four-component (H-**theo**)$^{+}$:(**26DBA**)$^{-}$ assemblies**,** (b) the 2D structure of **(**H-**theo)**$^{+}$:**(26DBA)**$^{-}$:(H_2O) assemblies viewed along the crystallographic *a* axis, and (d) the 3D structure of the (H-**theo**)$^{+}$·(**26DBA**)$^{-}$·(H_2O) salt viewed along the crystallographic *b* axis. 158

Figure 101 Perspective views: (a) molecular sheets composed of **theo** and **34DBA** molecules viewed along the crystallographic planes (1 1 0) and (0 0 1), and (b) sheets stacked in a "head-to-tail" fashion viewed along the crystallographic planes (0 1 -1) and (-2 2 1). 159

Figure 102 Perspective views: (a) "chess plates" composed of **theo** and **35DBA** dimers viewed along the crystallographic planes (116) and (1-20) (inset: space-fill view of the **theo**:**35DBA** resembling the tilling of a chess plate), (b) stacked "chess plates" being sustained by π(**theo**)···π(**35DBA**) and C-H···O forces viewed along the crystallographic planes (2 0 -1) and (0 1 0). 160

Figure 103 Chemical structures of **theo** and **caf** with highlighted structural moieties (in red) that are most likely to interact with a carboxylic acid. 164

Figure 104 Established synthon hierarchy in **theo** solids based on hydroxybenzoic acids..... 168

Figure 105 Theobromine and its substructures: imidazole (green), urea (blue) and amide (red) hydrogen-bonding sites. 169

Figure 106 Supramolecular landscapes of **theo** and **theb** (red: hydrogen-bond acceptor, blue: hydrogen-bond donor, green: structural moiety compatible to molecular fragments that act both as donors and acceptors); b) three probable binding modes of **theb** and a carboxylic acid. 170

Figure 107 Crystal structures of: a) CSATBR exhibiting binding mode I and II, b) HIJYEF displaying binding mode I and III, and c) HIJYAB exhibiting binding mode I and II. 172

Figure 108 Crystal structures of: a) (**theb**)·(gallic acid)·2(H_2O), and b) (**theb**)·(quercitin)·2(H_2O) 173

Figure 109 Crystal structure of **theb**: a) a **theb** dimer comprised of two crystallographically independent molecules, b) self-assembled **theb** dimers. 174

Figure 110 Perspective views: a) a discrete four-component assembly **theb**:**2HBA** assembly held together by O-H(amide)···N(amide), O-H(carboxy)···N(imidazole) and O-H(hydroxy)···O(carboxy) hydrogen bonds, b) a 2D layer composed of **theo**:**2HBA** assemblies being sustained by π(**theb**)···π(**2HBA**) interactions [viewed along the (0 1 10) and (1 0 0) crystallographic plane], and c) stacks of 2D layers held together by C-H···O interactions viewed along the (0 0 1) and (0 1 0) crystallographic planes. 180

Figure 111 Perspective views: (a) 1D ribbon composed of four-component **theo**:**3HBA** assemblies (highlighted in red), (b) offset stacked **theb**:**3HBA** ribbons being held together by π(**theo**)$\cdots\pi$(**3HBA**) interactions (the displayed ribbons are parallel to the (1 -5 -2) crystallographic plane; inset: viewed along the crystallographic planes (0 1 0) and (-1 0 2)), (c) stacks of **theb**:**3HBA** ribbons self-assembled by C–H$\cdots$O and C–H$\cdots\pi$ interactions exhibiting a herringbone motif (viewed along the crystallographic planes (0 1 0) and (-1 0 2)).++-.....181

Figure 112 Perspective views: a) six-component **theb**:**4HBA** assemblies hydrogen-bonded to water molecules b) 1D ribbons of six-component **theb**:**4HBA** assemblies held together by water molecules (inset: a lone theb:4HBA assembly), c) stacks of **theb**:**4HBA**:H_2O ribbons viewed along the crystallographic (1 0 0) and (0 0 1) planes, d) neighboring stacks of **theb**:**4HBA** held together by C-H$\cdots$O interactions (viewed along the crystallographic (-1 0 1) and (0 1 0) planes). 182

Figure 113 Perspective views: a) 1D chain composed of **theb**, **23DBA** and water molecules, b) hydrogen-bonded 2D sheet composed of **theb**:**23DBA**:H_2O assemblies (viewed along the crystallographic planes (0 1 0) and (1 0 -1)), c) layered 3D structure comprised of **theb**, **23DBA** and water molecules (viewed along the crystallographic planes (0 1 0) and (-3 -1 -1)), and d) fragments of two stacked sheets held together by O–H(water)$\cdots$O(urea) hydrogen bonds. 183

Figure 114 Perspective views of: a) an 1D **theb**:**24DBA** polymer (oxygen atoms depicted using the "ball and stick" model represent atoms participate in hydrogen bonding within two layers of 1D **theb**:**24DBA** polymers, and act as either donors or acceptors), b) a **theb**:**24DBA** bilayer viewed along the (0 1 0) and (1 0 -1) crystallographic planes, c) two stacked bilayers viewed along the crystallographic *a* axis. 185

Figure 115 Perspective views: a) 1D ribbons composed of four-component **theb**:**25DBA** assemblies (highlighted using van der Waals surfaces), b) stacked **theb**:**25DBA** ribbons held together by $\pi\cdots\pi$ interactions viewed along the crystallographic (0 1 0) and (1 0 2) planes, and c) stacks of **theb**:**25DBA** ribbons view along the crystallographic (0 1 0) and (1 0 1) planes.....186

Figure 116 Perspective views: a) discrete four-component **theb**:**26DBA** assembly**,** b) stacked **theb**:**26DBA** assemblies viewed along the crystallographic (-1 1 0) and (0 0 1) planes (inset depicts a view of **theb**:**26DBA** stacks viewed along the crystallographic *b* axis), and c) the 3D structure of the **theb**:**26DBA** solid viewed along the crystallographic (2 0 1) and (0 1 0) planes. 187

Figure 117 Perspective views: a) molecular sheet composed of **theb** and **34DBA** molecules viewed along the crystallographic *c* axis (the molecular tape is highlighted by using van der Waals surfaces; the four-component assembly is high-lighted in green), and b) stacked sheets viewed along the crystallographic planes (1 0 0) and (0 1 1). 188

Figure 118 Perspective views: a) 2D sheets viewed along the crystallographic *c* axis (inset depicts pores in the sheet; **theb** and **35DBA** dimers are highlighted using the "space fill" model), and b) stacked planes viewed along the crystallographic *b* axis. 189

Figure 119 Factors contributing to the lack of phenol:imidazole interactions in **theb** cocrystals. 193

Figure 120 Amides "A" and "B" in the structure of **theb**. 195

Figure 121 Number of hydrogen-bond donors in the xanthine alkaloid compared to the occurrence of discrete assemblies in xanthine-alkaloid cocrystals (or salts). 196

Figure 122 Established synthon hierarchy in **theb** solids based on hydroxybenzoic acids. 198

Figure 123 Chemical structures of **caf** and **26DBA**. 200

Figure 124 Caffeine 2,6-dihydroxybenzoate: a) caffeine (**caf**) and 2,6-dihydroxybenzoic acid (**26DBA**), X-ray crystal structures of: b) a two-component (H-caf)+·(26DBA)- assembly, c) stacks of (H-**caf**)+·(**26DBA**)$^-$ pairs, and d) stacks (in green and yellow) sustained *via* weak C–H···O interactions. 206

Figure 125 Dielectric constants of solvent used to determine the impact of solvent polarities on the O-H(carboxy, **26DBA**) →N(imidazole, **caf**). 207

Figure 126 Relative energies of "salt" and "cocrystal" minima, as calculated in various solvents. 209

Figure 127 Results of PES scans involving **caf**:**2HBA** and **caf**:**26DBA** complexes. 210

Figure 128 Results of PES scans involving **caf**:**26DBA** complexes wherein the H(*ortho*-OH,**26DBA**) assumes various positions along the O(COOOH) ·····(OH) trajectory. 211

Figure 129 Charged (H-**caf**)$^+$ and (**26DBA**)$^-$ species stabilized within molecular stacks in the solid state (blue: positive charged imidazolium moiety; red – negatively charged benzoate moiety). 212

Figure 130 X-ray crystal structure of (**dyp**)·(**23DBA**)·(H_2O) being sustained by O-H(hydroxy)···O(hydroxy), O-H(water)···N(imidazole) and O-H(carboxy)···O(hydroxy) hydrogen bonds. 216

Figure B1 ^{1}H-NMR spectrum of solid solution **1** before UV irradiation. 256

Figure B2 ^{1}H-NMR spectrum of solid solution **1** after UV irradiation. 256

Figure B3 ^{1}H-NMR spectrum of solid solution **2** before UV irradiation. 257

Figure B4 ^{1}H-NMR spectrum of solid solution **2** after UV irradiation. 257

Figure B5 ^{1}H-NMR spectrum of 2(**res**)·2(**4,4'-bpe**) (macro cocrystals before UV-irradiation). 258

Figure B6 ^{1}H-NMR spectrum of 2(**res**)·2(**4,4'-bpe**) (macro cocrystals after UV-irradiation)....258

Figure B7 ^{1}H-NMR spectrum of 2(**res**)·2(**4,4'-bpe**) (nanostructured cocrystals before UV-irradiation). 259

Figure B8 ^{1}H-NMR spectrum of 2(**res**)·2(**4,4'-bpe**) (nanostructured cocrystals after UV-irradiation). 259

Figure B9 ^{1}H-NMR spectrum of nanodimensional 2(**5-CN-res**)·(**4,4'-bpe**) cocrystals before UV irradiation. 260

Figure B10 ^{1}H-NMR spectrum of nanodimensional 2(**5-CN-res**)·(**4,4'-bpe**) cocrystals after UV irradiation. 260

Figure C1 ESI-mass spectrum of the UV irradiated solid solution **2**....261

Figure C2 Chromatogram of the physical mixture of photoproducts used to quantitatively analyze the products obtained from solid solution **2**. 261

CHAPTER 1: INTRODUCTION

1.1. Supramolecular chemistry and crystal engineering

1.1.1. Supramolecular chemistry

Supramolecular chemistry is known as *"...the chemistry of the intermolecular bond, covering the structures and functions of the entities formed by association of two or more chemical species*", or more colloquially as "*chemistry beyond the molecule*".[1] Supramolecular chemistry encompasses the design and synthesis of so-called "supermolecules",[2] *i.e.* chemical entities held together by non-covalent interactions such as hydrogen bonds, halogen bonds, coordination forces or $\pi\cdots\pi$ interactions (Fig. 1). Research in this new branch of chemistry is mainly focused on host-guest systems, coordination polymers, anion and cation binding, self-assembly processes, biological mimics, gels, polymers, fibers, liquid crystals and other topics and materials.[3]

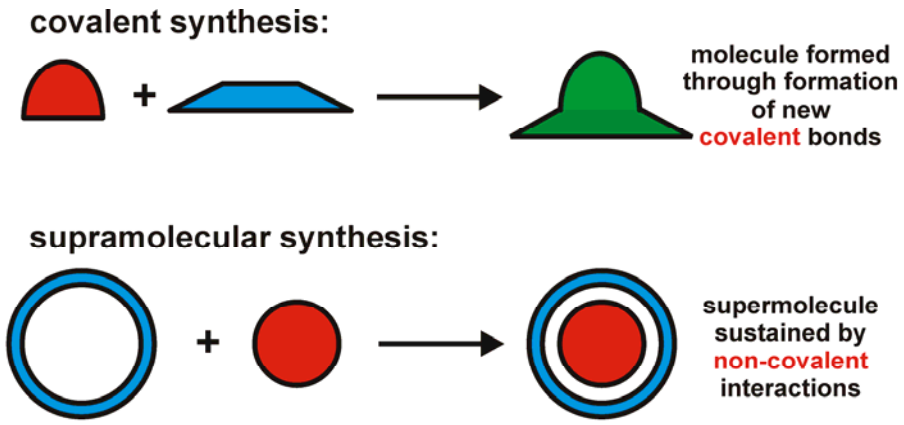

Figure 1 Supramolecular synthesis compared to conventional covalent synthesis.

1.1.2. Crystal engineering

Crystal engineering is a branch of supramolecular chemistry that concerns the crystalline solid state and "*...is defined as the understanding of intermolecular interactions in the context of crystal packing and in the utilization of such understanding in the design of new solids with desired physical and chemical properties*" (G. R. Desiraju, 1989).[4]

The term was originally introduced by R. Pepinsky in 1955 in the proceedings of the American Physical Society Meeting held in Mexico City.[5] The term was coined to describe a new concept in crystallographic structural analysis. Specifically, Pepinsky crystallized chiral ionic species with metal-organic complexes in order to determine absolute structures of enantionpure organic ions: "*Crystallization of organic ions with metal-containing complex ions of suitable sizes, charges and solubilities results in structures with cells and symmetries determined chiefly by packing of complex ions. These cells and symmetries are to a good extent controllable: hence crystals with advantageous properties can be 'engineered'...*".[5, 6] The term crystal engineering was then first applied in 1971 by Schmidt in the context of synthetic photochemistry: *"...we shall, in the present context of synthetic and mechanistic photochemistry, be able to 'engineer' crystal structures having intermolecular contact geometries appropriate for chemical reaction…*".[7] That reactive crystals can be engineered became obvious to Schmidt's upon the discovery that certain functional groups tend to be involved in interactions (*e.g.* chloro···chloro interactions) that can position two molecules for a intermolecular [2+2] photodimerization in the crystalline solid state. In the late 1980s, crystal engineering began to evolve from a concept to a scientific discipline focused on the design of organic solids with desired structures and properties engineered at the molecular level and derived from molecular building blocks associated by intermolecular forces (*i.e.* supramolecular synthons).[8, 9]

1.1.3. Supramolecular synthesis

Molecular cocrystals are, together with coordination compounds (*i.e.* coordination polymers or metal-organic frameworks), the most common synthetic targets in crystal engineering. Molecular cocrystals are multi-component crystals that can be envisioned as networks wherein the molecules represent nodes, whereas directional non-covalent interactions among the molecules represent node connections. The crystal engineer's ultimate goal is to develop a profound understanding of how molecules (*i.e.* network nodes) are being connected by intermolecular interactions (*i.e.* node linkers) within the crystalline network. Such knowledge can then be eventually utilized to construct molecular networks with designed architectures and specific physicochemical properties.

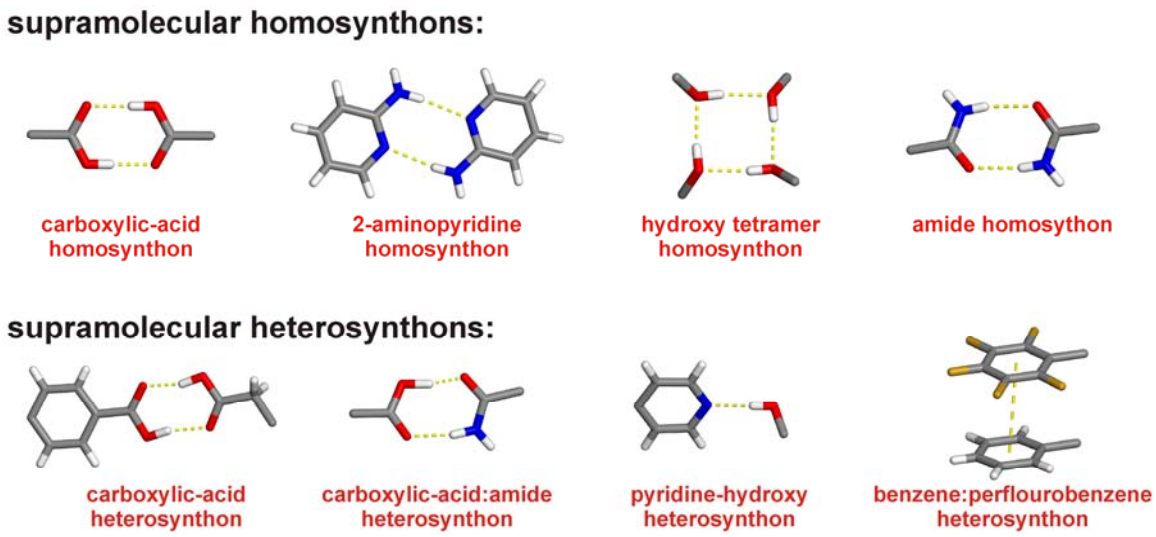

Figure 2 Examples of supramolecular homo- and heterosynthons commonly utilized in supramolecular chemistry and crystal engineering.

To construct a crystal structure, crystal engineers resort to retrosynthetic analyses[10, 11] of their crystalline synthetic targets. This means that the crystalline networks are transformed into simple precursors (*i.e.* molecules) with particular

functional groups that have the capacity to self-assemble into the targeted network. The results of retrosynthetic analyses are called supramolecular synthons, and were coined by Desiraju in the 1990s: *"Supramolecular synthons are structural units within supermolecules which can be formed and/or assembled by known or conceivable synthetic operations involving intermolecular interactions… Supramolecular synthons are spatial arrangements of intermolecular interactions and play the same focusing role in supramolecular synthesis that conventional synthons do in molecular synthesis."*[9]

The crystal engineer distinguishes two kind of supramolecular synthons: the homo- and heterosynthons. A homosynthon is a supramolecular entity sustained by two (or more) identical chemical entities, whereas heterodimers are supramolecular entities comprised of distinct chemical bodies with complementary functional groups (Fig. 2).[3, 9]

1.1.4. Crystal engineering: Where from and where to?

Crystal engineering is a very young scientific discipline that started to attract a great interest of both organic and inorganic solid-state chemists since the early 1990. The tremendous interest in supramolecular chemistry and crystal engineering is evidenced by a continuing growth of numbers of publications related to this field (Fig. 3). That crystal engineering continuously gains interest and recognition as valuable scientific discipline is also evidenced by the recent emergence of scientific meetings being exclusively focused on crystal engineering.[12, 13]

Crystal engineering nowadays covers a wide variety of different areas of interest. Within the last ten years, three topics, namely coordination polymers, pharmaceutical cocrystals and solid-state photoreactions, seemed to catch more attention than any other current topic in the field. The interest in these topics stems form the realization of potential long-term practical applications of designed crystalline materials. Coordination polymers (*i.e.* metal-organic frameworks) have been shown to exhibit exceptional gas-storage and uptake properties. In addition, it has been demonstrated that the confined

coordination spaces facilitate organic reactions that could so far not been achieved in solution. Pharmaceutical cocrystals have been shown to exhibit enhanced physicochemical properties that are superior to those of parent drugs, solvates, polymorphs and pharmaceutical salts. Finally, highly organized crystalline lattices have been recognized as perfectly suitable media for quantitative and stereospecific photo-induced reactions. Cocrystallization and synthetic templates are, therefore, nowadays commonly used as a means to align reactive molecules that are photostable in their single-component crystals.

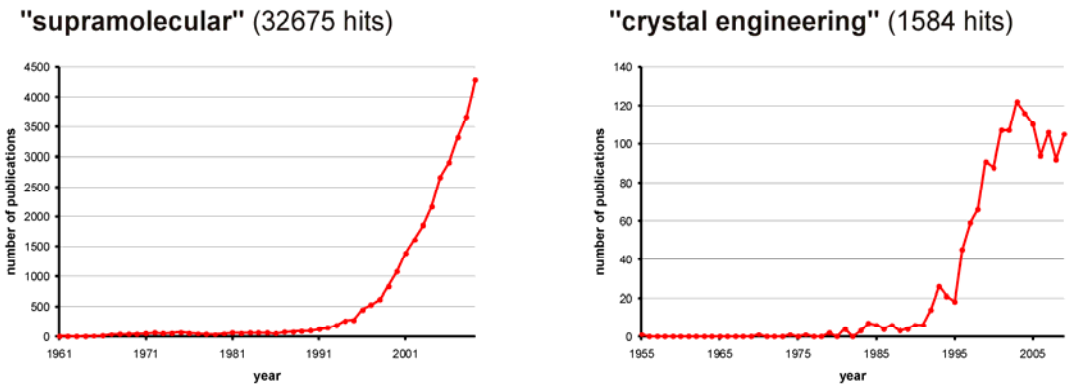

Figure 3 Number of publications published related to crystal engineering and supramolecular chemistry as determined *via* a SciFinder survey (the number of hits relates to number of entries found as entered; duplicates could only be removed in the survey on crystal engineering)

Although more and more intriguing applications of crystal engineering are reported weekly, crystal engineers still struggle to fully understand self-assembly processes of molecules and metal-containing chemical species. Specifically, our current understanding of self-assembly processes is, unfortunately, still limited to processes that involve barely more than two functional groups. Even in that case, we are only able to reliably predict synthon formation in crystals, whereas prediction of packing motives and

overall crystal structures remain hard to achieve at this point. Importantly and surprisingly, intriguing topics such as engineered nano-dimensional cocrystals, still remain unexplored despite the known importance and technological applicability of nanomaterials. Another important but neglected issue in crystal engineering is the design of molecular cocrystals composed of more than two components,[14] as well as the understanding of synthon hierarchies in the solid state or how *multiple* functional groups self-assemble in the solid state.[15, 16]

In order to gain full control over self-assembly processes in the solid state and to develop high-end functional materials with industrial applications (e.g. nano-computing, catalysis, biomimesys and implantology)[17], important processes such as crystallization, nucleation, crystal-structure prediction and synthon hierarchies need to be understood to a full extend.

1.2. Template-directed [2+2] photodimerization reactions in the solid state: principles and applications

1.2.1. Introduction

Reactions that occur in the organic solid state bear widespread relevance to organic synthesis and materials science. The homogeneous, confined, and surprisingly flexible nature[18] of a molecular lattice means that molecules can react in solids with perfect control of stereochemistry and in quantitative yield. That such reactions occur in the absence of solvent also means that reactions in the organic solid state bear relevance to the field of green chemistry.[19] Green chemistry has emerged owing to an accepted need to reduce and prevent pollution from the use and production of hazardous chemicals in synthetic chemistry. Thus, the development of strategies that employ reduced amounts of solvent, as well as other chemical auxiliaries, in chemical synthesis is a central goal of green chemistry[19] that our group started to pursue about a decade ago.

Photo-induced reactions in the organic solid state were first discovered well over hundred years ago. In the early 1900's, Riiber discovered that cynnamylidineacetic acid and cynnamylidinemalonic acid photoreacted in the solid state to give cyclobutanes.[20-22] Two decades later, Stobbe and de Jong discovered that the α- and β-forms of *trans*-cinnamic acid undergo solid-state [2+2] photodimerizations to give α-truxillic and β-truxinic acid, respectively. It was proposed that the reactions were a consequence of packing of the monomer units;[23-25] however, the mechanistic details of the reactions were not well understood. This was largely a result of a lack of efficient methods to characterize the structures of organic solids. Consequently, it was difficult, at the time, to foresee practical uses of reactions in organic solids. This contrasts reactivity in the liquid phase which was being systematically studied and becoming reasonably-well understood. Rapid progress in the area of crystallographic structural analysis (*e.g.* CCD area detectors) has enabled diffraction data to be collected and analyzed on timescales of minutes-to-hours (as contrasted to days-to-months data collections old-fashioned single-point detectors). In addition, recent studies in the areas of supramolecular chemistry[3] and crystal engineering[26] have resulted in significant improvements of our understanding of how weak intermolecular interactions direct the self-assembly process of molecules in the solid state. Consequently, the rational design and the construction of crystalline molecular solids with desired physicochemical properties (*e.g.* reactivity, optical) has now become a reality.

Based on X-ray crystal structure analyses of a wide range of cinnamic acids, Schmidt and co-workers identified, during the 1960's, structural requirements for two carbon-carbon double (C=C) bonds to undergo a [2+2] photodimerization in the solid state.[7] The requirements, collectively known as the topochemical [27] postulate, state that a [2+2] photodimerization can be expected to occur if the C=C bonds lie parallel and with a centre-to-centre distance < 4.2 Å. Thus, of the three known polymorphs of *o*-ethoxy-*trans*-cinnamic acid, namely α-, β- and γ-, the α- and β-forms are photoactive (Fig. 4).[28,

[29] In all three solids, the alkenes pack parallel in one-dimensional (1D) slipped stacks. In the cases of the *α*- and *β*-forms, C=C bonds of neighbouring monomers lie parallel and separated by approximately 4 Å. Adjacent monomers of the α-polymorph adopt an antiparallel orientation, being related by a crystallographic centre of inversion. This geometry leads to the formation of the 'head-to-tail' *α*-truxillic acid dimer upon photoreaction. Adjacent monomers of the *β*-polymorph adopt a parallel orientation, being related by a translation axis. Photodimerization of the *β*-polymorph produces a 'head-to-head' *β*-truxinic acid. The *γ*-polymorph is photostable, with the C=C bonds being too far apart to react.

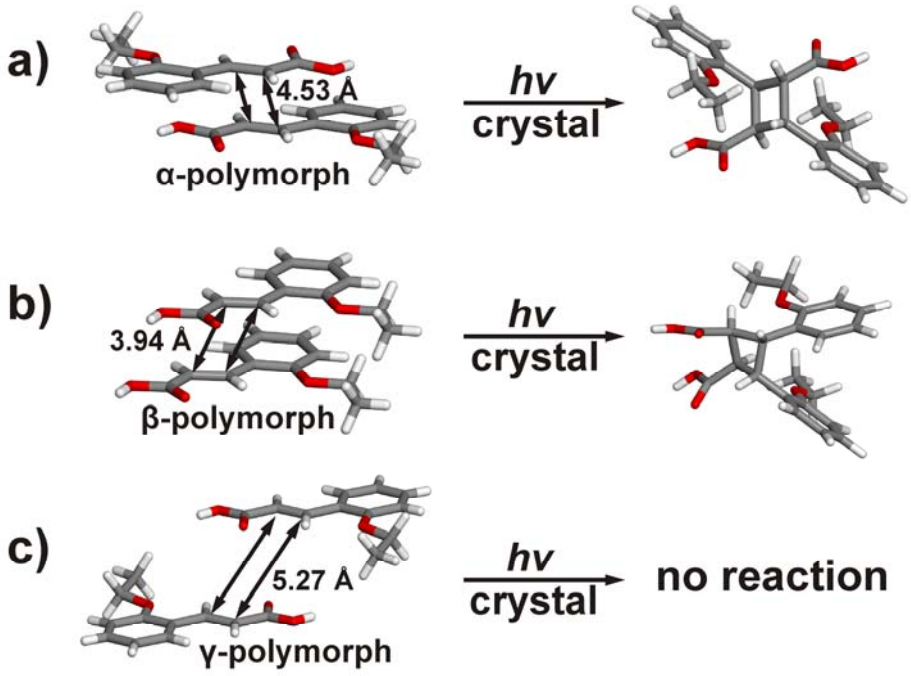

Figure 4 Solid-state reactivity of *o*-ethoxy-*trans*-cinnamic acid: (a) α-, (b) β- and (c) γ-polymorphs.

In recent years, we have introduced a method that provides an ability to direct [2+2] photodimerizations in the solid state using principles of molecular recognition and self-assembly.[30] The method has exploited the strength and directionality of hydrogen bonds to construct target molecules such as cyclophanes[31] and ladderanes[32] using small molecules in the form of templates. The template approach has also been expanded to principles of coordination-driven self-assembly.[33-35] We have also demonstrated how molecules constructed using the template method can be used as building blocks of finite and infinite coordination assemblies.[36]

1.2.2. Template-controlled photodimerizations using organic molecules

In 2000, we introduced a method to control chemical reactivity in the in molecular cocrystals using small organic molecules that function as linear templates.[30] The templates assemble olefins for [2+2] photodimerizations within multi-component supramolecular assemblies. In particular, we demonstrated that resorcinol (**res**) can be used as a linear template to assemble and juxtapose *trans*-1,2-bis(4-pyridyl)ethylene (**4,4'-bpe**) for photoreaction. Co-crystallization of **res** with **4,4'-bpe** produced the four-component assembly 2(**res**)·2(**4,4'-bpe**) held together by four O-H···N hydrogen bonds. The two olefins were oriented by res in a parallel fashion and at a distance of 3.65 Å (Fig. 5). This placed the C=C bonds of **4,4'-bpe** in a geometry that conformed to the topochemical postulate of Schmidt for reaction. UV-irradiation of crystalline 2(**res**)·2(**4,4'-bpe**) produced the corresponding photodimer, *rctt*-tetrakis(4-pyridyl)cyclobutane (**4,4'-tpcb**), regiospecifically and in 100% yield.[37]

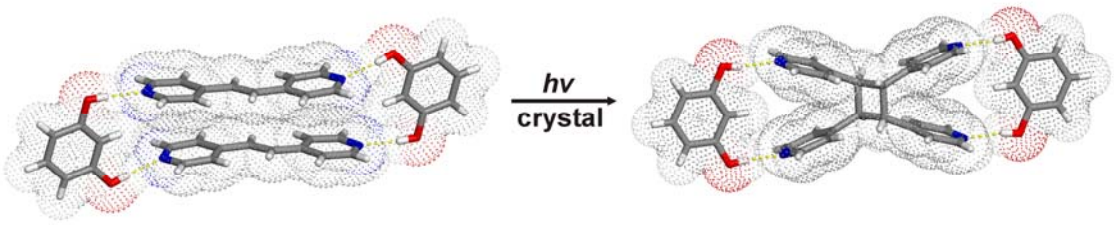

Figure 5 Solid-state synthesis of **4,4'-tpcb** using resorcinol as a template.

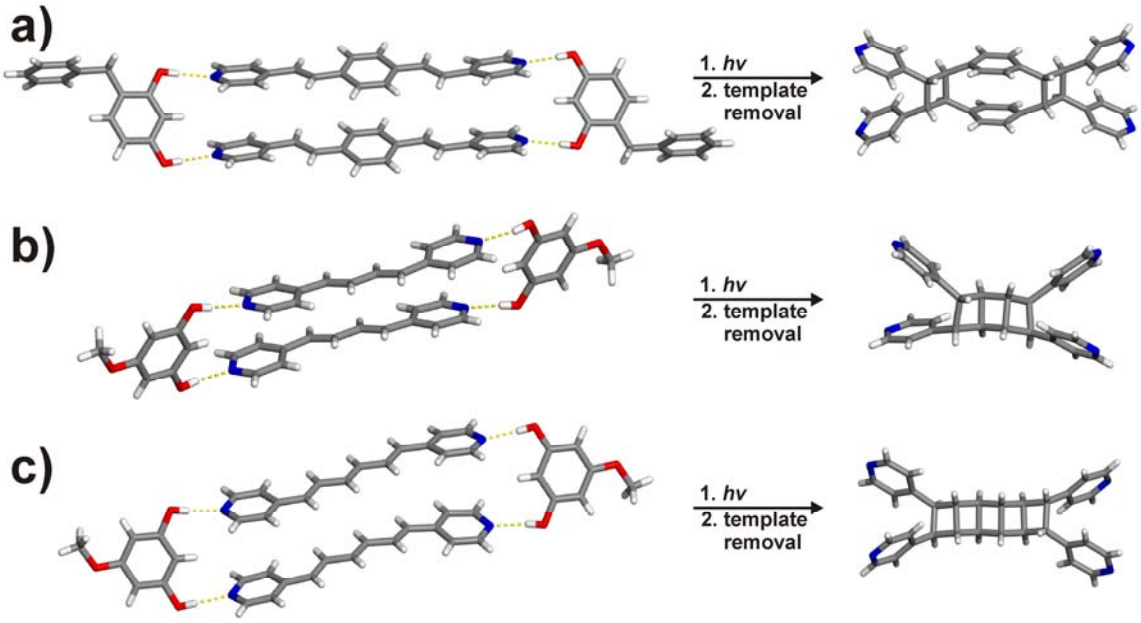

Figure 6 Solid-state synthesis of: (a) [2.2]-paracyclophane, (b) [3]-ladderane and (c) [5]-ladderane

In addition to **4,4'-tpcb**, we showed that the method can be used to construct relatively complex molecules such as a [2.2]paracyclophane and [*n*]-ladderanes (where: *n* = 3 or 5).[31, 32] Templates based on res were used to organize di- and triolefins, similar to 2(**res**)·2(**4,4'-bpe**), within four-component hydrogen-bonded assemblies. UV-irradiation

of the solids produced the targeted cyclophane and ladderanes regiospecifically and in quantitative yield (Fig. 6).

1.2.3. Template-controlled photodimerization using metal ions

Inspired by work in the field of coordination-driven self-assembly,[38-41] we have recently addressed whether transition-metal-ion complexes can be used as linear templates to direct the [2+2] photodimerization in the solid state. The field of coordination-driven self-assembly, which has experienced tremendous growth during the last decade,[41, 42] involves reactions of metal ions with bi- and polytopic ligands. The metal and organic components are used to form finite (*e.g.* metallomacrocycle) and/or infinite (*e.g.* metal-organic framework (MOF)) self-assembled frameworks. The frameworks are designed to exhibit properties (*e.g.* host-guest, magnetic) typically not encountered in the individual components. We wondered whether coordination bonds could be used to effectively replace the hydrogen bonds of a resorcinol-based template. In such a design, a dinuclear metal complex would assemble and preorganize two olefins to react in a solid. The ensuing solid-state reaction could also be used to affect bulk-physical properties[35] conferred by the metals in a solid.

Prior to our work, there were two examples in which a metal-ion complex facilitated a [2+2] photodimerization in the solid state (Fig. 7).[43] In particular, Praetorius and Korn reported the ability of a mononuclear complex of uranyl chloride and *trans*,*trans*-dibenzylideneacetone (**dba**) to undergo a stereospecific photodimerization to give the truxillic-type dimer *rctt*-1,3-bis(3-phenylprop-2-enol-oxo)-2,4-bis(phenyl)cyclobutane (Fig 7a).[44] X-ray crystal structures of both the unsolvated and solvated forms, $[(UO_2)Cl_2(\mathbf{dba})_2]$ and $[(UO_2)Cl_2(\mathbf{dba})_2]\cdot 2CH_3CO_2H$, showed that the metal ions adopted an octahedral geometry surrounded by two chlorine atoms, two

oxygen atoms of the uranyl group, and two keto-oxygen atoms of the **dba** ligand (Fig. 7a).[45]

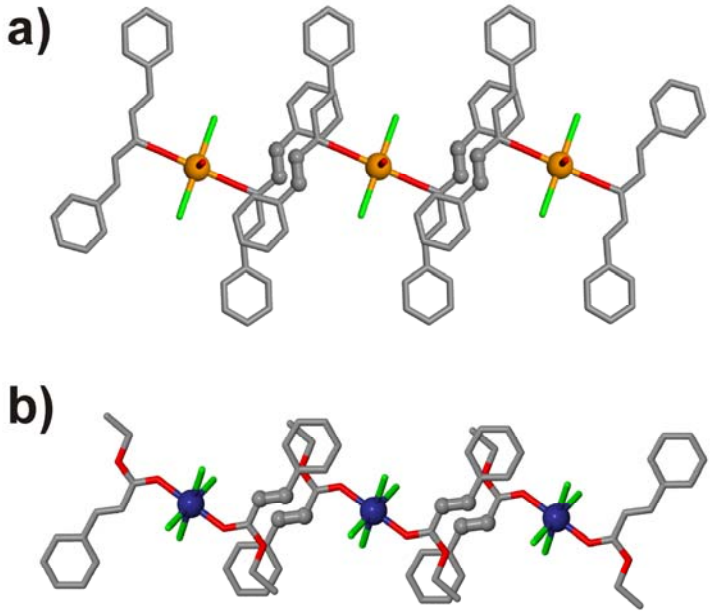

Figure 7 Crystal structures of the photoactive: (a) **dba**-UO_2Cl_2 complex and (b) ethyl-cinnamate-$SnCl_4$ complex. Reactive alkene groups highlighted using a ball and stick model (color scheme: C-gray, O-red, U-orange, Sn-blue, Cl-green).

The complexes assembled in the solid such that the distances between the alkenes of adjacent **dba** ligands were 4.09 Å and 3.51 Å in the unsolvated and solvated forms, respectively. The reactivity was, thus, largely the result of the packing of the complexes. Later, Lewis and co-workers demonstrated [2+2] photoreactivity in a series of crystalline cinnamic esters mediated by Lewis acids (*e.g.* $SnCl_4$).[46] The cinnamic esters formed 1:1 complexes with BF_3 and 2:1 complexes with $SnCl_4$. UV-irradiation of the solids produced truxillic-type dimers (Fig. 7b). A structure analysis of the ethyl cinnamate-$SnCl_4$ complex revealed an octahedral coordination environment around the Sn(IV) ion.

The photoreaction occurred between neighboring cinnamate ligands. Adjacent ligands were stacked in a head-to-tail fashion, being separated by 4.12 Å.

Our first study involving a dinuclear complex involved the Schiff-base complex $[Zn_2\mathbf{L}(OH)]^{2+}$ (where: **L** = 2,6-bis[*N*-(2-pyridylethyl)formimidoyl]-4-methylphenol) as a template (Fig. 8).[35] The Schiff-base ligand was originally introduced by Robson and Okawa as a model of enzymatic processes (Fig. 8a.).[47] An analysis of the Cambridge Structural Database (CSD) [48] revealed that the metal atoms of such complexes are separated on the order of 3.10 to 3.15 Å. This range was well within the distance criterion of Schmidt for photodimerization in a solid. We showed that reaction of $[Zn_2\mathbf{L}(OH)](ClO_4)_2$ with **4,4'-bpe** produces the tetranuclear assembly $[Zn_4\mathbf{L}(OH)_2(4,4'\text{-bpe})_2](ClO_4)_2$ (Fig. 8b).

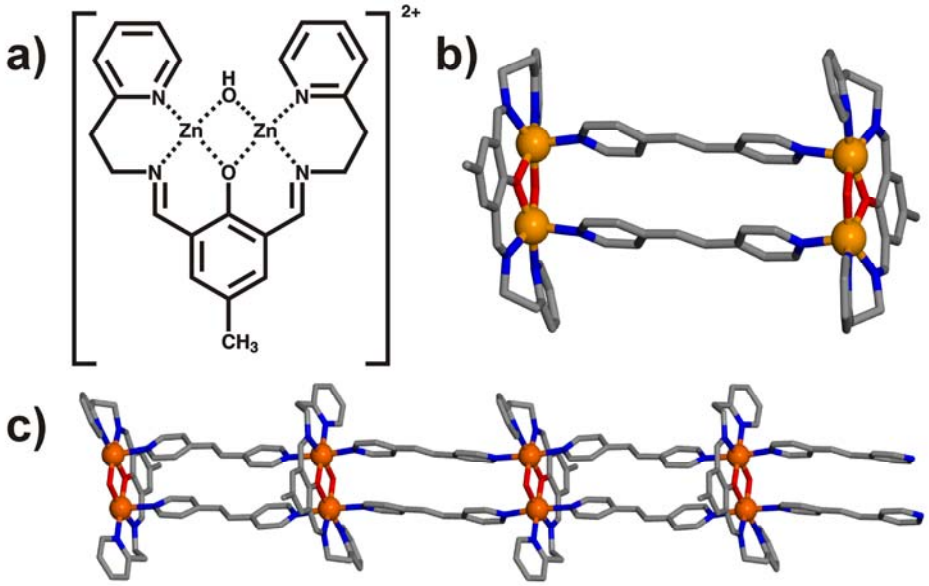

Figure 8 Schematic representation of: (a) the dinuclear template first reported by Robson and Okawa, and the wireframe models of: (b) a discrete photoactive assembly and (c) a photoactive linear polymer (color scheme: C-grey, N-blue, O-red, Zn-orange)/

The metal atoms of the assembly adopted a square pyramidal coordination environment, with two stacked pyridines located in the apical positions. The C=C bonds of the olefins were arranged parallel and separated by 3.64 Å. UV-irradiation of the solid produced **4,4'-tpcb** in quantitative yield. We later showed that stacked molecules of **4,4'-bpe** could be achieved within the 1D MOF $\{[Zn_2\mathbf{L}(OH)(4,4'\text{-bpe})_2](ClO_4)_2\}_\infty$.[49] In this case, each metal ion adopted an octahedral coordination environment. The solid reacted to give **4,4'-tpcb** in 95% yield (Fig. 8c).

During the course of our studies involving tetranuclear $[Zn_4\mathbf{L}(OH)_2(4,4'\text{-bpe})_2](ClO_4)_2$, we determined that the photoreaction proceeded *via* a rare single-crystal-to-single-crystal (SCSC) transformation (Fig. 9).[50, 51] We also discovered that the single crystals displayed different fluorescence emissions before and after the photoreaction.[35] Specifically, excitation of the crystals using 290 nm light prior to the photoreaction produced a blue emission at 464 nm, while the fully reacted solid produced a green emission at 520 nm.

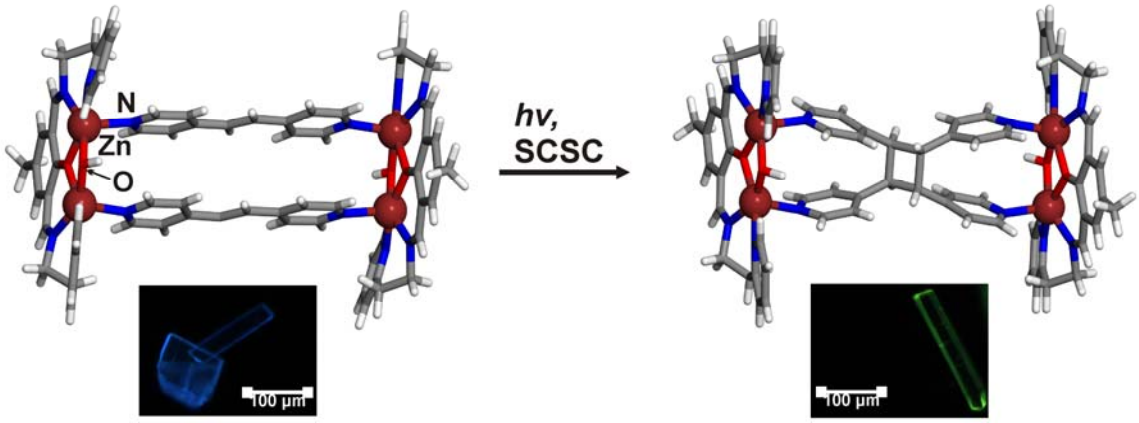

Figure 9 Photocontrolled fluorescence in single-crystalline $[Zn_4\mathbf{L}_2(OH)_2(\mathbf{4,4'\text{-}tpcb})](ClO_4)_4\cdot 4H_2O$ (color scheme: C-grey, N-blue, O-red, Zn-brown).

That the change in emission was a consequence of the solid-state reaction was supported by laser-scanning confocal fluorescence microscopy, which revealed a difference in fluorescence between the unreacted and reacted solid. To our knowledge, the tetranuclear assembly represented the first example of a SCSC reaction that exhibited photocontrolled fluorescence. The reaction involving the 1D framework $[Zn_2\mathbf{L}(OH)(\mathbf{4,4'\text{-}bpe})_2](ClO_4)_2$ did not occur *via* a SCSC transformation.

To expand the template method to an additional dinuclear unit, we turned to the Ag(I) ion.[34] It is well-established that Ag(I) exhibits linear coordination while also participating in Ag(I)···Ag(I), or argentophilic, forces.[52] Ag(I) ions engaged in argentophilic forces are separated on the order of 3.40 Å, which falls within the distance criterion of Schmidt. These observations encouraged us to investigate the ability of Ag(I) ions, in a T-shaped geometry, to steer *trans*-coordinated olefins for a [2+2] photodimerization. In this design, the argentophilic forces would stack two pairs of olefins for reaction in a solid. We determined the ability of Ag(I) ions to assemble *trans*-1-(4-pyridyl)-2-(phenyl)ethylene (**4-stilbz**) in crystalline $[Ag_2(\mathbf{4\text{-}stilbz})_4][CO_2CF_3]_2$ for a regiocontrolled head-to-head photodimerization to give *rctt*-1,2-bis(4-pyridyl)-3,4-bis(phenyl)cyclobutane (**4-pyr-ph-cb**) in quantitative yield (Fig. 10). The metal ions were separated by 3.41 Å while the C=C bonds of the stacked olefins exhibited a disordered criss-cross arrangement, being separated by 3.82 Å. That the photoreaction was able to proceed, despite the C=C bonds being crossed, was attributed to the olefins undergoing a pedal-like rotation.[34] Similar to $[Zn_4\mathbf{L}(OH)_2(\mathbf{4,4'\text{-}bpe})_2](ClO_4)_2$, the photoreaction proceeded *via* a SCSC transformation.[22]

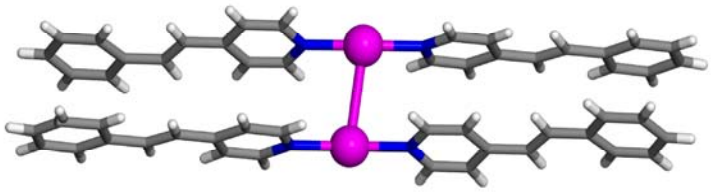

Figure 10 Alignment of **4-stilbz** molecules within the dinuclear complex $[Ag_2(\mathbf{4\text{-}stilbz})_4]^{2+}$.

The photoreaction involving $[Ag_2(\mathbf{4\text{-}stilbz})_4][CO_2CF_3]_2$ also converted the dinuclear complex into a 1D coordination network (Fig. 11).

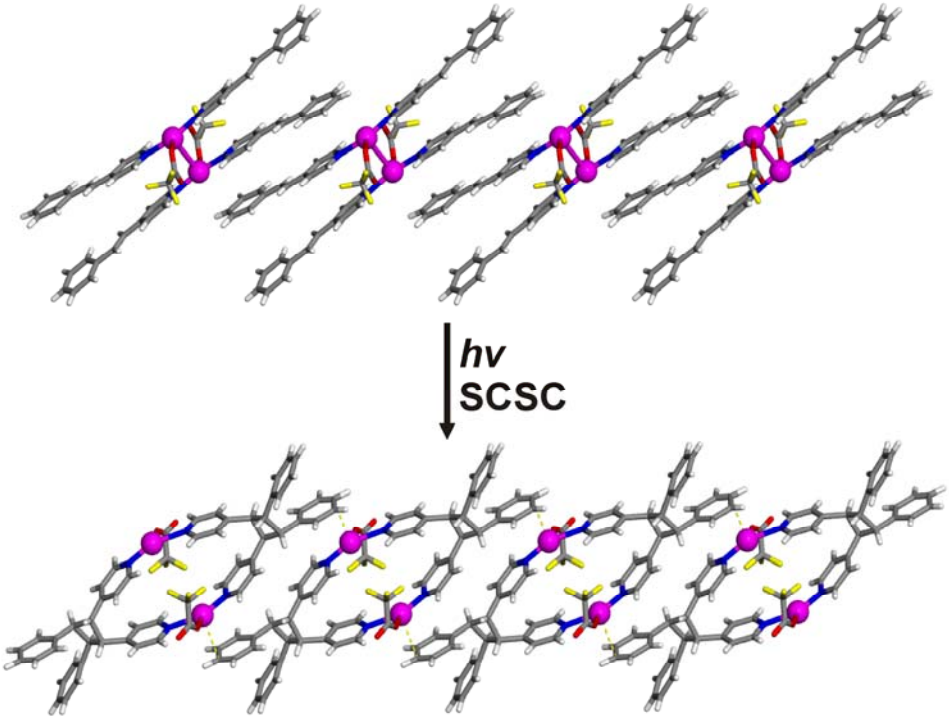

Figure 11 SCSC conversion of discrete $[Ag_2(\mathbf{4\text{-}stilbz})_4]^{2+}$ assemblies to 1D $[Ag_2(\mathbf{4\text{-}py\text{-}ph\text{-}cb})_2]^{2+}{}_\infty$ polymers (color scheme: C-grey, N-blue, O-red, Ag-pink, F-yellow).

The generation of the photoproduct involved major movements of the metal and organic components. The Ag(I) ions moved away from each other by approximately 1.16 Å (Ag(I)···Ag(I) distance: 5.73 Å), which broke the argentophilic forces. This movement was accompanied by an approximate 90º rotation of the carboxylate ions. As a result of these movements, Ag(I)···C(phenyl) forces (Ag(I)···C distance: 2.63 Å) formed between each repositioned Ag(I) ion and the *para*-carbon atom of the phenyl group of a neighbouring assembly. These new forces served, in effect, to link adjacent complexes to produce a linear coordination network. The photoconversion of $[Ag_2(\mathbf{4\text{-}stilbz})_4]^{2+}$ to $[Ag_2(\mathbf{4\text{-}py\text{-}ph\text{-}cb})_2]^{2+}$ was, to our knowledge, the first case in which a metal complex was transformed into an infinite coordination network *via* a photoreaction. In related and earlier work, Foxman had revealed the ability of the Ni(II) complex, $[NiBr_2(PCH_2CH_2CN)_3]$, to undergo a highly-stereocontrolled thermal polymerization in a solid that involved the formation of Ni-N coordination bonds.[53]

1.2.4. Applications of the products

The products of the [2+2] photodimerizations that we conduct in the solid state are functionalized with, in a minimal case, two pyridyl groups. The products also typically form in quantitative yield, gram amounts, and the absence of byproducts.[30] For us, these features made the products attractive for studies in coordination-driven self-assembly. We hypothesized that the products, once removed from the template, could serve as bi- and polytopic linkers of MOFs and related materials. A cyclobutane ring could serve as a hub[54] providing both acute and obtuse angles to propagate the coordination geometry of a metal in an assembly process. Importantly, whereas molecules synthesized in the liquid phase routinely encounter practical applications in areas such as pharmaceutical chemistry and materials science, the products of molecules synthesized in the solid state had experienced virtually none.[55, 56] This can be attributed

to difficulties of engineering solid-state structures wherein molecules undergo reactions "at will".[9]

1.2.4.1. 1D MOFs

In 2002, our group set out to determine whether the products obtained from linear templates in the solid state could be used as ligands to form MOFs. The major driving force behind the synthesis of MOFs is a promise to generate materials with tailorable electronic,[57] magnetic,[58] optical[59] and/or host-guest properties.[39, 41] Thus, MOFs with cavities and pores are expected to exhibit properties akin to zeolites and mesoporous materials, and, thereby, have applications in areas such separations,[60] gas storage,[42] and catalysis.[61]

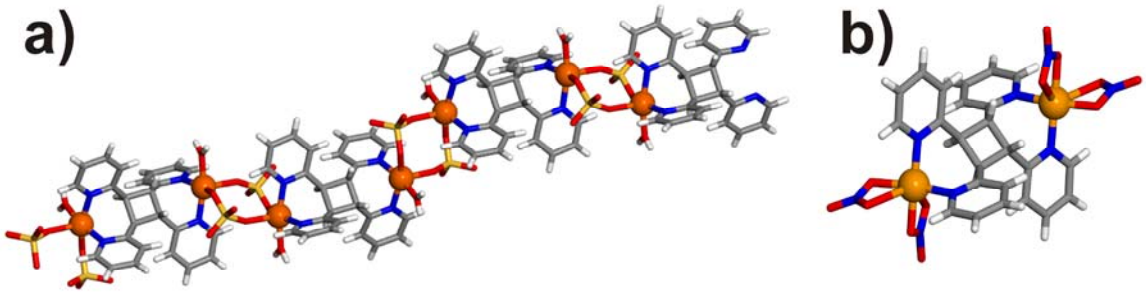

Figure 12 X-ray crystal structures of: (a) 1D polymer $[Cu_2(\mu_2\text{-}SO_4)_2(\mu\text{-}$**2,2'-tpcb**$)(H_2O)_2]_\infty$ and (b) dinuclear complex $[Cu_2(NO_3)_4(\mu\text{-}$**2,2'-tpcb**$)]$ and (b) space-filling of the stacking of two layers (color scheme: C-grey, N-blue, O-red, Cu-orange).

One of our first reactions involved **2,2'-tpcb** with $CuSO_4 \cdot 5H_2O$. We generated **2,2'-tpcb** using a hydrogen-bond-mediated synthesis.[62] In particular, we showed that the components assembled in the solid state to give a 1D MOF in which **2,2'-tpcb** served as a bis-chelating ligand in $[Cu_2(\mu_2\text{-}SO_4)_2(\mu\text{-}$**2,2'-tpcb**$)(H_2O)_2]_\infty$ (Fig. 12).[63] Each Cu(II) ion exhibited a square-pyramidal coordination environment with two N-atoms of two 2-

pyridyl groups, one O-atom of a sulfate ion, and one O-atom of a water molecule in the basal plane. The apical site was occupied by an O-atom of a second sulfate ion. The 1D polymer assembled in parallel and offset strands, with interstices occupied by solvent water molecules. In the same report, we showed that the self-assembly process was sensitive to changes to the counterion. Specifically, reaction of **2,2'-tpcb** with $Cu(NO_3)_2 \cdot 2.5H_2O$ produced the dinuclear complex $[Cu_2(NO_3)4(\mu$-**2,2'-tpcb**$)]$. Similar to the 1D framework, **2,2'-tpcb** served as a bis-chelating ligand. Two chelating nitrate ions completed a distorted octahedral coordination sphere.

1.2.4.2. 2D MOFs

That same year, we determined that **4,4'-tpcb** can be used as a 4-connected node of a porous 2D MOF. Specifically, reaction of 4,4'-tpcb with the copper paddle-wheel complex $[Cu_2(O_2CCH_3)_4(H_2O)_2]$ produced the 2D MOF $[Cu_4(O_2CCH_3)_8($**4,4'-tpcb**$)]_\infty$ (Fig. 10).[36] The cyclobutane and dicopper complex produced a 2D grid with identical rhombic cavities of approximate dimensions 17.2 Å × 17.2 Å and corner angles 75º and 104º (Fig. 13a). The 2D grids stacked to form a 3D framework with isolated 1D channels of approximate dimensions 10 Å × 12 Å (Fig. 13b). The channels were occupied by benzene solvent molecules, which assembled in an edge-to-face manner. We showed that the solvent molecules could be removed from the framework *via* a SCSC transformation.[50, 51] We also revealed that the methyl groups of the paddle-wheel complex were directed into the cavities. In doing so, the methyl groups segregated the space of the cavities into smaller compartments. These observations suggested that further functionalization of the cavities could be achieved by modifying the R-group of the paddle-wheel complex. We termed the framework an inverted MOF (IMOF) since the metal complex acted as a linear bridge and the organic spacer served as a node; thus, the roles of the metal and organic components, as compared to a more conventional

MOF,[38, 39, 41, 42] were inverted, or reversed. Moreover, that the metal component served as a linear bridge meant that the terminal carboxylates were available to decorate the cavities of the framework.

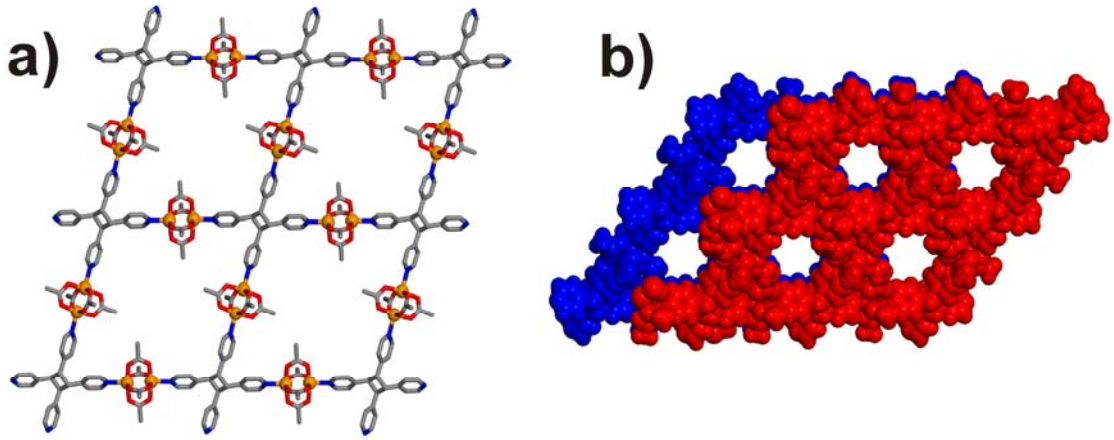

Figure 13 X-ray crystal structure of $[Cu_4(O_2CCH_3)_8(\mathbf{4,4'\text{-}tpcb})]_\infty$: (a) ball-and-stick model (color scheme: C-grey, N-blue, O-red, Cu-orange) and (b) space-filling of the stacking of two layers.

In a later report, our group described a 2D MOF based on **4,4'-tpcb** that involved metal and cyclobutane components that both served as 4-connected nodes.[64] In particular, reaction of **4,4'-tpcb** with $[Co(O_2CCH_3)_2(H_2O)_4]$ produced the 2D MOF $[Co(O_2CCH_3)_2(\mathbf{4,4'\text{-}tpcb})]_\infty$. The framework, similar to $[Cu_4(O_2CCH_3)_8(\mathbf{4,4'\text{-}tpcb})]_\infty$, possessed rhombic cavities with edge lengths of 7.3 Å. In contrast to $[Cu_4(O_2CCH_3)_8(\mathbf{4,4'\text{-}tpcb})]_\infty$, however, the framework was made up of two different rhombic cavities (Fig. 14). That the framework possessed two different cavities was a result of the stereochemistry of the cyclobutane ring, which provided two different angles (75º and 104º) for cavities within the network. The cavities stacked in an ABAB manner producing small interstices occupied by solvent methanol molecules. We also

demonstrated that the crystallinity of the solid was maintained upon removing the guests *via* heating.

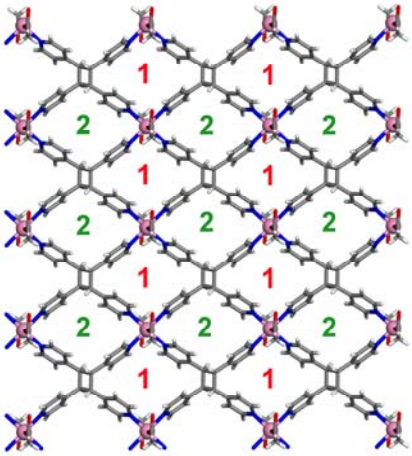

Figure 14 Perspective view of $[Co(O_2CCH_3)_2(\mathbf{4,4'\text{-}tpcb})]_\infty$ that illustrates the different cavities of the 2D MOF (color scheme: C-grey, N-blue, O-red, Co-pink).

More recently, we have demonstrated that a product of a template-directed solid-state synthesis forms a 2D MOF with a topology that conforms to a nonregular net (Fig. 15). Most 2D MOFs exhibit topologies of regular (*i.e.* tiling of regular polygons with identical nodes) or semiregular (*i.e.* tiling of different regular polygons with identical vertices) nets. In the minimal case, a MOF with a topology of a nonregular net will possess two different polygonal cavities and two nodes of different connectivity. It has been recently argued that the self-assembly process that produces a MOF is predisposed to generate high-symmetry frameworks based on identical nodes (*i.e.* regular and semiregular nets).[65] To design a MOF that conforms to a nonregular net, we reacted the [2.2]paracyclophane **4,4'-tppcp** and $Co(O_2CCH_3)_2 \cdot 4H_2O$, which afforded the 2D MOF $[Co(O_2CCH_3)_2(\mathbf{4,4'\text{-}tppcp})]_\infty$ (Fig. 12a).[64] The components self-assembled to give a 2D MOF with both square and hexagon cavities in which **4,4'-tppcp** and the Co(II) ion

served as 3- and 4-connected nodes, respectively. The paracyclophane effectively served as two covalently-fused 3-connected nodes in which the stacked rings of the cyclophane provided the covalent connection. Moreover, that the cyclophane acted as two fused 3-connected nodes meant that the formation of higher-symmetry MOFs with structures solely based on linkages between 3- and 4-connected nodes (*i.e.* with no linkages between two 3-connected nodes) was prohibited. The two different cavities hosted two different solvent molecules as guests. Specifically, a methanol molecule filled hydrophilic square cavities, while toluene molecules filled hydrophobic hexagon cavities (Fig. 15b).

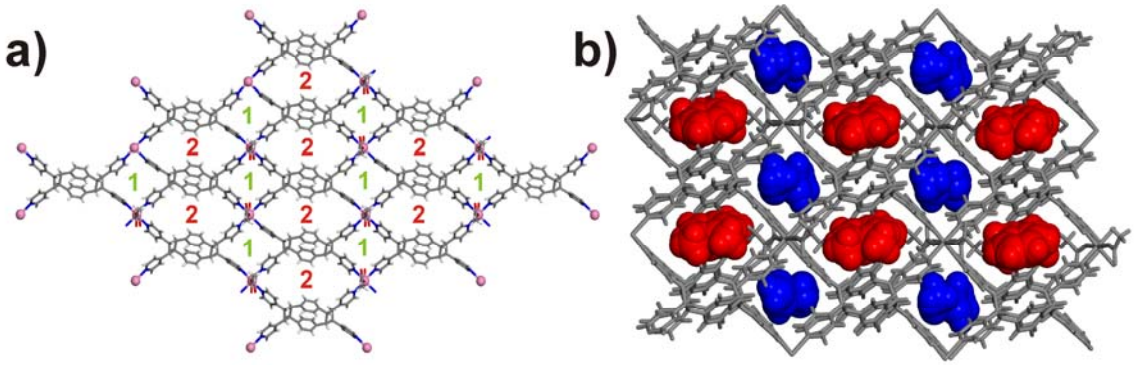

Figure 15 Perspective view of $[Co(O_2CCH_3)_2(\mathbf{4,4'\text{-}tppcp})]_\infty$: (a) different cavities of the 2D framework and (b) space-filling of the included solvent molecules (color scheme: C-grey, N-blue, O-red, Co-pink).

1.2.4.3. Metal-organic polygons and polyhedra

In addition to MOFs, we have discovered that products of linear templates in the solid state can generate metal-organic polyhedra and polygons. The internal cavities of such self-assembled frameworks have, in recent years, gained much attention as materials with applications in areas such as logical gates,[66] and reaction vessels[67]

Our first report described the self-assembly of the unsymmetrical tetrapyridine **2,4'-tpcb** (Fig. 13) with Cu(II) ions to form a polyhedron. Reaction of **2,4'-tpcb** with $Cu(ClO_4)_2 \cdot 6H_2O$ produced a hexanuclear polyhedron, in $[Cu_6(\mathbf{2,4\text{-}tpcb})_6(H_2O)_6][ClO_4]_{12}$, with a structure that conformed to a trigonal antiprism (Fig. 16).[68]

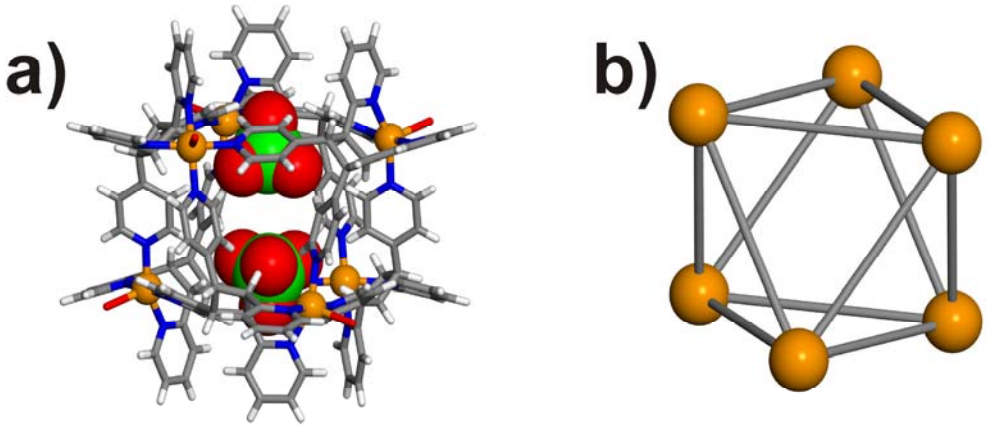

Figure 16 Schematic represenatation of (a) the polyfunctional ligand **2,4'-tpcb** and the perspective view of $[Cu_6(\mathbf{2,4\text{-}tpcb})_6(H_2O)_6]^{12+}$: (b) two encapsulated ClO_4^- ions in and (c) the trigonal antiprism formed by Cu(II) ions (color scheme: C-grey, N-blue, O-red, Cl-green, Cu-orange).

Each metal ion adopted a square pyramidal coordination environment and occupied a vertex of the polyhedron. The coordination environment consisted of two chelating 2-pyridyl groups and two monodentate 4-pyridyl groups that formed the base and a water molecule that formed the apex. Thus, the 4-pyridyl groups corresponded to the edges of the polyhedron while the 2-pyridyl groups corresponded to the corners. The coordination behaviour of the 2- and 4-pyridyl groups was consistent with the MOFs involving **4,4'-** and **2,2'-tpcb**.[36, 68] The assembly process produced a central cavity that hosted two ClO_4^- anions as guests.

Our group has also demonstrated that $[Cu_6(\mathbf{2,4\text{-}tpcb})_6(H_2O)_6]$ capsules can be noncovalently decorated to yield novel onion-shell capsules with alternating negative-positive-negative charges. The capsules were decorated with organosulfonates RSO_3^- [R = $-CF_3$, (+ or -)-10-camphor-sulfonate (**CPS**), -dodecylbenzenesulfonate (**DBS**), and resulted in the formation of a supramolecular entity with three concentric shells, namely a core of anionic guests, a cationic shell, and anionic exterior (Fig. 17). The decorated $[Cu_6(\mathbf{2,4\text{-}tpcb})_6(RSO_3)_6]^{12+}$ capsules, thereby, basically resemble reverse-micelles wherein the charged groups are segregated in the charged core, while hydrophobic groups pointing away from the core.[69] Remarkably, the decorated $[Cu_6(\mathbf{2,4\text{-}tpcb})_6(\mathbf{DBS})_6]^{12+}$ capsules were shown to be soluble in $CHCl_3$ (a relatively non-polar and non-coordinating solvent) unlike the undecorated $[Cu_6(\mathbf{2,4\text{-}tpcb})_6(H_2O)_6]^{12+}$ capsules.

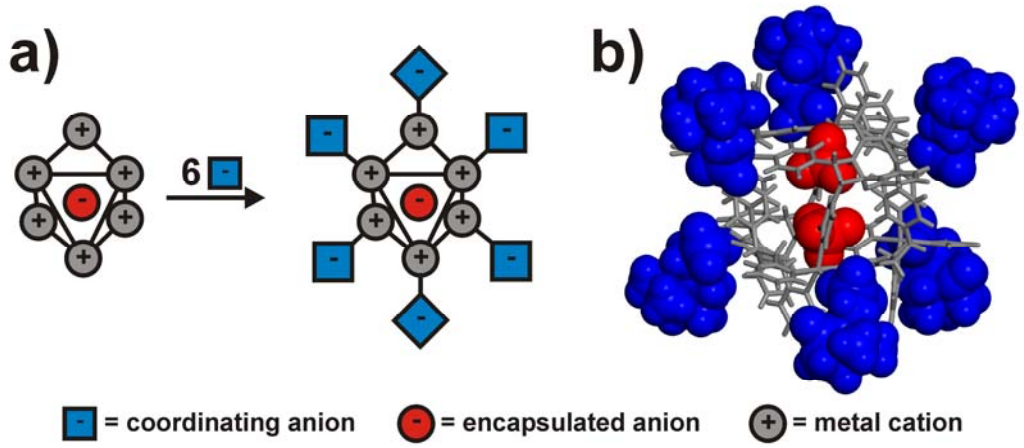

Figure 17 Supramolecular decoration of $\{[Cu_6(\mathbf{2,4\text{-}tpcb})_6(H_2O)_6](ClO_4^-)_2\}^{10+}$ and X-ray crystal structure of $\{[Cu_6(\mathbf{2,4\text{-}tpcb})_6((+)\text{-}CPS)_6](ClO_4)_2\}^{10+}$.

Very recently, we have shown that an unsymmetrical isomer of **2,4'-tpcb** ligand, namely **2,3'-tpcb**, assembles with Cu(II) ions to form a polyhedron exhibiting a structure that conforms to a tetrahedron (Fig. 18).[70] We anticipated that changing the 4-pyridyl

group to a 3-pyridyl group would result in a smaller polyhedron owing to a decrease in the angle of a coordination vector (Fig. 19). We employed a hydrogen-bond-directed synthesis to generate **2,3'-tpcb**. As expected**, 2,3'-tpcb** assembled with the metal ions to form a smaller polyhedron. To our surprise, the polyhedron, $[Cu_4(\mathbf{2,3'\text{-}tpcb})_4(H_2O)_4]^{8+}$, adopted a topology of a tetrahedron and exhibited a chiral D_2 topology. At the time, the structure represented a rare example of a chiral self-assembled polyhedron composed of achiral components. The chirality of the tetrahedral capsule was attributed to a geometric fit of the metal and organic components, which prohibited the formation of mirror planes in the structure. As in the case of the trigonal antiprism, the Cu(II) ions occupied the corners of the tetrahedron and exhibited a square pyramidal coordination environment. The tetrahedron also possessed a central cavity that hosted a NO_3^- ion as a guest.

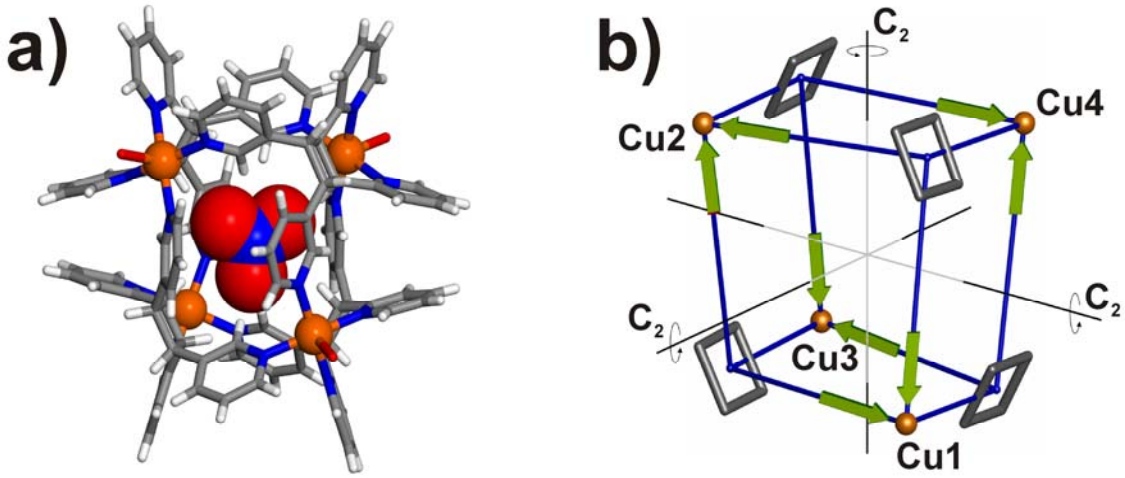

Figure 18 Perspective view of $[Cu_4(\mathbf{2,3'\text{-}tpcb})_4(H_2O)_4]^{8+}$: (a) space-filling of the encapsulated NO_3^- ion and (b) the tetrahedron topology ions (color scheme: C-grey, N-blue, O-red, Cu-orange)

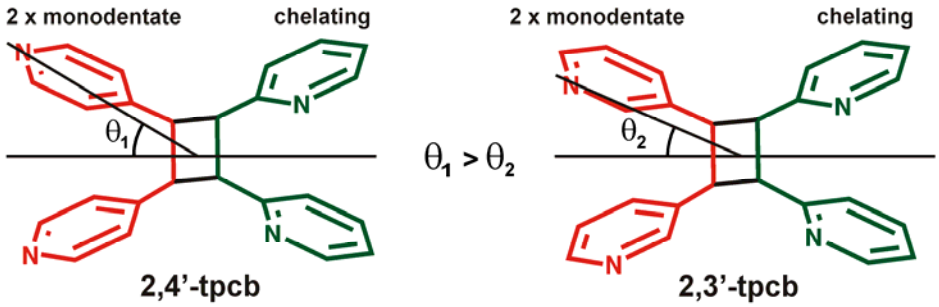

Figure 19 The chemical structures of polydentate **2,3'-tpcb** and **2,4'-tpcb** ligands (θ - angle of the coordination vector).

In addition to a polyhedron, we have demonstrated that **2,4'-tpcb** can form a polygon.[33] By changing from a non-coordinating (*i.e.* ClO_4^-) to chelating counter anion, in the form of the hexafluoroacetylacetonate anion (hfacac), we described the formation of the tetranuclear metal-organic rhomboid $[Cu_4(\mathbf{2,4\text{-}tpcb})_2(hfacac)_8]$ (Fig. 20a).

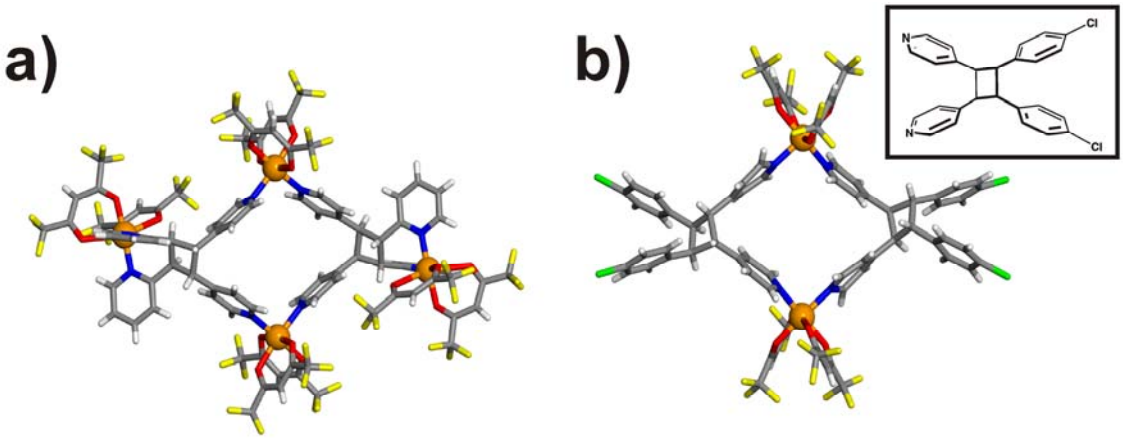

Figure 20 Perspective views of: (a) $[Cu_4(\mathbf{2,4\text{-}tpcb})_2(hfacac)_8]$, and (b) $[Cu_2(\mathbf{4\text{-}py\text{-}4\text{-}Cl\text{-}p\text{-}cb})_2(hfacac)_4]$ (inset: schematic representation of **4-py-4-Cl-p-cb)**.

In particular, two molecules of **2,4'-tpcb** assembled with the Cu(II) ions to give a dinuclear cavity of approximate dimensions 4.0 Å × 4.2 Å and corner angles of 79º and

101º. Monodentate 4-pyridyl groups defined the edges of the polygon. Each Cu(II) ion exhibited octahedral coordination with two 4-pyridyl units and two hfacac anions in a *cis* arrangement. Chelating 2-pyridyl groups were located along the periphery of the assembly, being coordinated to two Cu(II) ions. We also showed that the bifunctional cyclobutane *rctt*-1,2-bis(4-pyridyl)-3,4-bis(chlorophenyl)cyclobutane (**4-py-4-Cl-p-cb**) supports the formation of a dinuclear polygon *via*, similar to $[Cu_4(\mathbf{2,4\text{-}tpcb})_2(hfacac)_8]$, the 4-pyridyl groups (Fig. 20b).[33]

1.2.4.4. Outlook

Linear templates allow chemists to organize reactive molecules within finite supramolecular assemblies constructed *via* coordination-driven self-assembly. In such assemblies, olefins are preorganized to conform to Schmidt's topochemical postulates for a [2+2] photodimerization in a solid. The strategy has been, thus far, used to synthesize mono- and polyfunctional pyridyls in crystalline solids. We have also presented the diversity of products obtained in studies that apply the ligands in metallosupramolecular chemistry. We have revealed that the template method provides access to molecules that can be used as organic building units of self-assembled polygons and polyhedra, as well as MOFs. Our group has recently focused on the construction of new targets (*e.g.* heterodimers, see chapter 2), the use of synthetic templates to photodimerize molecules with highly flexible reaction centers (*e.g.* terminal olefins, see appendix B), to investigate metal-organic compounds based both on transition metals and other **tpcb** ligands (e.g. **3,4'-tpcb**, see chapter 2 and appendix C), as well as to study complexes involving lanthanides and **tpcb**s (see appendix D). The solid-state synthesis of highly complex multifunctional molecular targets, however, still remains unaddressed by our group owing to a lack of understanding how multiple (*i.e.* more than two) functional groups self-assemble in the solid state.

1.3. Pharmaceutical cocrystals

In the last four years, our group has generated a large interest in pharmaceutical cocrystals that stems from the opportunity to study hierarchies in molecular cocrystals. Pharmaceutically relevant compounds are rich in functional groups and provide a great opportunity and challenge to study synthon hierarchies that are also crucial to the development of strategies to construct molecular targets *via* photoinduced reactions in the solid state. Moreover, the common use of pharmaceutical cocrystals in the development of new design strategies for cocrystals[71] additionally raises our interest in this class of compounds.

1.3.1. A brief overview

The lack of required physicochemical properties for drug candidates (*e.g.* solubility/dissolution rate, mechanical properties, stability) represents a serious problem in drug formulation and product manufacturing.[72] To boost their performance, drug candidates are subjected to salt- and polymorph screening[73-75] to (generally successfully) identify solids with improved physicochemical properties. However, the salt- and polymorph approaches are somewhat limited in their scope.[76-78] Specifically, salt screening can only be performed on pharmaceutical agents (PAs) that are constituted of ionizable functional groups.[79] In addition, only a very few number of salt formers (*i.e.* about 120 acids and bases) are recognized as safe for use in drug formulation.[80] Polymorph formation, another commonly utilized approach to enhance physicochemical properties of drugs, also exhibits serious limitations. In particular, polymorph formation is a serendipitous event,[81, 82] and can, nowadays, hardly be predicted[83] nor designed. Also, polymorphs are known to spontaneously undergo phase transformations[84, 85] accompanied by undesired and unacceptable changes of physical properties.[86, 87] With these limitations in mind, drug formulators recently turned to crystal engineering and cocrystallization.[9, 26] The interest in crystal engineering stems from the opportunity to

from molecular complexes involving PAs that do not contain ionizable functional groups.[76, 77] The cocrystal approach also provides the drug formulators with more synthetic possibilities. Specifically, the US Food and Drug Administration recognizes several thousand food ingredients and additives are safe for human consumption, whereof a major portion is suitable for crystal engineering of pharmaceutical solids.[88] Outstandingly, recent studies have demonstrated that the cocrystallization of PAs can afford solids that exhibit physicochemical properties superior to those of the parent PA (Fig. 21).[89, 90] Physicochemical properties of pharmaceutical cocrystals, such as (*e.g.* solubility/dissolution rate,[91-93] bioavailability,[94] hygroscopicity,[95, 96] mechanical properties[97-99]) have recently been thoroughly reviewed by several groups, and will therefore not be discussed herein. The author rather refers the reader to excellent reviews published by Zaworotko *et al.*,[76] Jones *et al.* [77] and Schultheiss *et al.*[90]

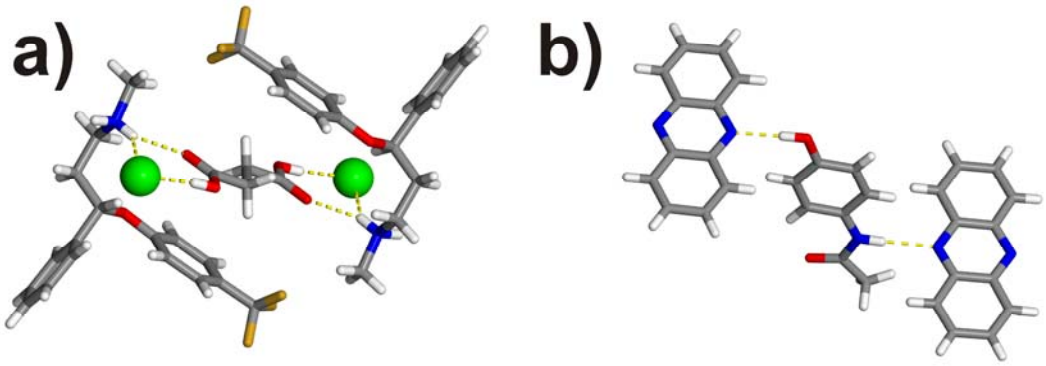

Figure 21 X-ray crystal structure of: a) 2(fluox·HCl)·(succinic acid) and b) (acetaminophen)·(phenazine). Whereas the cocrystal shown in a) exhibits a superior aqueous solubility compared fluoxetine HCl, the cocrystal depicted in b) displays superior mechanical properties as compared to neat crystalline acetaminophen.

1.3.2. Cocrystal-screening methods

1.3.2.1. Mechanochemical cocrystal screening

The discovery and characterization of an maximum of solid-state forms of a PA is of tremendous importance in drug formulation since a broad diversity of PA-based solid forms provides a greater opportunity to select a form with optimal physicochemical performance.[100] In this context, mechanochemistry[101] has been recognized as method of choice in screening for pharmaceutical cocrystals.[89] The popularity of "neat" and "liquid-assisted" grinding is attributed to the fact that these methods gain access to cocrystals most readily.[101] Besides enabling high "hit-rates" during cocrystal screening trials, mechanochemistry (and milling in particular) has been shown to yield cocrystals in high yields in very short time periods.[101] The short reaction times in mechanochemical cocrystal syntheses are highly important considering the high number of pharmaceutically acceptable cocrystal formers that can yield cocrystals of high clinical and commercial relevance. The importance of mechanochemistry in crystal engineering is also demonstrated by its ability to facilitate the systematic construction of three-component pharmaceutical solids,[71, 102] as well as to enable the dismantling of (pharmaceutical) cocrystals.[103]

1.3.2.2. Screening *via* solution-mediated phase transformation

Very recently, Zhang *et al.* developed a suspension/slurry technique designed specifically for cocrystal screening purposes.[104] The slurry approach is founded on the thermodynamic understanding of the physical stability of hydrates/solvates.[105] In their recent report, the authors proposed that a solid molecular complex (*i.e.* cocrystal) composed of a pharmaceutical agent (*i.e.* drug) and cocrystal former (**CCF**) has the same thermodynamic stability as the solid drug if the activity[106] of the **CCF** in the surrounding environment is at a critical value ($0 < a_{c,CCF} \leq 1$). Once the critical value is exceeded, the cocrystal exhibits a greater thermodynamic stability and, thus, crystallizes spontaneously

given sufficient time for nucleation and provided cocrystal formation is possible (Fig. 22).[107] The same analysis applies between the solid **CC** and **CCF**. Cocrystal nucleation readily occurs in slurries of physical mixtures of both cocrystal components where activities of both components are high. Subsequent conversion from a solid mixture of the individual components to a solid cocrystal will then proceed *via* a solution-mediated phase-transformation (**SMPT**) process until the activity of either component approaches its critical value. Not only does this method maximize the screening efficiency, the approach is also easy to perform and provides rapid access to multi-component crystalline solids.

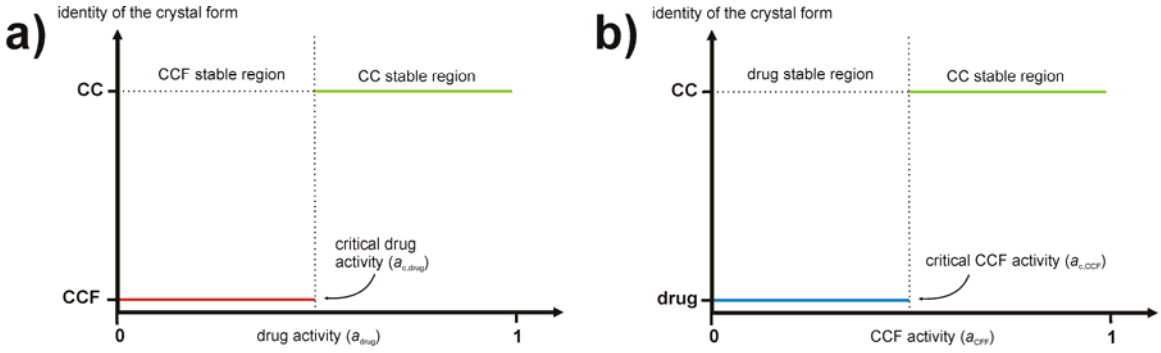

Figure 22 Physical stability phase diagrams of (a) cocrystals with respect to the activity of the drug, and (b) cocrystals with respect to the activity of the cocrystal former.

The efficiency of the SMPT screening method was demonstrated by its ability to reproduce cocrystals very quickly and quantitatively.[104] In addition, **SMPT** was successfully utilized to screen for cocrystal formation between caffeine and adipic acid. Caffeine and adipic acid were at various occasions reported not to form a cocrystal. Specifically, Jones *et al.* have explored co-crystal formation between caffeine and, among others, fumaric, L-tartaric and adipic acid. Under the conditions studied and with the screening method employed (*i.e.* solvent-drop grinding) cocrystallization attempts with

these acids were reported as unsuccessful. In addition, cocrystals involving caffeine and a variety of aliphatic dicarboxylic acids were studied over twenty five years ago by Nishijo and co-workers.[108] Co-crystals were successfully formed for oxalic, maleic, malonic, and glutaric acids, as characterized by powder X-ray diffractometry, IR spectroscopy and TG analysis. The authors also explored cocrystal formation with adipic acid. Interestingly, consistent with the more recent report by the Jones group,[95] they failed to obtain co-crystals comprising caffeine and adipic acid. Remarkably, Zhang *et al.* discovered a 1:1 cocrystal based on caffeine and adipic acid using **SMPT** as screening method. At the same time, the Jones groups also reported the discovery of the same cocrystal during a more recent study.[71] The facile formation of the caffeine:adipic acid cocrystal *via* the **SMPT** method prompted us to utilize the method in our attempt to establish synthon hierarchies of pharmaceutical cocrystals (see chapter 4).

1.4. Nanotechnology and crystal engineering

Nanosciences and nanotechnology are from their earliest days focused on the development of inorganic materials (*e.g.* metals, metal oxides) with applications in medicine, electronics and materials sciences.[109-113] The current demand for inexpensive nanomaterials with improved physicochemical properties (*e.g.* flexibility, weight, anisotropy) triggered the development of fabrication methods for organic nanomaterials based on single components. Notably, recent studies have shown that organic nanocrystals exhibit exceptional optical, electronic and thermotropic properties,[114] as well as single-crystal-to-single-crystal (SCSC) reactivity.[115] However, nanomaterials based on multi-component molecular crystal (*i.e.* cocrystals) have so far remained literary unexplored - despite their potential utility in various scientific areas (*e.g.* electronics, organic synthesis and pharmaceuticals).

That nano-dimensional cocrystals were not reported in the literature so far might be attributed lacking fabrication methods. Fabrication processes for inorganic particles

are expected to be inadequate for organics owing to their thermal instability. Noteworthy, inorganic nanoparticles are generally produced at temperatures whereat organics instantly decompose. As an alternative to high-temperature methods, reprecipitation methods have been found to be suitable and convenient for the preparation of single-component organic nanocrystals based on low-molecular-weight π-conjugated organics (*e.g.* perylenes, fullerenes).[114] The reprecipitation method, however, is not expected to be suitable to the formation of nano-dimensional cocrystals. Specifically, cocrystal components often display significant solubility differences and are, hence, expected to precipitate at different rates. Such distinct nucleation rates are likely to preclude cocrystal formation. The synthesis of nano-dimensional cocrystal therefore requires the development of alternative mild crystallization conditions.

1.5. Dissertation scope and overview

For about a decade, our group is focused on template-directed organic solid-state synthesis. Within the last couple of years, we expanded our interest to metal-organic compounds and have shown that products derived from the solid state give raise to metal-based supramolecular entities with exceptional features (*e.g.* chirality and unique shapes). It is the intention of this thesis to present results gained from our explorations of new and unexplored avenues of organic solid-state synthesis, and crystal engineering in general. Specifically, we will show how principles supramolecular chemistry and crystal engineering can be utilized to: 1) achieve cross-photoaddition reaction in multi-component organic solids, 2) to prepare metal-organic materials involving ligands derived from the solid state that exhibit unique and significant properties (*i.e.* thixotropy), 3) to develop methodologies for the preparation of nano-dimensional cocrystals, and to explore their properties, and 4) to investigate synthon hierarchies in molecular cocrystal (*i.e.* pharmaceutical cocrystals) based on multiple functional groups.

Finally, the overall objective of this dissertation is to demonstrate that studies involving nanostructured co-crystals and metal-organic compounds provide opportunities for studies in nanotechnology *via* templated-directed reactions in multi-component organic solids. Our efforts to establish synthon hierarchies in pharmaceutical cocrystal are envisioned to promote both the design and development of well performing drugs with superior physicochemical properties, as well as the development of strategies for the solid-state synthesis of complex photoproducts comprised of numerous functional groups.

CHAPTER 2:
SUPRAMOLECULAR CONTROL OF REACTIVITY IN MOLECULAR COCRYSTALS AND MATERIALS ARRISING FROM TEMPLATE-DIRECTED SOLID STATE REACTIONS

2.1. Introduction

In previous years, our group has shown that both hydrogen-bond- and coordination-driven self-assembly involving synthetic templates can be utilized to direct and control [2+2] photodimerizations in the solid state. We have also shown that templated solid-state reaction can enable access to synthetically challenging molecular targets (*i.e.* cyclophanes, ladderanes) stereospecifically and in quantitative yields. The ability to use synthetic templates, such as resorcinols, to direct [2+2] photodimerizations of olefins in the solid state provides an opportunity to develop a general method to design cross-photoaddition reactions in the solid state. So far, our group has not addressed the possibility of reacting two distinct molecules in the solid state using synthetic templates. In this chapter, however, we will demonstrate that a synthetic template in form of resorcinol can be utilized to achieve a [2+2] cross-photoaddition reaction between two distinct stilbazoles whereby an enantioneric pair of cyclobutanes forms stereospecifically and in nearly quantitative yields and stereospecifically.

In recent years, we have also demonstrated that molecules derived from template-directed solid-state synthesis are suitable ligands for a diverse range of metallosupramolecular assemblies (*e.g.* capsules, frameworks). Herein, we present the serendipitous formation of a thixothropic metallosupramolecular hydrogel. The gel is based on an unsymmetrical tetrapyridylcyclobutane obtained from a templated solid-state [2+2] photodimerization, and characterized using analytical state-of-art methodologies, such as scanning-transmission X-ray microscopy (STXM), transmission-electron microscopy (TEM) and atomic-force microscopy (AFM).

2.2. A Template-directed Asymmetric [2+2] Cross-photoaddition of olefins in the solid state

2.2.1. Introduction

[2+2] Cross-photoaddition reactions (CPR) of organic reagents in the solid state represent a challenging task for synthetic chemists, and only a small number of examples have been reported up to date.[116-123] CPRs were mainly observed within solid solutions that are based on molecules with functional groups being interchangeable in the solid state. The first reported CPRs, for example, involved cinnamic acid derivatives and 1,3-butadiene derivatives (Fig.23).[117, 118]

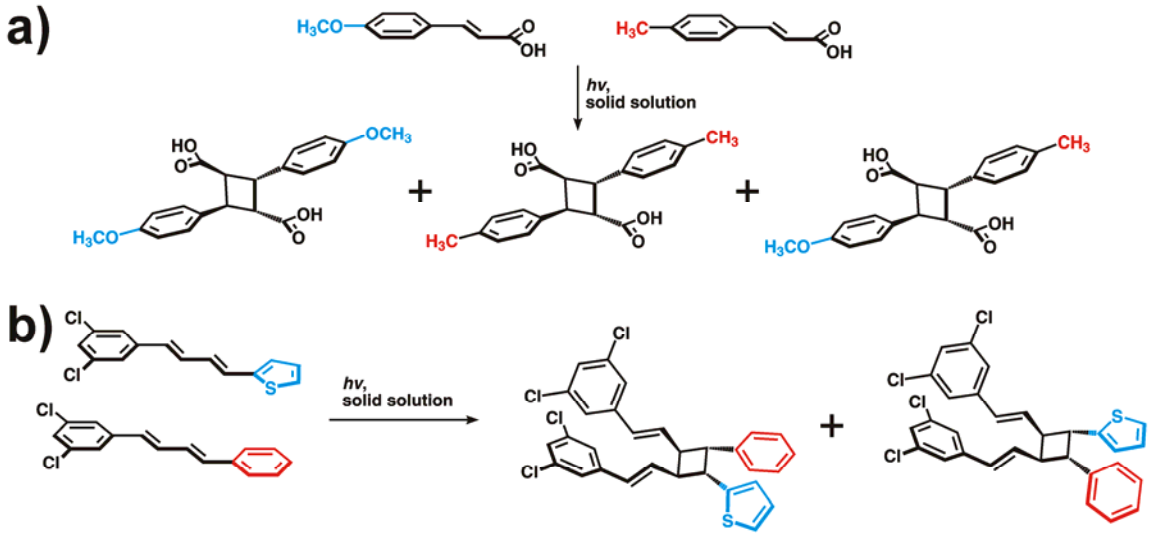

Figure 23 Examples of CPRs in solid solutions using: a) cinnamic acids, and b) 1,3-butadiene derivatives.

CPRs were also occasionally achieved within chiral cavities of inclusion compounds and metal organic capsules. In particular, Miyashi *et al.* reported a absolute asymmetric synthesis involving bis[1,2,5]thiadiazolotetracyanoquinodimethane and *o*-divinylbenzene.[122] The compounds were found to form weak electron donor-acceptor

complexes that crystallize in a chiral space group. The CPR was reported to occur in a single-crystal-to-single-crystal-transformation (Fig 24).

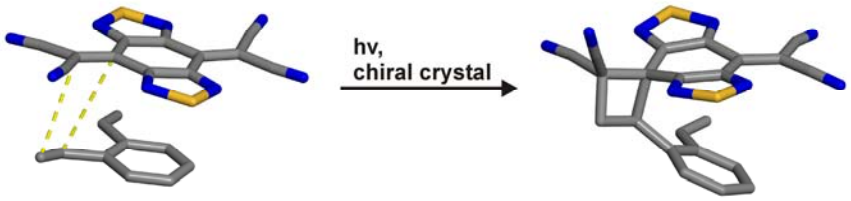

Figure 24 Absolute asymmetric synthesis involving bis[1,2,5]thiadiazolotetracyanoquinodimethane and *o*-divinylbenzene as reactants, as reported by Miyashi *et al* Hydrogen atoms are omitted for clarity.

The main obstacle in achieving CPRs in the solid state is represented by the difficulty of preparing both crystalline structures containing chiral cavities[124] and solid solutions[119] wherein the -C=C- double bonds of two distinct molecules conform to Schmidt's topochemical postulates.[7] CPRs are generally limited to solid solutions composed of structurally-related molecules that exhibit photoreactivity within their isomorphous one-component crystals.[119] Notably, it has also been demonstrated that two structurally-related molecules, whereof *only one* exhibits photoreactivity in the solid state, can be built-in into solid solutions wherein the photostable compound adapts to the crystal structure and solid-state reactivity of the photoreactive analogue (Fig 25).[120] However, a method that enables a CPR of two molecules that form a photostable solid solutions has, to our knowledge, not been reported.

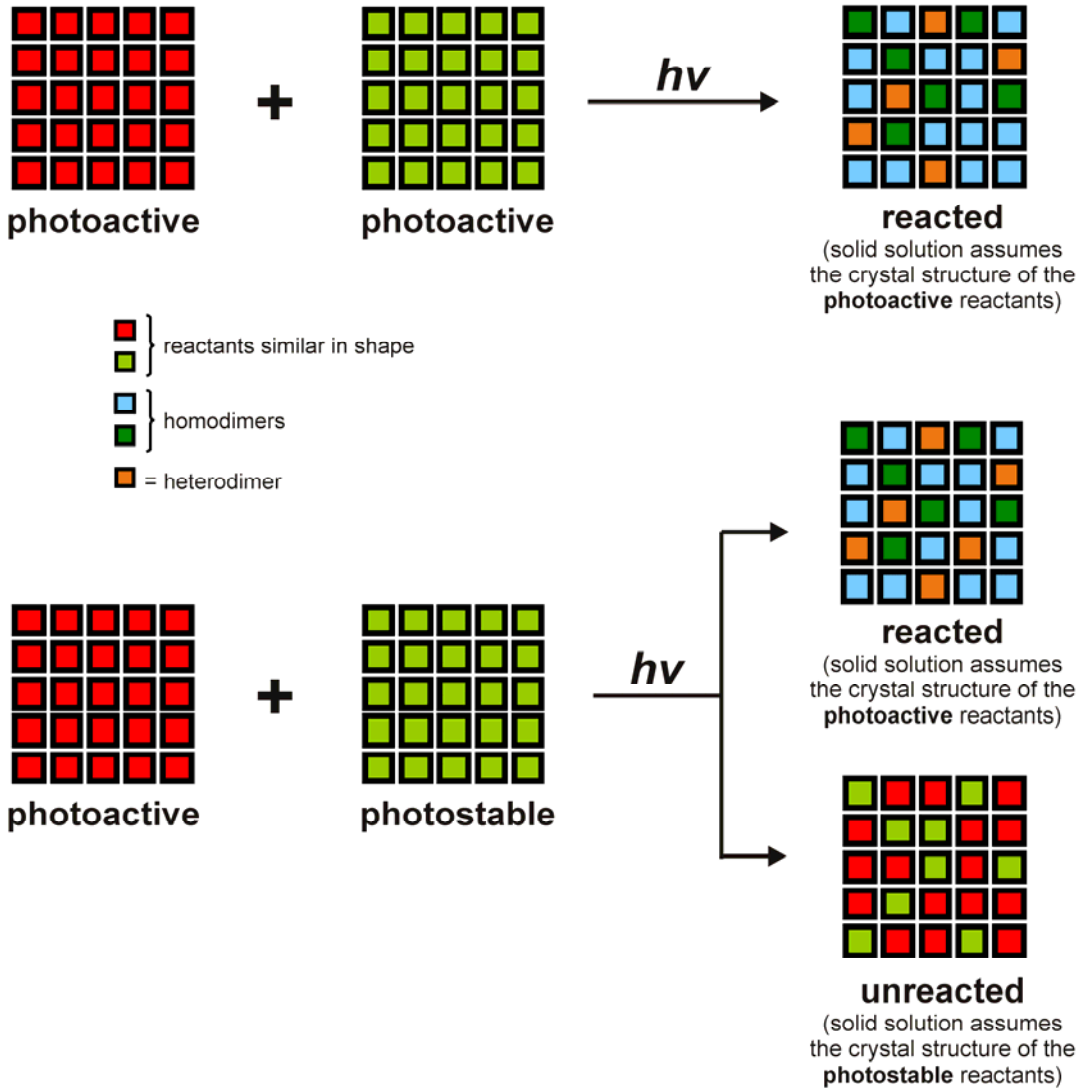

Figure 25 Photoreacitiy properties of solid solutions.

In recent years, we have demonstrated that synthetic templates (*i.e.* small ditopic molecules, dinuclear metal salts) can be utilized to achieve stereospecific and quantitative [2+2] photodimerization of olefins that are otherwise photostable in the crystalline solid state.[30] We, thus, expect that components of photostable solid solitions can be cross-coupled in the solid state using templates to facilitate a CPR (Fig 26).

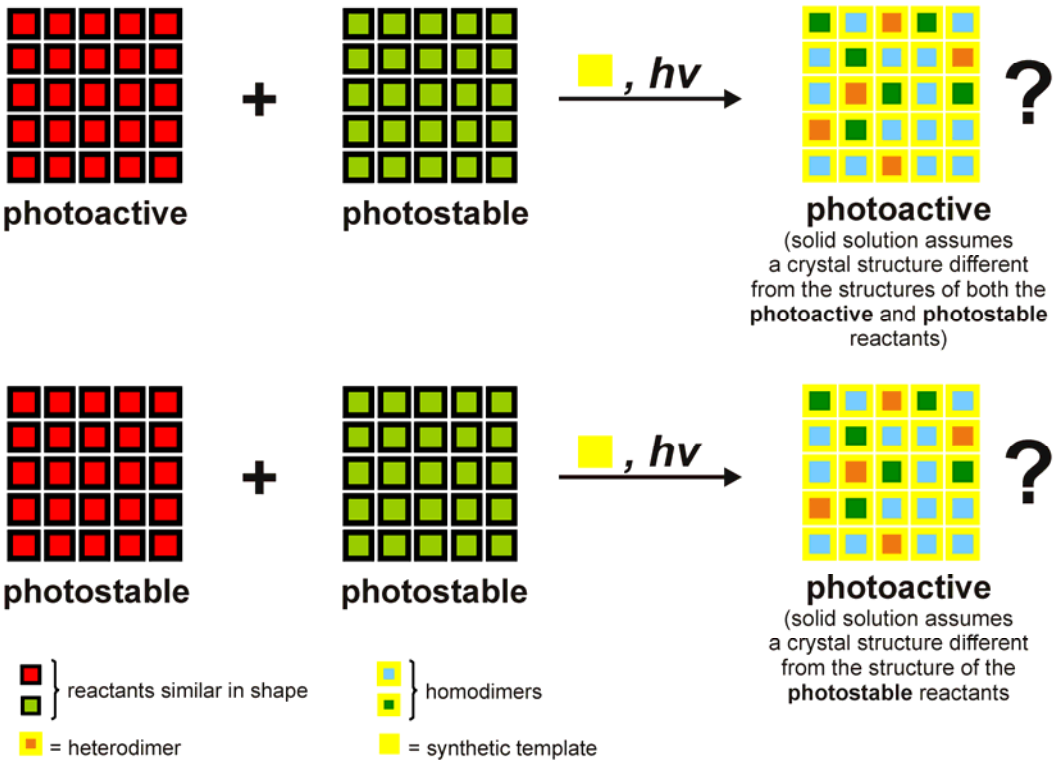

Figure 26 Enhancement of photoreactivity properties of solid solutions using synthetic templates.

The use of synthetic templates in solid-state CPRs is also motivated by a recent report by Fujita *et al.* wherein the authors reported a templated CPR between N-cyclohexylmaleimide and fluoranthene - an inert aromatic compound whose thermal or photochemical pericyclic reactions have never been reported. The photoproduct was obtained in enantiomeric excesses of up to 50%. The reaction was conducted in solution using a Pd-based M_6L_4 capsule as synthetic template. The peripheral chiral auxiliaries of the capsule were found to induce a minor deformation of in its ligands, thus producing considerable asymmetric induction (Fig 27).

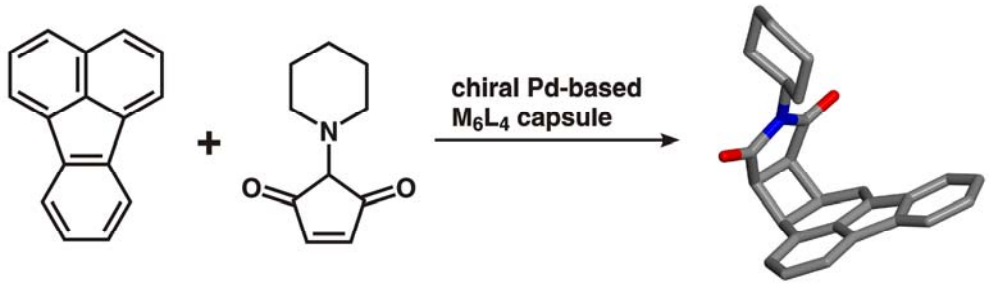

Figure 27 Asymmetric [2+2] cross photoaddition in a self-assembled Pd-based M_6L_4 capsule with remote chiral auxiliaries. Hydrogen atoms are omitted for clarity.

In this section, we report a CPR that occurs in a three-component cocrystal solid solutions[125, 126] composed of two distinct achiral molecules and a linear template (Fig 28). In particular, it was determined that resorcinol (*i.e.* 1,3-dihydroxybenzene) (**res**) self-assembles in the solid state with *trans*-1-(4-chlorophenyl)-2-(4-pyridyl)ethylene (**ClPE**) and *trans*-1-(4-methylphenyl)-2-(4-pyridyl)ethylene (**MePE**) to form a cocrystal solid solution, namely (**res**)·(**ClPE**)$_{(x)}$·(**MePE**)$_{(2-x)}$ (where x ~ 1) (**2**), that wherein the reactants undergo a CPR stereospecifically and in nearly quantative yields (*i.e.* >96%) upon UV irradiation.

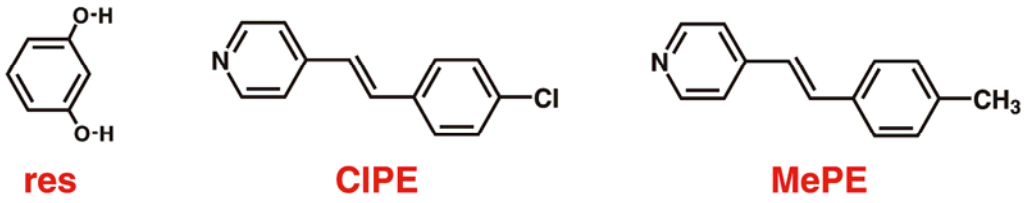

Figure 28 Structures of **res**, **ClPE** and **MePE**.

The photoreacted solid solution is composed of racemic *rctt*-1-(4-chlorophenyl)-2-(4-methylphenyl)-3,4-bis(4-pyridyl)cyclobutanes (**a,b**), *rctt*-1,2-(4-chlorophenyl)-3,4-bis(4-pyridyl)cyclobutanes (**c**) and *rctt*-1,2-(4-methylphenyl)-3,4-bis(4-

pyridyl)cyclobutane (**d**) (Scheme 29b). The significance of this result is demonstrated by the fact that a CPR involving **ClPE** and **MePE** achieved in a two-component solid solution of the pure olefins in the absence of the res template (Fig 29).[127]

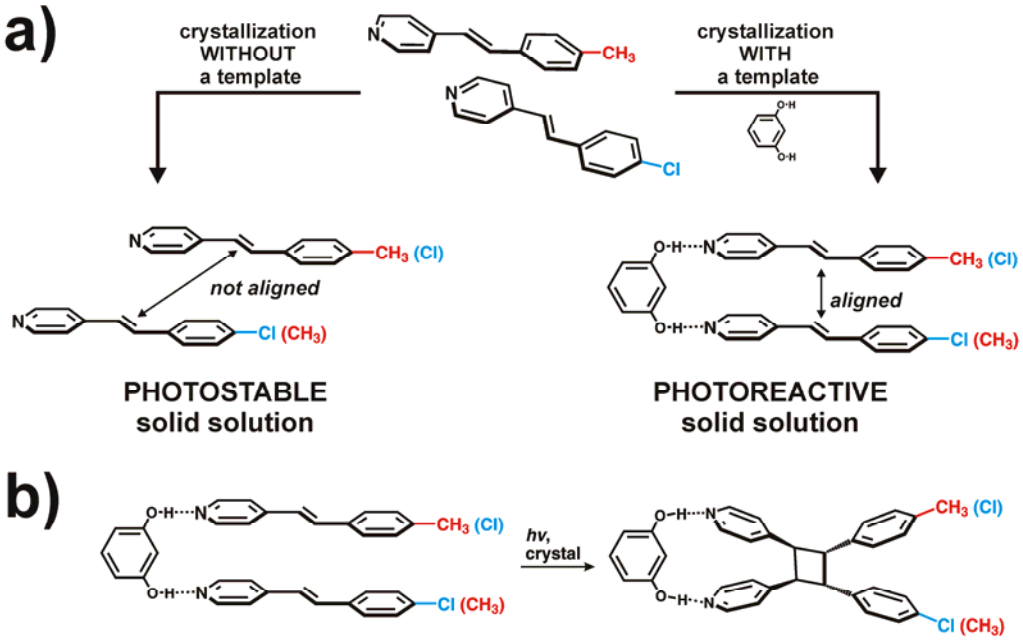

Figure 29 Template-directed synthesis in solid solutions.

2.2.2. Materials

4-Bromotoluene (98%), palladium(II) chloride (99.999%), triphenylphosphine (*ReagentPlus*®, 99%), potassium carbonate (ACS reagent, ≥99.0%), 4-vinylpyridine (95%), pyridine (anhydrous, 98%), chloroform (CHROMASOLV® Plus, for HPLC, ≥99.9%), 4-chlorobenzyl chloride (purum, ≥98.0%), triethylphosphine (99%), *tert*-butanol (anhydrous, ≥99.5%), 4-pyridinecarboxaldehyde (97%), potassium tert-butoxide (purum, ≥97.0%), sodium hydroxide (ACS reagent, ≥97.0%) and hydrobromic acid (48 wt. % in H_2O, ≥99.99%) were purchased from Sigma-Aldrich (Saint Louis, MO). All

reagents and solvents, except 4-vinylpyridine, were used as purchased. 4-Vinylpyridine was purified *via* distillation prior to use.

2.2.3. Experimental

2.2.3.1. Synthesis of **MePE**

MePE was prepared in two-phase palladium-catalyzed Heck-coupling reaction. Both bromotoluene (30 mmol, 5.13 g) and 4-vinylpyridine (45 mmol, 4.73 g; 50% excess) were added to a potassium carbonate solution (c = 0.38 mol dm^{-3}, 160 ml), followed by palladium(II) chloride (0.67 mmol, 120 mg) and triphenylphosphine (2.6 mmol, 690 mg). Lastly, 1.5 mL of tri(*n*-butyl)amine was added as a phase-transfer reagent to the suspension and refluxed with stirring for 24 hours. The resulting mixture is then left to cool to room temperature. The product was subsequently extracted with 3×50 mL of chloroform. The chloroform fractions were combined, dried over anhydrous sodium sulfate and finally evaporated to dryness using a rotary evaporator. The crude solid contained a significant amount of non-reacted 4-vinylpyridine and palladium-poisoned product. The solid was therefore dissolved in a *minimal* amount of hot pyridine to obtain a saturated solution. The solution was subsequently refluxed to separate polymerized 4-vinylpyridine and the remaining Pd-catalyst from the solid product. The solution is then cooled (<0 ºC) to allow precipitation of white **MePE** crystals. Yield: 3.98 g (68%).

2.2.3.1. Synthesis of **ClPE**

ClPE was prepared using a modified Wittig condensation reaction, namely the Horner-Wadsworth-Emmons reaction. 4-Chlorobenzyl chloride (0.0621 mol, 10.0 g) and triethylphosphite (0.0744 mol, 19.6 g) were refluxed for 8 hours to yield 4-chloro-benzyl(diethyl)phosphonate as clear liquid. The unpurified phosphonate and crude 4-pyridinecarboxyaldehyde (0.0745 mol, 7.98 g; 20% excess) were added to 20 ml of tert-

butanol. The obtained mixure was cooled to about -15 ºC in an ice bath upon which potassium tert-butoxide (0.0894 mol, 10.0 g) was slowly added while vigorously stirred. The reaction mixture was stirred overnight, and poured into cold water (<5 ºC, 100 mL). The precipitated bright yellow **ClPE** was filtered under vacuum, washed with 3×50 mL of water, and air-dried at in an oven overnight at 65 ºC. Overall yield: 8.93 g (71%)

2.2.3.2. Crystal growth

Crystals of **ClPE** and **MePE** were grown by slow solvent evaporation. For this purpose, 1 mmol of each olefin was dissolved in a minimal amount of acetonitrile, filtered through a cotton plug and left to cool and evaporate. Single crystals were obtained within 3 hours. Yield(**ClPE**): 52 mg (24%); yield(**MePE**): 104 mg (54%).

Solid solutions based on **ClPE** and **MePE** (**1**) were prepared by dissolving **ClPE** (1 mmol, 215.7 mg) and **MePE** (1 mmol, 195.3 mg) were separately dissolved in ACN (total volume 7 ml), refluxed for 1 hour, filtered through cotton and left to cool at room temperature. Crystalline plates suitable for single-crystal X-ray diffraction studies appear after 30 minutes. Yield: 48 mg (12%).

Single crystals of (**res**)·(**MePE**)$_x$·(**ClPE**)$_{(2-x)}$ (where x ~ 1) (**2**) were obtained by solvent evaporation. Specifically, **ClPE** (195.2 mg, 1 mmol) and **MePE** (215.7 mg, 1 mmol) were refluxed together with **res** (110.1 mg, 1 mmol) in 20 ml of acetonitrile for 20 min. The resulting solution was left to slowly cool to room temperature. Yellow single crystals of **1** suitable for single-crystal X-ray analysis were obtained after approximately 5 h. Yield: 115 mg (22%).

Single crystals of [(H$_2$-**2x**)$^{2+}$][Br$^-$]$_2$·0.7(H$_2$O) (**3**) (where **x** = **a**, **b**, **c**, **d**) were grown from an acetonitrile solution of photoreacted **2**. Upon photoreaction of **2**, the photoproducts were separated form the template by basic extraction using 1M NaOH and $CHCl_3$ to which less than 0.1 mL of HBr(aq) was added dropwise. Red-brown single crystals suitable for single crystal X-ray diffraction grew over a period of 4 days.

2.2.3.3. Photoreactivity studies

In a typical photoreaction experiment, 100 mg of solid were gently ground using a mortar and pestle. The obtained powder was placed between two Pyrex glass plates. The plates placed in a photoreactor cabinet equipped with a broad-band 450 W medium-pressure Hg-lamp. The powder distributed between the plates was mixed every 10 hours.

2.2.3.3. X-ray diffraction experiments

All crystal data were measured on a Nonius Kappa CCD single-crystal X-ray diffractometer at liquid nitrogen or room temperatures using MoK_α radiation (λ = 0.7107 Å). After anisotropic refinement of non-hydrogen atoms, hydrogen atoms bonded to sp^2 hybridized atoms were placed in idealized positions and allowed to ride on the atom to which they are attached. The resorcinol hydrogen atoms were calculated in an optimal hydrogen bonding geometry. Structure solution was accomplished with the aid of SHELXS-97 and refinement was conducted using SHELXL-97.[ref] Powder X-ray data were collected on a Bruker D-5000 diffractometer equipped with a Bruker SOL-X energy-sensitive detector using Cu$K_{\alpha 1}$ radiation (λ = 1.54056 Å).

2.2.3.4. NMR spectroscopy

^{1}H NMR data were collected on an AVANCE Bruker NMR spectrometer operating at 300 MHz using DMSO-d_6 as solvent.

2.2.4. Results and discussion

The choice of both the reactants and the template used to perform the CPR reported herein is based on several previously reported studies. First, we have recently utilized linear templates in form of resorcinol derivatives to align monopyridines (*i.e.* **ClPE)** for quantitative [2+2] photodimerizations in the solid state (Fig. 30).[128]

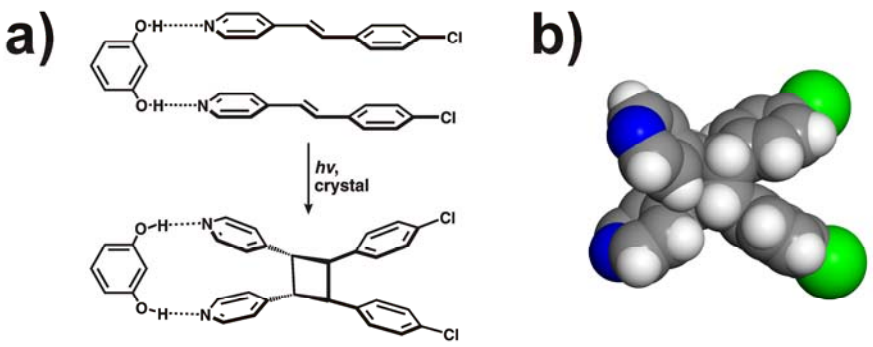

Figure 30 Template-directed solid state synthesis of *rctt*-1,2-bis(4-pyridyl)-3,4-bis(4'-chlorophenyl)cyclobutane (a) and its X-ray crystal structure.

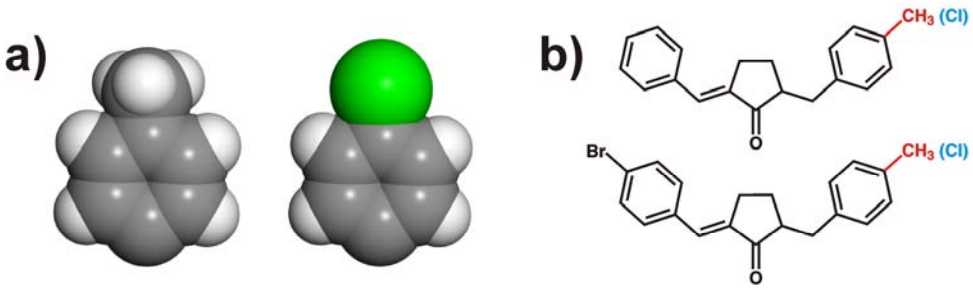

Figure 31 Chloro atoms and methyl groups being similar in shape and size (a) and benzylbenzylidenecyclopentanones used by Jones and Desiraju to engineer photoreactive solid solutions.

Second, Kitaigorodskii proposed the interchangeability of chloro atoms and methyl groups owing to their similarities in shape and size (19.9 *vs.* 23.5 $Å^3$, respectively) (Fig 31a).[129] And third, Jones and Desiraju demonstrated later on the utility of such interchangeability in the context of the crystal engineering of photoreactive solid solutions (fig. 31b).[119, 120, 130] Altogether, these three findings suggest that **ClPE**, **MePE** and **res** represent suitable candidates for a CPR in a three-component solid solution.

Both **ClPE** and **MePE** were determined to be photostable in the solid state. The photostability is attributed to the crystal packing unfavorable for a solid-state [2+2]

photodimerization. ^{1}H NMR spectra of the UV irradiated solids showed no changes that would indicate the occurrence of a [2+2] photocycloaddition in the solid state. Specifically, **ClPE** was found to crystallize in the triclinic $P\bar{1}$ space group. The unit cell consists of two crystallographically independent **ClPE** molecules. Within the crystal structure, the olefins are held together by Cl···N(pyridyl) halogen bonds. Closest neighboring olefins are aligned in a head-to-tail manner. Their –C=C- double bonds are not aligned in parallel and are separated by 6.12 and 6.18 Å. The olefins are, hence, not conforming to Schmidt's topochemical postulates (Fig 32).

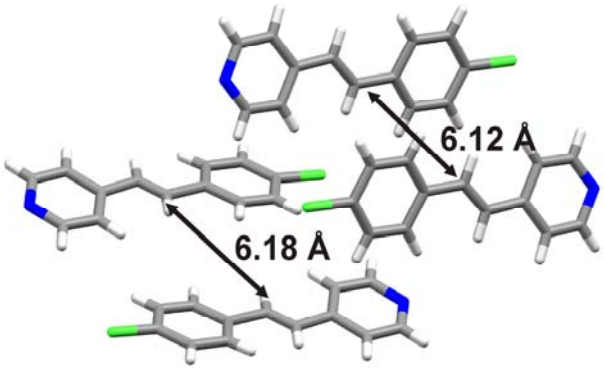

Figure 32 The crystal structure of the photostable **ClPE** polymorph obtained from acetonitrile (viewed along the crystallographic axes (1 0 -2) and (4 -1 0)).

MePE was found to crystallize in the orthorhombic space group $P2_12_12_1$ with one molecule of **MePE** in the asymmetric unit. The stilbazoles are stacked offset and in a head-to-head manner being sustained by C-H···N and C-H···π inteactions. Within the stacks, the olefin –C=C- double bonds are separated by 6.03 Å and are, hence, not satisfying the topochemical postulate (Fig 33). Altogether, both **ClPE** and **MePE** are expected to be photostable based on their crystal structures.

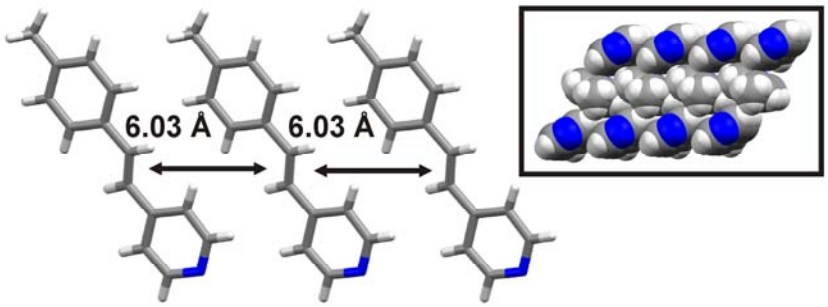

Figure 33 X-ray crystal structure of **MePE**: a) juxtaposed **MePE** molecules viewed along the crystallographic *b* axies, and b) layered stacks of MePEs viewed along the crystallographic (0 1 0) and (1 0 3) planes.

Considering that both **ClPE** and **MePE** solids are photostable, a solid solution composed of both stilbazoles is *not* expected to be photoactive. To form a two-component solid solution comprised of **ClPE** and **MePE**, equimolar amounts of both olefins were refluxed in acetonitrile. Yellow crystalline plates of the (**MePE**)$_x$·(**ClPE**)$_{(1-x)}$ (where x ~ 0.3) (**1**) solid solution formed upon slow cooling of the obtained reaction mixture after 1 hour. The composition of the solid solution was determined by means of ^{1}H NMR spectroscopy (Fig. B131, Appendix B). X-ray powder diffraction revealed that the solid solution resembles the crystal structure of **MePE** (Fig. 34). The solid solution was shown to be slightly reactive upon UV irradiation (broadband, 450 W Hg-medium-pressure lamp) for about 100 hours, as determined *via* ^{1}H NMR spectroscopy (Fig. B132, Appendix B). Specifically, a ^{1}H NMR spectra indicated the formation of cyclobutanes products in very small yields (<5%) being obtained during a non-topochemical reaction that, most likely, occurred during partial melting of the solid solution. The spectra also indicated the presence of oxidized stilbazoles, as evidenced by the occurrence of pyridy-N-oxide peaks in at ppm values above 8.5 ppm (see Appendix B).

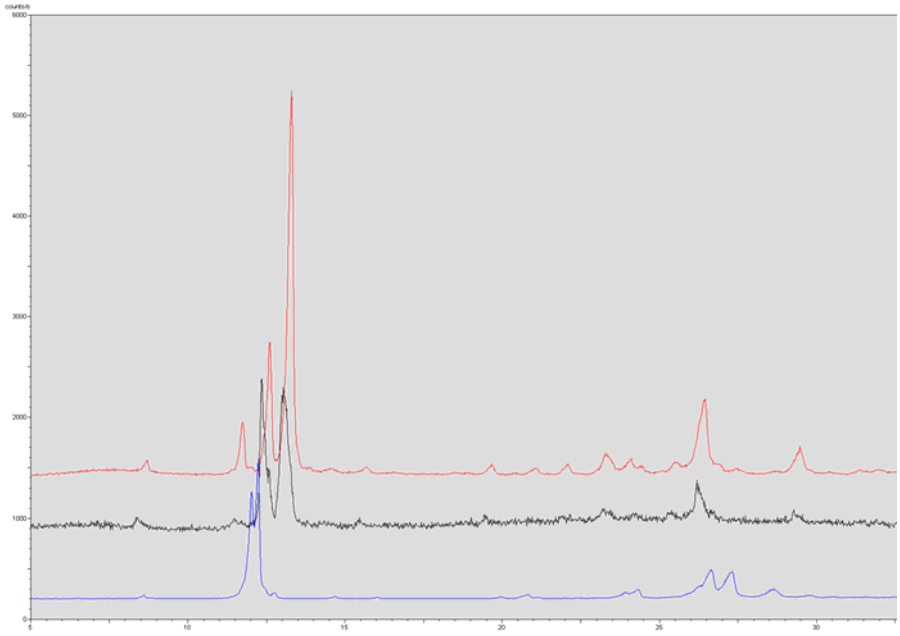

Figure 34 X-ray diffractograms of **MePE**, solid solution **1** and **ClPE** (color scheme: red-**MePE**, black - **2**, blue – **ClPE**).

To facilitate a CPR involving **MePE** and **ClPE**, both components were crystallized in the presence of resorcinol. Specifically, equimolar amounts of **res**, **ClPE** and **MePE** were refluxed in acetonitrile. Yellow single crystals of **2** suitable for single crystal X-ray diffraction experiments formed upon slow cooling of the resulting solution after 5 hours. The crystals were isolated in 81% yield by way of filtration. The formation of **2** was determined by means of X-ray crystallographic analyses (*i.e.* PXRD, SXRD) (Fig. 35, 36) and ^{1}H NMR spectroscopy (Fig. B133, Appendix B). A structural analysis based on single crystal X-ray diffraction data revealed that **2** crystallizes as a solid solution in the triclinic space group $P\bar{1}$. The asymmetric unit is partially occupied by two supramolecular isomers of three-component (**res**)·(**ClPE**)·(**MePE**) assemblies (**2a** and **2b**), and two-component assemblies of (**res**)·(**ClPE**)$_2$ (**2c**) and (**res**)·(**MePE**)$_2$ (**2d**) (Fig. 2a).

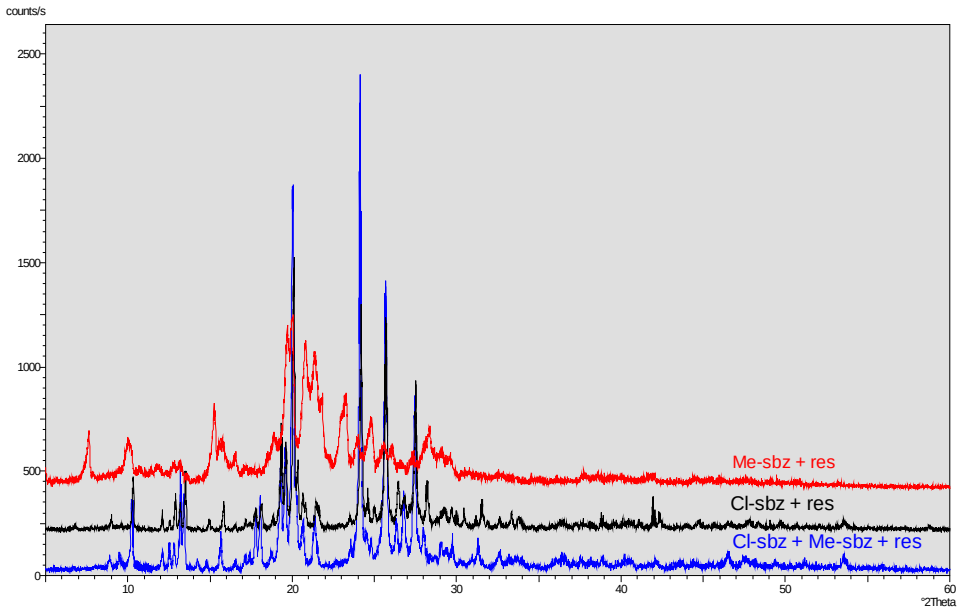

Figure 35 X-ray diffractograms of (**res**)·(**MePE**) (red), (**res**)·(**ClPE**) (black) and **2** (blue).

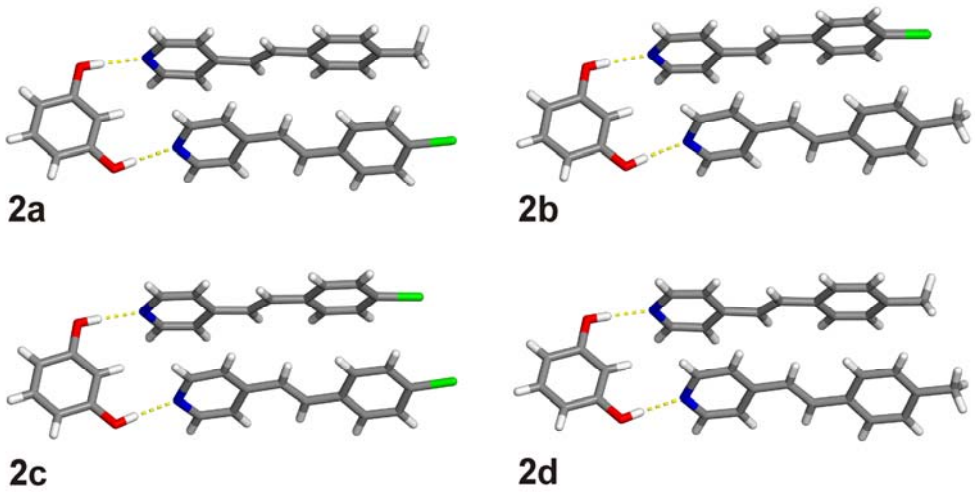

Figure 36 X-ray structures of: a) (**res**)·(**ClPE**)·(**MePE**), (**res**)·(**ClPE**)$_2$, (**res**)·(**MePE**)$_2$.

The occupancy factors of **2a** and **2b** refined to 0.479, whereas **2c** and **2d** refined to be 0.095 and 0.426, respectively. Correspondingly, in another single crystal of **2**, the

occupancies were determined to be 0.509 for **2a** and **2b**, 0.364 for **2c**, and 12.7 for **2d**, thus indicating that such consisting distributions can be expected throughout the bulk sample. The assemblies are held together by two O–H(hydroxy)···N(pyridyl) hydrogen bonds (*d*(O···N): 2.73 and 2.74 Å) (Fig. 37).Within the assemblies, the C=C double bonds of the olefins lie in a criss-cross fashion, being separated by 4.00 Å (other separation distances (Å): Cl/CH_3 4.03 and 4.09; Cl/Cl 4.12; CH_3/CH_3 3.98). The hydrogen-bonded assemblies stack in an anti-parallel manner. The C=C(olefin) double bonds of neighboring assemblies are separated by 4.64 Å (Fig. 37).

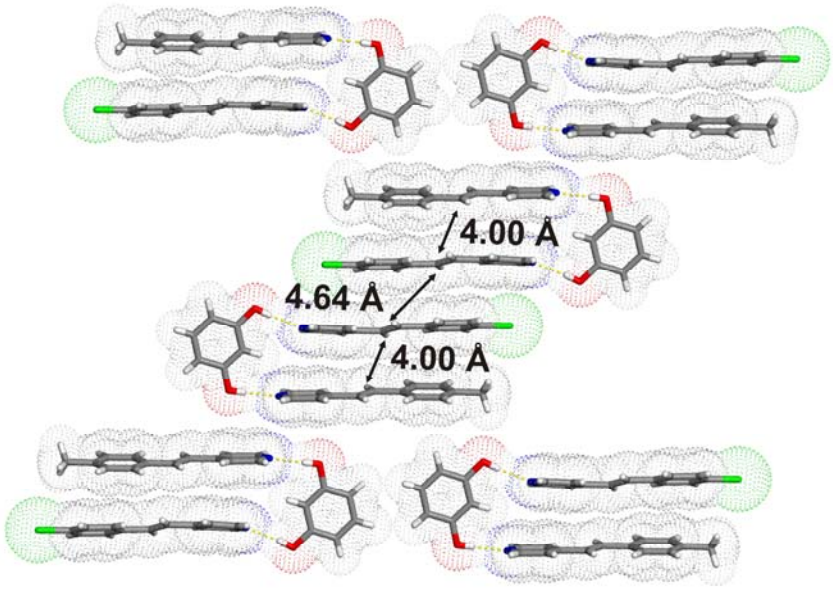

Figure 37 Crystal packing of solid solution **2** (only the **res**/**ClPE**/**MePE** component is shown for clarity).

As a consequence of such crystal packing, a [2+2] photodimerization can, according to Schmidt,[7] occur only within the two- and three-component assemblies to yield homodimers and heterodimers upon a [2+2] cycloaddition reacton (Fig. 38). The photoproducts are expected to exhibit a in a head-to-head geometry.

To evaluate the photoreactivity of **2**, a powdered crystalline sample was exposed to UV irradiation (broadband, 450 W Hg-medium-pressure lamp) for a total of 80 hours. The formation of a cyclobutanes was observed to occur in up to 95% yield within the first 40 hours. No significant increase of the yield was observed within another 40 hours. The formation of the photoproducts was evidenced by the disappearance of the olefin-proton peaks (δ = 7.4-7.7 ppm range) and the appearance of signals corresponding to cyclobutane protons (δ = 4.4-4.7 ppm range) (Fig. B134, Appendix B). The photoproducts were isolated from the irradiated sample of **1** by basic extraction and further investigated *via* mass spectroscopy. ESI-mass spectra revealed a peak at *m*/*z* 411, 431 and 391, thus confirming the formation of **2a**-**2d**, whereby **2a** and **2b** amounts to 61%, **2c** for 17% and **2d** for 22% of the bulk sample (see Appendix C). Combined HPLC and NMR studies are underway to determine the nature of the unreacted solid (~5% of the bulk).

To confirm the structure of the photoproducts, single crystals of $[(H_2\text{-}\mathbf{2}(\mathbf{x}))^{2+}][Br^-]_2 \cdot 0.7(H_2O)$ (**3**) (where **x** = **a**, **b**, **c**, **d**) were grown from an acetonitrile solution of photoreacted **1**, to which few drops of conc. HBr(aq) were added. Single crystal X-ray structure analysis revealed that **3** consists of protonated cyclobutanes **3a**-**d** (Fig. 38). Compound **3** crystallizes in the triclinic space group $P\bar{1}$. The asymmetric unit consists of $[(H_2\text{-}\mathbf{2a})^{2+}][Br^-]_2$, $[(H_2\text{-}\mathbf{2b})^{2+}][Br^-]_2$, $[(H_2\text{-}\mathbf{2c})^{2+}][Br^-]_2$, $[(H_2\text{-}\mathbf{2d})^{2+}][Br^-]_2$ and 0.7 water molecules. The occupancy factors of **2a**, **2b**, **2c** and **2d** were refined to be 0.342, 0.199, 0.230 and 0.229, respectively. The photoproducts exhibit a head-to-head geometry, which is consistent with the crystal structure of **2** (Fig. 37). The crystal structure of **3** is based on intercalated photoproducts of $[(H_2\text{-}\mathbf{2x})^{2+}][Br^-]_2$, (where **x** = **a**, **b**, **c**, **d**) being held together by weak C–H···Br^-, Cl···π, C–H···π and π···π interactions. The water molecules are partially occupying cavities formed between pairs of $[(H_2\text{-}\mathbf{3}(\mathbf{x}))^{2+}][Br^-]_2$.

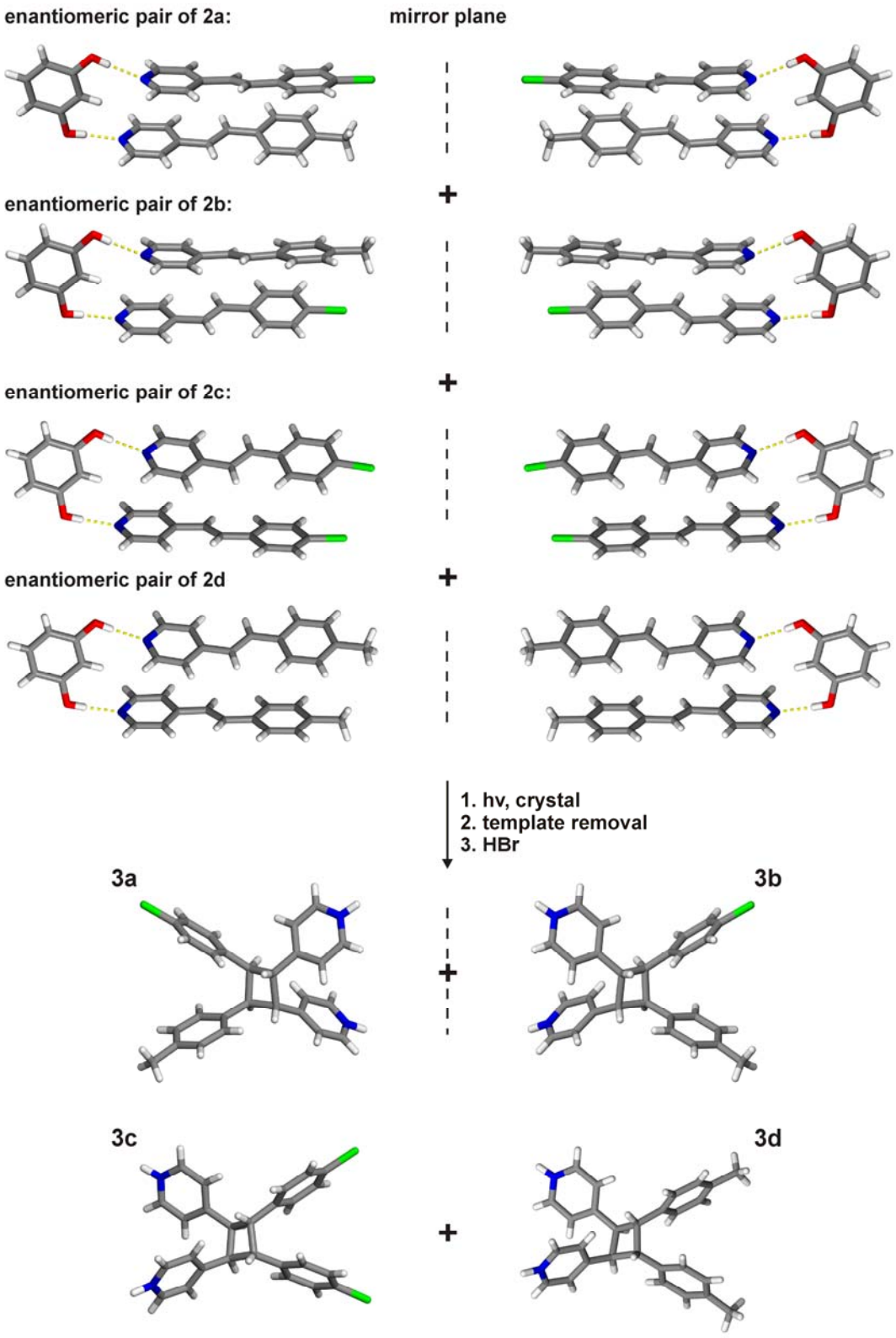

Figure 38 Template-directed CPR between **ClPE** and **MePE**.

22.2.5. Conclusion

We described herein a CPR in a solid solution involving two stilbazoles, namely **ClPE** and **MePE**. The two-component **ClPE**/**MePE** solid solution was found to be photostable owing to misaligned -C=C- double bonds of the stilbazoles within the solid. A photoactive solid-solution involving **ClPE** and **MePE** was, therefore, engineered using a synthetic template in form of resorcinol. Specifically, **ClPE** and **MePE** were cocrystallized with resorcinol to yield a three-component solid-solution wherein **ClPE** and **MePE** homo- and enantiomeric **ClPE**/**MePE** heterodimers form stereospecifically and in nearly quantitative yields upon UV irradiation. The results clearly demonstrate that cocrystallization and hydrogen-bonding can be utilized to facilitate CPRs in the solid state. Finally, asymmetric solid-state CPRs – a class of reactions considered as *highly important* and *undeveloped* – are expected to be readily achievable *via* cocrystallization of two achiral reagents in a chiral space group using homochiral synthetic templates. Such CPRs are envisioned to facilitate the synthesis of complex targets (*e.g.* natural products) in a reduced number of synthetic steps, higher overall yields and in a sustainable fashion.

2.3. A thixotropic hydrogel derived from an organic solid-state synthesis: Properties and measured densities of individual metal-organic nanoparticles

2.3.1. Introduction

The gelation of organic and aqueous solutions has applications in tissue engineering,[131] controlled drug release and delivery,[132-134] and pollutant sequestering.[135] Gelators are typically covalent polymers, however, gels sustained by molecular components that self-assemble *via* non-covalent forces (*e.g.* hydrogen bonding) are becoming more prevalent, particularly in the development of stimuli-responsive materials.[136-138] The process of gelation is considered to arise from the self-assembly of macromolecular components into networks that entangle and entrap solvent.[139] Indeed, the formation of a gel represents a balance between the tendency of the components to dissolve and aggregate, which is especially important in the case of water as the solvent since the self-assembly process must compete with a dynamic network and clustering of hydrogen bonds in the aqueous medium.[140]

In this context, metal-ligand bonding[141] is emerging as an attractive means to gel organic and, to a lesser extent, aqueous solvents.[132, 142-146] The incorporation of metals affords an opportunity to integrate the properties of metals (*e.g.* optical,[144, 145] redox[147], magnetic[148]) into a supramolecular gel environment. An approach often used to form a metal-organic gel, or metallogel,[146] involves the self-assembly of metal ions with an organic ligand that bridges the metals in one- (1D), two-, or three-dimensions. The organic bridges are typically symmetric with respect to sites for metal-ion coordination. To date, bridging ligands that support the formation of a metallogel have invariably been synthesized using conventional approaches to organic synthetic chemistry (*i.e.* solution-based methodologies).

In this section, we describe a metal-organic system that gels both organic and aqueous solvents[149, 150] and is based on the ligand *rctt*-1,2-bis(3-pyridyl)-3,4-bis(4-pyridyl)cyclobutane (**3,4'-tpcb**) that has been synthesized in the organic solid state (Fig. 39). We have recently described the template-directed solid-state synthesis[30] of **3,4'-tpcb** using 1,8-naphthalenedicarboxylic acid as a small-molecule hydrogen-bond-donor template.[151] The rigid and unsymmetrical tetratopic cyclobutane can bind up to four metal ions *via* the two different pyridine rings. The ability of the **3,4'-tpcb** to support an unusual 2D metal-organic framework (MOF) composed of three different cavities has recently been reported.[152] The tetrapyridine is available from the solvent-free environment quantitatively, stereospecifically, and on a gram scale, which means that, in contrast to a majority of solid-state reactions, the cyclobutane is readily available for applications in coordination chemistry.

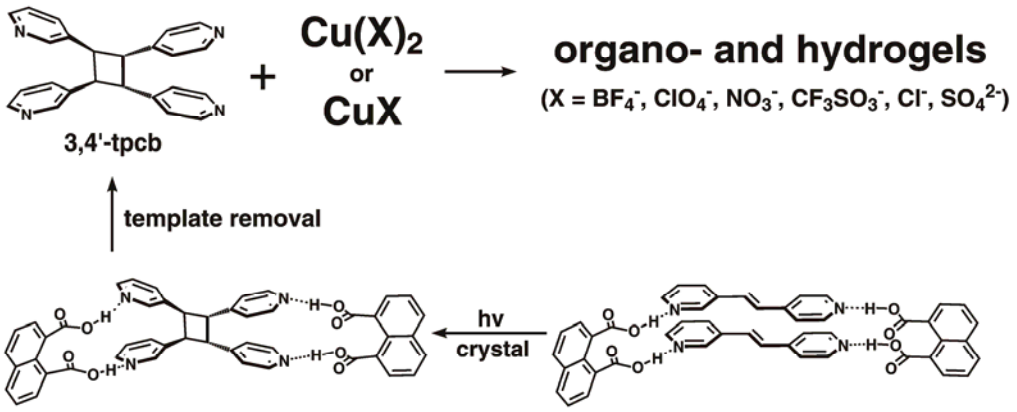

Figure 39 Synthesis of the 3,4'-tpcb-based hydrogel.

During studies aimed to construct crystalline MOFs with **3,4'-tpcb**,[30] our group has discovered the ability of **3,4'-tpcb** to form gels with Cu(II) ions and a variety of counter anions in organic solvents and water.[153] However, the gel remained

uncharacterized all until now. Atomic force microscopy (AFM) and scanning transmission X-ray microscopy (STXM) experiments were performed by Dr. A. V. Tivanski's group (Department of Chemistry, University of Iowa), while the rheology measurements were conducted by Prof. D. R. Flanagan's group (Division of Pharmaceutics, College of Pharmacy, University of Iowa). TEM micrographs were collected by Dr. J. Baltrusaitis (Central Microscopy Research Facility, University of Iowa).

From transmission electron microscopy (TEM), the structure of the hydrogel has been determined to be composed of recently-discovered amorphous nanoscale metal-organic particles (NMOPs).[154-166] NMOPs are a class of inorganic-organic materials with promising applications in areas such as drug delivery,[164, 165] molecular electronics,[157] biosensing,[162] and imaging.[166] To date, there have been no reports of NMOPs that support the formation of a gel, although colloidal metal-organic particles of micron dimensions have been reported.[154, 158] Upon application of mechanical force, the hydrogel based on **3,4'-tpcb** turns liquid-like and, thereby, exhibits thixotropic behavior, which has been quantified using a series of shear stress loop tests.[142, 144, 145, 167-169]

In addition to **3,4-tpcb** supporting a gel composed of NMOPs, we introduce here a combination of AFM and STXM as a means to determine size-dependent densities of individual NMOPs present in the gel. We use AFM to determine the morphologies of the individual NMOPs and STXM to measure C and N atomic absorbances that when combined facilitate density determination. The densities of individual nanoparticles are, in general, difficult to determine. Moreover, whereas the densities of crystalline nanoparticles are typically assumed comparable to the bulk solid (*e.g.*

Au = 19.3 g/cm^3),[170, 171] the densities of amorphous nanoparticles are expected to vary from the bulk owing to a presence of core particle inhomogeneities (*e.g.* voids).[171, 172] Developing an understanding of the properties of nanomaterials is critical for the fabrication of functional nanodevices. Differences in nanoparticle densities have recently been exploited in separation processes based on ultracentrifugation[170] while in biology and the related field of medical diagnostics correlations of densities of small biological particles with diseases are, for instance, known yet measurement techniques can be laborious.[172] We show here that a combination of AFM and STXM uniquely offers density quantification of nanoparticles on a single particle basis while, at the same time, is quite practical. The density determined for the NMOPs involving the thixotropic gel based on **3,4'-tpcb** is 1.37 g/cm^3, which is comparable to crystalline MOF materials.

2.3.2. Experimental section

2.3.2.1. Materials

$Cu(BF_4)_2 \cdot H_2O$ (97%), acetonitrile (anhydrous, 99.8%). Solvents and reagents were purchased from Sigma-Aldrich Co (Saint Louis, MO). All chemicals were used without any further purification. **3,4-Tpcb** was prepared according to the procedure described in a previous report.[151]

2.3.2.2. Synthesis of the hydrogel

Solutions of **3,4'-tpcb** and an appropriate copper salt were combined in a 1:1 stoichiometric ratio at 2.0 wt % or less (combined) in various solvents (4.0 mL total). For the hyfrogel, **3,4'-tpcb** (0.0485 g; 0.133 mmol) was dissolved in a *minimum* amount (0.150 mL) of anhydrous acetonitrile and combined with an aqueous solution of

$Cu(BF_4)_2 \cdot H_2O$. The Cu(II) solution was prepared by dissolving 0.0315 g (0.133 mmol) in 3.850 mL of doubly-deionized water. The resulting solution, containing 2.0 wt % of the gelator, yields a gel after periods of 3 to 4 h.

2.3.2.3. Single-crystal X-ray diffraction.

The diffraction data were measured on a Nonius Kappa CCD single-crystal X-ray diffractometer at low temperature using MoK_α radiation (λ = 0.71073 Å). Data collection, cell refinement and data reduction were performed using *Collect*[173] and *HKL Scalepack*/*Denzo*,[174] respectively. Structure solution and refinement were accomplished using SHELXS-97 and SHELXL-97,[175] respectively. The majority of non-hydrogen atom sites were identified upon structure solution using direct methods, whereas the remaining non-hydrogen atoms were indentified from the difference Fourier map within several refinement steps. All non-hydrogen atoms were refined anisotropically. Hydrogen atoms associated with carbon atoms were refined in geometrically constrained positions. Relevant crystallographic parameters are given in Table 17.

The structure contains highly disordered solvent molecules. The difference Fourier map revealed electron densities that could be ascribed to chloroform, acetonitrile, and water. Despite extensive use of restraints, an acceptable solvent model was achieved. The crystal structure was treated with the SQUEEZE routine of PLATON.[176] The solvent molecules were determined to occupy 899.5 $Å^3$ or 15.6% of the unit cell. An electron count of 385 electrons per unit cell corresponds to approximately one molecule of chloroform, one molecule of acetonitrile, and 1.6 molecules of water per asymmetric unit.

2.3.2.4. Rheology measurements

Rheological measurements were performed using a Haake Rheostress 1 controlled stress rheometer operating under RheoWin (version 2.96) software with a cone and plate sensor (35 mm dia., 4° cone angle). To test a gel, approximately 1.2 - 1.3 g of the gel was carefully applied to the lower plate and the cone sensor was lowered into position at

a final rate of 0.3 mm/min; excess gel that emerged from the cone/plate was carefully wiped away from the edge so that only gel retained between the cone and plate remained. Once the cone reached its final position, the gel was allowed to relax for 3 minutes before a rheological test was initiated. The rheometer was used in a controlled rate mode with a range of shear rates from about 0 to 100 sec^{-1}. The shear stress ramp increased from low to high stress over about 1 minute and then the stress was decreased back to zero in about 1 minute. The dwell time at each shear stress was 2 seconds. In a series of measurements, the gels exhibited nominally different separations between curves, with extrapolations of the nearly linear portions of the increasing shear stress profiles to the ordinate axis giving yield values ranging from 8 to 12 Pa.

2.3.2.5. Transmission-electron microscopy

The gel was placed on a carbon-coated copper grid and the excess removed with filter paper. The sample was then dried at reduced pressure and examined using a JEOL 1230 TEM at 80.0 kV accelerating voltage. Images were acquired using a Gatan UltraScan 1000 2k × 2k CCD camera.

2.3.2.6. AFM studies

The gel was placed on an atomically flat mica substrate or a Si_3N_4 window (Silson Ltd., England) and dried for at least 24 hours under ambient environment. The sample was examined using a commercial AFM (MFP 3D, Asylum Research, Santa Barbara, CA). AFM height image measurements were obtained at room temperature using silicon probes (Mikromasch, San Jose, CA, CSC37) with a typical tip radius of curvature of 10 nm. Topographic images were collected using intermittent contact mode (AC mode) at a typical scan rate of 1 Hz. All experiments were performed at room temperature under ambient environment.

2.3.2.7. STXM studies

The gel was placed on a Si_3N_4 window (Silson Ltd., England) and dried for at least 24 hours under ambient environment. Single energy images, and carbon, oxygen and nitrogen K-edge NEXAFS spectra were acquired using STXM instrument on beamline 5.3.2 of the Advanced Light Source (Berkeley, CA) in a ~0.5 atm He-filled chamber. For these measurements, the X-ray beam is focused with a custom made Fresnel zone plate onto the sample with the diffraction limited spot size of 25 nm and the transmitted light intensity is detected. Images at a single energy are obtained by raster-scanning the sample at the focal plane of X-rays and collecting transmitted monochromatic light as a function of sample position. Spectra at each image pixel or a particular sample region are extracted from a collection of images recorded at multiple, closely spaced photon energies across the absorption edge. Dwell times used to acquire an image at a single photon energy were typically 1 ms per pixel. To quantify the absorbance signal, the measured transmitted intensity (I) is converted to optical density (OD) using the Beer-Lambert's law:

$$OD = -\ln\frac{I}{I_0}$$ (where I_0 is the incident photon flux intensity)

The incident beam intensity is measured through the sample-free region of the substrate. The particle spectrum is obtained by averaging over the particle deposited on the substrate. The X-ray energy calibration (accuracy of ±0.05 eV) is afforded by addition of CO_2 gas (6 torr) to the STXM chamber through comparison of the position of CO_2 Rydberg transitions at 292.74 and 294.96 eV.[177]

NEXAFS spectra from 1s electrons for C, N and O atoms were collected in the energy regions of 280-320 eV, 395-420 eV, and 525-550 eV, respectively. The pre-edge background typically arises from the weak but finite absorption of other elements at that energy. The post-edge absorbance depends on the number of corresponding atoms at the

particular edge (*i.e.*, the number of carbon atoms at C-edge or oxygen atoms at O-edge). The total C, N, or O atomic absorbances were defined as the difference between the corresponding post-edge and pre-edge absorbences. Pre-edge absorbences at 280, 395, and 525 eV and post-edge absorbences at 320, 425 and 550 eV were used to quantify the total amount of C, N, and O atoms.

2.3.3. Results and discussion

When **3,4'-tpcb** (0.0314 g; 0.086 mmol) was reacted with $Cu(BF_4)_2 \cdot H_2O$ (0.0210 g; 0.088 mmol, 1:1 ratio) in acetonitrile (4.0 mL), a blue solution immediately formed that after 10-12 hours became a transparent blue gel (Fig. 40). The experiment involving the organic solvent represents 2.0 wt% gelator, which is low compared to most metallogels.[178] Gels also formed at gelator concentrations between 1.0 and 2.0 wt% (see: T. D. Hamilton, PhD thesis, University of Iowa, 2005)[153]. Thus, at 1.0 wt%, one gelator unit traps 1,463 molecules of acetonitrile. Similar results were obtained using nitromethane as the solvent. A gel was not obtained, however, using either highly polar dimethylsulfoxide or dimethylformamide, instead, blue powders formed. Gels were obtained in methanol at higher wt% gelator (*ca.* 10 wt%), however, below 2.0 wt% solutions were obtained. Gels formed in acetonitrile and nitromethane using Cu(II) salts of ClO_4^-, NO_3^-, SO_4^{2-}, $SO_3CF_3^-$, and Cl^-. With Cu(II) hexfluoroacetylacetonate (hfac), a crystalline powder was obtained.

The metallogels obtained from the organic solvents were thermally stable and did not display a change in morphology to well beyond the boiling points of each solvent. The level of stability has been only reported with gels based on purely organic

compounds.[179-181] When heated beyond the boiling point, the gels did not revert to a solution, instead, a sticky, rubbery substance was present. The gels were also stable in capped vials on the benchtop without heating for more than six months.

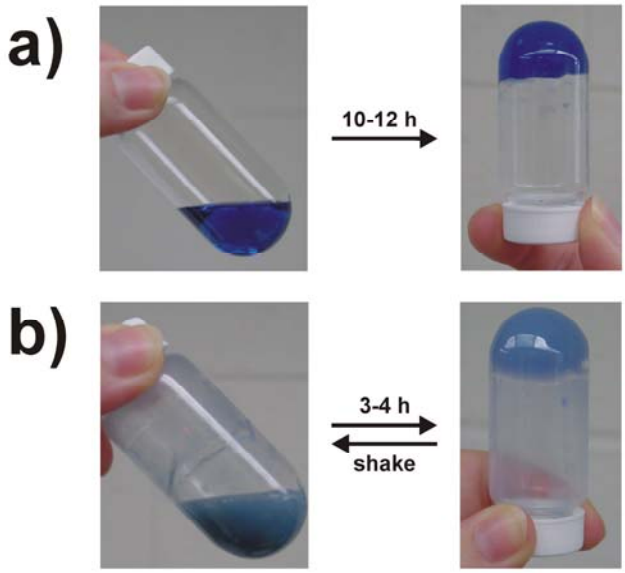

Figure 40 Metallogels upon combining $Cu(BF_4)_2{\cdot}H_2O$ and **3,4'-tpcb**: (a) acetonitrile and (b) water (T.D. Hamilton, PhD thesis, University of Iowa, 2005; reproduced with permission of the author)[153]

To gain insight into the structures of the metallogels, single crystals from the reaction of **3,4'-tpcb** with $Cu(hfac)_2{\cdot}H_2O$ were studied using X-ray diffraction. Thus, $[Cu_2(hfac)_4(\mathbf{3,4'\text{-}tpcb})]_\infty$ was prepared by layering a 10 mL acetonitrile solution of $Cu(hfac)_2{\cdot}H_2O$ (0.034 g, 0.0685 mmol) on a 10 mL chloroform solution of **3,4'-tpcb** (0.025 g, 0.0685 mmol) (1:1 mol ratio). After a period of one day, green rectangular single crystals of $[Cu_2(hfac)_4(\mathbf{3,4'\text{-}tpcb})]_\infty{\cdot}1.6H_2O{\cdot}CH_3CN{\cdot}CHCl_3$ suitable for X-ray diffraction analysis formed at the solvent interface (yield: 0.037 g, 41 %).

The components of $[Cu_2(hfac)_4(\mathbf{3,4'\text{-}tpcb})]_\infty$ assemble in the solid state to form a 1D coordination polymer that is composed of rhomboids wherein **3,4'-tpcb** defines opposite corners of the polygons (Fig. 2). The rhomboids are of dimensions ~ 6.3 Å × 6.3 Å with corner angles ~ 80.2º and 110º.

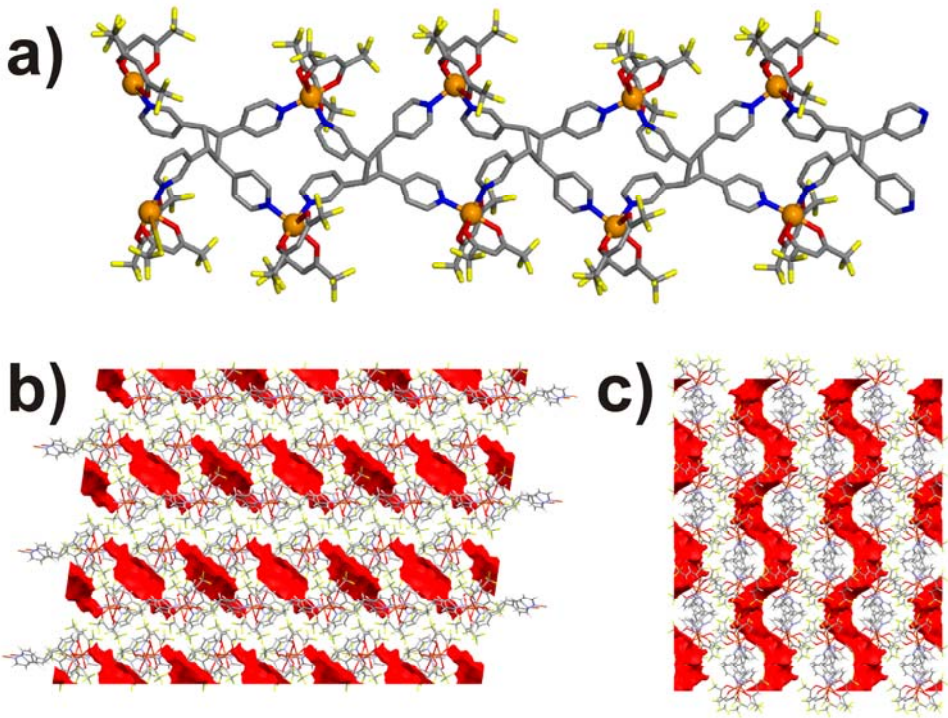

Figure 41 X-ray crystal structure of 1D $[Cu_2(hfac)_4(\mathbf{3,4'\text{-}tpcb})]_\infty$: a) crystallographic *a*-axis, b) crystal packing showing solvent-inclusion along *b*-axis, and c) packing showing solvent along *c*-axis. Solvent-occupied areas in red (color scheme: C = gray, N = blue, O = red, F = yellow, Cu = orange).

Each Cu(II) ion lies in an octahedral coordination environment and is coordinated by 4-pyridyl units and 3-pyridyl units in *cis* positions, as well as two chelating $hfac^-$ anions. The separation distance between the metal centers is 7.87 Å within a polygon and 9.38 and 11.59 Å between adjoining polygons (Fig. 41a). The cyclobutane ligand within each 1D polymer points in the same direction, or lies unidirectional, within each

polymer strand as demonstrated by the orientations of the pyridyl groups. Neighboring strands pack anti-parallel with included water, chloroform, and acetonitrile solvent molecules being disordered and filling space between the strands (Figs. 41b,c). The solvent present in the solid occupies approximately 16% of the unit cell contents. From the structure of $[Cu_2(hfac)_4(\mathbf{3,4'\text{-}tpcb})]_\infty$, we conclude that **3,4'-tpcb** lends itself[182] to form infinite networks, which are considered the basic building units of gels.

We have also discovered that reaction of **3,4'-tpcb** (0.0485 g; 0.133 mmol) with $Cu(BF_4)_2 \cdot H_2O$ (0.0315 g; 0.133 mmol, 1:1 ratio) in water (4.0 mL) with minimum acetonitrile (< 5%) results in a light blue solution that after 3-4 hours becomes a gel (Fig. 40b). The experiment involving the water represents 2.0 wt% gelator. These observations make the metal-organic system a hydrogelator and a rare amphiphilic gelator. Gels also formed in water at concentrations between 1.4 and 2.0 wt%. Thus, at 1.4 wt%, one gelator unit traps 2,387 water molecules. Importantly, upon shaking, the hydrogel reverted to a sol that, upon standing for 3-4 h, reformed the gel. The transition between gel and sol was repeatable indefinitely. The ligand **3,4'-tpcb**, thus, supports the formation of a thixotropic hydrogel. Similar to the organogels, the hydrogel was thermally stable beyond the boiling point of the aqueous solvent. The hydrogel was also stable on a benchtop without heating or agitation for more than six months. When placed in a dessicator, the gel turned to a blue powder while re-exposure of the powder to water vapor resulted in *complete reformation* of the gel.

To obtain a picture of the aggregation mode of the hydrogel, samples at 2.0 wt% gelator were studied by TEM. A representative sample of a freshly-prepared gel revealed spherical NMOPs of diameter approximately 50 to 300 nm (Fig. 42a). The NMOPs were the primary particles visible in the TEM micrograph. The particles compare in shape and size to recently reported NMOPs.[154, 156, 158, 159, 163, 183] To our knowledge, the observation that NMOPs support the formation of a gel has not been described, although colloidal metal-organic particles of micron dimensions that support a gel have been reported.[154, 158]

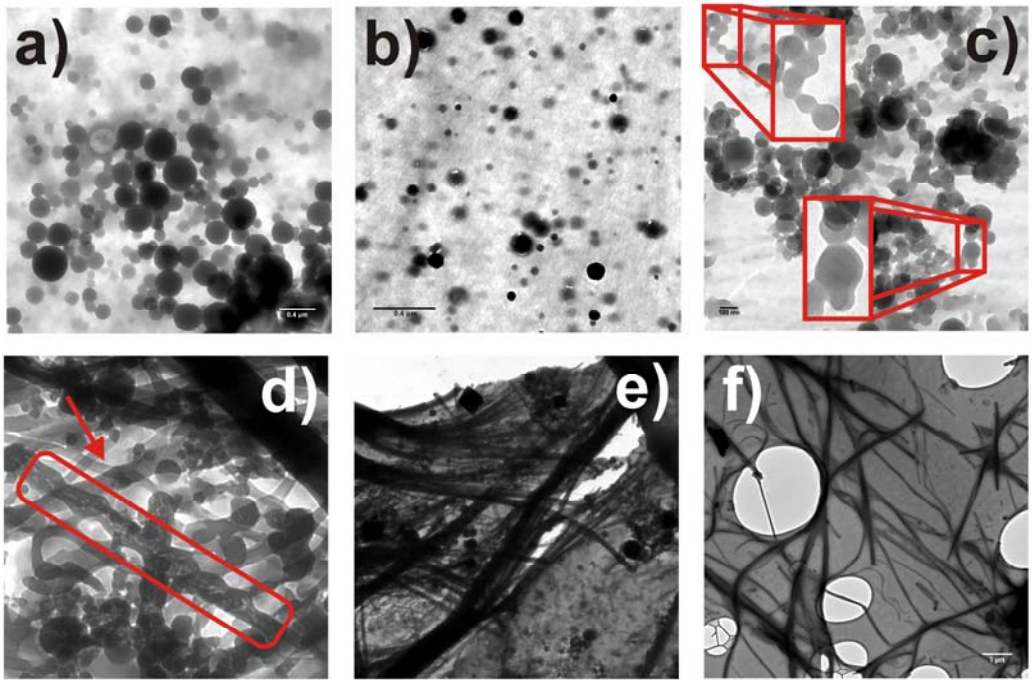

Figure 42 TEM micrographs of hydrogel: a) fresh gel upon standing (> 4 h), b) sol after shaking (5 min), c) transition of NMOPs of reformed gel into "pearl-necklace" structures (in red) (3-6 weeks), d) pearl-necklace nanostructures (red rectangle) and 1D nanobundles (red arrow) (6-12 weeks), e) nanobundles and nanospheres (6-12 weeks), and f) nanobundles in aged gels (about a year).

Representative images of the sol that immediately formed upon shaking (Fig. 42b), as well as the reformed gel (Fig. 42c), demonstrated that the NMOPs remained the primary particles within the sol and gel materials. Upon aging over periods of weeks, however, the spherical particles underwent a morphological transition into nanobundles and a 2D film (Figs. 42d,e). The bundles appeared as pearl-necklace[184] structures from fusion of the NMOPs. Similar transformations involving an organic charge-transfer dye[184] and a block co-polymer have been described,[160] with the origin of the transformations being attributed to strain release of the high curvature-energy contents of spherical particles and surface defects. For the system described here, the reversible nature of the metal-ligand bonding[154, 183] in combination with the ability of the rigid tetrapyridine to enforce the components into 1D arrays likely accounts for the fusion of

the NMOPs into thermodynamically more stable[184] bundles upon aging. The TEM micrographs also demonstrated that hydrogels aged for up to one year to consist of aggregated and interwoven networks of nanobundles (Fig. 42f).

To gain further insight into the morphology of the hydrogel, samples at 2.0 wt% gelator were studied using AFM (Fig. 43). A representative AFM height image of a freshly-prepared gel revealed the presence of NMOPs with base sizes approximately 300 nm (Fig. 43a), which were consistent with the TEM results. The heights, however, were several times smaller than the bases. In particular, an examination of 40 individual nanoparticles with sizes ranging between 50 and 900 nm revealed a height-to-diameter ratio of 0.36 ± 0.01. We attribute the deformation of the spheres to a release of included water *via* drying. A close inspection of the 2D film also showed the material to be composed of NMOPs of dimensions significantly smaller than the free nanoparticles (Fig 43b).

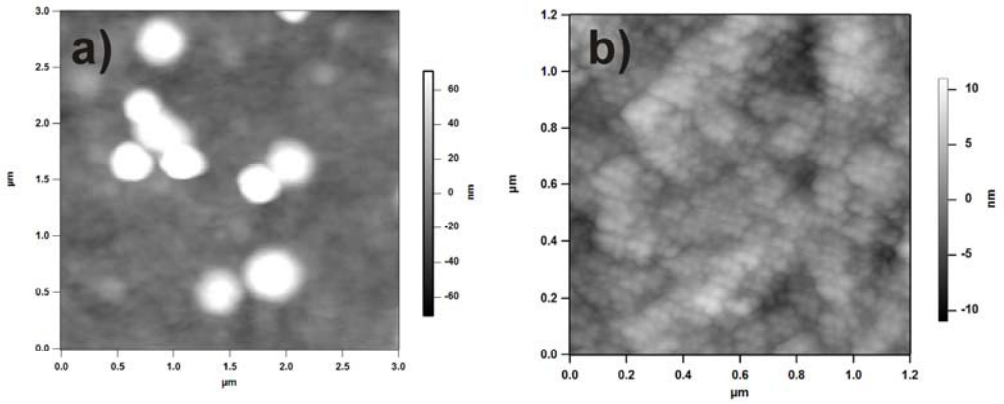

Figure 43 AFM height images showing main particle morphologies of the hydrogel: a) free nanoparticles with base sizes of approximately 300 nm and b) nanoparticles within the films with typical heights of 4 to 5 nm and base size of approximately 40 nm.

The nanoparticles within the films exhibited heights between 4 and 5 nm and bases of approximately 40 nm. With the films also being a major component of the gel, it is likely that the larger nanoparticles are able to transform to the smaller nanoparticles of the film.[154]

To quantify the thixotropic behavior of the hydrogel, a series of shear stress loop tests were conducted. In particular, an extrapolation of the nearly-linear portion of the increasing shear stress profile to the ordinate axis was determined to give a yield value of 8.33 Pa (Fig. 44).

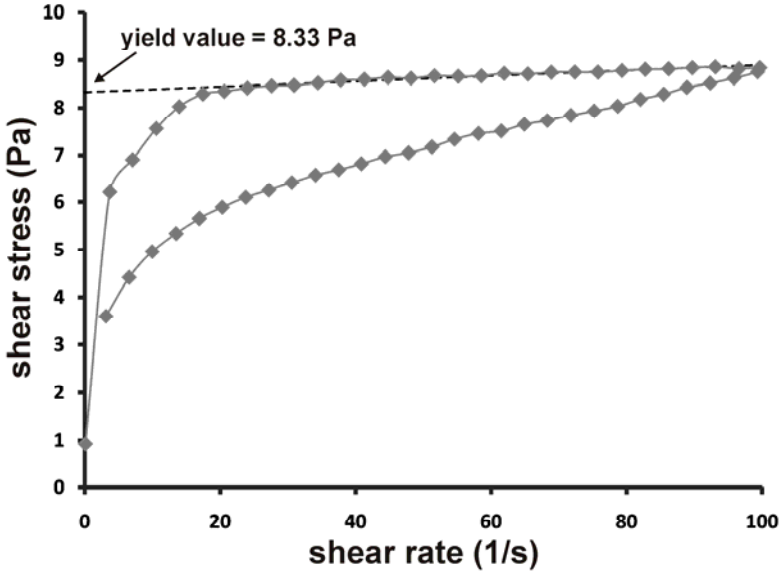

Figure 44 Shear stress versus shear rate graph for the 2% w/w thixotropic hydrogel based on $Cu(BF_4)_2$ and **3,4'-tpcb** showing a yield stress value of 8.33 Pa (indicated by arrow). A stress ramp up and down producing shear rates from about 0 to 100 sec^{-1} was used to elucidate the thixotropy of the hydrogel.

The stress value is less than previously reported metallogels that gel organic solvents[167] and likely reflects difficulties of the NMOPs to maintain strong surface contacts in the polar aqueous medium upon agitation. The low stress value can also be

attributed to the relatively low concentration of the gelator (*ca.* 2%). Nevertheless, the ability of the components to form a gel in the highly-polar aqueous medium is likely a result of the relative small size of the NMOPs, which can provide a high surface area that supports many interparticle contacts and cross-links.[167] The formation of a large number of contact and cross-links would also account for the high stabilities of the gels in the organic solvents.

Our characterization of the morphologies of the NMOPs using AFM prompted us to turn to determine the densities of the nanoparticles using a combination of synchrotron-based STXM and AFM.[185] STXM provides spatially-resolved (~ 25 nm resolution) particle atomic absorbances (OD) that can quantified using the Beer-Lambert's law: [185]

$$OD_i = \rho_i \mu_i h$$

where i is the atom type (*i.e.* C, N or O), OD_i is the total atomic absorbance in units of optical density (*OD*), μ_i is the mass absorption coefficient for the corresponding atom, ρ_i is the atomic density of the particle, and h is the particle height. Since STXM essentially measures a product of particle density and thickness, a density determination required knowledge of the 3D shapes of the particles, which we obtained from the AFM results. Understanding the physical properties of individual nanoparticles (*e.g.* density) is, in general, important in the manipulation of nanoparticles and the fabrication of functional nanomaterials and devices. Moreover, by combining the AFM and STXM data, we expected to be able to determine atomic density on a single particle basis, according to Equation 1. The method could also, in principle, be extended to other nanoparticles and nanomaterials (*e.g.* aerosols).

In our STXM studies involving the NMOPs, single energy (320 eV) STXM images of the particles (Fig. 45a) were measured and determined to be consistent with the TEM and AFM results. For the density quantification, absorbance maps for 36 and 25 individual NMOPs with size ranges between 200 nm and 1.2 μm were collected at the C

(320 eV – 280 eV) and N (420 eV – 395 eV) edges, respectively.[185] Oxygen absorbance maps (550 eV – 525 eV) were also collected for 15 individual NMOPs of various sizes; however, the maps to our surprise displayed a *complete absence* of oxygen in the particles. We attribute the lack of O-atoms to the NMOPs losing water and, thus, becoming fully dehydrated. On the other hand, both C and N maps indicated the presence of C and N atoms with uniform distributions throughout each particle (25 nm resolution). Total C and total N absorbances in OD units were next recorded at the center of each particle along with particle diameter. The height of each NMOP was determined by multiplying the diameter from STXM by 0.36, as determined from the AFM studies. The mass absorption coefficients were then calculated from the atomic scattering factors and determined to be 3.8 x 10^4 cm^2/g and 2.9 x 10^4 cm^2/g for C and N, respectively.[186] The single NMOP C and N atomic density could then be determined by dividing the total C or N absorbance by particle height and corresponding mass absorption coefficient.

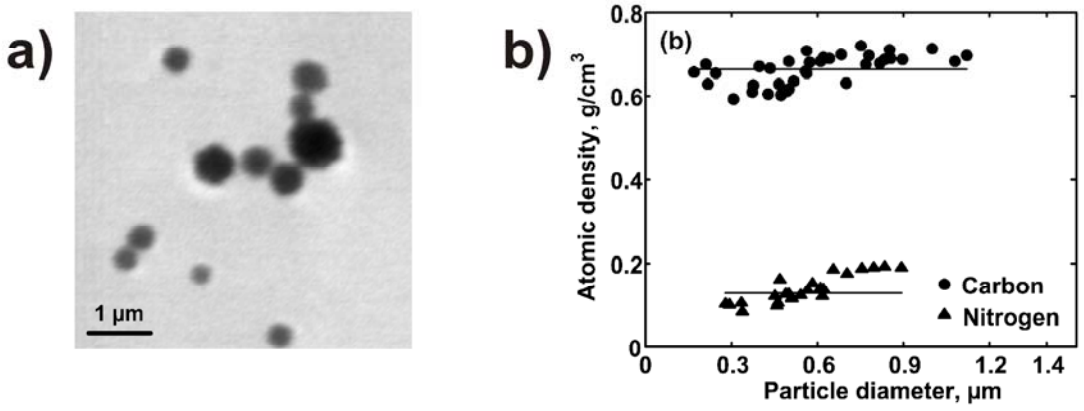

Figure 45 STXM data: a) single energy (320 eV, 5µm x 5 µm) STXM image of NMOPs within the hydrogel and b) single particle C (•) and N (▲) atomic density *versus* particle diameter. Symbols are the data and solid lines correspond to the averaged density.

The single particle C and N atomic densities were determined and plotted against particle diameter (Fig. 45b). From the data, the mean values for the C and N densities were found to be 0.66 ± 0.04 g/cm^3 and 0.13 ± 0.03 g/cm^3, respectively. The C:N ratio of atomic densities was, thus, calculated to be 5.14 ± 0.13. By scaling the C:N atomic density ratio with the atomic C and N weights, the ratio of the number of C to N atoms present in each NMOP was determined to be 6 ± 0.15. The resulting C:N ratio of approximately 6 is in excellent agreement with the expected molecular formula $C_{24}N_4H_{20}Cu(BF_4)_2$. Moreover, by using the molecular formula and assuming all H, Cu, B and F atoms to be homogeneously distributed throughout each particle,[172] as determined by the STXM data, the atomic density was scaled to the total density of the nanoparticle. *We calculated an average nanoparticle density of 1.37 ± 0.07 g/cm^3.* The calculated density is significantly smaller than nanocrystals composed purely of metals (*e.g.* Au 19.30 g/cm^3)[171] yet comparable to solvated crystalline MOFs and related metal-organic materials.[41, 42, 187, 188] For the NMOPs described here, the density would correspond to a desolvated particle, which is consistent with the reduced height, or collapsed morphologies, of the individual particles. Metal-free nanoparticles such as polystyrene aerosols[189] (1.04 g/cm^3) and single-walled carbon nanotubes[170] (1.10 g/cm^3) generally exhibit smaller densities. To the best of our knowledge, the density of a NMOP has not been reported.

2.3.4. Conclusion

In conclusion, we have reported the ability of the multitopic ligand **3,4-tpcb** obtained from the organic solid state to support the formation of an amphiphilic metallogel. The resulting hydrogel is thixotropic, which can be explained on the basis of the gel being composed of NMOPs that support many particle contacts. A novel combination of AFM and STXM has been developed and used to determine the density of the NMOPs, with the measured density being comparable to MOFs. The NMOPs have

been determined to transform into bundles and films upon aging. We are currently employing additional ligands available from the organic solid state, and less available from solution, as unique building blocks of metallogels. We are also focused upon determining whether the NMOPs can be developed for molecular encapsulation[156, 163] with an aim to expand the ability of self-assembling gels to accommodate guest components trapped from aqueous media.

CHAPTER 3:
PREPARATION AND PROPERTIES OF ORGANIC NANO-COCRYSTALS

3.1. Introduction

In recent years, crystal engineering has become a commonly used method in the preparation of organic materials with specific physicochemical properties, and has also generated a plenty of interest among pharmaceutical solid-state scientists, organic synthetic chemists as well as materials chemists. Despite the large interest in crystal engineering, the filed has not addressed the preparation of nano-dimensional multi-component molecular crystals. Having in mind the utility of nanomaterials in technology and medicine, we aimed to explore the possibility of "nano-sizing" molecular cocrystals. In this chapter, we present a sonochemical "bottom-up" method for the preparation of nano-dimensional cocrystal, as well as selected results obtained from studies of their physical properties.

3.2. Preparation and reactivity of nanocrystalline cocrystals formed *via* sonocrystallization

3.2.1 Introduction

A recent study by Nakanishi has described a method to achieve single-crystal-to-single-crystal (SCSC) chemical reactivity in organic solids by reducing crystal size.[115] Specifically, pure diolefin crystals of nano- and micrometer dimensions synthesized *via* a reprecipitation method exhibited SCSC photoreactivity to give a polycyclobutane polymer. This contrasted diolefin crystals of macroscopic dimensions that cracked during the photoreaction (Fig. 46).

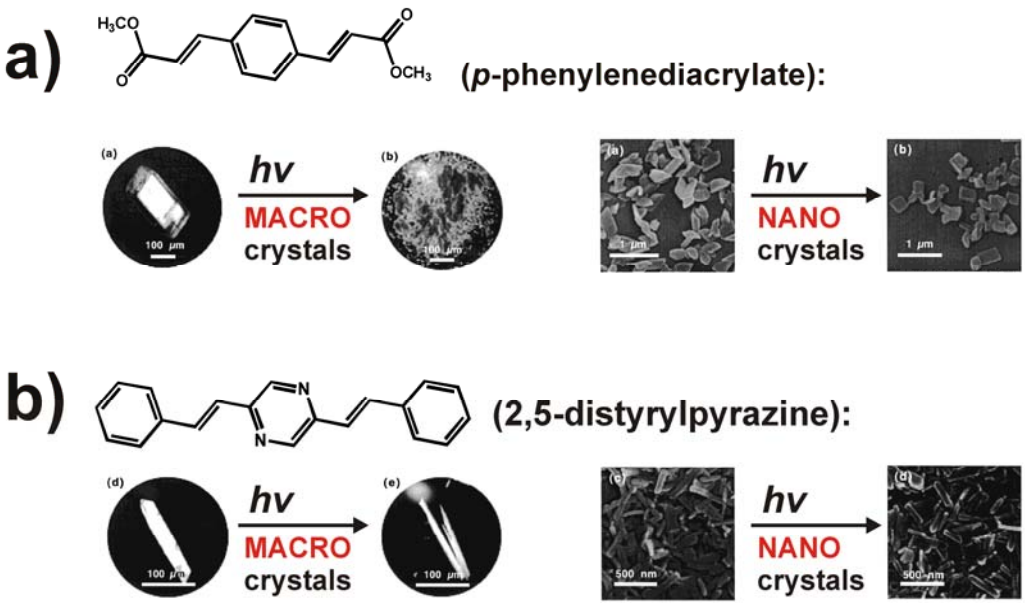

Figure 46 SCSC reactivity of nanodimensional crystals of: a) *p*-phenylenediacrylate and b) 2,5-distyrylpyrazine (SEM micrographs adopted from Nakanishi *et al.*[ref] and used with permission of the American Chemical Society).

Nano- and micrometer-sized crystals often exhibit different physical properties (*e.g.* magnetic) relative to macrocrystalline solids. Solids that exhibit SCSC behavior are also rare and promising for sensor and high-density data storage applications. In the case of the diolefin,[115] that the solid exhibited SCSC reactivity was attributed to a large deformability of the nano crystals, which enabled the solid to maintain single-crystallinity under the stressful UV-conditions of the photoreaction.

Despite possessing prerequisite reactive centers, olefins are typically not reactive in the solid state. This is attributed to unpredictable effects of molecular close packing, which contrast stringent geometric parameters for a reaction in a solid. To help alleviate this problem, we have described a method to control reactivity in the solid state based on molecular co-crystals.[30] Co-crystallization of ditopic template molecules (*e.g.* resorcinol, **res**) with functionalized olefins [*e.g.* *trans*-1,2-bis(4-pyridyl)ethylene) (**4,4'-bpe**)] has

produced hydrogen-bonded aggregates [*e.g.* 2(**res**)·2(**4,4'-bpe**)] with olefins that reliably undergo [2+2] photodimerizations (Fig. 47).

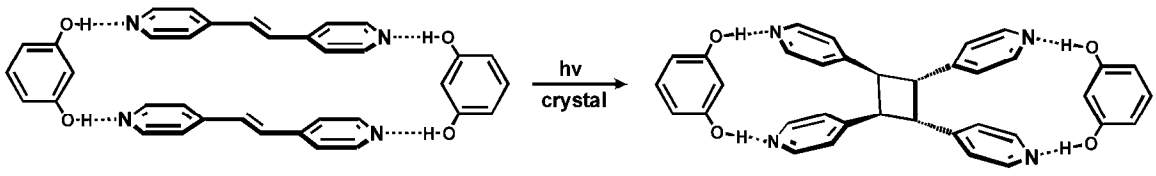

Figure 47 Templated-directed conversion of **4,4'-bpe** into **4,4'-tpcb**.

The observation of Nakanishi described herein suggests that an important step toward generalizing co-crystals as media for controlling chemical reactivity would be to achieve reaction in co-crystals of nano- and micrometer-sized dimensions. Co-crystals, in contrast to single-component solids, however, present a different challenge with respect to the reprecipitation methods used to form organic nanocrystals[190] since the molecular components of a co-crystal will, *de facto*, exhibit different solubilities. Moreover, critical matching of solubilities for controlled precipitation and growth is important and expected to be difficult. This is particularly true in the context of supramolecular co-crystals where the complementary nature of the noncovalent bonds, or heterosynthons,[9] that hold the components together will tend to be associated with molecules that exhibit considerably different solubilities.

With this in mind, we wish to introduce here a convenient sonochemical method[191, 192] to prepare organic co-crystals of nano- and micrometer-sized dimensions. In particular, we demonstrate that the application of low-intensity ultrasonic radiation to co-crystals of composition 2(**res**)·2(**4,4'-bpe**) (**1**) through sonocrystalliation produces nano- and micrometer-sized co-crystals that exhibit SCSC reactivity. We demonstrate

that combined sonocrystallizationa and reprecipitation succeed where sole sonication or reprecipitation fail (Fig. 48).

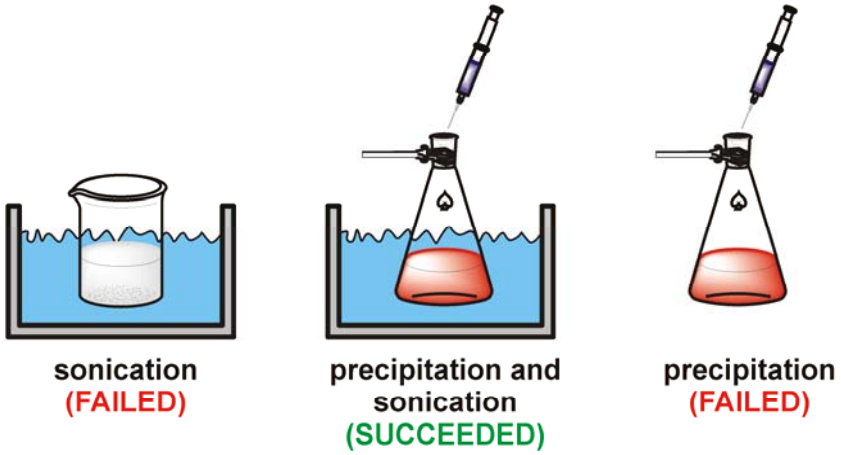

Figure 48 Crystallization methods used to synthesize nano-dimensional cocrystals.

While sonochemistry is typically used to prepare nanostructured inorganic solids,[193] to induce rapid crystallization,[194] and effect properties of pharmaceutical materials,[195] the application of sonochemistry to prepare a nanostructured organic solid has, to the best of our knowledge, not been reported.

3.2.2. Materials

Trans-1,2-bis(4-pyridyl)ethylene) (MP Biomedicals), resorcinol (ACS reagent, ≥99.0%, Sigma-Aldrich), ethanol (ACS reagent, ≥99.5%, Sigma-Aldrich)

3.2.3. Experimental procedures

3.2.3.1. Crystallization experiments

Macro-sized crystals of 2(**res**)·2(**4,4'-bpe**) were grown through slow solvent evaporation. Specifically, **4,4'-bpe** (0.018 g, 0.1 mmol) and **res** (0.011 mg, 0.1 mmol)

were separately dissolved in ethanol (15 ml total). The solutions were combined and filtered through a cotton plug. The solution was left to evaporate over a period of 5 days to afford crystals suitable for single X-ray diffraction. The nanodimensional-cocrystals were obtained *via* precipitation combined with sonochemistry. In particular, both **4,4'-bpe** (0.182 g, 1 mmol) and **res** (0.110 g, 0.1 mmol) were separately dissolved in a minimal amount EtOH (96%) (2 ml total). The solutions were filtered through a Millex syringe filter (PVDF, 0.2 μm, 13mm) directly into 225 ml of cool hexanes (*ca.* 0 °C) while exposed to low-intensity ultrasonic radiation (ultrasonic cleaning bath Branson 2510R-DTM, frequency: 42 kHz, 6% at 100 W). The resulting suspension was further sonicated for 1-2 min, filtered, and dried at room temperature.

3.2.3.2. Photoreactivity studies

In a typical photoreaction experiment, 50 mg of the cocrystal were gently ground using a mortar and pestle. The obtained powder was placed between two Pyrex glass plates and placed in a photoreactor equipped with a broad-band 450 W medium-pressure Hg-lamp. The powder distributed between the plates was mixed every 10 hours.

3.2.3.3. X-ray diffraction studies

Powder X-ray data were collected on a Bruker D-5000 diffractometer equipped with a Bruker SOL-X energy-sensitive detector using Cu$K_{\alpha 1}$ radiation (λ = 1.54056 Å).

3.2.3.4. NMR spectroscopy

^{1}H NMR data were collected on an AVANCE Bruker NMR spectrometer operating at 300 MHz using DMSO-d_6 as solvent. The ^{1}H NMR spectra are presented in Appendix B (Fig. B135-B138).

3.2.3.5. Scanning-electron microscopy

The crystalline samples were placed on a silicon wafer, and subsequently coated *in vacuo* with Au/Pd (Emitech K550 sputter coater, 1.5 min, 35 mA). Prior to coating,

the vacuum was compromised with Ar gas to enable omnidirectional coating. All samples were investigated on a Hitachi S-4000 scanning electron microscope using 5.0 kV and 10 kV accelerating voltages.

3.2.4. Results and discussion

Our first experiment involved growing macro-sized single crystals of **1**. Macro-dimensional crystals of **1** were prepared by slow evaporation of a solution of resorcinol and **4,4'-bpe** in ethanol at room temperature. A SEM micrograph of the solid revealed the presence of well-defined millimeter-sized prisms. The dimensions of the prisms varied from 0.5 to 4 mm (Fig. 49a).

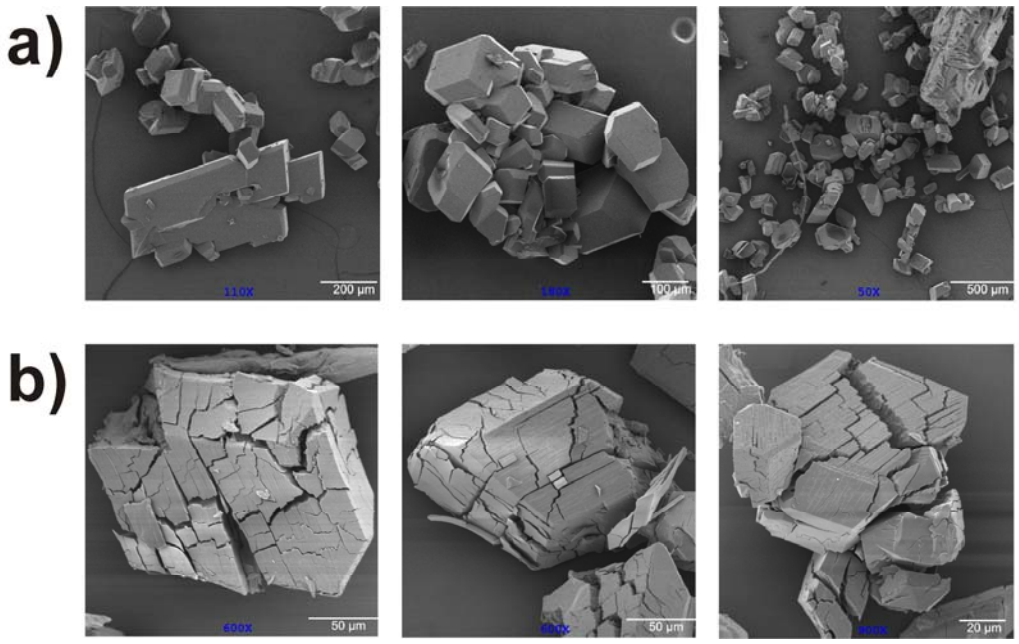

Figure 49 SEM micrographs of macro-sized cocrystals of **1**: a) before, and b) after UV-irradiation.

An X-ray powder pattern of the co-crystals confirmed that the structure of the solid corresponded to the photoactive hydrogen-bonded aggregate **1** (Fig. 50).

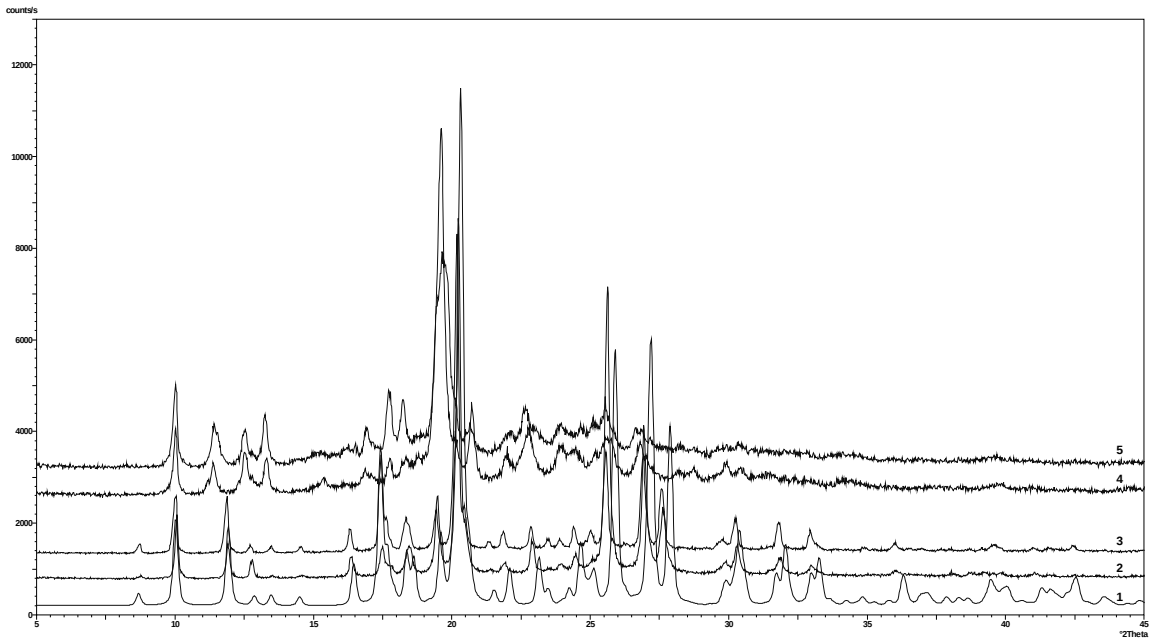

Figure 50 X-ray powder patterns of 2(resorcinol)·2(4,4'-bpe): 1) calculated, 2) macro co-crystals (before UV-irradiation), 3) nanostructured co-crystals (before UV-irradiation), and 2(resorcinol)·(4,4'-tpcb): 4) macro co-crystals (after UV-irradiation), 5) nanostructured co-crystals (after UV-irradiation).

To determine the photochemical properties of the macro-crystals, the co-crystals were irradiated with UV-irradiation (medium pressure Hg lamp) for 1 day. A ^{1}H NMR spectrum indicated that the olefins reacted to give *rctt*-tetrakis(4-pyridyl)cyclobutane (**4,4'-tpcb**) in 100% yield. A SEM micrograph demonstrated that the prisms lost structural integrity upon reaction (Fig. 49b). In particular, the crystals cracked into smaller particles to eventually give a powder. The cracking can be attributed to the release of accumulated strain, the result of molecular movement induced by the UV-light.

Our next experiment involved attempts to grow nano- and microsized crystals of **1** *via* the reprecipitation method. Thus, 200 μL of a ethanol solution of resorcinol and **4,4'-bpe** (5 mmol/L) was injected using a microsyringe into pure water (100 ml) that was vigorously stirred. The addition of the ethanolic solution produced a cloudy suspension. A SEM micrograph of the resulting solid revealed crystals of predominantly micrometer

dimensions (*i.e.* > 5 μm) (Fig. 51a). In contrast to the millimeter-sized prisms, a majority of the crystals were non-uniform in shape, exhibiting jagged edges and flake-like morphologies.

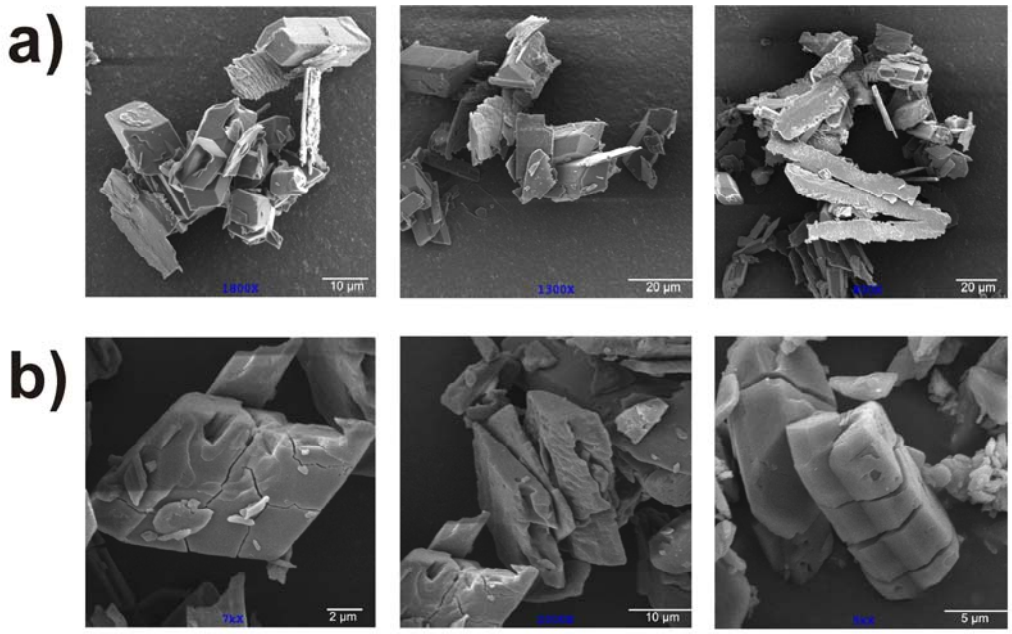

Figure 51 SEM micrographs of co-crystals of **1** grown *via* the reprecipitation method: (a) before and (b) after photoreaction.

An X-ray powder pattern confirmed that the structure of the solid corresponded to the photoactive hydrogen-bonded aggregate 2(**res**)·2(**4,4'-bpe**). Similar to the prisms, UV-irradiation of the solid largely resulted in cracking and destruction of the cocrystals (Fig. 51b).

To synthesize nano- and microsized co-crystals of **1**, we next turned to sonochemistry. For this experiment, low-intensity ultrasonic radiation using an ultrasonic cleaning bath was applied to **1** grown using the reprecipitation method. Thus, ultrasonic radiation was immediately applied to a cloudy low temperature suspension (5 ºC) of resorcinol, **4,4'-bpe**, ethanol, and water prepared using a microsyringe for a period of 3

hours. In contrast to the solid obtained using reprecipitation alone, a SEM micrograph revealed the formation of well-defined crystals of nano and microsized dimensions (Fig. 52a). The crystals obtained *via* the sonocrystallization were uniform in shape, exhibiting prism morphologies.

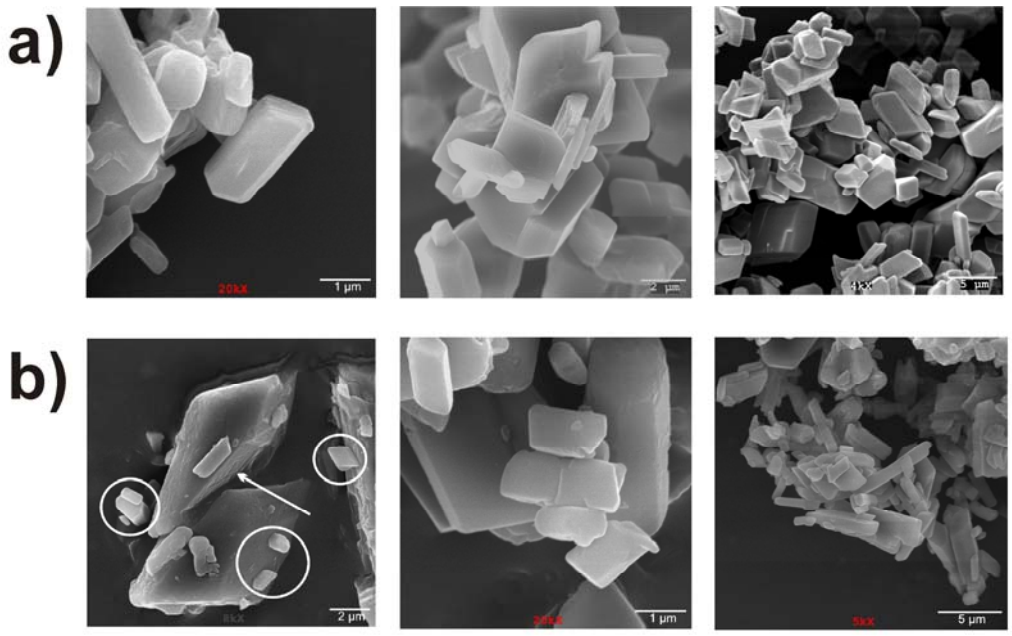

Figure 52 SEM micrographs of crystals of **1** grown *via* sonocrystallization: (a) before and (b) after UV irradiation.

The size distribution ranged from 500 nm to 8 μm. An X-ray powder pattern demonstrated that the structure of the solid corresponded to the photoactive aggregate 2(**res**)·2(**4,4'-bpe**). Importantly, in contrast to the co-crystals prepared using the reprecipitation method, UV irradiation of the solid resulted in a SCSC reaction of **1**. The SCSC transformation generally occurred in crystals smaller than 2 μm. This is clearly evident in a SEM micrograph taken following the photodimerization in which the larger microsized crystals exhibited cracks while the submicron and nanosized crystals remained intact (Fig. 52b).

That the sonochemical treatment yielded well-defined nano and microsized co-crystals of **1** may be attributed to effects of cavitation. In this process, the formation, growth, and collapse of bubbles of micrometer-sized dimensions associated with intense, shortly-lived heating and pressure occurs.[192] Although shear forces and crystal fragmentation from cavitation enhance nucleation and crystallization rates, respectively, it has been suggested that the process may also reduce or eliminate supersaturation in the immediate vicinity of the bubbles and, thus, remove a driving force to nucleation.[7] In other words, cavitation can also provide a mechanism to solubilize component molecules. Indeed, we believe that our observations are consistent with this model. In effect, the ultrasonic radiation can be considered to have provided an environment that favors rapid solubilization of the components of the co-crystal **1** (*i.e.* irrespective of the inherent solubility of each component) while also providing a mechanism for rapid precipitation and formation of the small (*i.e.* nano and submicron) crystals. These observations are important since they suggest that the sonocrystallization method may be more generally applied to additional co-crystal systems.

3.2.5. Conclusion

In this section, we have introduced sonochemistry as a method to prepare nanostructured co-crystals. This method takes into account differences in solubilities encountered in inherently modular co-crystal systems and has been shown to succeed where reprecipitation alone fails. Our group is currently working to apply this method to other reactive co-crystals, and anticipate that the approach can be applied to other co-crystal systems[11] (*e.g.* pharmaceutical co-crystals, see section 1.3.) to affect additional properties (*e.g.* solubility).

3.3. Size-dependent softening and hardening of macro- and nano-sized organic cocrystals in a single-crystal transformation

3.3.1. Introduction

The structures and properties of organic solids have great potential for flexible rational design through principles of organic chemistry and supramolecular synthesis.[9, 26] Cocrystals, or multi-component solids, are an emerging class of materials in this regard as they allow the deliberate and tunable integration of molecular building blocks with desired functionality.[98, 196] Understanding how to control properties of organic solids, however, remains a challenge owing primarily to the sensitivity of close packing to subtle changes to molecular structure.[7, 197] The reactivity of organic solids is of a particular interest, especially those that undergo photo-induced homogeneous single-crystal-to-single-crystal (SCSC) transformation.[50, 198] There are numerous potential applications of solids that undergo SCSC reactions in pharmaceutical and materials science,[89, 199, 200] supramolecular synthesis,[30] and device applications such as photoactivated molecular switches,[201, 202] 3D data storage,[161, 203, 204] and nanoscale photomechanical actuators.[205] However, these advantages are limited by a rarity of molecular crystals that undergo such transformations. As photo-irradiating a molecular crystal typically involves significant atomic motion, there is invariably an accumulation of stress and strain that is often sufficient to cause the crystal to crack and even shed into a powder.[206]

Recent reports demonstrate that a SCSC reaction may become possible in nanocrystals even in cases where corresponding macro-dimensional crystals do not display SCSC transformation.[115, 205, 207] The possibility to induce SCSC reactions through miniaturization of reactive macro-dimensional crystals to nano-dimensions can open possibilities in the development of functional nanomaterials. The small size of nanocrystals can also frequently result in physical and chemical properties distinctly

different from macroscopic solids. The ability of nanocrystals to undergo photoinduced SCSC transformations can be attributed to a high surface-to-volume ratio that leads to a more efficient stress and strain relaxation mechanism that may be absent for macro-dimensional solids.[205] The exact nature of the relaxation is, however, unknown. Surprisingly, while the relaxation mechanism can be considered to be inherently related to the mechanical properties of a photo-reactive solid, mechanical properties of a solid that undergoes a SCSC transformation have, to the best of our knowledge, not been investigated.[198] In addition to being related to the nature of a SCSC reaction, mechanical properties of organic solids are important, for example, to define solid functionality and establish allowable operating limits in device applications.[208] Gaining knowledge of mechanical properties of crystals that undergo SCSC transformations will, in addition to applications in technology, be likely critical to develop a better understanding of the strain relaxation mechanism and possibly allow *a priori* prediction of reactive properties.

3.3.2. Materials

Trans-1,2-bis(4-pyridyl)ethylene (MP Biomedicals), 5-cyanoresorcinol (ACS reagent, ≥99.0%, Sigma-Aldrich), hexanes (anhydrous, ≥99%, Sigma-Aldrich), ethanol (ACS reagent, ≥99.5%, Sigma-Aldrich)

3.3.3. Experimental section

3.3.3.1. Synthesis of macro- and nano-sized cocrystals

Millimeter-sized crystals of 2(**5-CN-res**)·2(**4,4'-bpe**) (where: **5-CN-res** = 5-cyanoresorcinol) were grown through slow solvent evaporation. **4,4'-Bpe** (0.182 mg, 1 mmol) and **5-CN-res** (135 mg, 1 mmol) were separately dissolved in extra dry acetonitrile (99.9%) (15 ml total). The solutions were combined and filtered through a Millex syringe filter (PVDF, 0.2 μm, 13mm). The solution was left to evaporate over a period of 5 days to afford crystals suitable for single X-ray diffraction. The nano-

cocrystals were obtained *via* precipitation combined with sonochemistry. In particular, both **4,4'-bpe** (0.182 mg, 1 mmol) and **5-CN-res** (135 mg, 1 mmol) were separately dissolved in a minimal amount EtOH (1 ml for **5-CN-res** and 4 ml for **4,4'-bpe**). The solutions were filtered through a Millex syringe filter (PVDF, 0.2 μm, 13mm) directly into 225 ml of cool hexanes (*ca.* 0 °C) while exposed to low-intensity ultrasonic radiation (ultrasonic cleaning bath Branson 2510R-DTM, frequency: 42 kHz, 6% at 100 W). The resulting suspension was further sonicated for 1-2 min, filtered, and dried at room temperature.

3.3.3.2. AFM measurements

Nanometer-sized crystalline samples were suspended in hexanes at 0.25 mg/mL and then deposited on a freshly cleaved atomically flat mica substrate (V-I grade, SPI Supplies, Westchester, PA). Millimeter-sized crystals were directly placed on a clean glass cover slip. All AFM studies were conducted using a Molecular Force Probe 3D AFM (Asylum Research, Santa Barbara, CA). AFM height images and nanoindentation measurements were collected at room temperature using silicon probes (Mikromasch, San Jose, CA, CSC37) with a nominal spring constant of 0.35 N/m and a typical tip radius of curvature of 10 nm. The tip radius of curvature was verified using scanning electron microscopy and was found to be approximately 10 nm, as expected. Actual spring constants were determined using built-in thermal noise method.[209] Topographic images were collected using intermittent contact mode (AC mode) or contact mode at a typical scan rate of 1 Hz.

Force-displacement curves were recorded at 1 Hz in an organic solvent (*i.e.* olefin free n-tetradecane) that served to minimize the adhesion force between the probe and the surface. Each force-displacement curve was collected during AFM probe motion towards and away from the sample. The probe started motion toward the sample from the height of approximately 200 nm above the surface that continued until the predetermined force

of 10 nN was reached. Then the motion was reversed bringing the probe to approximately the initial height above the surface. The maximum force of 10 nN was used as no sign of mechanical damage on a crystal surface has been observed under such conditions after a series of repeated force-displacement measurements. To insure the reproducibility of the measurements, typically 10 to 15 repeated force measurements were collected at each crystal location. In addition, force plots were collected on a substrate approximately 100-150 nm away from the corresponding crystal position. Measurements on the substrate were used to calibrate the deflection sensitivity of the AFM instrument to convert the force-displacement curve to force *versus* tip-sample separation plot.[210] Overall, 16 different AFM probes were used for the nanoindentation measurements.

The force *versus* tip-sample separation data were used to estimate the Young's modulus of a crystal by fitting the nanoindentation plots to a rearranged form of the Hertzian model,[210-213] which assumes elastic contact. Since practically all force-displacement plots showed no deviation between the approach and the retract data, the indentation can be assumed purely elastic thus facilitating the use of the Hertzian elastic model employed here. The substrate-induced effects on the measured Young's modulus values were negligible under our experimental conditions since a typical height of a nanocrystal (ranging from 50 to 400 nm) is more than one order of magnitude larger than typical indentation depth of 3.5 nm.

3.3.3.3. AFM nanoindentation measurements

The Young's modulus (stiffness) of unreacted and photoreacted millimeter and nanometer-sized cocrystals were studied using AFM nanoindentation technique.[210, 214-221] The force *versus* tip-sample data were used to determine the Young's modulus of a cocrystal using the rearranged form of the Hertzian model:[212]

$$F^{2/3} = C - \left[\frac{4}{3}\frac{ER^{1/2}}{(1-\sigma^2)}\right]^{2/3}\Delta$$

where F is the loading force, R is the tip radius of curvature, Δ is the tip−sample separation, E is the Young's modulus, C is a constant and σ is the Poisson's ratio of the crystal. A major advantage of using the rearranged form is as it eliminates the necessity of knowing the exact contact position between the tip and the sample, which otherwise is required.[222] Based on the equation 1, a plot of the force to the 2/3 power *versus* the tip-sample separation should be linear in the contact region. The Young's modulus of the sample can then be calculated from the linear slope of the $F^{2/3}$ *versus* Δ dependence in the contact region and using known or reported values of the tip radius of curvature and the Poisson's ratio. As the Hertzian model assumes purely elastic contact without adhesion interactions, force curves with the adhesion force greater than 0.5 nN were not used in the data analysis. Additionally, force plots where variation between the approach and retract data was observed were also not considered. The deviation is due to inelastic effects.[210, 216] Both criteria resulted in a removal of less than 3% of the total number of individual force indentation measurements used in the analysis.

Figure 53 shows a typical force to the 2/3 power *versus* the tip-sample separation plot collected on the unreacted (crosses) and photoreacted (triangle) nano-cocrystal. As can be seen, the contact region (negative tip-sample separation) of the force plot is indeed linear for both systems, thus confirming the applicability of the Hertzian model in the form of the equation presented above. The inset in Figure 53 displays a typical force *versus* tip-sample separation. The force plot clearly illustrates that the exact determination of the tip-sample contact point is challenging and may be inaccurate due to the relatively small short-range repulsive forces experienced by the tip near the tip-surface contact point. The contact force region in the force to the 2/3 power *versus* the tip-sample separation was fit to a straight line for both the unreacted and photoreacted crystals.

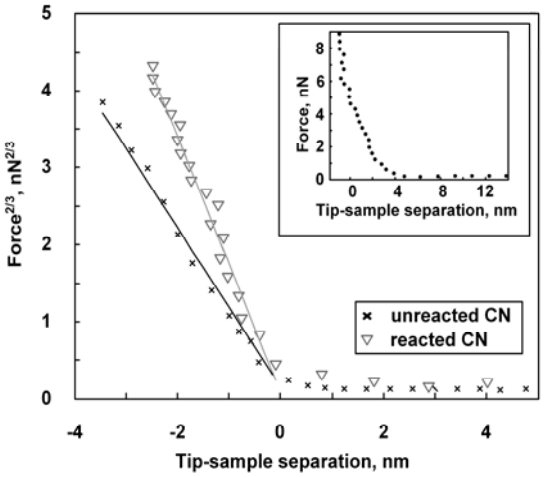

Figure 53 Typical force to the 2/3 power *versus* the tip-sample separation nanoindentation plot for unreacted (crosses) and photoreacted (triangles) nano-cocrystal. Solid lines represent linear fits and the fitted slopes were used to calculate the Young's modulus. A clear difference in slopes between the unreacted (504.5 MPa) and photoreacted (701.6 MPa) nano-cocrystals indicate different elastic properties of the two systems. The inset shows a typical force curve obtained for a single measurement on a nano-cocrystal.

The fitted lines are shown in Figure 53 by solid lines and the R^2 values for both fits were 0.96. From the linear fit, the resultant slope was used to estimate the stiffness (Young's modulus) using equation 1. The AFM tip radius of curvature and the Poisson's ratio have been estimated to be 10 nm (using SEM) and 0.3 (typical for organic solids[223]), respectively. The Young's modulus values obtained using this approach for the data set shown in Figure 53 are 504.5 MPa and 701.6 MPa for the unreacted and photoreacted nano-cocrystals, respectively. Thus, for this particular, yet representative data set, the nano-cocrystal becomes harder after the photoreaction.

3.3.3.4. SEM experiments

The crystalline samples were placed on a silicon wafer, and subsequently coated *in vacuo* with Au/Pd (Emitech K550 sputter coater, 1.5 min, 35 mA). Prior to coating, the vacuum was compromised with Ar gas to enable omnidirectional coating. All

samples were investigated on a Hitachi S-4800 scanning electron microscope using 1.0 kV accelerating voltages.

3.3.3.5. Single-crystal X-ray diffraction measurements

The diffraction data were measured on a Nonius Kappa CCD single-crystal X-ray diffractometer at room temperature (*i.e.* 25 °C) using MoK_α radiation (λ = 0.71073 Å). Structure solution and refinement were accomplished using SHELXS-97 and SHELXL-97, respectively.[175] All non-hydrogen atoms were refined anisotropically. Hydrogen atoms associated with carbon atoms were refined in geometrically constrained positions. Hydrogen atoms associated with oxygen atoms were calculated in an optimal hydrogen bonding geometry. The details of the structural analysis of all solids are summarized in Table S1.

3.3.3.6. Powder X-ray diffraction measurements

XRPDs were obtained on a Siemens D5000 X-ray diffractometer using Cu$K_{\alpha1}$ radiation (λ = 1.54056 Å) (scan type: locked coupled; scan mode: continuous; step size: 0.02º; scan time: 2 s/step). The samples were mounted on glass slides. Figure S4 depicts the diffractograms of nano-dimensional cocrystals of 2(**5-CN-res**)·(**4,4'-bpe**) before and after UV irradiation, respectively.

3.3.3.7. NMR spectroscopy

^{1}H NMR data were collected on an AVANCE Bruker NMR spectrometer operating at 300 MHz using DMSO-d_6 as solvent. The ^{1}H NMR spectra are presented in Appendix B (Fig. A139, A140).

3.3.4. Results and discussion

Herein, we report a two-component cocrystal that undergoes a SCSC[50, 198] transformation wherein the crystals undergo either softening or hardening depending on

their size (Fig 54). The components of the cocrystal interact by hydrogen bonds and undergo an intermolecular [2+2] photodimerization.[30] Using atomic force microscopy nanoindentation analysis,[210, 211, 217, 220, 224-227] we find that unreacted single cocrystals of millimeter dimensions are extremely soft and become 40% softer after photodimerization. We also find that the unreacted cocrystals undergo an 85% increase in stiffness upon being reduced to nanoscale dimensions and become 40% harder following the photoreaction. The remarkable changes in the mechanical properties are accompanied by a < 0.1 % change in density, which is attributed to the close spatial arrangement of the reactants and minimal movement that occurs during the single-crystal transformation. To the best of our knowledge, our observations that organic crystals undergo an increase in stiffness upon being decreased to the nanoscale and undergo either softening or hardening during a chemical reaction that depends on crystal size have not been reported. Our findings provide a new perspective into understanding the properties of organic solids and we believe open avenues towards the construction of solids with unique mechanical and chemical properties (*e.g.* strong and light-weight materials).

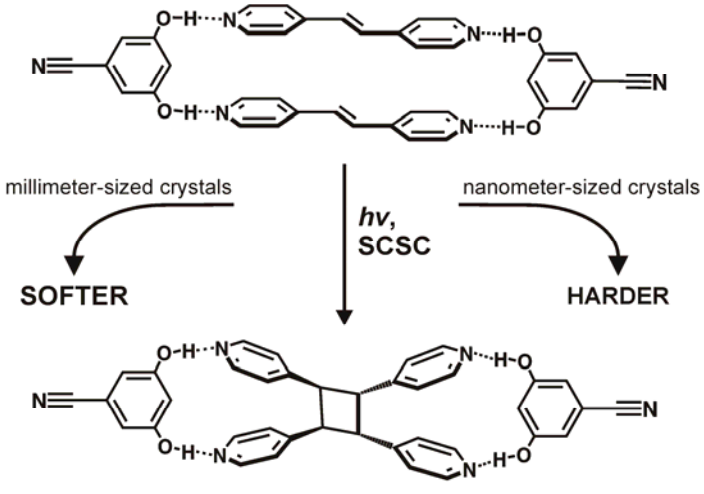

Figure 54 Size-dependent softening and hardening of macro- and nano-sized organic cocrystals in a single-crystal transformation.

AFM has been used to quantify the change in stiffness (*i.e.* elasticity) of millimeter- and nanometer-sized single cocrystals of composition 2(**5-CN-res**)·2(**4,4'-bpe**). The millimeter crystals form through slow solvent evaporation while the nano-cocrystals form using reprecipitation combined with sonochemistry.[207] The cocrystal is composed of hydrogen-bonded assemblies wherein 5-CN-res preorganizes **4,4'-bpe** for a [2+2] photodimerization (Fig. 55a,b). The cross-linking reaction produces two carbon-carbon single (C-C) bonds in the form of *rctt*-tetrakis(4-pyridyl)cyclobutane (**4,4'-tpcb**) in 100% yield.[30] A single-crystal X-ray diffraction study of millimeter-sized crystals of 2(**5-CN-res**)·2(**4,4'-bpe**) prior to being exposed to UV radiation demonstrates the two components self-assemble *via* four O-H···N hydrogen bonds (O···N separations (Å): 2.725(2), 2.728(2), 2.737(2), 2.744(2)).

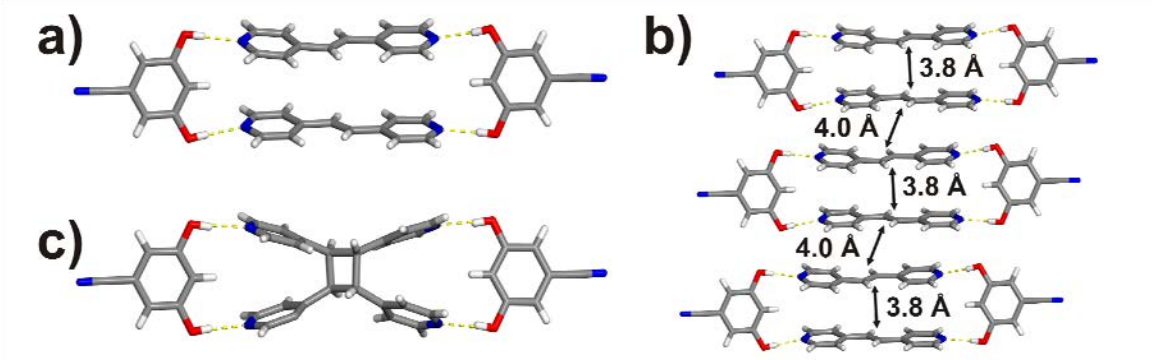

Figure 55 X-ray crystal structure of 2(**5-CN-res**)·2(**4,4'-bpe**): a) an assembly before UV-irradiation, b) crystal packing, c) an assembly after UV-irradiation.

Powder X-ray diffraction (PXRD) confirms the structure of the bulk solid. As shown in Fig. 55a, **5-CN-res** enforces **4,4'-bpe** into a reactive face-to-face geometry. The stacked –C=C– bonds are separated at 3.82 Å (Fig 55b). The geometry satisfies the criteria for a photodimerization.[7] The molecules pack in 2D layers in the crystallographic (0 1 0) plane. The layers consist of infinite stacks of **4,4'-bpe** with the -C≡N groups of **5-CN-**

res forming pairwise dipole-dipole interactions (C≡N separation: 3.41 Å). The C=C bonds of nearest-neighbor assemblies within the stacks are separated by 4.03 Å. Upon exposure to UV-radiation, 4,4'-bpe reacts, as determined by NMR spectroscopy, to form **4,4'-tpcb** in 100% yield (Fig 55c). Optical microscopy also revealed that the crystals retained transparency and general morphology, which suggested that the crystals underwent a SCSC transformation.[50, 198] A single-crystal X-ray analysis confirmed the reaction to proceed *via* a single-crystal transformation (Table 1).

Table 1 X-ray crystallographic data and Young's moduli for unreacted and reacted cocrystals of 2(**5-CN-res**)·2(**4,4'-bpe**).

	Unreacted	**Photoreacted**
X-ray crystallography		
space group	$P\bar{1}$	$P\bar{1}$
a / Å	7.6903(9)	7.7709(9)
b / Å	9.4154(11)	9.8124(11)
c / Å	24.120(3)	23.620(3)
α / °	86.888(5)	86.635(5)
β / °	89.295(5)	89.850(5)
γ / °	71.235(5)	66.617(5)
V / Å^3	1651.2(3)	1649.9(3)
ρ_{calc} / g cm^{-3}	1.277	1.278
T / K	298(2)	298(2)

The photoreaction resulted in the C=C bonds being converted into C-C bonds within each assembly (Fig. 1a), which means the hydrogen bonds were maintained in the solid (O···N separations (Å): 2.675(2), 2.699(3), 2.724(3), 2.737(3)). A comparison of the cell dimensions before and after photoreaction demonstrated that the unit cell underwent a significant change in the reaction. Whereas the volume and density remained virtually unchanged (Table 1), the γ angle decreased from 71.2° to 66.6° (Table 1, Fig. 56).

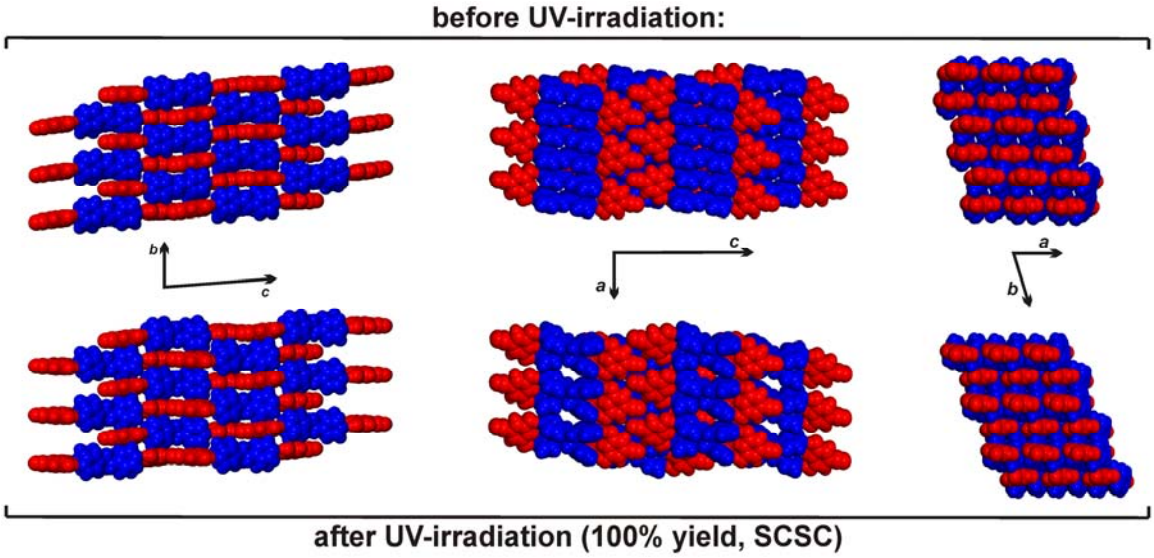

Figure 56 Crystal packing of 2(**5-CN-res**)·2(**4,4'-bpe**): a) before and b) after a quantitative [2+2] photodimerization in the solid state (viewed along the crystallographic *a*, *b* and *c* axes).

The decrease corresponds to an orientational rearrangement of the 5-CN-res molecules. More specifically, each 5-CN-res molecule underwent a tilt along the –C≡N axis (tilt angles: 3.3° and 4.9°) (Fig. 57). The tilt accommodates the generation of the photoproduct whilst maintaining the dipole-dipole interactions (C≡N separation: 3.43 Å). Thus, any physical stress the crystal experienced during the photodimerization was absorbed by the movements of the components to allow the solid to retain single-crystal character.

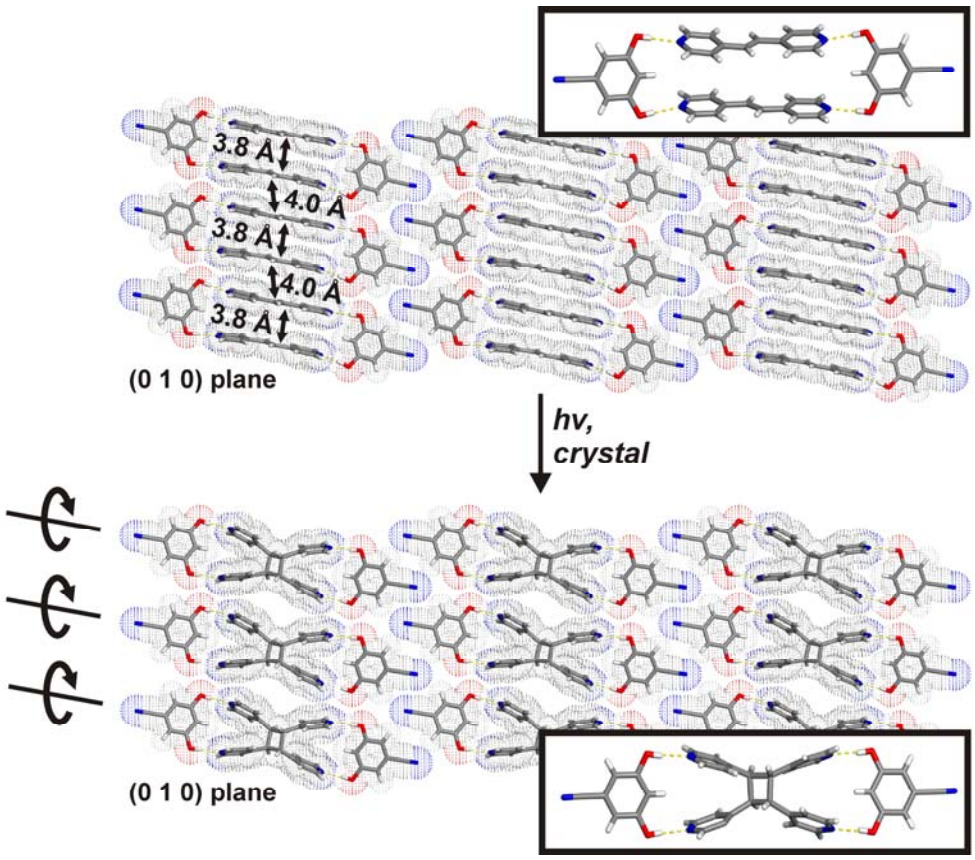

Figure 57 SCSC reactivity x of 2(**5-CN-res**)·2(**4,4'-bpe**) to form 2(**5-CN-res**)·(**4,4'-tpcb**). The depicted layers are parallel to the (0 1 0) crystallographic plane of the cocrystal.

That 2(**5-CN-res**)·2(**4,4'-bpe**) underwent a single-crystal transformation[50] prompted us to investigate mechanical properties of the solid using AFM nanoindentation technique. Whereas AFM has been used to measure changes in elastic behavior of chemical cross-links in polymers[227] and thin films,[217] as well as morphological changes of reactive single crystals,[228, 229] we are unaware of any example wherein AFM nanoindentation has been used to study mechanical properties associated with a single-crystal transformation.

Our first studies involved the millimeter-sized crystals. The crystals were determined, using optical microscopy, to exhibit prism morphologies with a base of

approximately 0.40 mm × 0.60 mm and height 0.10 mm. The dimensions of the base and height influence how the crystals orient on a surface for AFM analysis. In particular, the crystals typically lie on a surface with the base parallel to the substrate. As a result, only the top and bottom faces of the crystals were amenable to characterization using AFM. Prior to examining the crystals using AFM, the top and bottom faces were indexed using X-ray diffraction. The two faces correspond to the crystallographic (0 1 1) and (0 -1 1) planes (Fig. 58).

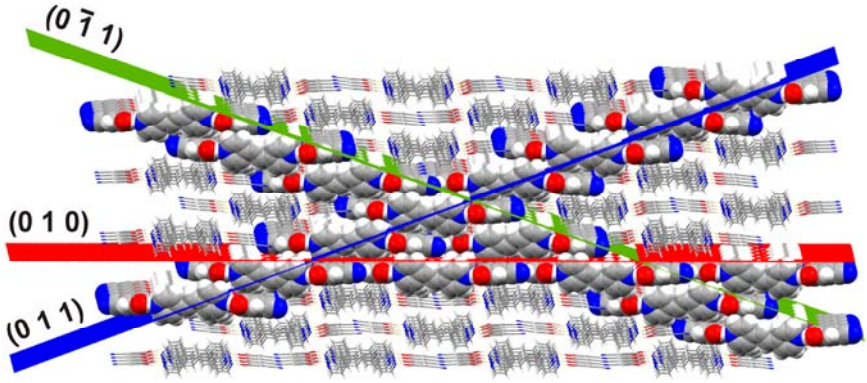

Figure 58 View of 2(**5-CN-res**)·2(**4,4'-bpe**) showing the crystallographic planes (010), (0 1 1) and (0 -1 1) displayed in red, blue and green, respectively (color scheme: C, grey; H, white; O, red; N, blue).

Each plane lies parallel to the crystallographic *a*-axis and at 20° to the packed 2D layers. That the two planes are parallel to the same axis and at the same angle to the layers means the two crystal faces that correspond to the planes are chemically equivalent. The two faces are composed of **5-CN-res** and **4,4'-bpe** molecules that interact by hydrogen bonds and edge-to-face π-π forces.

Despite being chemically equivalent, our AFM studies revealed the two crystal faces to exhibit distinct topographies. Representative AFM height images of the faces are shown in Figs. 59a and 59c.

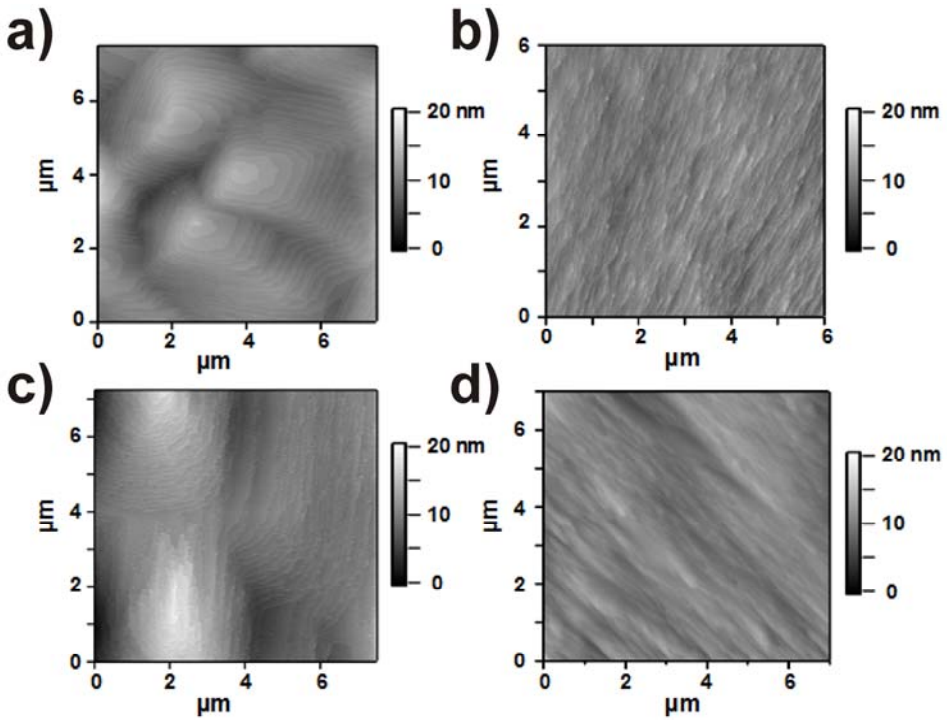

Figure 59 AFM height images millimeter-sized 2**(5-CN-res)**·2(**4,4'-bpe**) before and after photoreaction. (a) unreacted (0 1 1) crystal surface showing terraces and spiral pyramids and (b) unreacted (0 -1 1) face displaying uniform layer-type morphology. Photoreacted (0 1 1) (c) and (0 -1 1) (d) surfaces of the same crystal show the crystal morphology remained largely intact after reaction.

In particular, the (0 1 1) face is composed of terraces and small spiral pyramids that increase in the vertical direction from the plane. A typical pyramid base size is approximately 1 µm and pyramid height from bottom to crest is 20 nm. Measurements of the step height of the pyramid step and the normal terrace revealed a constant height of approximately 7 Å. The height corresponds to edge-to-face π-π interactions (*ca.* 7 Å) involving **5-CN-res** and **4,4'-bpe** within each plane. In contrast, the (0 -1 1) face, despite being chemically identical to the (0 1 1) face, displays a uniform and nearly-flat morphology with an approximate 5 nm height variation over a 6 × 6 μm^2 surface area. The fundamental unit of crystal growth can, thus, be considered to be propagated by the edge-to-face π-π interactions with growth beginning along the flat (0 -1 1) face and

ending with the spiral pyramids of the (0 1 1) face. The pyramids likely form at a conclusion of the crystal growth process.[230]

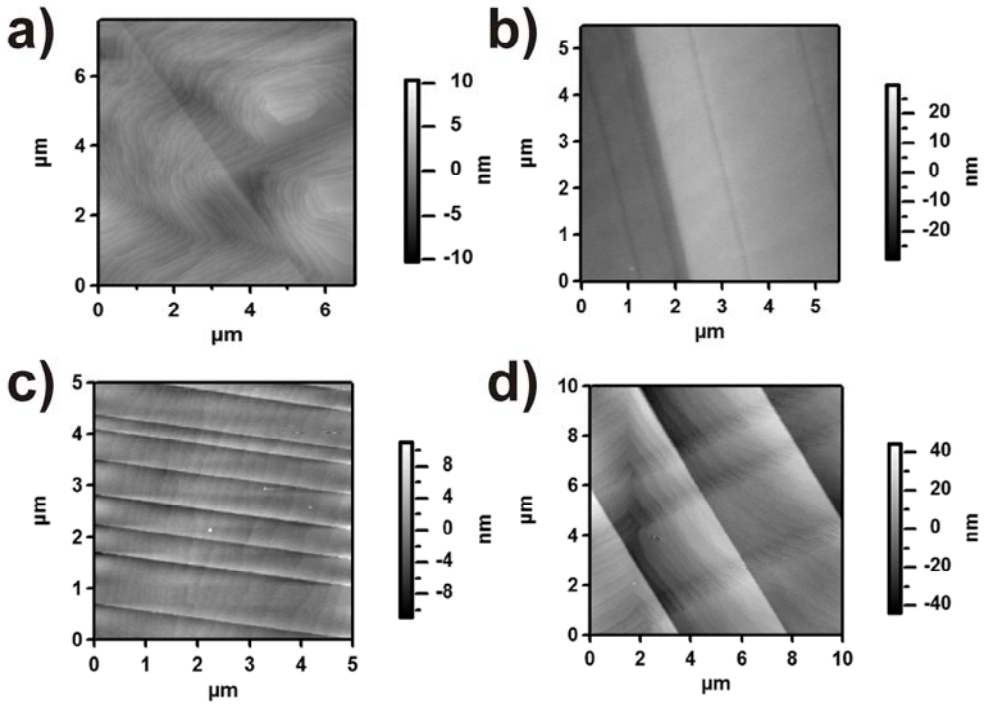

Figure 60 Representative AFM height images displaying the cleavage planes for (a) unreacted (0 1 1) crystal surface, (b) unreacted (0 -1 1) face, (c) photoreacted (0 1 1) face, and (d) photoreacted (0 -1 1) face.

AFM height images collected for the millimeter-sized crystals after photoreaction are shown in Figs. 59b and Fig.59d for the (011) and (0-11) faces, respectively. Both morphologies remained largely intact after the photoreaction, although slight irregularities as rough edges and granular sub-nanometer features appeared on the outer terrace regions of the (0 1 1) face. For the (0-11) surface, slight irregularities similarly appeared along with additional cleavage planes with a typical height jump of *ca.* 10 nm. Cleavage or slip planes[231-233] were present for both (0 1 1) and (0 -1 1) faces of unreacted and photoreacted millimeter-sized cocrystals. Representative AFM images displaying

cleavage planes are shown in Figure 60 for the unreacted and photoreacted crystals at both crystal faces.

The height variation for the cleavage planes typically ranges between 5-50 nm and likely originates from the inhomogeneous distribution of the crystal growth centers and unequal growth rates of the crystals.[97, 232, 233] The cleavage planes were also observed for unreacted crystals and, thus, do not necessarily form as a result of the photoreaction. The nominal changes in the morphologies of the millimeter-sized crystals are consistent with the photodimerization proceeding *via* a SCSC transformation.

Mechanical measurements were next obtained on the (0 1 1) and (0 -1 1) faces of three millimeter-sized crystals both before and after the photoreaction using AFM nanoindentation.[210, 211, 217, 220, 224-227] Approximately 100 crystal positions were selected and repeated force-displacement curves were recorded at each crystal position to determine the local crystal stiffness, or Young's modulus. The Young's moduli determined for all crystal positions were combined into a single ensemble and histograms of the values for the (0 1 1) and (0 -1 1) faces from three different crystals before and after photoreaction are summarized in Table 2 and shown in Figs. 61.

Table 2 Young's moduli for both unreacted and reacted cocrystals of 2(**5-CN-res**)·2(**4,4'-bpe**).

AFM nanoindentation (stiffness (MPa) / # of positions*)	**Unreacted**	**Photoreacted**
millimeter-sized, (011)	260 ± 20 / 120	150 ± 12 / 75
millimeter-sized, (0-11)	240 ± 28 / 100	150 ± 11 / 125
nanometer-sized	460 ± 40 / 90	635 ± 70 / 110

The elasticity measurements yielded an average Young's modulus (mean ± s.d.) for the (0 1 1) face of 260 ± 20 MPa before photoreaction (Fig. 2e) that *decreased* to 150 ± 12 MPa (42% change) after photoreaction (Fig. 2g). The (0 -1 1) face similarly showed

a *decrease* in crystal stiffness with the Young's modulus values of 240 ± 28 MPa and 150 ± 11 MPa (38% change) before and after the photoreaction, respectively (Figs. 2f,h). These Young's modulus values are comparable to that of protein crystals (165 MPa),[210] hyperbranched macromolecules (190 MPa),[220] and low density polyethylene (100 MPa),[234] but up to 25 times softer than crystalline acetaminophen (8.4 GPa),[235] high density polyethylene (7.5 GPa),[234] and aspirin (7.1 GPa).[236]

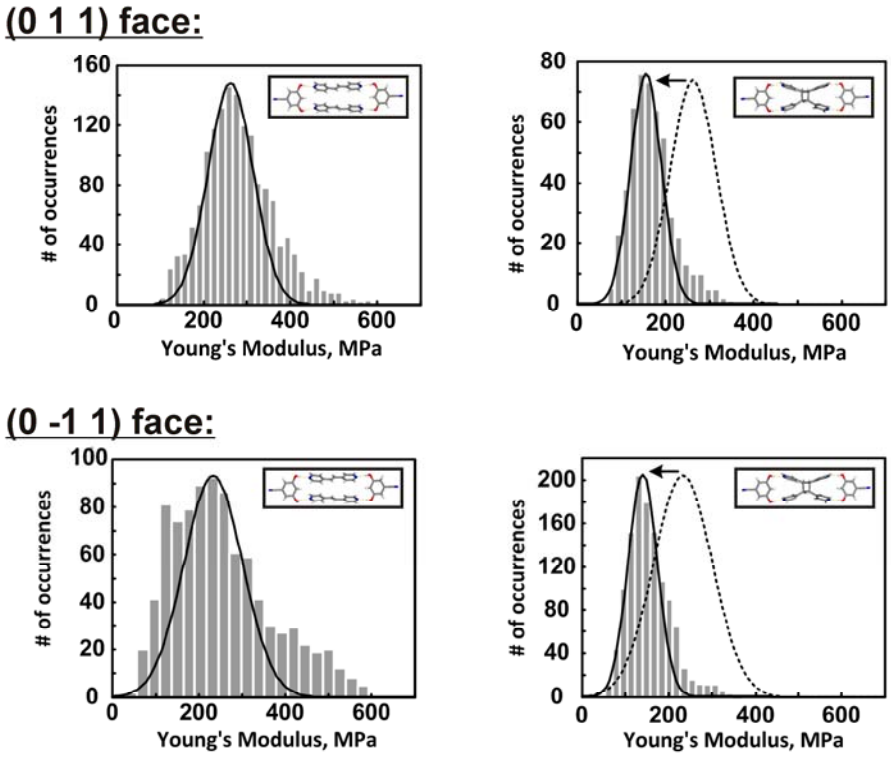

Figure 61 Young's modulus distributions of measured on crystal faces (0 1 1) and (0 -1 1) before and after a photoreaction. Face (0 1 1) showed a 42% decrease in stiffness upon reaction, whereas the (0 -1 1) face displayed an 18% decrease in stiffness. Black lines shown in represent Gaussian fits. Dotted lines represent Gaussian fits for the corresponding faces in unreacted cocrystals.

Two important conclusions can be drawn from the AFM data. First, the millimeter-sized crystals clearly become softer, or less stiff, as a result of the SCSC

transformation. Second, the extent of softening is similar for both the (0 1 1) and (0 -1 1) faces, with an average decrease in the modulus value of approximately 40%. An identical response would be expected given that both faces are chemically equivalent. The changes in the mechanical properties after photoreaction are especially noteworthy since the change in crystal density is less than 0.1% (Table 1) while a cross-linking reaction would, *a priori*, be expected to result in hardening similar to those cross-links formed in polymers where an *increase* in density is also typically observed.[237-239] At the moment, we attribute the crystal softening to difficulties of the millimeter-sized crystals, despite undergoing a SCSC reaction, to effectively relax a build up of stress and strain created during the photoreaction. The inability of the large crystals to relax stress and strain buildup presumably prevents crystal hardening following the cross-linking reaction. We also note that the width of the Young's moduli distributions became narrower relative to the unreacted response.

We next turned to the mechanical properties of the nanometer-sized cocrystals. Since the crystal planes at a surface can relax more easily at the nanoscale,[211] the higher surface-to-volume ratio of the nanocrystals was expected to lead to more efficient strain relaxation than the macroscopic cocrystals. Single cocrystals of nanometer-scale dimensions were, thus, expected to become harder following the photoreaction. To test our hypothesis, SEM micrographs (Figs. 62a,b) and representative AFM 3D height images (Figs. 62c,d) were collected for the nano-cocrystals before and after the photoreaction, which are shown in. The images revealed the solid to consist of prism morphologies, similar to the millimeter-sized crystals, with a base size distribution from 150 nm to 1 μm and typical height of 100 nm. XRPD data confirmed the structure to correspond to photoactive 2(**5-CN-res**)·2(**4,4'-bpe**). Exposure of the nano-cocrystals to UV-radiation, consistent with the millimeter-sized crystals, afforded the photodimer **4,4'-tpcb**. The micrographs demonstrated that the crystals maintained integrity following the photoreaction, which was confirmed using XRPD.

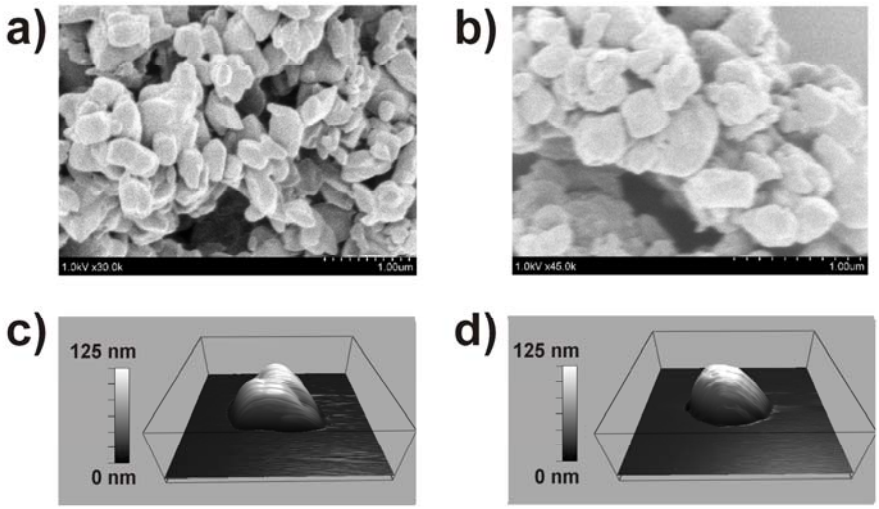

Figure 62 SEM and AFM images and histograms of Young's modulus values for 2(**5-CN-res**)·2(**4,4'-bpe**) nano-cocrystals before, during, and after the photoreaction. SEM images of the: a) unreacted and b) photoreacted nano-cocrystals showing prism-like shapes. AFM height images (1 μm x 1 μm) of two nano-cocrystals showing approximately the same height: c) unreacted and d) reacted nano-cocrystals.

Nanomechanical measurements were performed on individual nano-cocrystals before and after the photoreaction. The experiments involved 14 unreacted and 18 photoreacted single nano-cocrystals. Histograms of the Young's modulus values for all nano-cocrystals before and after the photoreaction are shown in Figs. 63. Mechanical measurements of the nano-cocrystals yielded average Young's modulus values (mean ± s.d.) of 460 ± 40 MPa for the unreacted nanocrystals that *increased* to 635 ± 70 MPa after the photoreaction. The change in the dimensions of the unreacted cocrystals from millimeter to nanometer-size, thus, resulted in an increase of the Young's modulus from approximately 250 MPa to 460 MPa, or an 85% increase in crystal stiffness. Additionally, the nanometer-sized crystals became 40% stiffer, or harder, as a result of the single-crystal transformation. The stiffening of the nano-cocrystals is in sharp contrast with the millimeter-sized crystals, where a completely opposite trend was observed with the crystals becoming 40% softer following the photoreaction. That the

mechanical response of the nano-cocrystals is different compared to the millimeter-sized solid is consistent with our hypothesis that the smaller crystals would be more efficient at relaxing stress and strain in the solid. Related effects have been noted for a thin film with dimensions less than several hundred nanometers[211] where size dependences being attributed to an increase in the surface-to-volume ratio. In the current study, there is a surface-to-volume ratio increase from approximately 10 nm^{-1} to 12000 nm^{-1} as the cocrystals decrease from millimeter to nanometer-size, respectively.

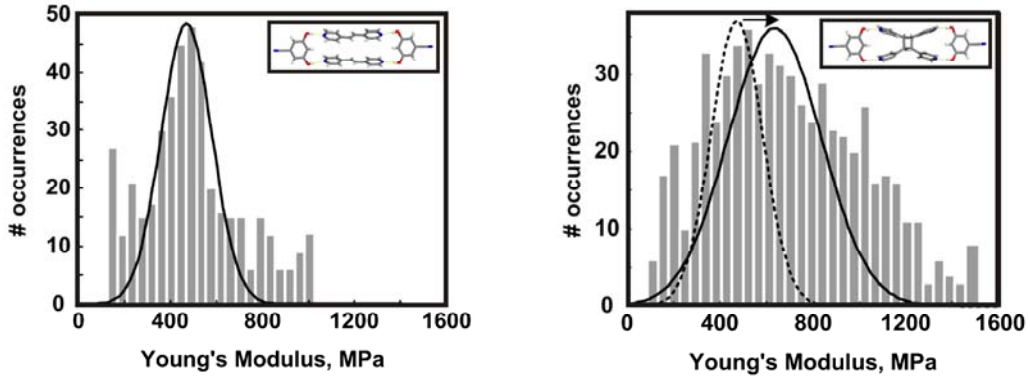

Figure 63 Distributions of Young's modulus values before and after a photoreaction showing a 40% increase in stiffness. Black lines represent Gaussian fits.

A series of sequential *in-situ* UV exposures and AFM nanoindentation measurements were also performed on a selected nano-cocrystal to study further the mechanical response. The indentation measurements determined the average Young's modulus of the nanocrystal before UV exposure to be 435 ± 35 MPa. Exposures to UV light (365 nm) were achieved using an objective located below a UV transparent quartz slide, thus, allowing the AFM measurements to be performed *in real time* during the course of the photoreaction. Four sequential 15 sec UV exposures were applied and after each exposure the nano-cocrystal was reimaged and multiple force-displacement curves were recorded. Figs. 64 illustrate AFM height images of the nano-cocrystal before and

after exposing to the UV light for the total 60 s. The crystal remained intact and no changes in the crystal size were observed. On the other hand, a steady increase in the Young's modulus was observed as shown in Fig. 64. The nano-cocrystal became harder after each exposure to the UV radiation, becoming 30% harder after the full exposure time. The overall change is lower than that for the ensemble-average response (40%), which is likely due to incomplete photoreaction. Since the *in situ* measurements were performed on the same nanocrystal, the result unambiguously supports the nano-cocrystals to become harder after photoreaction.

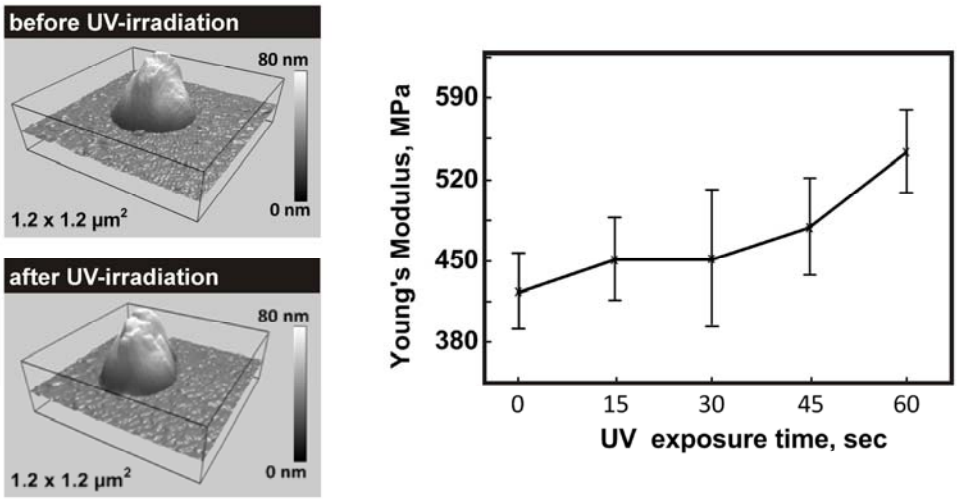

Figure 64 *In situ* AFM measurements performed during a [2+2] photoreaction of 2(**5-CN-res**)·2(**4,4'-bpe**): AFM height image of the nanocrystal before (a) and after (b) the UV exposure for a total 60 sec; (c) increase in the Young's modulus of the nanocrystal *versus* UV exposure time. Crosses are averaged moduli and error bars represent the standard deviation of the mean.

3.3.5. Conclusion

In conclusion, AFM nanoindentation has been used to study changes in mechanical properties of millimeter- and nanometer-sized organic crystals before, during, after a SCSC [2+2] photodimerization. Crystals of millimeter dimensions become 40%

softer while crystals of nanoscale dimensions of the same material become 40% harder following the photoreaction. The changes are accompanied by a < 0.1% change in density of the solid. The change in the crystal size from millimeter- to nanometer-scale dimensions also led to an 85% increase in crystal stiffness. Given a current ability to tailor the compositions and structures of organic crystals using functional groups and multiple molecular components, we expect our findings to open possibilities toward tailoring the hardness and softness of organic solid-state materials to afford materials with unique properties (*e.g.* diamond-like materials).

CHAPTER 4:
SYNTHON HIERARCHIES IN PHARMACEUTICAL COCRYSTALS BASED ON XANTHINE ALKALOIDS

4.1 Introduction

Having in mind that pharmaceutical agents (PAs) generally consist of multiple functional groups, it is expected that a PA-based cocrystals are sustained by multiple supramolecular homo- and heterosynthons.[240] Unfortunately, the ability to fully control the formation of multiple synthons in cocrystals (and thereby their physicochemical properties) is limited owing to the lacking knowledge of hierarchies of supramolecular synthons in organic solids.[15, 16, 241, 242] We anticipate that the understanding of synthon hierarchies in cocrystals will provide more control in the design of pharmaceutical solids with desired properties, and also facilitate the development of strategies for the construction of ternary[14, 243] and quaternary[243] cocrystals (*i.e.* cocrystals of more than two components). The ability to design such cocrystals is expected to enable the development of solids that can function as drug cocktails with advanced performance.

The majority of recent structural studies involving pharmaceutical cocrystals[1] were focused on either: a) the development of new supramolecular synthons suitable for cocrystal design, or b) the design of pharmaceutical cocrystals based on known synthons. Notably, only a small number of studies addressed so far the design of cocrystals based on both multiple homo- and heterosynthons. The first study of synthon hierarchies in cocrystals was published in 2007. Zaworotko's group studied a group of cocrystals composed of aromatic compounds involving pyridyl, cyano and hydroxy groups, and determined that that the O-H(hydroxy)···N(pyridyl) and the O-H(hydroxy)···N(cyano)

supramolecular heterosynthons are both favored over the O-H(hydroxy)···O-H(hydroxy) homosynthon (Figure 1a). The same group reported in 2008 a cocrystal series of aromatic molecules involving pyridyl, carboxy and hydroxy groups. Structural analyses of the cocrystals revealed that the O-H(carboxy)···N(pyridyl) and O-H(hydroxy)···N(pyridyl) heterosynthons are clearly favored to the O-H(carboxy)···O-H(carboxy) and O-H(hydroxy)···O-H(hydroxy) homosynthons (Fig. 65).

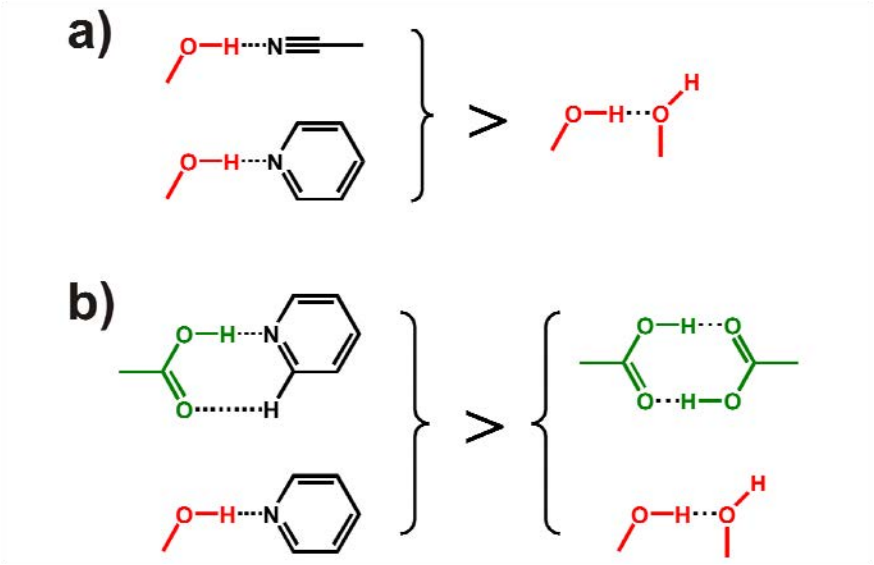

Figure 65. Synthon hierarchies determined by Zaworotko and coworkers.

In a combined CSD and experimental study study, Zaworotko and coworkes more recently investigated synthon hierarchies in cocrystals composed of carboxylate zwitterions and polyphenols, as well as CCFs with weakly acidic O-H functional groups (*e.g.* citric acid). The study revealed that the charge-assisted O-H(hydroxy)···O^- (carboxy) hydrogen bond persists frequently enough to be considered as reliable synthon

in crystal engineering. In addition, the authors established a hierarchy of synthons and structural motives involving O-H(hydroxy)···O$^-$(carboxy) hydrogen bond (Fig. 66).

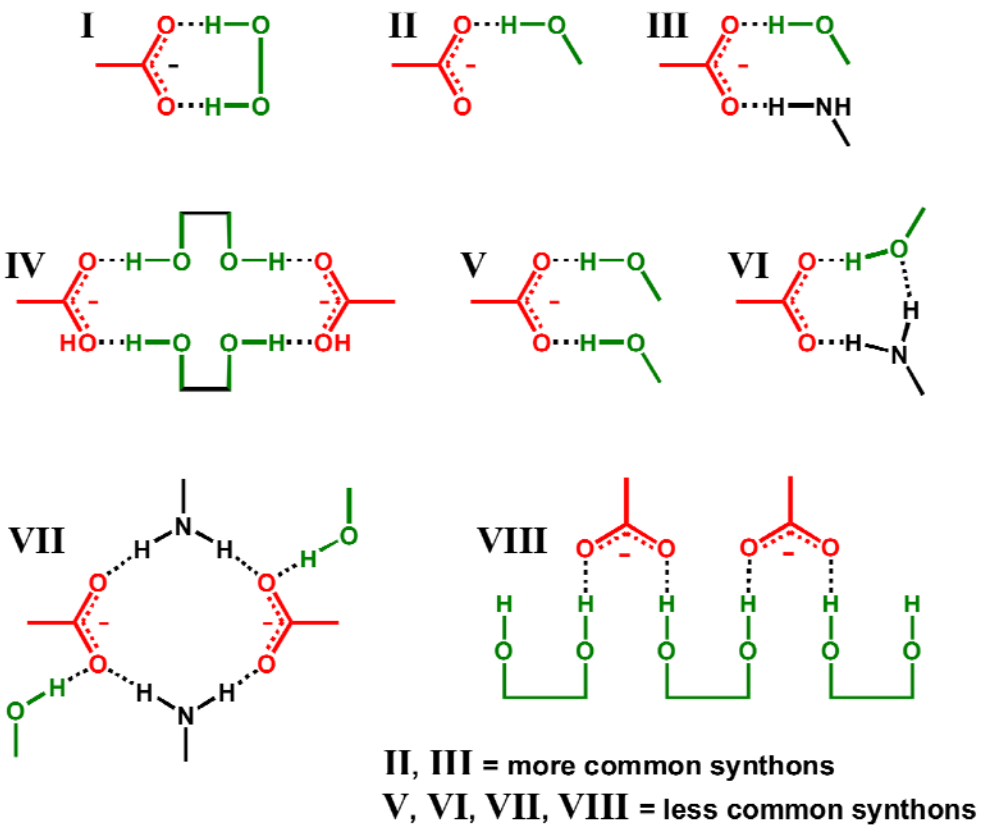

Figure 66. Synthons based on O-H(hydroxy) and O$^-$(carboxy) groups observed in the CSD.

To study the hierarchy of supramolecular synthons in cocrystals composed of multiple synthons, we selected a series of xanthine alkaloids (*i.e.* caffeine, theophylline, theobromine, xanthine, 8-chlorotheophylline, acephylline and dyphylline) as model PAs (Fig. 67), and both benzoic and naphthoic acids as CCFs.

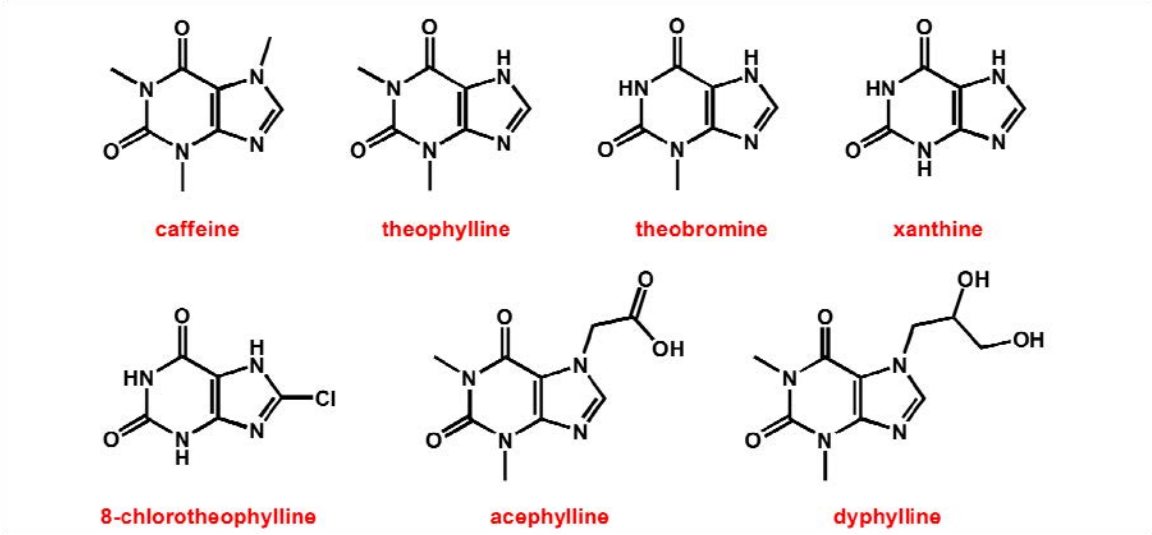

Figure 67 Chemical structures of xanthine alkaloids used to study synthon hierarchies in cocrystals involving (di)hydroxybenzoic and (di)hydroxynaphthoic acids.

Xanthine alkaloids are a class of common pharmaceutical model compounds that are constituted of a purine ring being derivatized with *N*-methyl groups, whereby the position of the *N*-methyl groups defines the pharmacological profile of each alkaloid.[244] Notably, the purine moiety of xanthines involves structural fragments that commonly occur in relevant actual PAs, as well as in potential drug candidates, thus justifying their use as model compounds. The selected CCFs are regioisomers of (di)hydroxybenzoic and (di)hydroxynaphthoic acids (Fig. 68). The CCFs, hence, provide an opportunity to *systematically* study synthon hierarchies in cocrystals, as well as the impact of structural isomerism on self-assembly processes. Importantly, the CCFs are comprised of functional groups that commonly occur in PAs, CCFs and salt formers generally used to alter physicochemical properties of PAs in drug formulation processes.

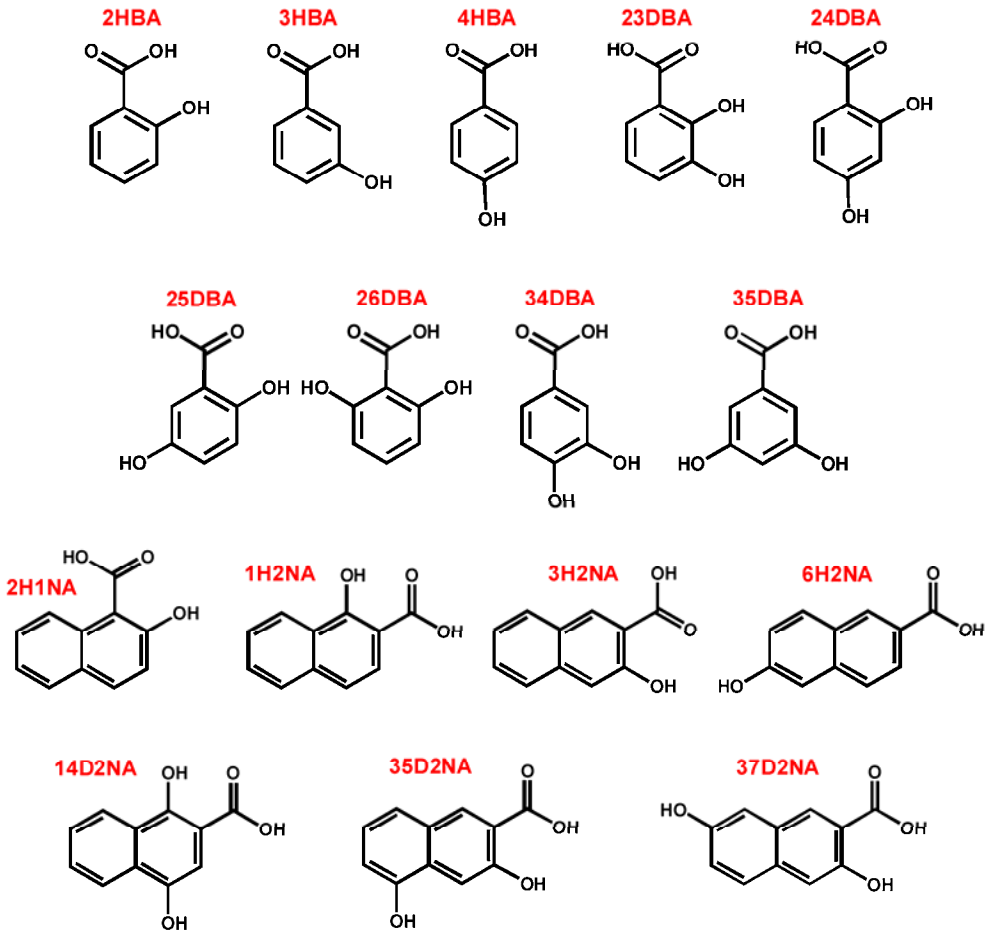

Figure 68 Chemical structures of both benzoic and naphthoic acid derivatives used as CCFs in the described study: 2-hydroxy- (**2HBA**), 3-hydroxy- (**3HBA**), 4-hydroxy- (**4HBA**), 2,3-dihydroxy- (**23DBA**), 2,4-dihydroxy- (**24DBA**), 2,5-dihydroxy- (**25DBA**), 2,6-dihydroxy- (**26DBA**),3,4-dihydroxy- (**34DBA**), 3,5-dihydroxybenzoic acid (**35DBA**), and 1-hydroxy-2- (**1H2NA**), 2-hydroxy-1- (**2H1NA**), 3-hydroxy-2- (**3H2NA**), 6-hydroxy-2- (**6H1NA**), 1,4-dihydroxy-2- (**14D2NA**), 3,5-dihydroxy-2- (**35D2NA**), 3,7-dihydroxy-2-naphthoic acid (**37D2NA**).

The results reported in this chapter represent a segment of the author's work related to the project "Pharmaceutical Co-crystals based on GRAS and EAFUS Compounds". The project is based on an ongoing collaboration between Abbott Laboratories and the MacGillivray Research Group, Department of Chemistry, University of Iowa. The project aims to explore principles and applications of

pharmaceutical cocrystals. The studies are expected to contribute to the lacking body of knowledge related to the design of cocrystals with increasing diversity in chemical functionalities so that more complex cocrystal design strategies can be recognized, developed, and pursued.

4.2. Cocrystals of caffeine and (di)hydroxybenzoic acids: Structural characterization and synthon hierarchies

4.2.1. Introduction

Caffeine (**caf**) is a xanthine alkaloid compound[245] commonly used as a formulation or food additive and as a pharmaceutical model compound (Fig. 69).[246] Cocrystals of caffeine and carboxylic acids were recently subjected to a crystal engineering study, which demonstrated that cocrystal formation can be utilized to improve the stability of caffeine against hydration under extremely humid conditions.[95] In a more recent report, caffeine was used as a model to demonstrate the facility to improve mechanical properties of pharmaceutical materials *via* cocrystallization.[97] In addition, caffeine-carboxylic-acid cocrystals were recently employed as model compounds to study cocrystal-cocrystal reactivity,[103] as well as to explore preparative methods for the synthesis of three-component solids.[71, 102]

A combined literature and Cambridge Structural Database (CSD) survey of all previously reported caffeine-carboxylic-acid cocrystals has revealed that the carboxy groups typically interact with the imidazole moieties of caffeine *via* an O–H···N hydrogen-bond, forming either a $R_2^2(7)$ heterosynthon or a $R_3^3(11)$ network based on $R_2^2(7)$ and $R_2^2(6)$ heterosynthon (Fig 70).

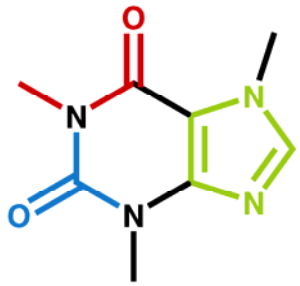

Figure 69 Caffeine and its substructures: the imidazole (green), urea (blue) and amide (red) acceptor site.

The objective of this study is to explore the feasibility of introducing additional supramolecular heterosynthons to caffeine-carboxylic-acid cocrystals. We choose structural isomers of (di)hydroxybenzoic and (di)hydroxynaphthoic acids to investigate the structural effects of an additional hydrogen-bond forming group along the periphery of the carboxylic acid (*i.e.* hydroxy groups). The choice of hydroxy- and dihydroxybenzoic acids as cocrystal formers is based on two observations. First, further literature and CSD analyses revealed structures wherein the carbonyl groups of caffeine form O–H(hydroxy)···O(carbonyl) hydrogen-bonds with the hydroxy group of methyl-3,4,5-trihydroxybenzoate and C-(n-propyl)calix(4)resorcinarene (Fig. 6c,d).[97, 247, 248] Second, a recent solid-state study reported a cocrystal of caffeine and citric acid based on three supramolecular heterosynthons (Fig. 6e). In this cocrystal, caffeine and citric acid are sustained *via* three types of hydrogen bonds (*i.e.* O–H(hydroxy)···O(urea), O–H(carboxy)···N(imidazole) and O–H(carboxy)···O(amide)).[249] Both observations suggested that caffeine could systematically form cocrystals with hydroxybenzoic acids *via* both O–H(hydroxy)···O(urea), O–H(hydroxy)···O(amide) and O–H(carboxy)···N(imidazole) hydrogen bonds.

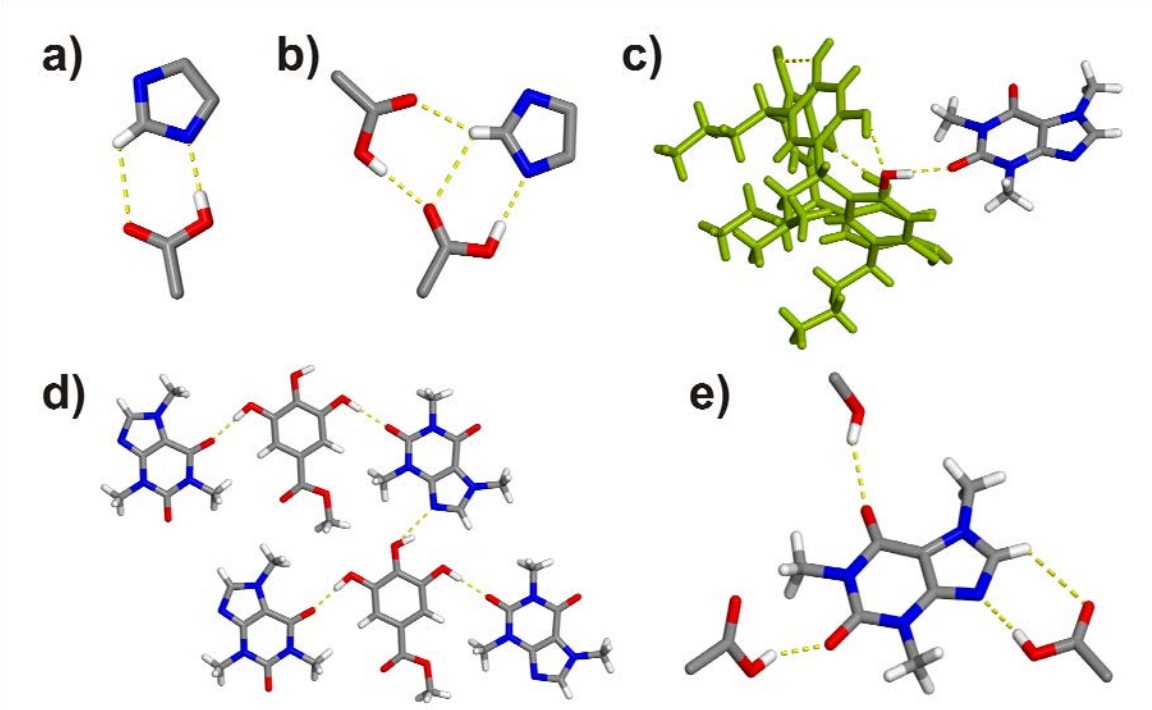

Figure 70 Perspective views of: a,b) the most common imidazole-acid heterosynthon observed in caffeine-carboxylic-acid cocrystals (*i.e.* $R_2^2(7)$ and $R_3^3(11)$ motifs, respectively), c) crystal structure of caffeine and C-(n-propyl)calix(4)-resorcinarene, d) methyl-3,4,5-trihydroxybenzoate, and e) caffeine being involved in three supramolecular heterosynthons.

(Di)hydroxybenzoic and (di)hydroxynaphthoic acids selected in this study are regioisomers. From a fundamental standpoint, these acids enable us to study the impact of systematic changes to the positioning of the identical functional groups on the self-assembly process of pharmaceutical cocrystals, which is rather unexplored to date. Previous studies in our laboratories demonstrated that structural isomerism can significantly affect molecular recognition during the self-assembly process. Specifically, we have shown in preliminary studies that 6-hydroxy-2-naphthoic acid, unlike its geometrical isomers, self-assembles with caffeine to form a cocrystal based on multiple

supramolecular synthons in which the largely expected O–H(carboxy)···N(imidazole) interaction did not form. Instead, both an O–H(hydroxy)···O(urea) heterosynthon and an O–H(carboxy)···O(carboxy) homosynthon, in the form of a carboxylic acid dimer, formed (Fig. 71 and Appendix D).[250]

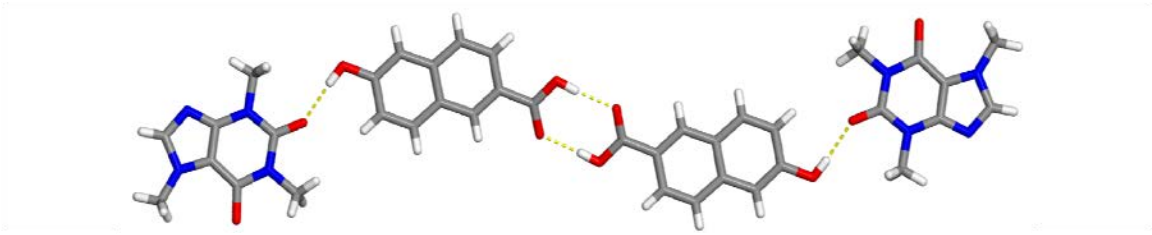

Figure 71 The crystal structure of the 1:1 **caf**:**6H2NA**.

Assemblies in which a carboxylic-acid dimer coexists with a heterosynthon are rare, but suggests that caffeine could also form cocrystals with hydroxybenzoic acids *via* O–H(hydroxy)···N(imidazole), O–H(hydroxy)···O(urea) and O–H(hydroxy)···O(amide) hydrogen bonds. In the hydroxybenzoic acid cocrystals, the caffeine hydrogen-acceptor sites are not expected to interact with the weak -CH_3(caffeine) groups. As shown in the crystal structures of its two polymorphs, caffeine is in the solid state sustained by weak C–H···O and C–H···N interactions that are inadequate to preorganize caffeine into robust and ordered hydrogen-bonded networks. The formation of caffeine dimers is, therefore, also not expected to occur in cocrystals involving (di)hydroxybenzoic acids.

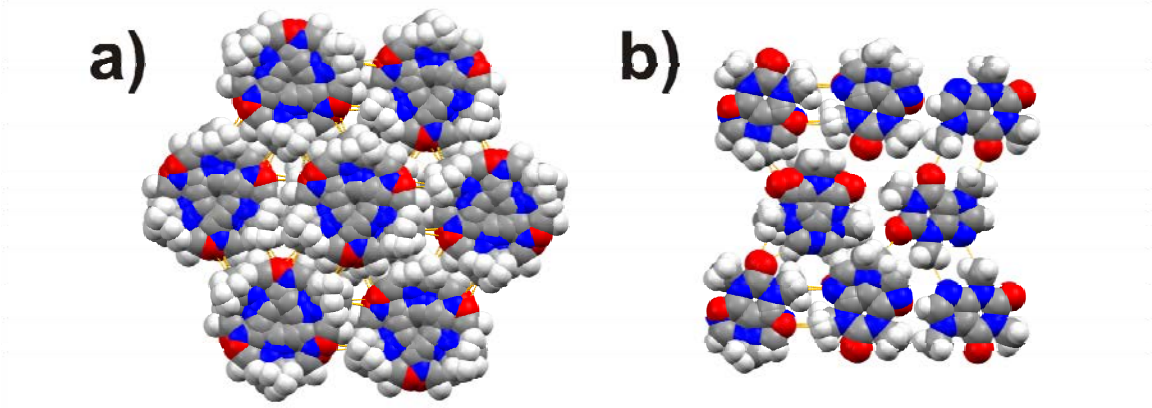

Figure 72 Crystal structures of two caffeine polymorphs: a) form 1, b) form 2 (C–H···O and C–H···N interactions are highlighted in orange)

4.2.2. Experimental section

4.2.2.1. Materials

Caffeine (*ReagentPlus*™), 2-hydroxybenzoic acid (≥99.0%), 3-hydroxybenzoic acid (99.0%) , 4-hydroxybenzoic acid (≥99.0%), 2,3-dihydroxybenzoic acid (≥97.0%), 2,4-dihydroxybenzoic acid (≥98.0%), 2,5-dihydroxybenzoic acid (≥98.0%), 3,4-dihydroxybenzoic acid (≥97.0%), 3,5-dihydroxybenzoic acid (≥97.0%), and acetonitrile (anhydrous, 99.8%) were purchased from Sigma-Aldrich (St. Louis, MO, USA) and were used as received.

4.2.2.2. Survey of the Cambridge Structural Database

A survey of the Cambridge Structural Database (version 5.29, update of November 2007) was carried out using ConQuest[251] (version 1.10) and limited to organic and non-ionic compounds with determined 3D-coordinates and $R \leq 0.075$. A CSD survey revealed 21 entries with a caffeine-containing structure, wherein 12 involve caffeine and a carboxylic acid.[252]

4.2.2.3. Hydrogen-bond pattern analysis

To identify hydrogen-bond patterns, the following criteria were applied: 1) the donor (*i.e.* O, N atoms) must be covalently bound to at least one hydrogen, 2) the acceptor (*i.e.* O, N atoms) must have at least one lone electron pair, 3) the donor-acceptor distance mus be less than the sum of van der Waals radii of both the hydrogen-bond donor and acceptor, and 4) the contact can be either intramolecular or intermolecular involving hydrogen-bond donor and acceptor atoms being separated by at least 3 covalent bonds within the molecule (default definition of hydrogen bonds in CCDC program *Mercury*, version 2.3).[251] In addition to the four default *Mercury* criteria, another one was considered to in the definition of hydrogen bonds: 5) required presence of a hydrogen atom that satisfies the following criteria: D-H$\cdots A \geq 100°$ (where D = hydrogen-bond donor, A = hydrogen-bond acceptor). The hydrogen-bond parameters were calculated using the CIFTAB routine in WinGX.[253]

4.2.2.3. Cocrystal screening

To explore cocrystal formation of hydroxy- and dihydroxybenzoic acids with caffeine, we employed our recently reported **SMPT**-based suspension screening method.[104] In a typical screening experiment, caffeine (2 mmol) was mixed with an equimolar amount of a hydroxy- or dihydroxybenzoic acid and a low volume of solvent (1-4 mL), acetonitrile or acetonitrile/water 1/1 v/v. The resulting suspension was either vortexed using an analog vortex mixer (VWR VM-3000, power; 150W) or sonicated using a sonicator bath (Branson 2510R-DTM; frequency: 42kHz, 6% at 100W) to facilitate the **SMPT** process. For most screening trials, a phase change was visually evident within one minute and, in some instances, after only a *few seconds*. Regardless of the rates of phase transformation, the slurries were equilibrated, at least overnight, at ambient conditions to ensure complete conversion. Each suspension was then filtered and the residual solid was examined by powder X-ray diffraction (PXRD). All new

crystalline phases discovered were studied further using IR spectroscopy, single crystal X-ray diffraction and, in some instances, computational quantum-mechanical methods.

4.2.2.4. Single crystal preparation of (di)hydroxybenzoic acid cocrystals

Single crystals of (**caf**)·(**2HBA**) (1:1 ratio; **caf1**), (**caf**)·(**3HBA**) (1:1 ratio, **caf2**), (**caf**)·2(**4HBA**) (1:2 ratio, **caf3**), 2(**caf**)·(**4HBA**) (2:1 ratio, **caf4**), (**caf**)·(**23DBA**)·(H_2O) (1:1:1 ration, **caf5**), (**caf**)·(**24DBA**)·(H_2O) (1:1:1 ratio, **caf6**), (**caf**)·(**25DBA**) (1:1 ratio, **caf7**) and (**caf**)·(**35DBA**)·(H_2O) (1:1:1 ratio, **caf8**), were obtained by slow evaporation from solution. To obtain single crystals of all solids, the corresponding polycrystalline solids (20 mg) (obtained during the screening procedure) were dissolved in acetonitrile or acetonitrile/water 1/1 v/v (2 ml) at 80 ºC and filtered. Crystals suitable for single crystal X-ray diffraction of all solids were obtained from the filtrate via slow evaporation within ten days. During an attempt to grow single crystals of the product obtained from the screening experiment involving **caf** and **4HBA**, single crystals of (**caf**)·2(**4HBA**) and 2(**caf**)·(**4HBA**) were obtained simultaneously from the same crystallization trial. Extensive efforts in growing single crystals of the **caf**:**34DBA** cocrystal did not yield crystals of sufficient quality for structure determination.

4.2.2.5. Infrared (IR) spectroscopy

Transmission infrared spectra of the solids were obtained using a Fourier-transform infrared spectrometer (Nicolet Magna 750 FT-IR Spectrometer) equipped with a Nicolet NIC-PLAN microscope. The microscope has an MCT-A liquid nitrogen cooled detector. The samples were rolled on a 13 mm × 1 mm BaF_2 disc sample holder; 64 scans were collected at 4 cm^{-1} resolution.

4.2.2.6. Powder X-ray diffraction measurements

PXRD data were collected using a G3000 diffractometer (Inel Corp., Artenay, France) equipped with a curved position sensitive detector and parallel beam optics. The

diffractometer was operated with a copper anode tube (1.5 kW fine focus) at 40 kV and 30 mA. An incident beam germanium monochrometer provided monochromatic $K_{\alpha 1}$ radiation. The diffractometer was calibrated using the attenuated direct beam at one-degree intervals. Calibration was checked using a silicon powder line position reference standard (NIST 640c). The instrument was computer controlled using the Symphonix[254] program and the data was analyzed using the Jade[255] (version 6.5). The sample was loaded onto an aluminum sample holder and leveled with a glass slide.

4.2.2.7. Single crystal X-ray diffraction analyses

Single crystals of the new caffeine phases were individually mounted on glass fibers. Intensity data were collected on a Bruker SMART system equipped with an APEX CD camera. Data were collected at 173 K with graphite-monochromated MoK_{α} radiation (λ = 0.71073 Å). Data were collected using omega-phi scans with omega steps of 0.3º and phi steps of 90º. The diffraction frames were collected with 20 second frame exposures. Data were processed using Saint*Plus*.[256] Corrections for Lorentz-polarization effects were applied. Absorption was negligible. All structures were solved using direct methods that yielded the non-hydrogen atoms. All presented hydrogen atoms were located in Fourier-difference electron density maps. All non-hydrogen atoms were refined anisotropically. Hydrogen atoms associated with carbon atoms were refined in geometrically constrained riding positions. Hydrogen atoms associated with oxygen atoms were included in the located positions. Refinement was achieved with the use of SHELX-97.[175] Crystallographically relevant parameters related to the **caf**-based solids are given in Appendix A (Tables 19, 20, 21)

4.2.3. Results

Nine new caffeine phases based on the (di)hydroxybenzoic acids were discovered utilizing the screening method based on **SMPT**.[104] The PXRD patterns clearly indicated the generation of new solid phases (Fig. 73). Specifically, cocrystal screening in

acetonitrile led to the generation of anhydrous cocrystals, whereas screening experiments involving a 1:1 acetonitrile/water mixture yielded cocrystal hydrates. The crystal structures of eight phases were determined *via* single-crystal X-ray diffraction. The solids have been confirmed as neutral molecular complexes (*i.e.* cocrystal) based on the analyses of the carboxy-group geometries (Table 3) and FT-IR data (Fig 74), as well as inspections of Fourier difference maps.

The details of the structural analysis of all solids are summarized in Table A1 (see appendix A). Structural features of all solids are described below in succession. Hydrogen bond parameters are listed in Table 4. The carbon-oxygen bond distances in all eight solids were consistent with the formation of a cocrystal (Table 3). In addition, the Fourier difference maps of these complexes revealed that the acidic protons are positioned in close proximity to the O-atom of the carboxylic acid at distances that correspond to a carboxylic acid group. Based on these observations, all solids were classified as cocrystals. These classifications were also supported by IR spectroscopy. In particular, the carbonyl stretching bands were observed above 1600 cm^{-1} (Fig. 74), which is consistent with unionized carboxylic acids.

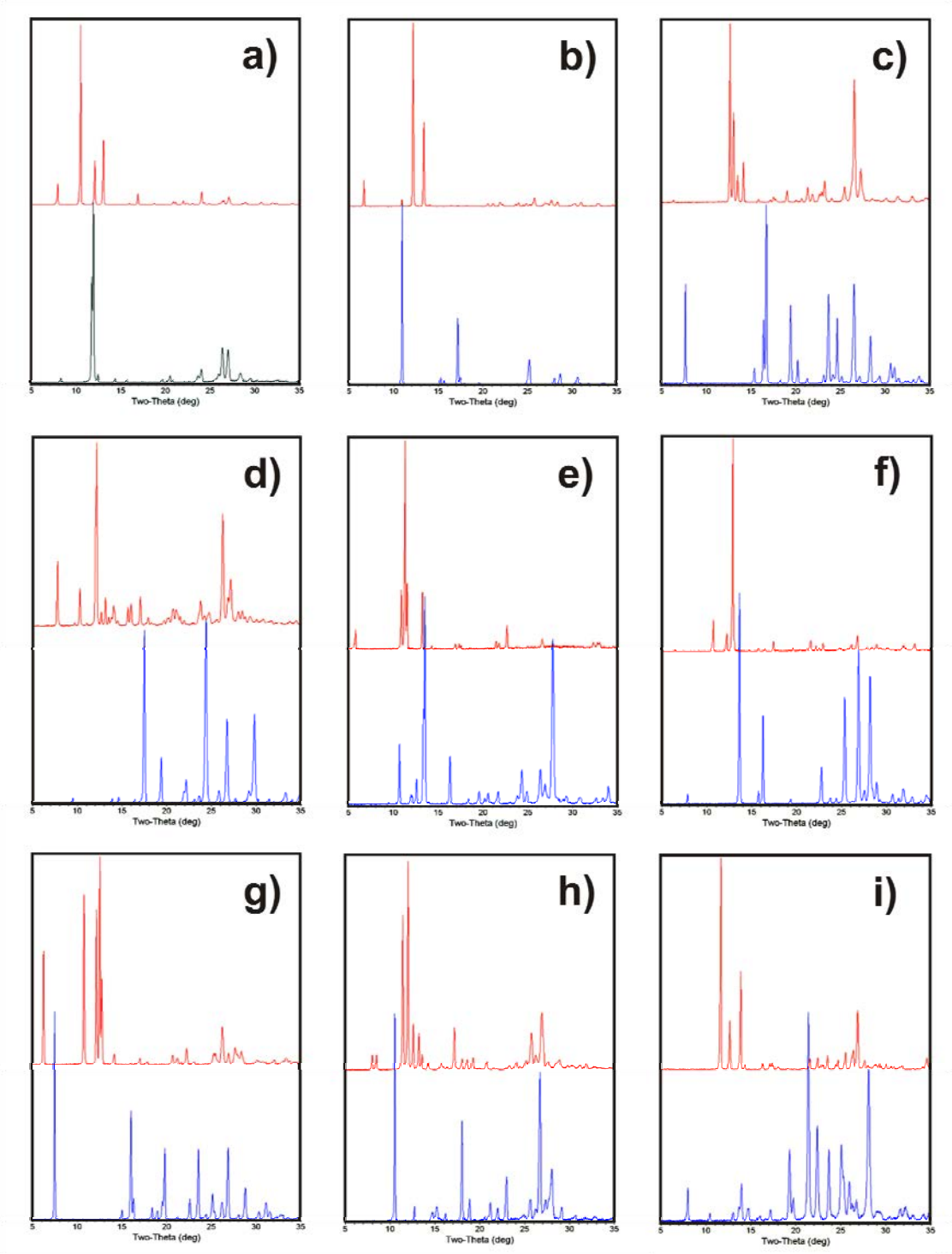

Figure 73 PXRD patterns of solids recovered from the screening experiments. Top/bottom: a) **caf**-hydrate/anhydrate; b) **caf-2HBA/2HBA**; c) **caf-3HBA/3HBA**; d) **caf-4HBA/4HBA**; e) **caf-23DBA/23DBA**; f) **caf-24DBA/24DBA**; g) **caf-25DBA/25DBA**; h) **caf-34DBA/34DBA**; i) **caf-35DBA/35DBA**

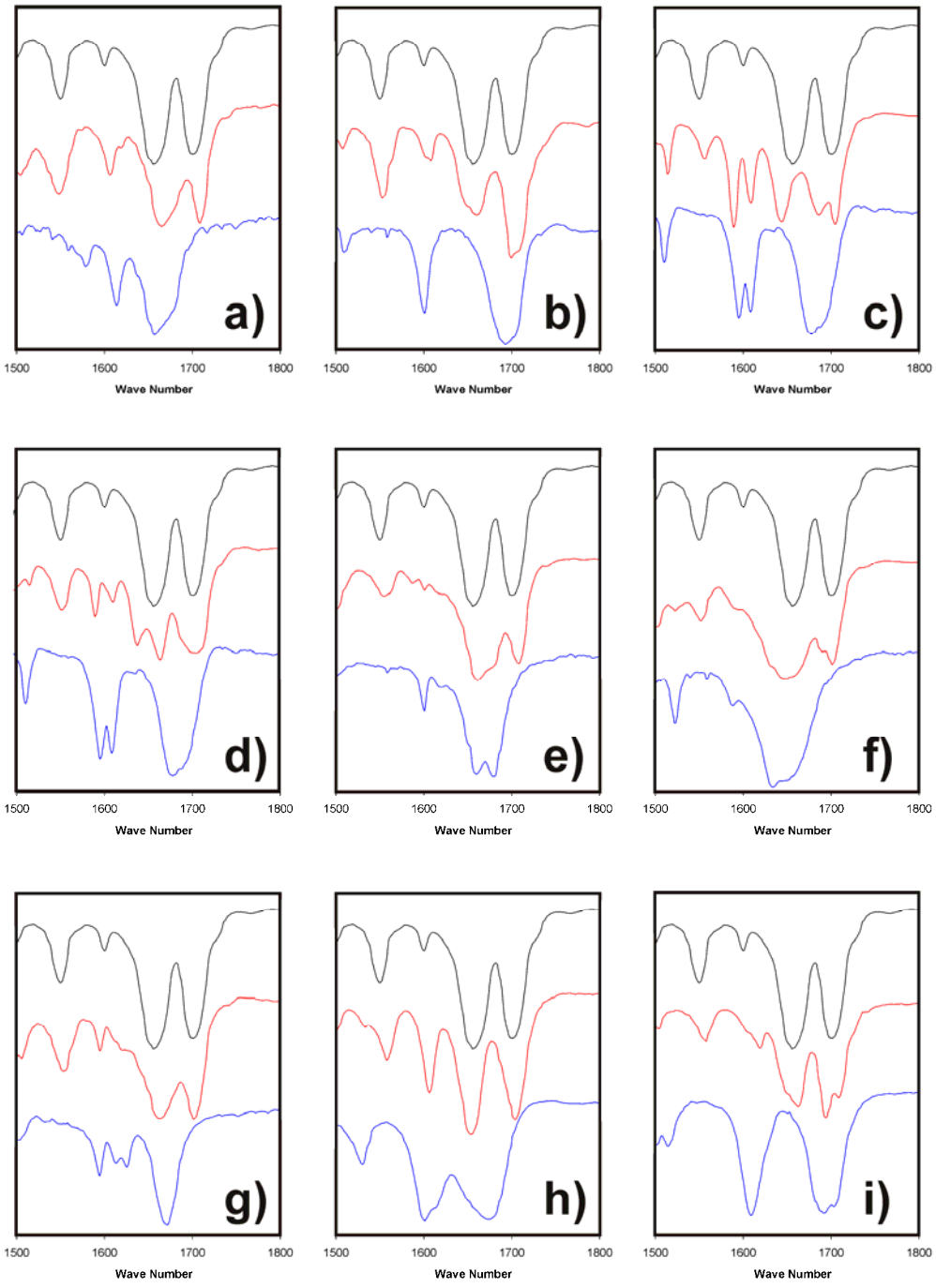

Figure 74 The carbonyl-stretching region in the FT-IR spectra of the obtained cocrystals (red) in comparison with caffeine (black) and the cocrystal former (blue). a) **2HBA**; b) **3HBA**; c) **4HBA** 1:2; d) **4HBA** 2:1; e) **23DBA**; f) **24DBA**; g) **25DBA**; h) **34DBA**; i) **35DBA**.

Table 3 Carbon-oxygen bond distances of the carboxylic groups of the acids.

cocrystal	*d*(C–O) / (Å)	*d*(C=O) / (Å)	*Δd* / (Å) (*)
caf1	1.310(2)	1.237(2)	0.073(3)
caf2	1.333(2)	1.216(2)	0.117(3)
caf3	1.317(3)	1.228(3)	0.089(4)
	1.347(3)	1.202(3)	0.145(4)
caf4	1.315(2)	1.207(2)	0.108(3)
caf5	1.314(4)	1.239(4)	0.075(6)
caf6	1.319(4)	1.240(4)	0.079(6)
caf7	1.301(3)	1.219(3)	0.082(4)
caf8	1.336(2)	1.225(2)	0.111(3)

* ***Δd*** **= [(C–O) - (C=O)]**

4.2.3.1. Cocrystal (**caf**)·(**2HBA**)

Cocrystal (**caf**)·(**2HBA**) crystallizes from acetonitrile in the monoclinic $P2_1/c$ space group. The asymmetric unit consists of one molecule of caffeine and one molecule of **2HBA**. Caffeine and **2HBA** form a two-component assembly based on a $R_2^2(7)$ hydrogen-bond pattern that involves a carboxyl(**2HBA**) and an imidazole(**caf**) moiety (Fig 75a). The hydroxy-group of **2HBA** is involved in an intramolecular O−H(hydroxy)···O(carboxy) hydrogen bond with the carboxylic group to form a $S_1^1(6)$ ring (Fig 75a), consistent with other α-hydroxybenzoic and α-hydroxynaphthoic acids.[257] The two-component assemblies stack parallel in an offset "head-to-tail" manner (Fig 75b), being held together by weak van der Waals interactions. The stacks are sustained by C−H···O hydrogen bonds to form a 2D sheet (Fig 75c). Adjacent sheets are held together by van der Waals forces (Fig 75c).

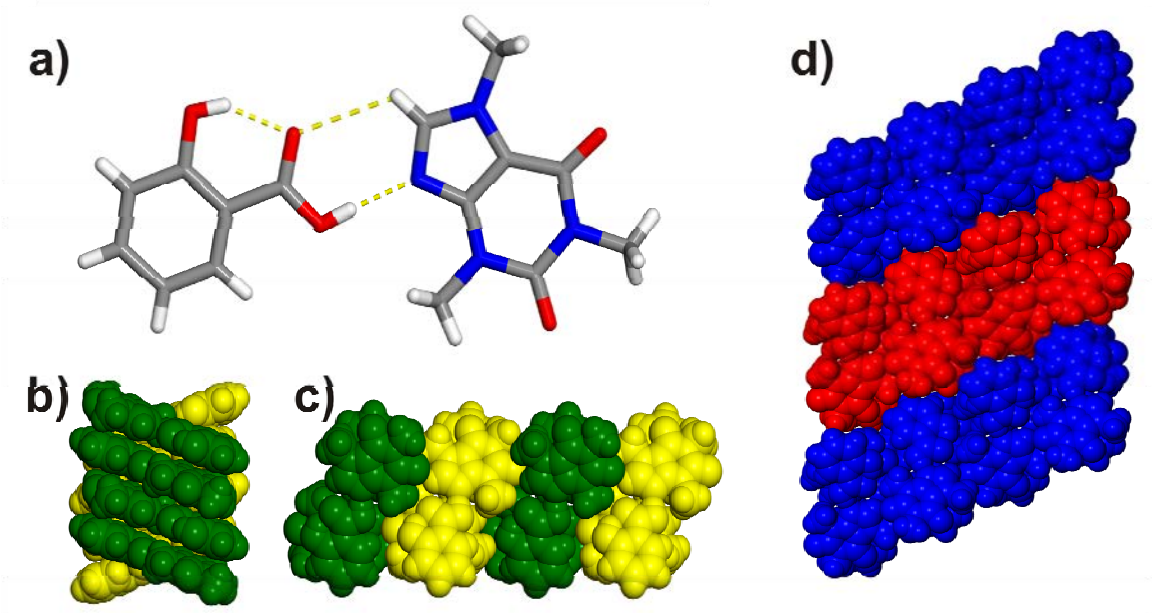

Figure 75 Perspective views: a) two-component complex of caffeine and **2HBA** defined by a $R_2^2(7)$ hydrogen-bond pattern, b) caffeine:**2HBA** complexes stacked in a "head-to-head" manner, c) stacks of caffeine:**2HBA** complexes linked via C–H···O interactions and d) adjacent sheets of caffeine:**2HBA** assemblies in (**caf**)·(**2HBA**).

4.2.3.2. Cocrystal (**caf**)·(**3HBA**)

Cocrystal (**caf**)·(**3HBA**) crystallizes from acetonitrile in the monoclinic space group $P2_1/c$ with both one molecule of caffeine and **3HBA** in the asymmetric unit. The crystal structure is based on a four-component centrosymmetric assembly involving two molecules of caffeine and two molecules of **3HBA** linked *via* O–H(carboxy)···N(imidazole) and O–H(hydroxy)···O(urea) hydrogen bonds (Fig 76a). The complexes assemble to form a molecular tape *via* C–H···O hydrogen bonds (Fig 76b). The molecular tapes interact in a parallel and offset manner *via* weak van der Waals forces to form stacks (Fig 76c), which are sustained *via* C–H···O hydrogen bonds (Fig 76d).

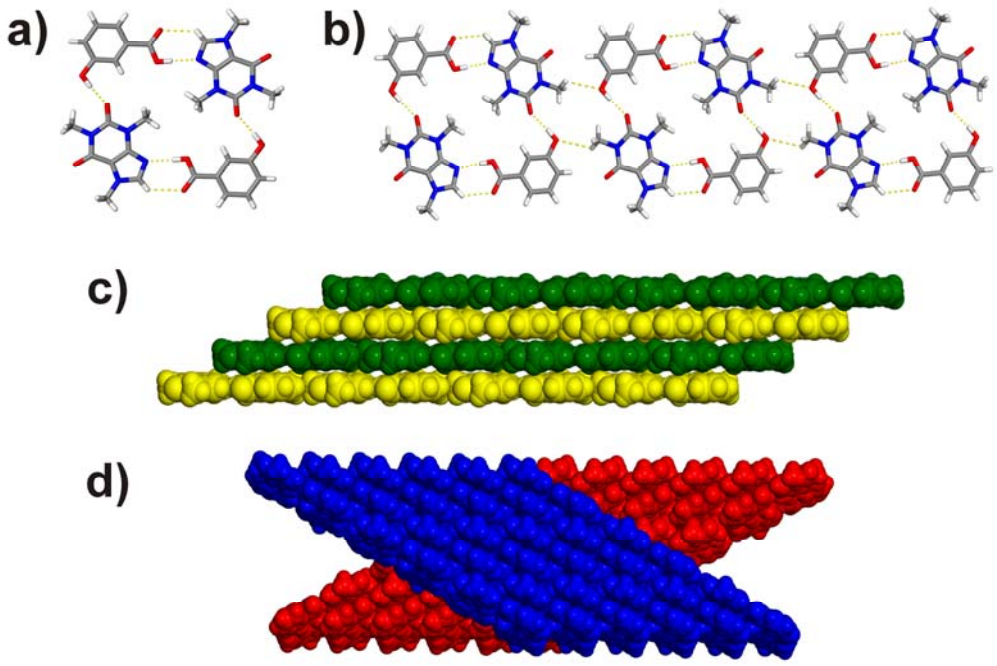

Figure 76 Perspective views: a) four-component discrete assembly of caffeine and **3HBA** defined by a $R_2^2(7)$ hydrogen-bond pattern, b) molecular tape composed of caffeine:**3HBA** assemblies, c) molecular tapes of caffeine:**3HBA** assemblies stacked in a offset manner and d) adjacent stacks of caffeine:**3HBA** tapes linked *via* C–H···O hydrogen bonds.

4.2.3.3. Cocrystal (**caf**)·2(**4HBA**)

Cocrystal (**caf**)·2(**4HBA**) crystallizes from acetonitrile in a 1:2 ratio in the monoclinic space group $P2_1/c$ with one molecule of caffeine and two **4HBA**s in the asymmetric unit. Caffeine and **4HBA** form an linear chain *via* O–H(carboxy)···N(imidazole) and O–H(hydroxy)···O(amide) hydrogen bonds. The linear chain of opposite directionality are cross-linked by **4HBA** molecules *via* O–H(carboxy)···O(carboxy) and O–H(hydroxy)···O(urea) hydrogen bonds forming a wave-like molecular sheet (Fig 77a, 77b). The caffeine:**4HBA** pairs and the cross-linking **4HBA** molecules within the wave-like sheet are defining an angle of $\varphi \approx 111°$. The sheets stack in a offset manner being held together by π(caffeine)···π(**4HBA**) interactions (Fig 77c).

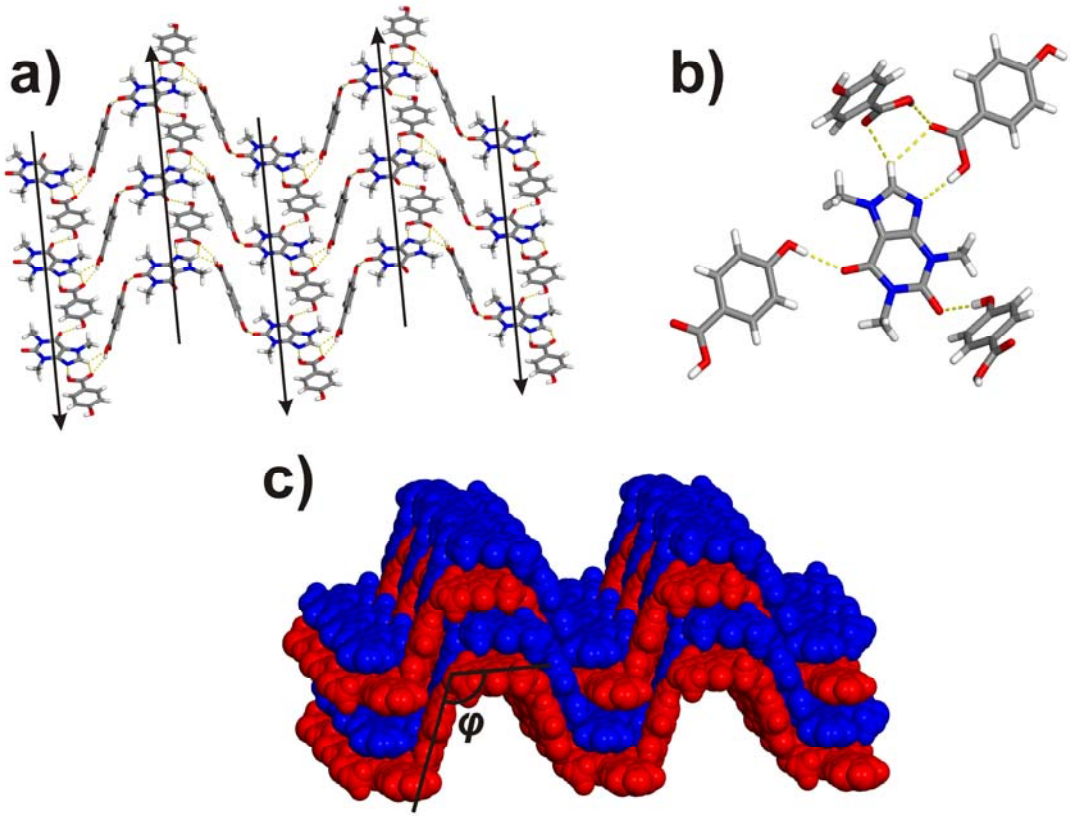

Figure 77 Perspective views: a) **caf** involved in hydrogen-bonding with all three acceptor groups, b) molecular sheet composed of **caf** and **4HBA,** and c) sheets stacked in an offset manner being stabilized by face-to-face π-forces.

4.2.3.4. Cocrystal 2(**caf**)·(**4HBA**)

Cocrystal 2(**caf**)·(**4HBA**) crystallizes from acetonitrile in the monoclinic space group $P2_1/n$. The asymmetric unit contains two molecules of caffeine and one molecule of **4HBA**. The structure consists of discrete three-component assemblies involving two caffeine molecules and one **4HBA** linked *via* O–H(carboxy)···N(imidazole) and O–H(hydroxy)···O(urea) hydrogen bonds (Fig 78a). The caffeine molecule linked to **4HBA** through a O–H(hydroxy)···O(urea) hydrogen bond is disordered over two positions with site occupancies 0.785:0.215. The imidazole moiety does not participate in a hydrogen

bond (Fig 78a). The three-component assemblies form a "zipper"-like ribbon *via* weak C–H···O hydrogen bonds, wherein the disordered caffeine molecules effectively lie on the edge of each ribbon (Fig 78b). The ribbons interact in a parallel (head-to-head) and offset manner *via* π(caffeine)···π(**4HBA**) interactions to form layers. The layers stack *via* π(caffeine)···π(**4HBA**) interactions to form a structure in which the ribbons of each layer point in opposite directions (head-to-tail) (Fig 78c).

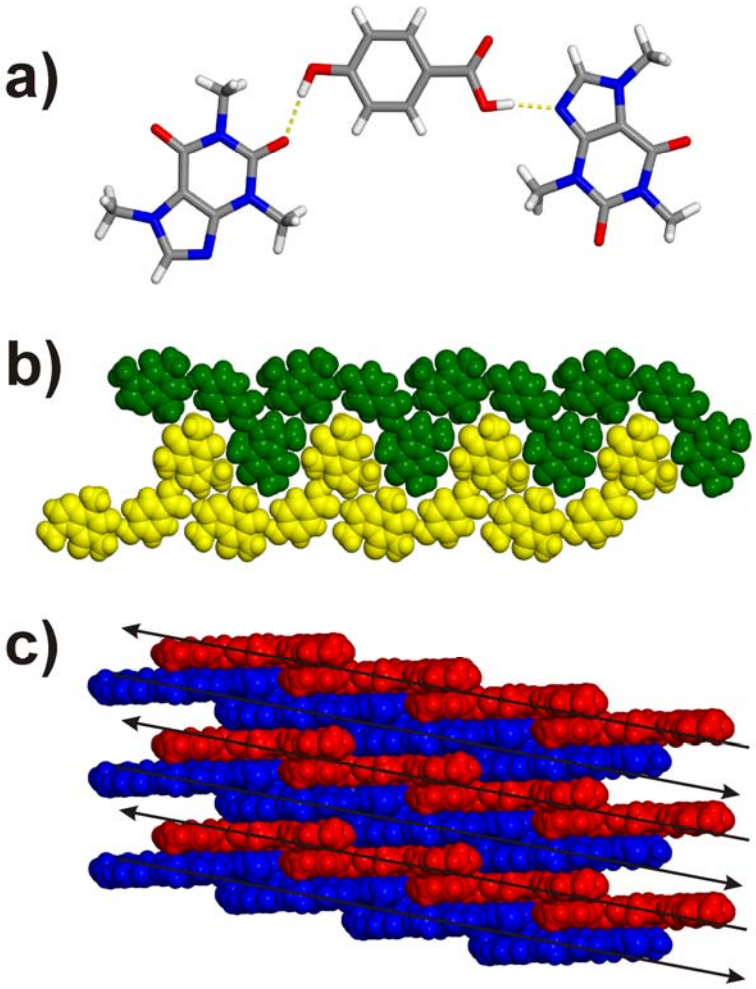

Figure 78 Perspective views: a) three-component discrete 2:1 assembly of caffeine and **4HBA** (only one orientation of the disordered caffeine molecule is shown for clarity), b) "zipper" motif within caffeine:**4HBA** ribbons and c) layers of caffeine:**4HBA** ribbons stacked *via* π(caffeine)···π(**4HBA**) interactions.

4.2.3.5. Cocrystal (**caf**)·(**23DBA**)·(H_2O)

Single crystals of (**caf**)·(**23DBA**)·(H_2O) were obtained from an acetonitrile/water solution. The cocrystal contains one molecule of caffeine, **23DBA** and water in a crystallographically independent asymmetric unit, crystallizing in the triclinic space group $P\bar{1}$.

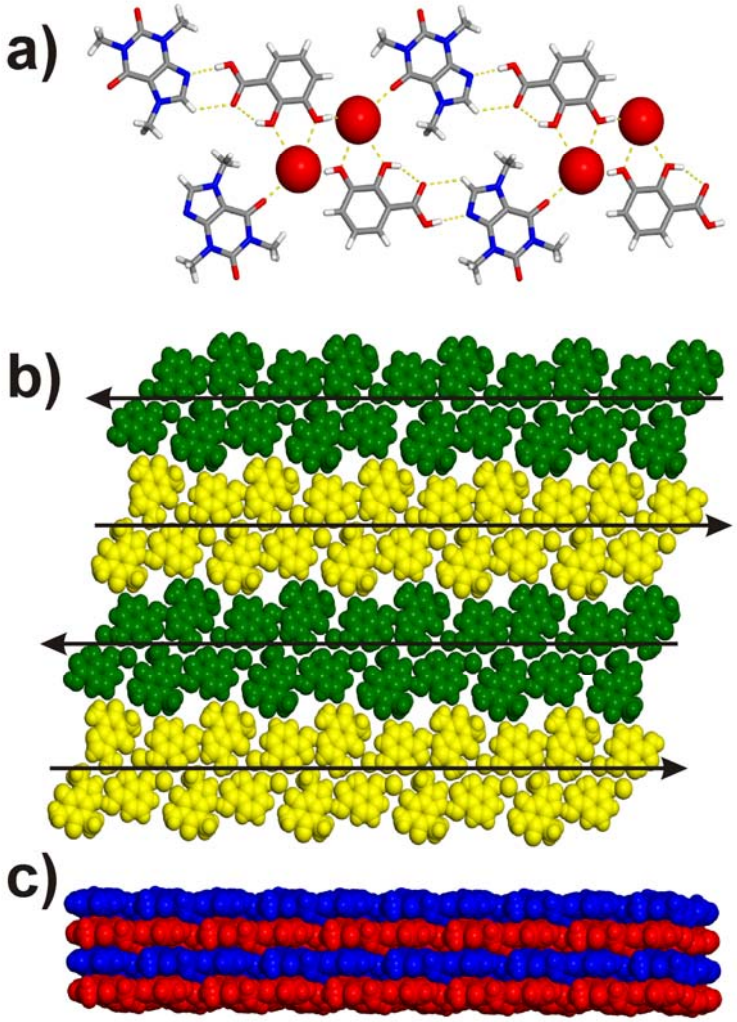

Figure 79 Perspective views: a) polymeric ribbon containing caffeine, 23DBA and water cross-linked *via* O–H(water)···N(imidazole), O–H(carboxy)···N(imidazole) and O–H(water)···O(hydroxy) hydrogen bonds, b) molecular sheet formed by molecular ribbons *via* C–H(benzene)···O(urea) interactions and c) offset stacked molecular sheets stabilized *via* π(caffeine)···π(**23DBA**) interactions.

The crystal structure of (**caf**)·(**23DBA**)·(H_2O) reveals that caffeine and **23DBA** form a molecular complex involving both an intramolecular O−H(hydroxy)···O(carboxy)[257] and intermolecular and O−H(carboxy)···N(imidazole) hydrogen bond. These complexes are cross-linked through water molecules *via* O–H(water)···O(amide) and O–H(water)···O(hydroxy) hydrogen bonds forming a polymer ribbon. Each water molecule within the ribbon links three caffeine:**23DBA** assemblies, which are related through an inversion center (Fig 79a). The ribbons are connected *via* C–H···O hydrogen bonds forming a molecular sheets (Fig 79b). The sheets stack offset, being stabilized *via* π(caffeine)···π(**23DBA**) interactions (Fig 79c).

4.2.3.6 Cocrystal (**caf**)·(**24DBA**)·(H_2O)

Caffeine, **24DBA** and water cocrystallize from an acetonitrile/water solution in the triclinic space group $P\bar{1}$. The asymmetric unit contains one molecule of each component.

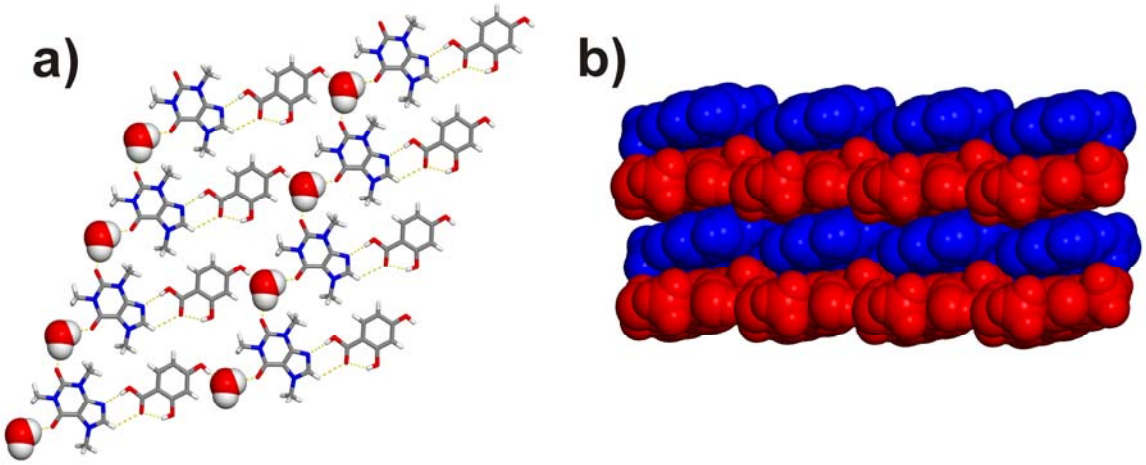

Figure 80 Perspective views: a) 2D network involving caffeine, **24DBA** and water sustained by O−H(water)···O(carbonyl) and O−H(hydroxy)···O(water) hydrogen bonds, and b) caffeine-**24DBA**-water networks stacked in an ABAB manner.

Caffeine and **24DBA** form a two-component supramolecular assembly involving an intramolecular O−H(hydroxy)···O(carboxy)[257] and an intermolecular O−H(carboxy)···N(imidazole) hydrogen bond. The assemblies are linked through water molecules *via* O−H(water)···O(urea), O−H(water)···O(amide) and O−H(hydroxy)···O(water) hydrogen bonds forming a 2D network. Each water molecule is linked to two caffeine molecules and one **24DBA** (Fig 80a). The networks stack in an ABAB manner (Fig 80b) being offset along the (011) crystallographic plane. The stacks are held together held together by π(caffeine)···π(**24DBA**) interactions.

4.2.3.7. Cocrystal (**caf**)·(**25DBA**)

Caffeine and **25DBA** cocrystallize from acetonitrile in a 1:1 ratio in the monoclinic space group *P*21/*c* with one molecule of caffeine and **25DBA** in the asymmetric unit. Caffeine and **25DBA** assemble to form 1D wave-like polymers involving intermolecular O−H(carboxy)···N(imidazole) and O−H(hydroxy)···O(amide) hydrogen bonds, as well as intramolecular O−H(hydroxy)···O(carboxy)[257] hydrogen bonds (Fig 81a).

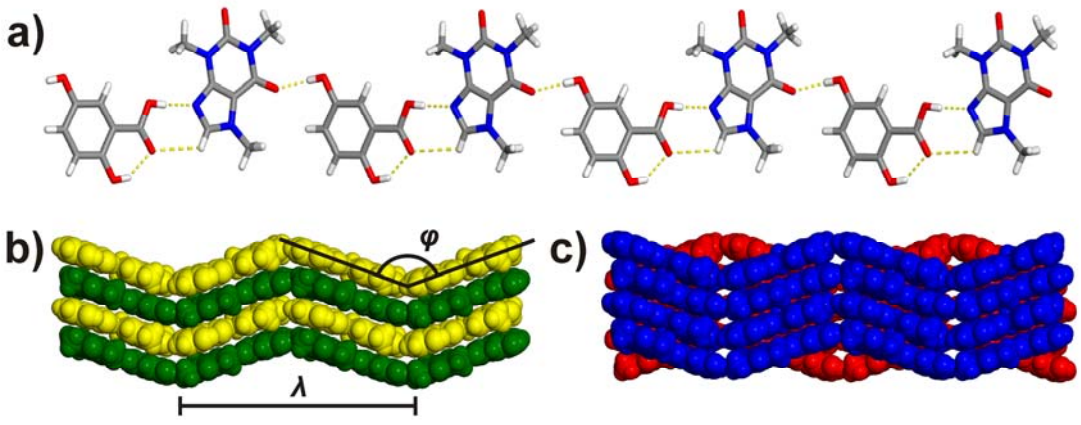

Figure 81 Perspective views: a) wave-like 1D polymer based on caffeine and **25DBA**, b) stack of the 1D caffeine:**25DBA** polymers, and c) stacked caffeine:**25DBA** polymers sustained by weak C−H···O hydrogen bonds.

The caffeine:**25DBA** complexes within the "wavy" polymers are inclined by φ=144º. The 1D polymers form "head-to-tail" stacks that are sustained by π(caffeine)···π(**25DBA**) forces (Fig 81b). The stacks are held together by weak C−H···O hydrogen bonds. The caffeine:**25DBA** pairs of neighboring stacks are offset by one half of a wavelength ($\lambda/2 \approx 14$ Å) of wave-like polymer (Fig 81c).

4.2.3.8. Cocrystal (caf)·(35DBA)·(H_2O)

Single crystals of (**caf**)·(**35DBA**)·(H_2O) were grown from an acetonitrile/water solution. In the cocrystal, **caf** and **35DBA** assemble with water in the monoclinic space group $P2_1/c$. The asymmetric unit consists of one molecule of caffeine, **35DBA**, and water. Similar to (**caf**)·(**3HBA**), caffeine and **35DBA** form discrete centrosymmetric four-component assemblies composed of two molecules of caffeine and **35DBA** (Fig 82a).

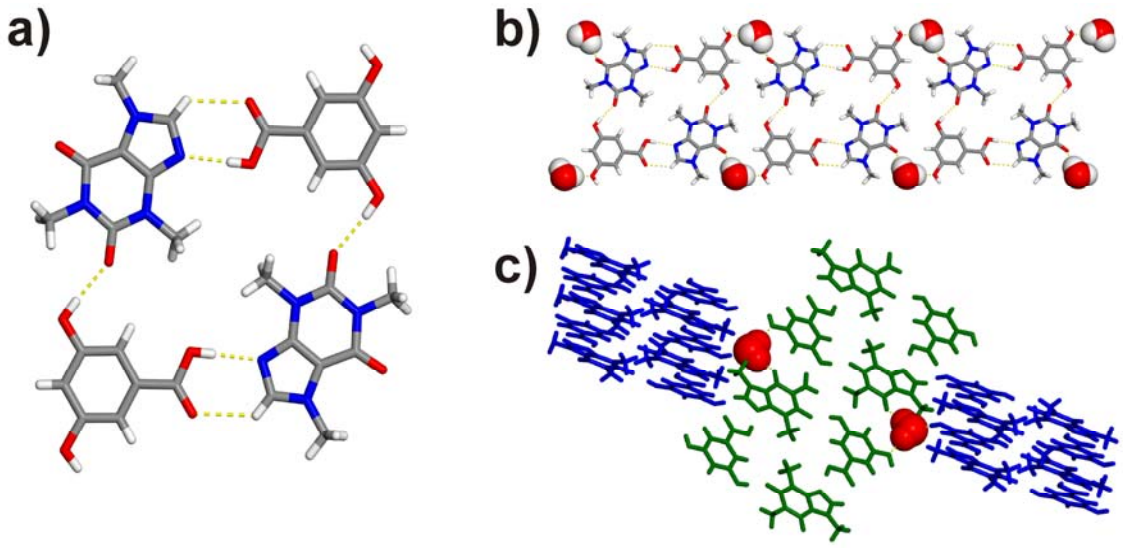

Figure 82 Perspective views: (a) four-component **caf**:**35DBA** assembly, (b) molecular tape consisting of caffeine, **35DBA** and water and (c) a fragment of the 3D network being based on caffeine:**35DBA** tapes that are cross-linked by water molecules

Table 4 Selected hydrogen-bond parameters of the studied cocrystals (with estimated standard deviations except for fixed and riding hydrogen atoms).

	D*–H···*A	***d*(*D*–H)/Å**	***d*(H···*A*)/Å**	***D*(*D*···*A*)/Å**	***θ*/ º**
caf1	O3–H3···N2	0.82	1.81	2.625(2)	177.7
	O5–H5···O4	0.82	1.85	2.576(2)	146.8
caf2	O4–H1···N4	0.88(3)	1.86(3)	2.743(2)	180(3)
	O5–H2···O2^{i}	0.90(3)	1.83(3)	2.726(2)	176(3)
caf3	O4-H1X...N2	0.90(4)	1.79(4)	2.689(3)	175(4)
	O5-H2X...O2^{ii}	0.77(3)	1.98(3)	2.749(3)	174(3)
	O7-H3X...O3^{iii}	0.76(3)	2.04(4)	2.716(3)	148(3)
	O8-H4X...O1	0.85(3)	1.85(3)	2.702(3)	173(4)
caf4	O5–H3X···N8	0.90(2)	1.79(2)	2.681(2)	168(2)
	O7–H2X···O2^{iv}	0.87(2)	1.82(2)	2.690(2)	176(2)
caf5	O1–H1···N4	0.82	1.85	2.659(4)	171.7
	O3–H3···O2	0.82	1.83	2.547(3)	146.1
	O4–H7···O7^{v}	0.82	1.84	2.596(4)	152.5
	O7–H···O3	N/A^{a}	N/A^{a}	2.996(4)	N/A^{a}
	O7–H···O4	N/A^{a}	N/A^{a}	2.950(4)	N/A^{a}
	O7–H···O5	N/A^{a}	N/A^{a}	2.730(4)	N/A^{a}
caf6	O1–H1···N4	0.82	1.86	2.676(4)	176.6
	O3–H3···O2	0.82	1.87	2.600(4)	147.1
	O7–H1W···O6^{vi}	0.86(5)	1.87(5)	2.721(4)	170(5)
	O7–H2W···O5	0.71(6)	2.08(6)	2.789(4)	173(6)
	O4–H5···O7^{vii}	0.82	1.81	2.621(4)	173.3
caf7	O1–H1···N4	0.82	1.79	2.609(3)	176.5
	O3–H3···O2	0.82	1.87	2.584(3)	145.5
	O4–H4···O5^{viii}	0.82	1.88	2.672(3)	162.4
caf8	O4–H4···N1	0.82	1.94	2.764(2)	178.7
	O5–H5···O7	0.82	1.82	2.634(2)	173.7
	O6–H6···O1^{ix}	0.82	1.92	2.739(2)	175.8
	O7–H1W···O2^{x}	0.86(3)	1.91(3)	2.756(2)	169(2)
	O7–H2W···O5^{xi}	0.81(3)	1.96(3)	2.771(2)	177(3)

The hydrogen atoms of water molecules in **caf5** were not allocatable. The symmetry codes for all cocrystals in table 4 are as follows: (i) -x+1, -y+1, -z+1; (ii) x+1, y, z+1; (iii) -x+2, y+1/2, -z+1/2; (iv) x, y-1, z ; (v) -x-1, -y+3, -z+1; (vi) x, y-1, z; (vii) x-1,

y+1, z-1; (viii) x-1, -y+1/2, z-1/2; (ix) -x+2, -y+2, -z ; (x) -x+2, y+1/2, -z+1/2; (xi) -x+4, y-1/2, -z+1/2.

The (**caf**)·(**35DBA**)·(H_2O) assemblies are sustained *via* O–H(carboxy)···N(imidazole) and O–H(hydroxy)···O(urea) hydrogen bonds. The assemblies are further linked into tapes by water molecules *via* of O–H(water)···O(hydroxy) and O–H(water)···O(amide) hydrogen bonds (Fig 82b). In addition, each water molecule is involved in a third hydrogen bond that links two molecular tapes *via* a O–H(hydroxy)···O(water) hydrogen bond, thus, forming a three-dimensional network (Fig 82c). The molecular tapes linked *via* water molecules are inclined at an angle of about 62º.

4.2.3.9. Hydrogen-bond parameters

The hydrogen bond parameters (Table 4) were calculated using the HTAB command in SHELX.[175]

4.2.4. Discussion

Caffeine possesses a total of three sites that can act as hydrogen-bond acceptors. One group is based on an N-atom of an imidazole while the remaining two groups are based on O-atoms of carbonyl groups of a urea and an amide moiety (Fig. 69, 83). We selected CCFs able to act as multiple hydrogen-bond donors to increase the diversity of synthons in caffeine-based cocrystals. A CCF with multiple hydrogen-bond donor and acceptor groups can be expected to interact with more than one PA and, hence, afford assemblies with high PA:CCF ratios. Keeping in mind that the imidazole-carboxylic acid

interaction is the most prevalent heterosynthon in reported caffeine-based cocrystals, we selected a carboxylic acid with single and multiple donor groups along the periphery as a CCF.

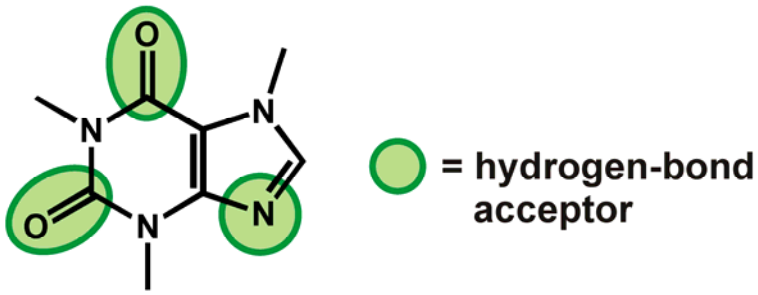

Figure 83 Chemical structure of caffeine with highlighted hydrogen-bond accepting functional groups.

Since hydroxy groups are known to participate extensively in hydrogen bonds with carbonyl groups, mono- and dihydroxybenzoic acids were selected as CCFs. A search of the CSD suggested that both the urea and amide carbonyl groups of caffeine could interact with the pendent hydroxy groups of the CCFs. In particular, the survey revealed 15 entries that contain urea and amide moieties in the presence of an alcoholic hydroxy moiety. The CSD survey was based on urea and amide moieties identical to those present in caffeine (Fig. 84).

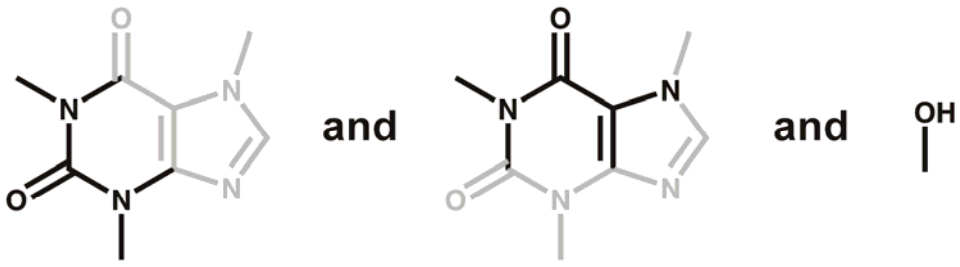

Figure 84 Structural fragments investigated to determine the occurrence of O-H···O(amide) and O-H···O(urea) hydrogen bonds in the CSD.

A total of six entries contained the O-H(hydroxy)···O(urea) and/or O-H(hydroxy)···O(amide) heterosynthon (CSD reference codes: DIJVOH, KABVEO, MACPTL, NEMPOK, DOTGOI, ZENQEO). Two solids (CSD reference codes: MACPTL, NEMPOK) contained only the O-H(hydroxy)···O(urea) heterosynthon and two solids (CSD reference codes: DOTGOI, ZENQEO) contained only the O-H(hydroxy)···O(amide) synthon. The O-H(hydroxy)···O(urea) and O-H(hydroxy)···O(amide) synthon were both observed in two cases (CSD reference codes: DIJVOH, KABVEO).

All structurally-characterized solids were determined to involve the prevalent O-H(carboxy)···N(imidazole) heterosynthon (Fig. 70a). The O-H(acid)···N(imidazole) distances range from 2.61 to 2.76 Å (Table 4). For the acid components, the carboxyl group and aromatic ring lie approximately co-planar, as revealed by the dihedral angle involving the acid group and benzene ring. The lowest dihedral angles are associated with the *ortho* hydroxy groups, which participate in an intramolecular O-H(hydroxy)···O(carboxy) hydrogen bond in the form of a $S_1^1(6)$ motif.[257] The dihedral angles (θ_1) range from 1.0 to 4.8°. The rings of the caffeine and acid components in each solid, each of which is virtually planar, lie slightly twisted with respect to one another.

Table 5 Twist angles θ_1 and θ_2.

cocrystal	θ_1 / °	θ_2 / °
caf1	0.97(9)	0.64(4)
caf2	4.81(11)	2.21(5)
caf3	3.32(15)	7.33(6)
caf4	1.89(13)	4.24(3)
caf5	3.58(15)	0.56(9)
caf6	2.17(25)	1.75(8)
caf7	2.78(24)	2.70(8)

caf8	2.02(12)	2.89(4)

The twist angles of the aromatic rings of the caffeine and acid components (θ_2) range from 0.6 to 7.3°. All dihedral and twist angles are given in Table 5. To determine the robustness of the O-H(carboxy)···N(imidazole) heterosynthons in structures deposited in the CSD, we search the CSD for entries with a carboxylic acid, an N-methylimidazole- and a hydroxy moiety (Fig. 85). A total of 11 entries were found. The O-H(carboxy)···N(imidazole) heterosynthon was observed in six entries (CSD reference codes: CSATBR, FINMEV, KIDNOB, KIDNUH, NEXWUJ, PIDSAW). Four solids possessed only the OH(carboxy)···N(imidazole) heterosynthon while two involved both the O-H(carboxy)···N(imidazole) and OH(hydroxy)···N(imidazole) synthon (CSD reference codes: FINMEV, KIDNOB). Collectively, the structural data deposited in the CSD, as well as our experimental findings, attest to the robustness of the O-H(carboxy)···N(imidazole) heterosynthon.

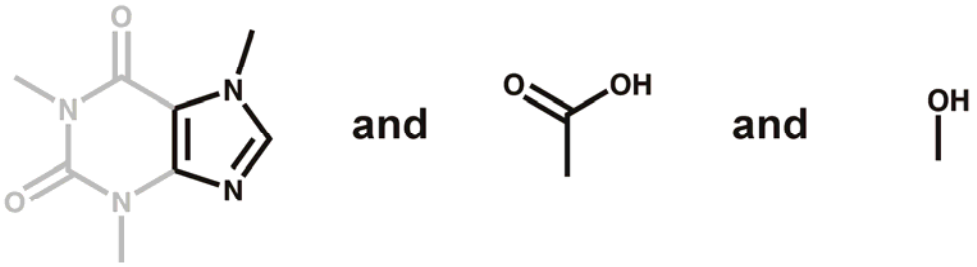

Figure 85 Structural fragments investigated to determine the robustness of the O-H(hydroxy)···N(imidazole) heterosynthons in structures deposited in the CSD.

In line with our design, the pendent hydroxy group of the CCF interacts with the carbonyl groups of caffeine. In particular, the O-H(hydroxy)···O(amide) and O-H(hydroxy)···O(urea) synthons are present in five of the eight solids. Three solids

involve only the O-H(hydroxy)···O(urea) heterosynthon [(**caf**)·(**3HBA**); 2(**caf**)·(**4HBA**); (**caf**)·(**35DBA**)·(H_2O)], one solid involves only the O-H(hydroxy)···O(amide) synthon [(**caf**)·(**25DBA**)], while one solid contains both the O-H(hydroxy)···O(urea) and O-H(hydroxy)···O(amide) synthons [(**caf**)·2(**4HBA**)]

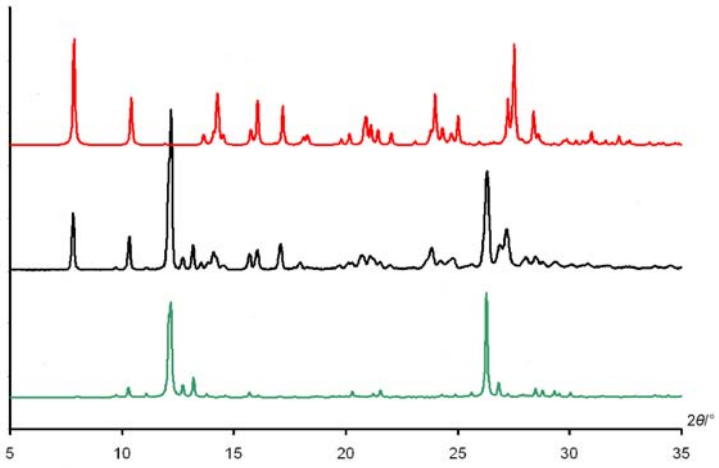

Figure 86 Simulated X-ray diffractogram of cocrystals (**caf**)·2(**4HBA**) and 2(**caf**)·(**4HBA**) in comparison to the diffractogram of the solid obtained from a screening experiment involving caffeine and 4-hydroxybenzoic acid. To overlay the powder patterns of (**caf**)·2(**4HBA**) and 2(**caf**)·(**4HBA**), a two-phase Rietveld refinement was performed to improve the fit of the experimental and calculated patterns. This was particularly necessary in the case of the 1:2 4-hydroxybenzoic acid/caffeine cocrystal, which appears to be more strongly effected by the temperature difference between the single-crystal and powder data collections. Color scheme: green = 2(**caf**)·(**4HBA**), red = (**caf**)·2(**4HBA**), black = physical mixture of (**caf**)·2(**4HBA**) and 2(**caf**)·(**4HBA**)).

All solids are based on a 1:1 caffeine-to-carboxylic acid ratio and involve both discrete and infinite hydrogen-bonded structures (Table 6). Discrete hydrogen-bonded assemblies were achieved using **2HBA**, **3HBA**, **23DBA**, **24DBA** and **35DBA.** Cocrystallization of caffeine with **2HBA**, **23DBA** and **24DBA** yielded discrete two-component caffeine:CCF assemblies, while the cocrystallization of caffeine with either

3HBA or **35DBA** afforded discrete four-component assemblies (*i.e.* 2:2 ratio). An infinite 1D assembly was obtained in the case of **25DBA** as a cocrystal former. In the case of **4HBA**, cocrystals of both 1:2 and 2:1 ratios were obtained (Table 6). Moreover, **4HBA** was determined to not generate a 1:1 cocrystal in utilized experimental conditions. A physical mixture of cocrystals (**caf**)·2(**4HBA**) and 2(**caf**)·(**4HBA**) (ratio: 0.45:0.55) was identified from the screening experiment using XRPD analysis[258] wherein the diffractogram of the product corresponded to the simulated diffractograms of both cocrystals (Fig. 86).

Table 6 Overview of structural features in caffeine cocrystals involving (di)hydroxybenzoic acids.

solid	caf:CCF ratio	structure of assembly	hydrogen-bond acceptor group of caffeine			
			imidazole	urea	amide	total
caf1	1:1	discrete	√			1
caf2	1:1	discrete	√	√		2
caf3	1:2	2D infinite	√	√	√	3
caf4	2:1	discrete	√	√		2
caf5	1:1	discrete[a]	√		√	2
caf6	1:1	discrete[b]	√	√	√	3
caf7	1:1	1D infinite	√		√	2
caf8	1:1	discrete[c]	√	√	√	3

[a] 1D infinite based on included H_2O; [b] 2D infinite based on included H_2O; [c] 3D infinite based on included H_2O.

Since each *ortho*-hydroxy group of each acid participated in an intramolecular O-H(hydroxy)···O(carboxy) hydrogen bond, the group was largely prohibited from participating in an intermolecular interaction.[16] This observation is consistent with other *ortho*-substituted acids reported in the literature. It is, therefore, unsurprising that discrete two-component assemblies formed in the case of **2HBA**. In the cases of **23DBA**, **24DBA**, and **25DBA**, however, the hydroxy groups participated in both intramolecular and

intermolecular hydrogen bonds. Specifically, each 'additional' hydroxy group participated in an intermolecular O-H···O hydrogen bond with either a carbonyl group of caffeine (**25DBA**) or an included water molecule (**23HBA**, **24HBA**). For **25HBA**, the urea carbonyl group participated in the intermolecular hydrogen bond.[250] This observation compares favorably to our preliminary studies involving 6-hydroxy-2-naphthoic acid (see Appendix D) as a CCF and contrasts that of Jones *et al.* wherein the amide carbonyl group forms a hydrogen bond with the hydroxy group of citric acid.[249] The inclusion of the water in the case of **23DBA** resulted in the formation of a 1D ribbon-like architecture. In this solid, the *ortho*- and *meta*-hydroxy groups of **23DBA** serve as hydrogen-bond acceptors, participating in a bifurcated hydrogen bond with a water molecule. The water molecules link caffeine-**23DBA** pairs *via* hydrogen bonds to the amide carbonyl group of caffeine to give 1D ribbon-like arrays (Fig 79a). In the case of (**caf**)·(**24HBA**)·(H_2O), the water molecules facilitate the self-assembly of caffeine-**24DBA** pairs into 2D networks that involve hydrogen bonds to both the urea and amide carbonyl groups of caffeine (Fig 80a).

In addition to **25DBA**, the added hydroxy group of the **CCF** formed a O-H(hydroxy)···O(carboxy) hydrogen bond to caffeine in the cases of **34DBA** and **35DBA**. Intermolecular O-H(hydroxy)···O(carboxy) hydrogen bonds were also observed in the cases of **3HBA** and **4HBA**. For both **3HBA** and **35DBA**, the components assembled to form 2:2 caffeine:CCF assemblies composed of two molecules of caffeine and two CCFs that are held together *via* O-H(carboxy)···N(imidazole) and O-H(hydroxy)···O(urea) hydrogen bonds. The formation of the discrete assemblies can be attributed to the *meta*-positioning of the hydroxy group along the periphery of the benzene ring. The water inclusion in the case of **35DBA** results in a complex 3D network wherein both the amide and urea carbonyl groups of caffeine act as hydrogen bond acceptors (Fig 82c). In general, the inclusion of water molecules into the crystal lattices of the cocrystals is not surprising. Specifically, hydrate formation is generally observed in organic crystals

wherein the number hydrogen-bond acceptor and donor sites does not match, which is the case in the studied cocrystals.

Both **SMPT** and single-crystal growth afforded cocrystals of caffeine and **4HBA** in 1:2 and 2:1 ratios. The structure of (**caf**)·2(**4HBA**) is based on a 2D network in which all three acceptor groups of caffeine participate in hydrogen bonds, as with **24DBA** and **35DBA**. On the other hand, the structure of 2(**caf**)·(**4HBA**) is based on three-component assemblies wherein two caffeine molecules are hydrogen-bonded to **4HBA** with one hydrogen bond *via* a hydrogen-bond acceptor group (*i.e.* imidazole) or an acceptor group (*i.e.* urea moiety). The **caf** molecule that interacts with **4HBA** *via* a O-H(hydroxy)···N(imidazole) hydrogen bond is disordered over two positions (Fig. 87).

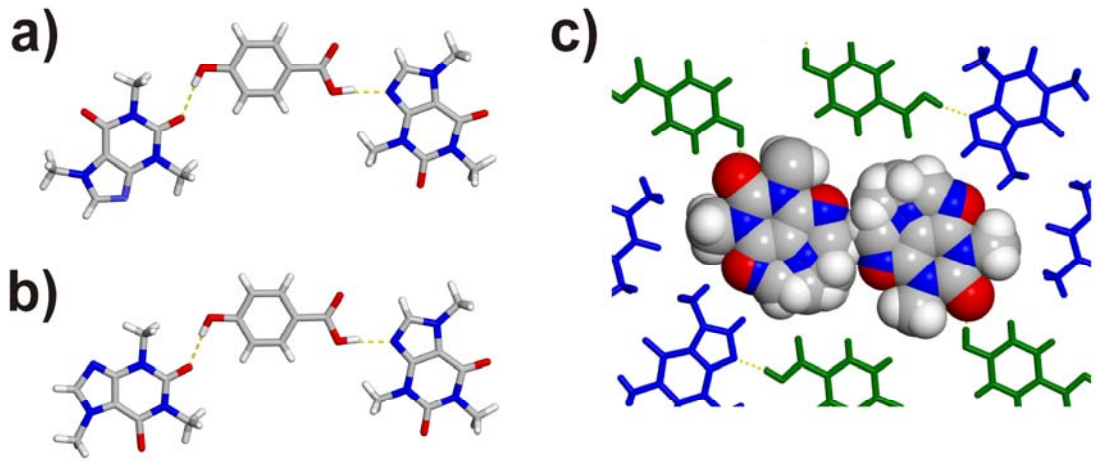

Figure 87 Perspective view of: (a,b) the two positions of the disordered **caf** molecule within the 2(**caf**)·(**4HBA**) assembly, and (c) disordered **caf** molecules belonging to two neighboring "zipper"-like ribbons.

A disorder of this type was previously observed in the cocrystal of the **caf** and 6-hydroxy-2-naphthoic-acid (Fig 71).[257] In both cocrystals, one **caf** participates in a single O-H(hydroxy)···N(imidazole) hydrogen bond. The disorder of these **caf** molecules is not surprising since the O-H(hydroxy)···N(imidazole) is not preorganized to lock the **caf**

molecule in a single position unlike the O-H(carboxy)···N(imidazole) hydrogen bonds, which are further stabilized by a complementary C-H(imidazole)···O(carboxy) interaction. Reasons for the concurrent formation of two stoichiometric cocrystals based on **4HBA** are not clearly evident, but can likely be ascribed to the activity of **4HBA** during the equilibration and crystallization process. That **SMPT** provides access to both of these solids does, however, further establish **SMPT** as a viable strategy for the discovery of co-crystalline solids.

Shortly upon publication of the results described herein,[240] our experimental findings triggered several studies of **caf** cocrystals involving hydroxybenzoic acids. In particular, the Price group (Imperial College, London, UK) used cocrystal **caf1-caf4** as model compounds to determine whether cocrystal formation can be accurately predicted using computational methods. Whereas the structures of **caf1** and **caf2** (i.e. **caf**:**2HBA** and **caf**:**3HBA**) were accurately foretold, the prediction of the **caf**:**4HBA** crystal structure was shown to be incorrect. Particularly, a 1:1 **caf**:**4HBA** cocrystal (Fig. 88) was found to be more stable than the (experimentally observed) combination of the 1:2 and the 2:1 cocrystal (*i.e.* **caf3** and **caf4**, respectively). The formation of a **caf3**/**caf4** mixture, thereby, highlights the existence "*of a selection criterion for crystal structures that is partly based around the growth mechanism rather than purely on thermodynamics*".[259]

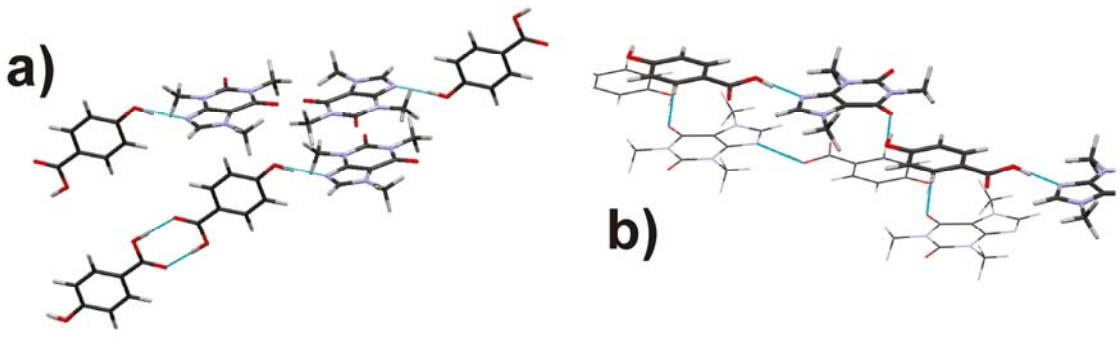

Figure 88 The global minimum (a) and the second ranked structure (b) of the 1:1 **caf**/**4HBA** crystal energy landscape, as determined by Price and coworkers.[259] Reproduced with permission of the American Chemical Society.

In a second study, He and Tan (Institute of Chemical & Engineering Sciences, A*STAR, Singapore and National University of Singapore, Singapore) determined that, depending on initial concentration ratios, **caf**:**4HBA** solutions are yielding single-component **caf** and **4HBA** crystals, **caf3** and **caf4** cocrystals, or mixtures thereof. Pulsed gradient spin-echo nuclear magnetic resonance was utilized to show that "*intermolecular interactions determined in the solution state may serve as qualitative and predictive indicators for the final crystalline products*"[260]

4.2.5. Conclusion

We have described nine cocrystals involving caffeine and structural isomers of (di)hydroxybenzoic acids. The cocrystals were discovered using **SMPT**[104] and shown to exhibit structurally-diverse architectures based on combinations of O-H(carboxy)···N(imidazole), O-H(hydroxy)···O(urea) and O-H(hydroxy)···O(amide) heterosynthons. The established synthon hierarchy in the studied cocrystal series is shown in Fig. 89.

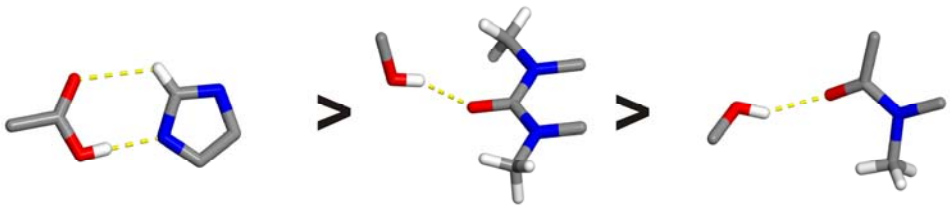

Figure 89 Synthon hierarchy: 1º O-H(carboxy)···N(imidazole), 2º O-H(hydroxy)···O(urea) and 3º O-H(hydroxy)···O(amide).

Keeping in mind the paucity of structural data based on combinations of amide-, urea, and imidazole groups as in the case in caffeine, and the prevalence of these groups in PAs, we anticipate our results to provide further groundwork for designing and modulating the structures of pharmaceutically-relevant solids. The ease of the highly-efficient screening method to discover cocrystals is also expected to further benefit the area of solid-state chemistry of multi-component solids.

4.3. Cocrystals of theophylline and (di)hydroxybenzoic acids: Structural characterization and synthon hierarchies

4.3.1 Introduction

Theophylline (**theo**) (Fig. 90) is a naturally occurring PA that was first isolated from tea extract[245] in 1888. The xanthine alkaloid triggered clinical interest once sufficient amounts became available through synthesis. **Theo** has been medically used for more about a century for the treatment of various conditions.[244] Particularly, **theo** has been used as a cardiac stimulant bronchodilator, but mainly to treat astma. In addition, **theo** has stimulant properties similar to those of caffeine, and also shares some oh the diuretic properties of theobromine. **Theo** exhibits low water solubility that represented a serious problem in drug administration.[245] **Theo** is therefore commonly administred as salt (*i.e.* **theo** ethylenediamine, known as aminophylline).[244] In addition, highly water soluble covalent derivatives, such as 7-dihydroxypropyltheophylline (dyphylline), were prepared to circumvent problems related to **theo**'s low aqueous solubility.[244]

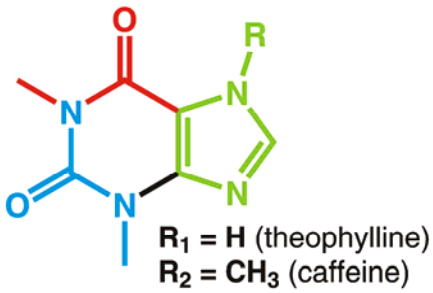

Figure 90 Theophylline and its substructures: imidazole (green), urea (blue) and amide (red) hydrogen-bond accepting sites.

The molecular structure of **theo** exhibits, just as **caf**, one hydrogen-bond acceptor based on an N-atom (belonging to the imidazole moiety), and two groups based on O-atoms (belonging to urea and amide moieties), Notably, **theo** also possesses one hydrogen-bond donating N-H(imidazole) functional group (Fig. 90). Each of the four functional groups has the ability to participate in hydrogen bonding with the hydroxy and carboxy functional group of the (di)hydroxybenzoic acids, as demonstrated in a CSD survey. The presence of the additional N-H functional group provides **theo** with a *supramolecular landscape* (*i.e.* areas of particular supramolecular activity) being more complex and unpredictable than the one observed in **caf** (Fig 91).

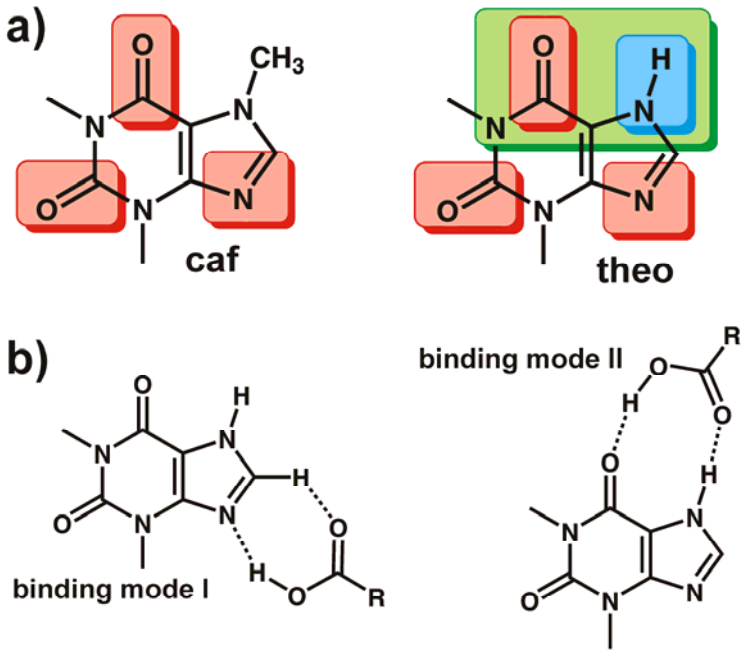

Figure 91 a) Supramolecular landscapes of **caf** and **theo** (red: hydrogen-bond acceptor, blue: hydrogen-bond donor, green: structural moiety compatible to molecular fragments that act both as donors and accptors); b) two most likely binding modes of **theo** and a carboxylic acid.

Specifically, **caf** is "equipped" with only one functional group that is likely to undergo synthon formation with the carboxylic group of a **CCF**, *i.e.* the imidazole moiety. **Theo**, on the other hand, exhibits two structural moieties that are likely to form heterosynthons with a carboxylic acid (Fig 91). The first one is the imidazole unit that can participate in the formation of an O-H(carboxy)···N(imidazole) heterosynthons (*i.e.* binding mode I) (Fig. 91a). The second one is comprised of the closely positioned N-H(imidazole) and C=O(amide) units that can interact with carboxylic acids through a cyclic array of N–H(imidazole)···O(carboxy) and O–H(carboxy)···O(amide) hydrogen bonds with a $R_2^2(9)$ motif (*i.e.* binding mode II) (Fig 91b). Such binding multitude, naturally, decreases the likelihood of accurate predictions regarding the formation of hydrogen-bond patterns in **theo** cocrystals.

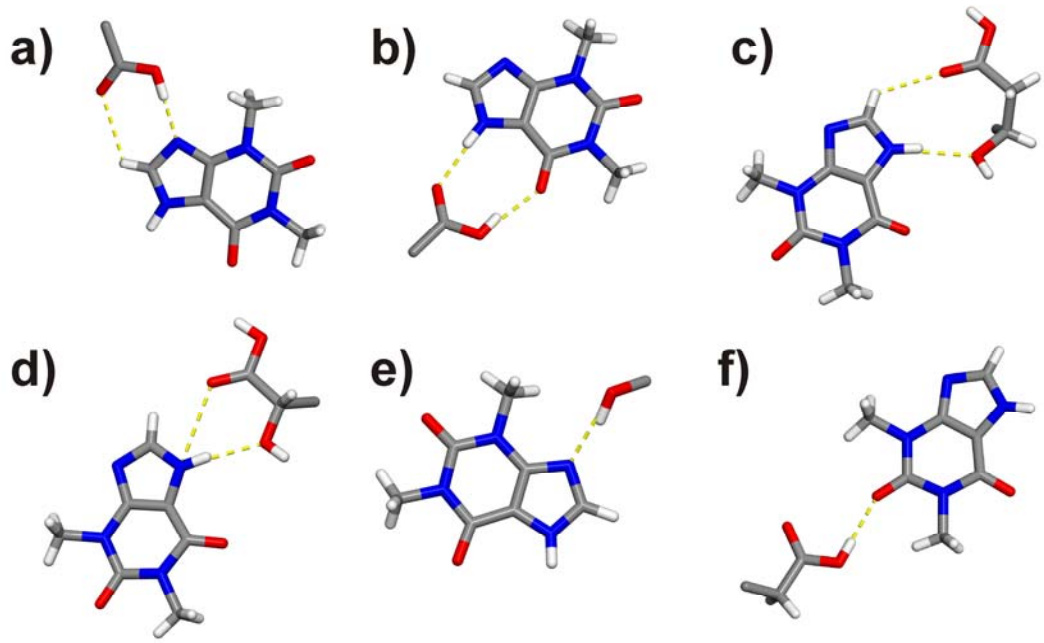

Figure 92 Structural fragments Hydrogen bond accepting and donating sites of **theo** (green – imidazole, red – amide, blue – urea) (a), and supramolecular synthons formed between **theo** and hydroxylated carboxylic acids.

In particular, **theo** and hydroxylated carboxylic acids were reported to form O-H(carboxy)···N(imidazole) heterosynthons ($R_2^2(7)$ motive) (Fig. 92a), cyclic arrays of O-H(carboxy)···O=C(amide) and N-H(imidazole)···O=C(carboxy) hydrogen bonds ($R_2^2(9)$ motive) (Fig. 92b), cyclic arrays of N-H(imidazole)···O-H(hydroxy) and C-H(carboxy)···O=C(carboxy) hydrogen bonds (Fig. 92c), bifurcated C=O(carboxy)···N-H(imidazole)···O-H(hydroxyl) hydrogen bonds ($R_1^2(5)$ motive) (Fig. 92d), as well as O-H(carboxy)···O(urea) and O-H(hydroxy)···N(imidazole) hydrogen bonds (*D* motive) (Fig 92e,f).

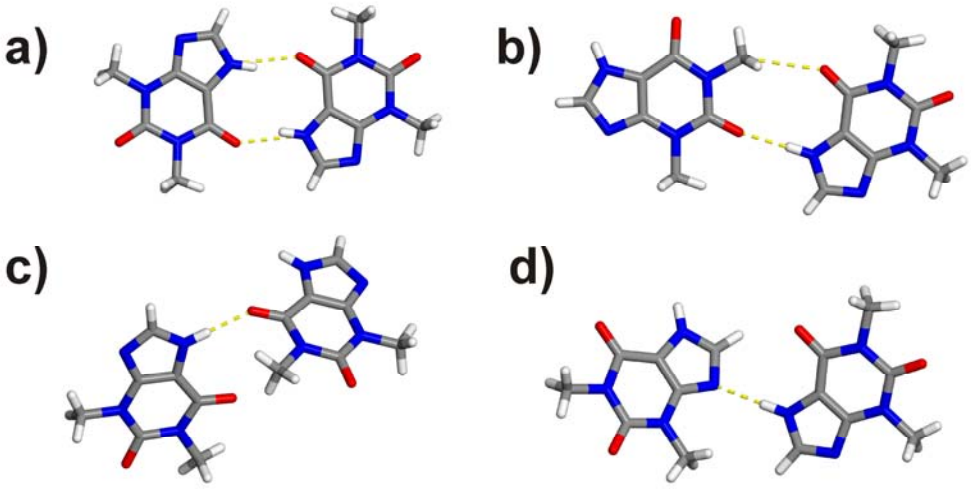

Figure 93 Interactions among **theo** molecules found in cocrystals based on theo and hydroxylated carboxylic acids (a-c), as well as between **theo** molecules in the crystal structure of **theo** (d).

The CSD survey also showed that, when cocrystallized with hydroxylated carboxylic acids, **theo** molecules tend to interact with each other to form either cyclic arrays of N-H(imidazole)···O=C(amide) hydrogen bonds ($R_2^2(10)$ motive) (Fig. 93a), cyclic arrays of N-H(imidazole)···O=C(urea) and C-H(amide)···O=C(urea) hydrogen bonds ($R_2^2(10)$ motive) (Fig. 93b), or N-H(imidazole)···O=C(amide) hydrogen bonds (*D* motive) (Fig 93c). **Theo** molecules can also self-assemble into infinite structures *via* N-H(imidzole)···N(imidazole) hydrogen bonds (*C*(4) motif), as seen in the crystal structure of **theo** (Fig 93d).

The results described above attest to the difficulty of predicting outcomes of self-assembly processes involving molecules with multiple functional groups. Furthermore, the results are underlining the importance of extensive and systematic structural studies that aim to understand synthon hierarchies in molecular cocrystals based on multiple synthons.

4.3.2. Experimental section

4.3.2.1. Materials

Theophylline (anhydrous, minimum 99%), 2-hydroxybenzoic acid (≥99.0%), 3-hydroxybenzoic acid (99.0%) , 4-hydroxybenzoic acid (≥99.0%), 2,3-dihydroxybenzoic acid (≥97.0%), 2,4-dihydroxybenzoic acid (≥98.0%), 2,5-dihydroxybenzoic acid (≥98.0%), 3,4-dihydroxybenzoic acid (≥97.0%), 3,5-dihydroxybenzoic acid (≥97.0%) and acetonitrile (anhydrous, 99.8%) were purchased from Sigma-Aldrich (St. Louis, MO, USA) and were used as received. Millex syringe filters (PVDF, 0.2 μm, 13mm) were purchased from Millipore (Bedford, MA, USA).

4.3.2.2. Survey of the Cambridge Structural Database

The CSD[48] (version 5.31, update of November 2009) was searched for entries involving **theo** by applying the following filters: "3D coordinates determined" and "only organics". The search was conducted with the help of the program ConQuest[251] (version 1.12). The survey revealed 29 entries related to **theo**-containing structures, whereof 17 involve theophylline and a carboxylic acid (*i.e.* CIZTAH, CODCOO, CSATEO, DEYREF, KIGKAN, KIGLAO, KIGLES, KIGLIW, KIGLOC, NEXWOD, NEYCIE, WUYROX, WUYRUD, XEJWUF, XEJXAM, XEJXEQ, XEJXIU).

4.3.2.3. Hydrogen-bond pattern analysis

To identify hydrogen-bond patterns, we have utilized the default definition of hydrogen bonds in the CCDC program *Mercury*[251] (version 2.3): 1) the donor atoms must be covalently bound to at least one hydrogen, 2) the acceptor atoms must have at least one lone electron pair, 3) the donor-acceptor distance must be less than the sum of van der Waals radii of both the hydrogen-bond donor and acceptor, and 4) the contact can be either intramolecular or intermolecular involving hydrogen-bond donor and acceptor atoms being separated by at least 3 covalent bonds within the molecule. In addition, we

have considered another criterion: 5) required presence of a hydrogen atom that satisfies the following criteria: *D*-H···*A* ≥ 100° (where *D* = hydrogen-bond donor, *A* = hydrogen-bond acceptor). Hydrogen-bond parameters were calculated using the CIFTAB routine in WinGX.[253]

4.3.2.4. Cocrystal screening

To investigate potential cocrystal formation of **theo** with hydroxy- and dihydroxybenzoic acids, we utilized a **SMPT**-based suspension screening method.[104] In a typical screening experiment, **theo** (1 mmol) was mixed with an equimolar amount of a hydroxy- or dihydroxybenzoic acid, and a low volume of acetonitrile (1-4 mL). The obtained suspension was vortexed (VWR VM-3000, power; 150W) or sonicated using a sonicator bath (Branson 2510R-DTM; frequency: 42kHz, 6% at 100W) to facilitate the **SMPT** process. A phase change was visually evident within few minute or, in some instances, after only a few seconds. To ensure complete conversions of **theo** and the **CCF** into the cocrystal, the slurries were equilibrated for a week at ambient conditions. The suspensions were filtered, and the residual solids were investigated *via* powder X-ray diffraction (PXRD). The crystalline phases were further studied *via* IR spectroscopy and single crystal X-ray diffraction.

4.3.2.5. Single crystal growth

Single crystals of (**theo**)·(**3HBA**) (1:1 ratio, **theo2**), (**theo**)·(**4HBA**) (1:1 ration, **theo3**), (**theo**)·(**23DBA**) (1:1 ration **theo4**), (**theo**)·(**24DBA**) (1:1 ratio, **theo5**), (**theo**)·(**25DBA**) (1:1 ratio, **theo6**), $(\mathbf{theo})^{+}\cdot(\mathbf{26DBA})^{-}\cdot(H_2O)$ (1:1:1 ratio, **theo7**), (**theo**)·(**34DBA**) (1:1 ration, **theo8**), and (**theo**)·(**35DBA**) (1:1 ratio, **theo9**) were obtained by slow evaporation from solution. To obtain single crystals of the **theo** phases, 20 mg of the corresponding polycrystalline solids, obtained during the screening procedure, were dissolved in acetonitrile (4 ml) at 80 ºC, filtered through a Millex syringe filters (PVDF, 0.2 μm, 13 mm), and left to evaporate at ambient conditions. Crystals

suitable for single crystal X-ray diffraction of all solids were obtained from the filtrate *via* slow evaporation within two weeks.

4.3.2.6. IR spectroscopy

Transmission infrared spectra of the obtained solid phases were collected using a Nicolet Magna 750 FT-IR Spectrometer equipped with a Nicolet NIC-PLAN microscope. The microscope has an MCT-A liquid nitrogen cooled detector. The solids were rolled on a 13 mm × 1 mm BaF_2 disc sample holder. The spectra were scanned 64 times at a resolution of 4 cm^{-1}.

4.3.2.7. Powder X-ray diffractometery

The diffractograms were obtained using an *Inel G3000* diffractometer equipped with a curved position sensitive detector and parallel beam optics. The instrument was operated with a copper-anode tube (1.5 kW, fine focus) at 40 kV and 30 mA. An incident-beam germanium monochrometer was utilized to obtain monochromatic $K_{\alpha 1}$ irradiation. The diffractometer was calibrated using the attenuated direct beam at one-degree intervals. The calibration was established using a Si standard reference material (*i.e.* NIST 640c). The instrument was operated using the *Symphonix*[254] program, whereas the data was analyzed using the *Jade*[255] software (version 6.5). The samples was loaded onto an aluminum sample holder and leveled with a glass slide.

4.3.2.8. Single-crystal X-ray diffraction

The crystallographic analysis of (**theo**)·(**3HBA**), (**theo**)·(**4HBA**), (**theo**)·(**24DBA**) and (**theo**)·(**35DBA**) were performed on a *Bruker SMART* diffractometer equipped with an APEX1 CCD camera, while the data for (**theo**)·(**23DBA**), (**theo**)·(**25DBA**), (H-**theo**)$^{+}$·(**26DBA**)$^{-}$·(H_2O) and (**theo**)·(**34DBA**) were obtained using a *Bruker APEX2* diffractometer. The single crystals of (**theo**)·(**3HBA**), (**theo**)·(**4HBA**), (**theo**)·(**24DBA**), and (**theo**)·(**35DBA**) were mounted on a glass pin using epoxy glue, whereas the single

crystal of (**theo**)·(**2HBA**), (**theo**)·(**23DBA**), (**theo**)·(**25DBA**), (H-**theo**)$^{+}$·(**26DBA**)$^{-}$·(H_2O), and (**theo**)·(**34DBA**) were positioned on a *MiYeGen* mount with vacuum grease. Both X-ray diffraction data sets were collected using graphite-filtered MoK_α radiation (λ = 0.71069 Å) at temperatures indicated in Table 1, processed using *SAINT-Plus*[256], and corrected for Lorentz-polarization effects. The data sets were collected with omega scans with 0.5° steps. Structure solution and refinement were accomplished using *XSHELL*.[261] All non-hydrogen atoms were refined anisotropically. All hydrogen atoms bonded to carbon atoms were located in the Fourier-difference electron density map, fixed in geometrically constrained riding positions, and refined isotropically on the basis of corresponding C-atoms [U(H) = 1.2 U_{eq}(C)]. In the case of (**theo**)·(**26DBA**)·(H_2O)**,** the hydrogen atoms associated with O- and N-atoms were included in the located positions (*i.e.* coordinates refined) and treated isotropically. The hydrogen atoms belonging to N- and O-atoms were fixed in geometrically constrained riding positions, and refined isotropically in the cases of (**theo**)·(**4HBA**), (**theo**)·(**23DBA**) and (**theo**)·(**24DBA**). In the structures of (**theo**)·(**3HBA**), (**theo**)·(**25DBA**), (**theo**)·(**34DBA**) and (**theo**)·(**35DBA**), hydrogen atoms bonded to N- and O-atoms were refined either independently (*i.e.* coordinates and U_{iso} refined) or in a constrained fashion (*i.e.* coordinates constrained and U_{iso} refined). Crystallographic data of the investigated compounds are listed in Appendix A (Tables 22, 23 and 24). Geometry parameters of selected hydrogen-bonds are listed in Table 8.

4.3.3. Results

Nine solid phases involving **theo** and (di)hydroxybenzoic acids were identified using **SMPT**[104, 262, 263] as screening method, whereof seven are new. The formation of a solid phase involving both **theo** and the (di)hydroxybenzoic acids was revealed *via* PXRD. The two-component solid phases were further investigated *via* FT-IR spectroscopy and SXRD to determine whether cocrystal or salt formation has occurred.

Specifically, the **theo** solids were identified as either neutral molecular complexes (*i.e.* cocrystal) or salts based on the analyses of the carboxy-group geometries, the inspection of Fourier difference maps, and FT-IR data. The carbon-oxygen bond distances in seven solids were consistent with the formation of a cocrystal, while one solid exhibits a carboxylic-acid group with a geometry characteristic for a deprotonated carboxy-group (Table 7). The Fourier difference maps were consistent with the formation of the seven cocrystals and one salt. Specifically, difference maps of eight cocrystals revealed an acidic protons being positioned in close proximity to the O-atom of the carboxylic acid, at distances that correspond to a protonated carboxylic acid group. In one case, the acidic proton was found in close proximity of the imidazole moiety of **theo**. Moreover, the results of the spectroscopic studies are in agreement with the SXRD studies. In particular, it was found that the carbonyl stretching bands of the cocrystal samples appeared above 1600 cm^{-1} in the IR spectra being consistent with unionized carboxylic acids, while the salt exhibited a carbonyl stretching band below 1600 cm^{-1}.

Crystallographic information related to all solids are summarized in Tables 21, 22 and 23.

The structural features of the solid **theo** phases are described as follows, while all hydrogen bond parameters are provided in Table 8.

Table 7 Carbon-oxygen bond distances of the carboxylic groups of the acids

cocrystal	*d*(C–O) / (Å)	*d*(C=O) / (Å)	*Δd* / (Å) (*)
theo2	1.329(2)	1.208(2)	0.121(3)
	1.327(2)	1.211(2)	0.166(3)
theo3	1.351(4)	1.233(4)	0.118(6)
theo4	1.314(5)	1.226(6)	0.088(8)
theo5	1.325(1)	1.233(2)	0.092(2)
theo6	1.323(2)	1.225(2)	0.098(3)
theo7	1.280(3)	1.253(3)	0.027(4)
theo8	1.318(2)	1.235(2)	0.083(3)
theo9	1.319(2)	1.218(2)	0.101(3)

* ***Δd* = [(C–O) - (C=O)]**

4.3.3.1. Cocrystal (**theo**)·(**2HBA**)

PXRD studies of the solid recovered from the screening experiment involving **theo** and **2HBA** yielded revealed the formation of (**theo**)·(**2HBA**) 1:1 cocrystal (CSD reference code: KIGLES) (Fig 94d), a cocrystals initially reported by Madarasz *et al.* in 2002.,[264] and later on structurally characterized by Childs *et al.* in 2007.[265] Childs *et al.* showed that **theo** and **2HBA** crystallize in the monoclinic $P2_1/n$ space group with both one molecule of **theo** and **2HBA** in the asymmetric unit. It was found that the cocrystal components self-assemble to form 1D ribbons. Within the ribbons, **theo** and **2HBA** interact *via* O-H(carboxy)···N(imidazole) hydrogen bonds, while both **theo** and **2HBA** form dimers. Whereas **theo** molecules form dimers *via* a cyclic array of N-H(imidazole)···O(amide) hydrogen bonds, **2HBA** molecules were found to form dimers *via* a bifuracated hydrogen bonds. In the bifurcated hydrogen bond, the *ortho*-hydroxy group acts as bifurcated hydrogen donor that participates in the formation of both an inter- and intramolecular[257] O-H(hydroxy)···O(carboxy) hydrogen bond (Fig. 94a). The

theo:**2HBA** ribbons are forming "wavy" 2D sheets that are held together by C-H···O and van der Waals interactions. Within the sheets, the ribbons are inclined by φ=29.2º (Fig 94b). The 2D sheets are stacking in the solid state being held together by π(**theo**)···π(**2HBA**) interactions (Fig 94c).

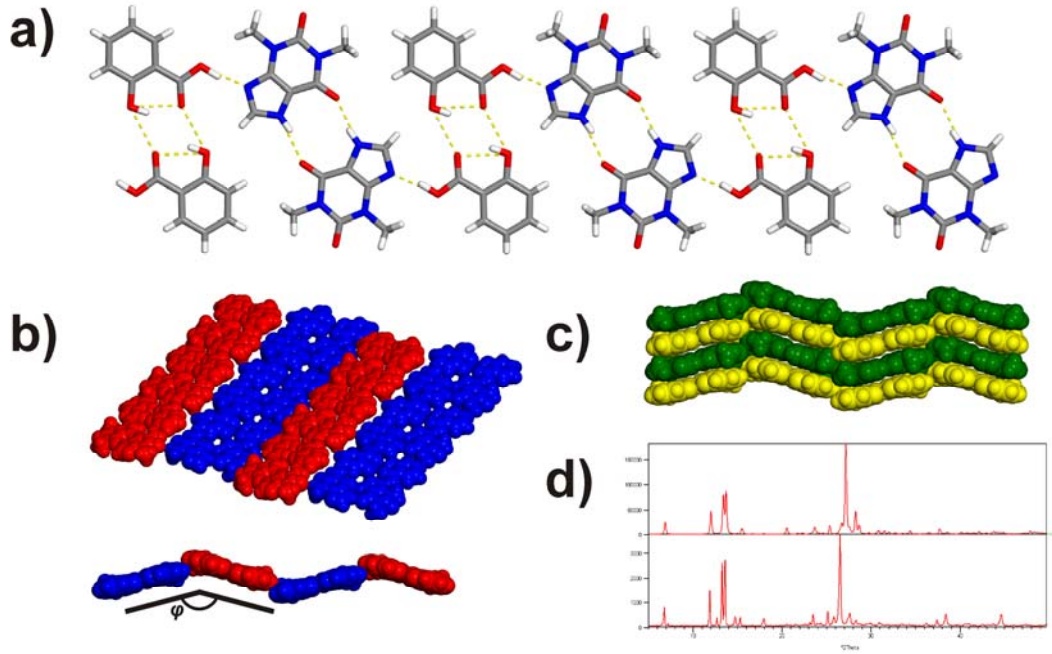

Figure 94 Perspective views: (a) a molecular ribbon based on **theo** and **2HBA** being held together by O-H(carboxy)···N(imidazole), N-H(imidazole)···O=C(amide) and bifuracated O-H(hydroxy)···O(carboxy)··· O-H(hydroxy) hydrogen bonds, (b) a 2D sheet composed of **theo**:**2HBA** ribbons, and (c) stacks of **theo**:**2HBA** sheets sustained by π(**theo**)···π(**2HBA**) interactions viewed along the (-2 0 1) and (0 1 0) crystallographic planes, d) PXRD of the **theo**/**2HBA** slurry sample compared to simulated PXRD of the **theo**:**2HBA** cocrystal.

4.3.3.2. Cocrystal (**theo**)·(**3HBA**)

Cocrystal (**theo**)·(**3HBA**) crystallizes in the triclinic space group $P\bar{1}$ with both two **theo** and **3HBA** molecules in the asymmetric unit. **Theo** and **3HBA** form a "wavy" 1D polymer constituted of centrosymmetric four-component **theo:3HBA** aggregates being

sustained *via* O-H(carboxy)···N(imidazole) and O-H(hydroxy)···O(urea) bonds. The aggregates are interlinked to form infinite "wavy" 1D structures through cyclic arrays of N-H(carboxy)···O=C(amide) hydrogen bonds (Fig 95a). The **theo**:**3HBA** aggregates within the "wavy" polymers are inclined by φ=39.5º (Fig. 95a, botton). The 1D polymers self-assemble to form 2D sheets being sustained by π(**theo**)···π(**3DBA**) and C-H···O interactions (Fig. 95b). The sheets stack in an offset manner to form a 3D structure being held together *via* π(**theo**)···π(**3HBA**) and C-H···O interactions (Fig. 95c).

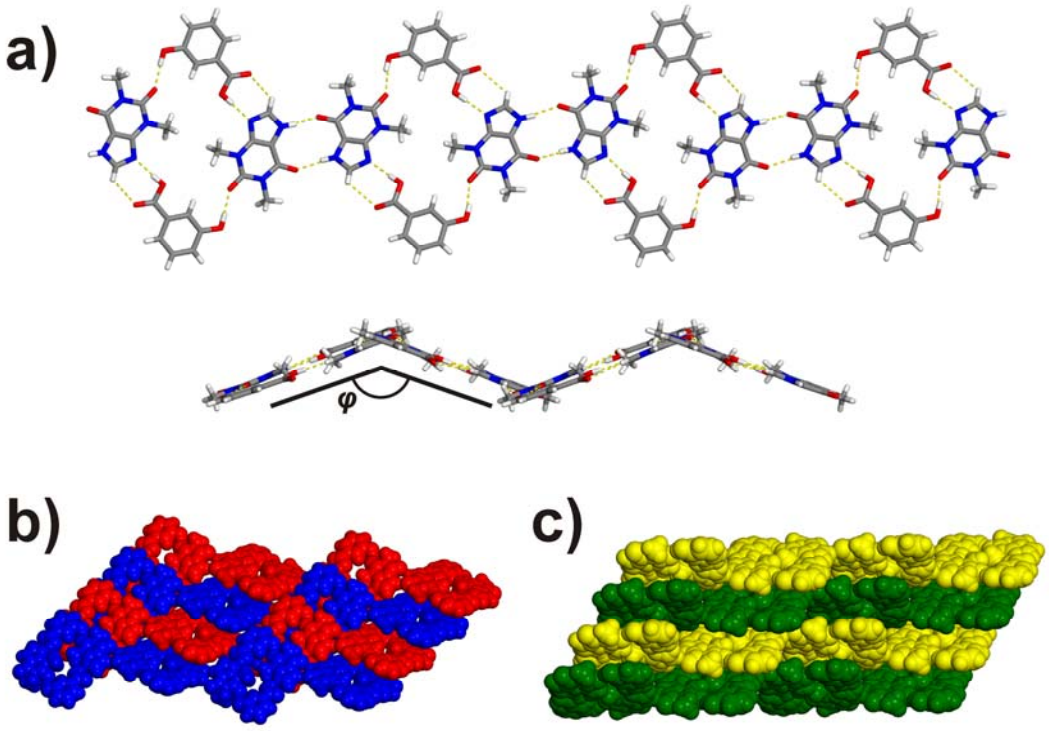

Figure 95 Perspective views: (a) four-component assemblies of **theo** and **3HBA** forming a "wavy" 1D polymer, (b) molecular sheet composed 1D polymers held together by π(**theo**)···π(**25DBA**) and C-H···O interactions (viewed along the crystallographic planes (100) and (001)), (c) 3D structure composed of the stacked 2D sheets held together by π(**theo**)···π(**25DBA**) interactions and C–H···O hydrogen bonds (viewed along the crystallographic planes (1-10) and (001)).

4.3.3.3. Cocrystal (**theo**)·(**4HBA**)

The crystal structure of (**theo**)·(**4HBA**) was also reported by Childs *et al.* in 2007 (CSD reference code: KIGLOC).[265] Cocrystal (**theo**)·(**4HBA**) crystallizes in a 1:1 ratio in the monoclinic space group $P2_1/c$ with both one molecule of **theo** and **4HBA** in the asymmetric unit. **Theo** and **4HBA** form "zig-zag" chains held together by cyclic arrays of N–H(imidazole)···O(carboxy) and O–H(carboxy)···O(amide) hydrogen bonds, and a O–H(hydroxy)···N(imidazole) hydrogen bond being supported by a C–H(urea)···O(hydroxy) hydrogen bonds (Fig. 96a). Within the "zig-zag" chain, the **theo**:**4HBA** pairs are inclined by φ=39.9º. The chains interact *via* π(**theo**)···π(**4DBA**) interactions to form stacks (Fig. 96b). Neighboring stack are interdigitated and held together by π(**theo**)···π(**4HBA**) forces and a set of C-H···O interactions (Fig 96c).

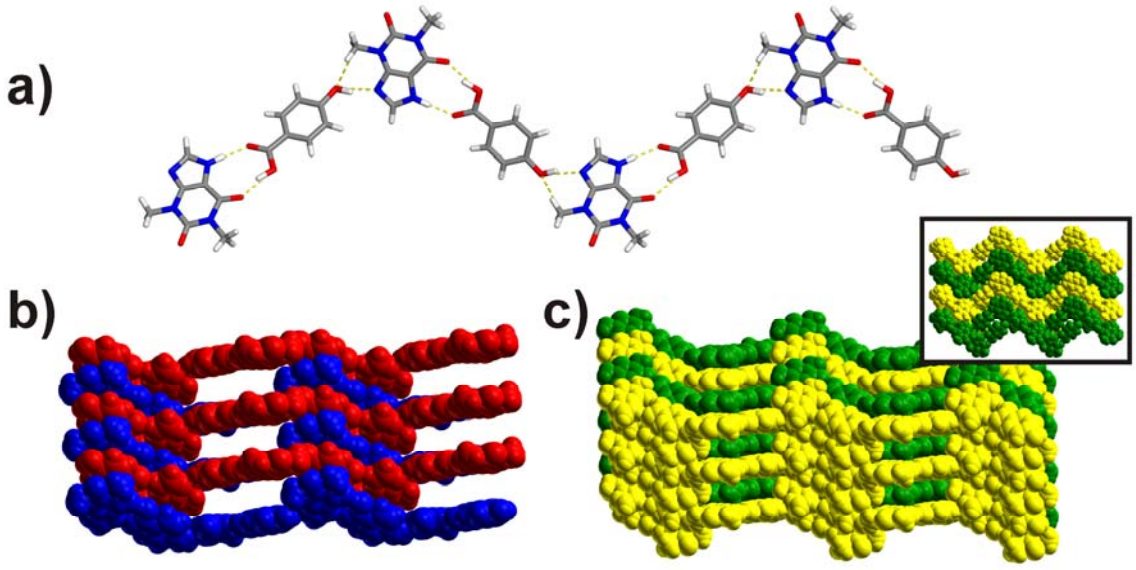

Figure 96 Perspective views: (a) hydrogen-bonded "zig-zag" chains involving **theo** and **4HBA**, (b) stacks of **theo**:**4HBA** chains viewed along the crystallographic planes (2 1 0) and (0 0 1), (c) intercalated stacks of **theo**:**4HBA** held together by face-to-face π-forces viewed along the crystallographic planes (2 1 0) and (0 0 1), and the crystallographic axis *a* (inset).

4.3.3.4. Cocrystal (**theo**)·(**4HBA**)

Theo and **23DBA** crystallize in the monoclinic space group $P2_1/c$ with both one molecule of **theo** and **23DBA** in the asymmetric unit. In the crystal structure, **theo** and **23DBA** were found to form a helical structure held together by cyclic arrays of N–H(imidazole)···O(carboxy) and O–H(carboxy)···O(amide) hydrogen bonds, O–H(hydroxy)···N(imidazole) intermolecular hydrogen bonds., and polar N(imidazole)···O(hydroxy) interactions (N···O distance: 3.05Å). The *ortho*-hydroxy group participates in an intramolecular O–H(hydroxy)···O(carboxy) hydrogen bond.[257]

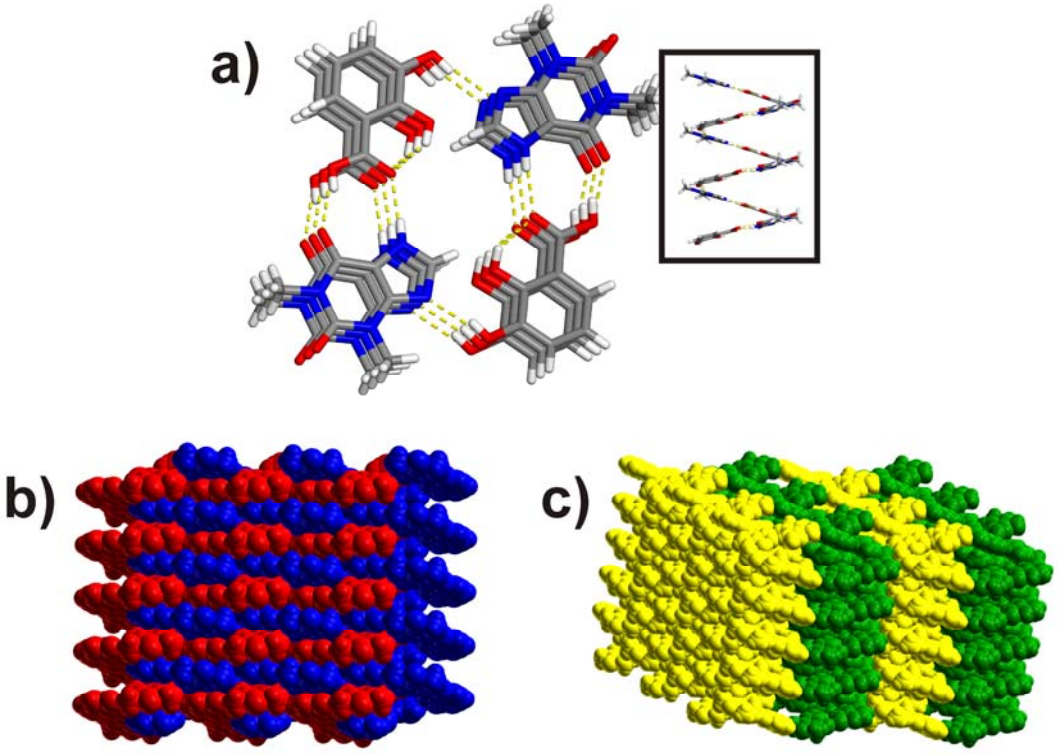

Figure 97 Perspective views: (a) helical **theo**:**23DBA** assemblies, (b) interdigitated helices sustained *via* π(**theo**)···π(**4HBA**) interactions viewed along the crystallographic *a* axis (the red and blue helices are of opposite handedness), c) 2D sheets of **theo**:**23DHBA** helices interlinked via C–H···N and C–H···O interactions viewed along the crystallographic planes (1 0 1) and (2 -1 1) (the green and yellow molecular aggregates represent neighboring.

The structure consists of helices of both hands being related by a center of inversion. The pitch of the helix is 6.8 Å, and it contains both two molecules of **theo** and **23DBA** per turn. The helix exhibits a diameter of approximately 16 Å (Fig. 97a). Helices of opposite hands are intercalated and held together *via* π(**theo**)···π(**23DBA**) forces to form a two-dimensional sheet that propagates along the crystallographic *c* axis (Fig. 97b). The 2D sheets further self-assemble into a 3D structure being held together by C–H···N and C–H···O interactions (Fig. 97c).

4.3.3.5. Cocrystal (**theo**)·(**24DBA**)

The cocrystal of (**theo**)·(**24DBA**) crystallizes in the monoclinic space group $P2_1/c$ with both one molecule of **theo** and **24DBA** in the asymmetric unit. The crystal structure reveals that **theo** and **24DBA** form 1D polymers held together by cyclic arrays of N–H(imidazole)···O(carboxy) and O–H(carboxy)···O(amide) intermolecular hydrogen bonds, O−H(hydroxy)···O(urea) intermolecular hydrogen bonds, as well as intramolecular O−H(hydroxy)···O(carboxy) hydrogen bonds.[257] The 1D polymers form bilayers that resemble 2D grids (Fig. 98a). Within each of the two layers, the 1D polymers are aligned in parallel being separated by approximately *d*=6 Å. The parallel 1D polymers are hydrogen-bonded to a set of parallel polymers form the second layer *via* O−H(hydroxy)···N(imidazole) hydrogen bonds (Fig. 98a). Within the bilayer, the two sets of parallel polymers are inclined by φ=70.9º (Fig. 98a.). The bilayers form a 3D structure wherein neighboring bilayers are intercalated interlinked through π(**theo**)···π(**24DBA**) and C−H···O interactions (Fig 98b,c).

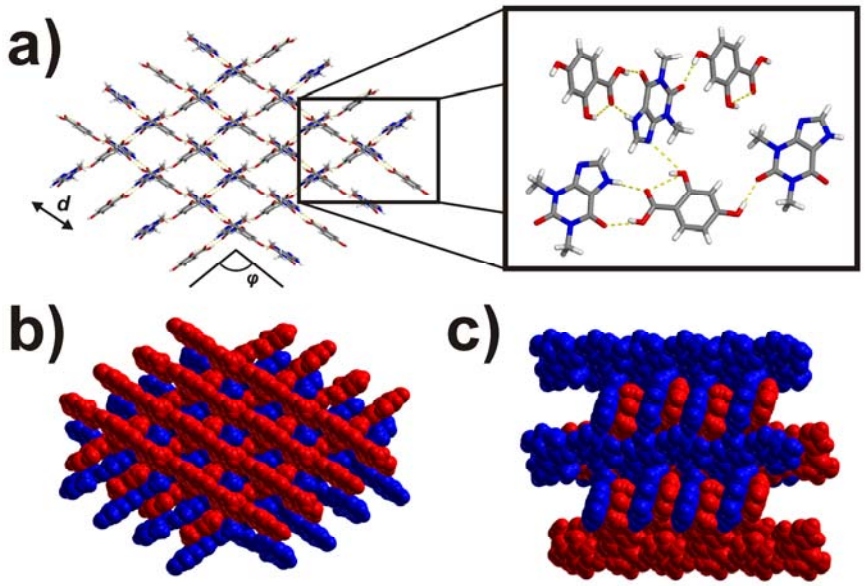

Figure 98 Perspective views of a molecular bilayer composed of hydrogen-bonded 1D **theo**:**24DBA** polymers viewed along the crystallographic *c* axis (the inset depicts a close-up view a structural fragment of the bilayer highlighting the hydrogen-bond patterns occurring within and among 1D polymers in the bilayer) (a), intercalated bilayer held together by $\pi\cdots\pi$ forces, viewed along the crystallographic *c* axis (b), and the crystallographic planes (1 1 0) and (0 0 1) (c).

4.3.3.6. Cocrystal (**theo**)·(**25DBA**)

Theo, and **25DBA** cocrystallize in the triclinic space group $P\bar{1}$. The asymmetric unit contains one molecule of each component. **Theo** and **25DBA** self-assemble to form molecular sheets being sustained by a set of intra- and intermolecular interactions. Specifically, each **theo** molecule interacts with two **25DBA** and one **theo** molecule, whereas each **25DBA** interacts with two **theo** and one **25DBA**s. **Theo** and **25DBA** are hydrogen-bonded by through O–H(carboxy)···N(imidazole) and O–H(hydroxy)···O(urea) interactions. The **theo** molecules form dimers *via* cyclic arrays of N–H(imidazole)···O(carboxy) and O–H(carboxy)···O(amide) hydrogen bonds, while the **25DBA** molecules dimerize *via* bifuracated hydrogen bonds, as seen in the case of the

(**theo**)·(**25DBA**) cocrystal: the *ortho*-hydroxy moiety of **25DBA** acts as bifurcated donor being involved in both an intra- and intermolecular O-H(hydroxy)···O(carboxy) hydrogen bonds (Fig. 99a). The 2D structures stack being offset along the (2 1 -1) crystallographic plane, and are held together by π(**theo**)···π(**25DBA**) forces (Fig. 99b).

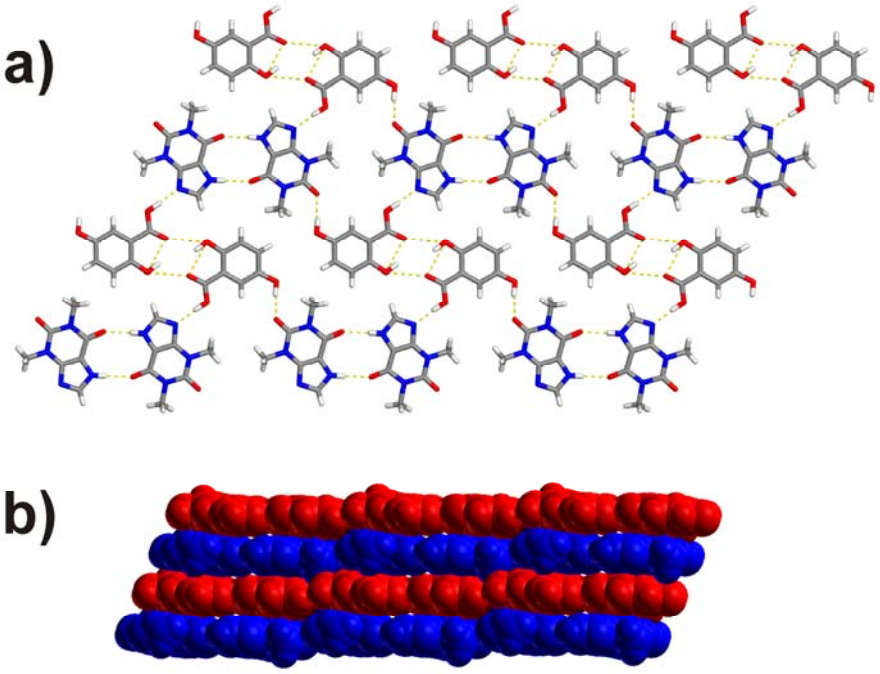

Figure 99 Perspective views: (a) 2D **theo**:**25DBA** network involving **theo** and **25DBA** sustained by hydrogen bonds, and (b) stacked **theo**:**24DBA** networks held together by $\pi\cdots\pi$ interactions (viewed along the crystallographic (2 1 0) and (0 0 1) planes).

4.3.3.7. (H-**theo**)$^+$·(**26DBA**)$^-$·(H_2O) salt

Theo, **26DBA** and water crystallize from acetonitrile in a 1:1:1 ratio in the monoclinic space group *P*21/*c* with a (H-**theo**)$^+$ cation, a (**26DBA**)$^-$ anion, and one water molecule in the asymmetric unit. (H-**theo**)$^+$ and (**26DBA**)$^-$ form a centrosymmentric four-component assembly wherein (H-**theo**)$^+$ and (**26DBA**)$^-$ interact *via* a N^+–

H(imidazole)···O$^-$(carboxy) hydrogen bond, while (**26DBA**)$^-$ anions interact with each other *via* bifurcated O-H(hydroxy)···O(carboxy) hydrogen bond (Fig. 100a). The four-component assemblies are interlinked through water molecules to form molecular ribbons held together by N-H(imidazole)···O(water) and O-H(water)···O(amide) hydrogen bonds (Fig. 100b, upper inset). The ribbons are stacked in an offset manner to form a layered 2D structure (Fig. 100b). The layers are held together by O-H(water)···O$^-$(carboxy) hydrogen bonds (Fig 100b, lower inset). The 2D structures further self-assemble in the solid state to form a 3D structure, and are sustained by a set of C-H···O interactions (Fig. 100c).

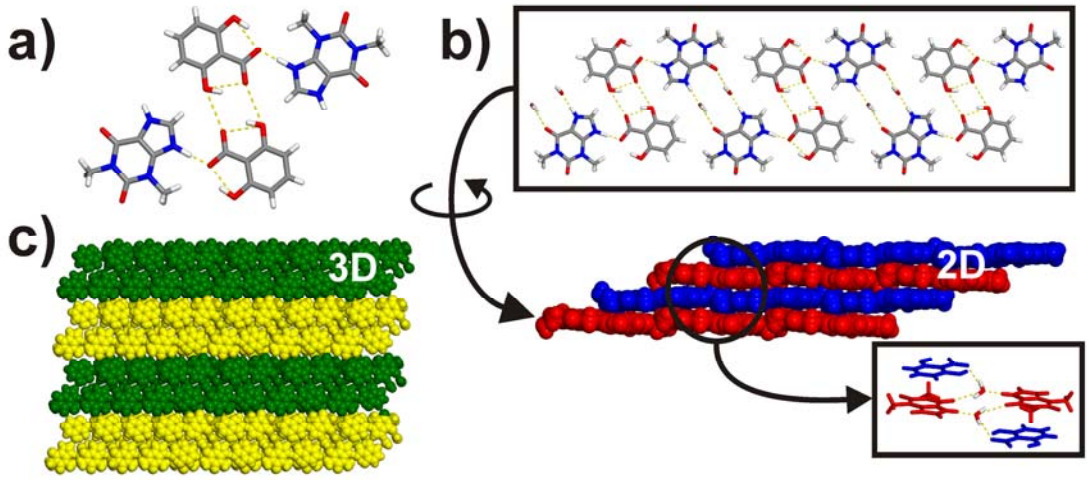

Figure 100 Perspective views: (a) four-component (H-**theo**)$^+$:(**26DBA**)$^-$ assemblies**,** (b) the 2D structure of **(**H-**theo)**$^+$:**(26DBA)**$^-$:(H_2O) assemblies viewed along the crystallographic *a* axis, and (d) the 3D structure of the (H-**theo**)$^+$·(**26DBA**)$^-$ ·(H_2O) salt viewed along the crystallographic *b* axis.

4.3.3.8 Cocrystal (**theo**)·(**34DBA**)

Theo and **34DBA** self-assemble to form a 1:1 solid that crystallizes in the triclinic space group $P\bar{1}$ with both one molecule of **theo** and **34DBA** in the asymmetric unit. The cocrystal components form a planar infinite molecular sheet. Within the sheet, **theo** and

34DBA are hydrogen bonded *via* O–H(hydroxy)···N(imidazole) and O–H(hydroxy)···O(urea) interactions. At the same time, both **theo** and **34DBA** form dimers within the molecular sheet (Fig. 101a). Specifically, **theo** dimer are sustained by N–H(imidazole)···O(amide) hydrogen bonds, while the **34DBA** dimers are being held together *via* O–H(hydroxy)···O(carboxy) hydrogen bonds (Fig. 101a). The planar sheets are stacked in an offset and "head-to-tail" manner being sustained by π(**theo**)···π(**34DBA**) forces, as well as weak C–H···O, and C–H···π interactions (Fig. 101c).

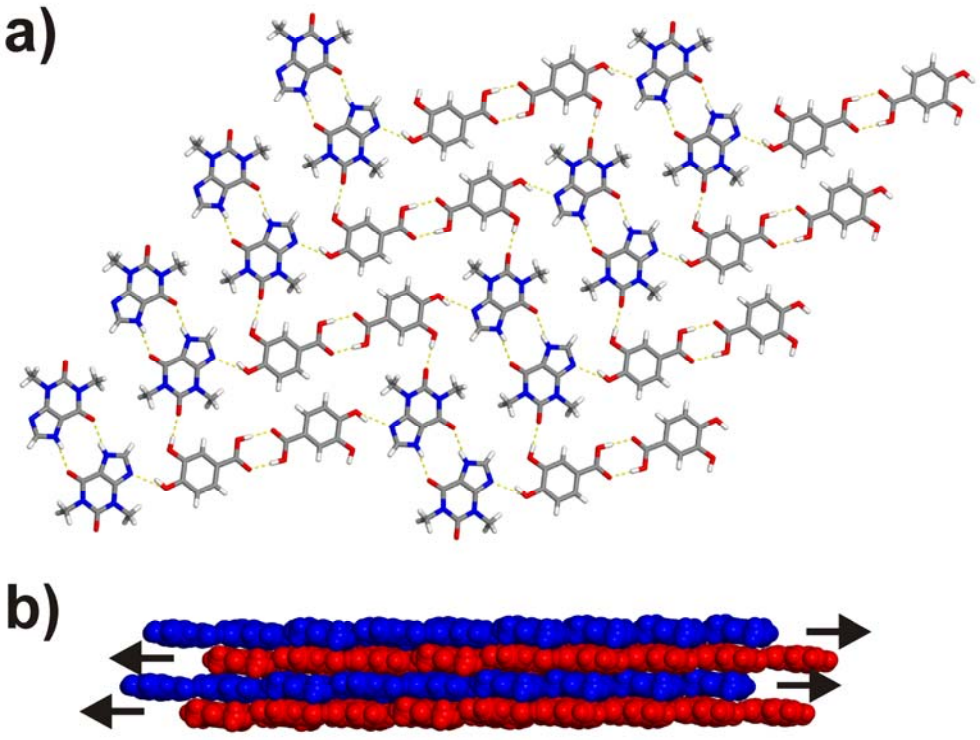

Figure 101 Perspective views: (a) molecular sheets composed of **theo** and **34DBA** molecules viewed along the crystallographic planes (1 1 0) and (0 0 1), and (b) sheets stacked in a "head-to-tail" fashion viewed along the crystallographic planes (0 1 -1) and (-2 2 1).

4.3.3.9. Cocrystal (**theo**)·(**35DBA**)

The 1:1 cocrystal of **theo** and **35DBA** crystallizes in the triclinic space group $P\bar{1}$ with one molecule of each cocrystal component in the asymmetric unit. The components form an infinite planar 2D structure comprised of both **theo** and **35DBA** form dimers (Fig. 102a) that are arranged within to planar structure to resemble the tilling of a chess plate (Fig. 102a, inset).

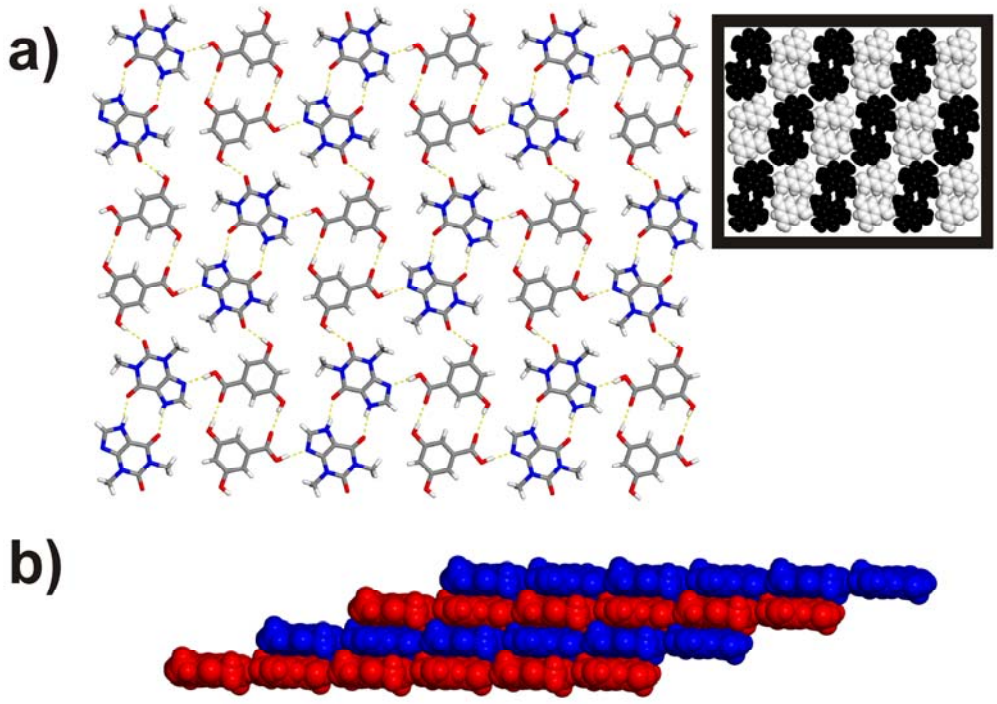

Figure 102 Perspective views: (a) "chess plates" composed of **theo** and **35DBA** dimers viewed along the crystallographic planes (116) and (1-20) (inset: space-fill view of the **theo**:**35DBA** resembling the tilling of a chess plate), (b) stacked "chess plates" being sustained by π(**theo**)···π(**35DBA**) and C-H···O forces viewed along the crystallographic planes (2 0 -1) and (0 1 0).

Table 8 Selected hydrogen-bond parameters of in **theo** cocrystals (with estimated standard deviations except for fixed and riding hydrogen atoms).

Compound	*D*–H···*A*	*D*–H	*d*(H···*A*) / Å	*d*(*D*···*A*) / Å	*θ*(*D*–H···*A*)/º
theo2	N1-H1N···O3	0.86	1.92	2.764(2)	168.8
	N5-H5N···O1	0.86	2.00	2.831(2)	163.0
	O6-H6O···N4	0.89(4)	1.85(4)	2.733(2)	177(3)
	O7-H7O···O2^{i}	0.91(3)	1.82(3)	2.713(2)	168(3)
	O9-H9O···N8	0.88(3)	1.86(3)	2.744(2)	177(3)
	O10-H10O···O4^{ii}	0.93(3)	1.79(3)	2.702(2)	170(3)
theo3	N4-H4···O4	0.86	1.91	2.751(4)	166.6
	O3-H3···O2	0.82	1.87	2.682(3)	169.9
	O5-H5···N1^{iii}	0.82	1.94	2.703(4)	153.8
theo4	N1-H1N···O3	0.86	1.92	2.773(5)	174.3
	O4-H4O···O1	0.82	1.79	2.587(5)	162.0
	O5-H5O···O3	0.82	1.85	2.563(4)	145.1
	O6-H6O···N4^{iv}	0.82	2.14	2.871(6)	147.8
theo5	N1-H1N···O4	0.86	1.96	2.808(2)	171.1
	O3-H3O···O1	0.82	1.82	2.608(1)	160.5
	O5-H5O···O4	0.82	1.96	2.669(1)	144.3
	O5-H5O···N4^{v}	0.82	2.56	3.058(2)	120.3
	O6-H6O···O2^{vi}	0.82	1.89	2.708(1)	177.3
theo6	N1-H1A···O1^{vii}	0.86	1.95	2.806(2)	174.7
	O4-H4O···N4	0.95(3)	1.71(3)	2.662(2)	177(2)
	O5-H5O···O3	0.89(3)	1.88(3)	2.664(2)	145(2)
	O5-H5O···O3^{viii}	0.89(3)	2.29(2)	2.847(2)	121(2)
	O6-H6O···O2^{ix}	0.94(2)	1.81(2)	2.752(2)	174(2)
theo7	N1-H1N···O7	0.94(3)	1.72(3)	2.654(2)	176(3)
	N4-H4N···O4	1.12(3)	1.48(3)	2.598(2)	177(3)
	O5-H5O···O4	0.97(3)	1.66(3)	2.549(2)	151(3)
	O6-H6O···O3	0.93(3)	1.70(3)	2.545(2)	149(3)
	O6-H6O···O3^{x}	0.93(3)	2.61(3)	2.968(2)	103(3)
	O7-H1W···O3^{viii}	0.89(1)	1.93(1)	2.788(2)	163(3)
	O7-H2W···O1^{iv}	0.89(1)	1.99(2)	2.823(2)	155(3)
theo8	N1-H1N···O1^{i}	0.86	1.92	2.757(1)	164.3
	O4-H4O···O3^{xi}	0.91(3)	1.72(3)	2.632(1)	178(2)
	O5-H5O···O2^{xi}	0.90(2)	1.80(2)	2.692(1)	177(2)
	O6-H6O···N4	0.87(2)	1.94(2)	2.744(2)	153(2)
theo9	N1-H1N···O1^{xiii}	0.86	1.91	2.730(2)	159.1
	O4-H4O···N4	0.90(3)	1.82(3)	2.710(2)	169(3)

O5-H5O···O3^{xiv}	0.82	1.99	2.794(2)	165.0
O6-H6O···O2	0.82	1.92	2.732(2)	169.1

Symmetry codes : (*i*) -*x*,-*y*+1,-*z*; (*ii*) -x+3,-y+2,-z+1; (*iii*) x,-y+3/2,z-1/2; (*iv*) -x+1,y+1/2,-z+1/2; (*iv*) -x+1,y+1/2,-z+3/2 ; (*v*) x+1,y+1,z ; (*vi*) -x,-y+2,-z ; (*vii*) -x+1,-y,-z ; (*viii*) -x+1,-y+1,-z+1 ; (*ix*) -x,-y,-z+2; (*x*) 1-*x*, -*y*, 1-*z* ; (*xi*) x-1,y-1,z ; (*xii*) -x+2,-y,-z+1 ; (*xiii*) -x+1,-y+2,-z+1 ; (*xiv*) -x+1,-y+1,-z.

Within the 2D (**theo**)·(**35DBA**) structure, each **theo** dimer is surrounded by four **35DBA** dimers and *vice versa*. The **theo** dimers are held together by cyclic arrays of N–H(imidazole)···O(carboxy) and O–H(carboxy)···O(amide) hydrogen bonds, while the **35DBA** molecules form dimers through O–H(hydroxy)···O(carboxy) hydrogen bonds (Fig. 102a). The **theo** and **35DBA** dimers are connected through O–H(hydroxy)···N(imidazole) and O–H(hydroxy)···O(urea) hydrogen bonds. The "chess plates" are stacked in an offset manner being held together by both π(**theo**)···π(**35DBA**) and weak C–H···O interactions (Fig. 102b).

4.3.4. Discussion

A CSD survey revealed that **theo** and carboxylic acids predominantly self-assembly through binding mode I (see section 4.3.1). Specifically, out of 17 CSD entries involving **theo** and a carboxylic acid, 11 structures exhibit a **theo**:acid interaction *via* binding mode I (*i.e.* CIZTAH, CODCOO, CSATEO, KIGLES, KIGLIW, NEXWOD, NEYCIE, XEJWUF, XEJXAM, XEJXEQ, XEJXIU), whereas only three **theo**:acid structures exhibited binding mode II (*i.e.* DEYREF, KIGLAO, KIGLOC). This observation is in fair agreement with the reported persistency of the O-H(carboxy)···N(pyridine) heterosynthon in cocrystals based on of **caf** and (di)hydroxybenzoic acids carboxylic acids.[240] The presented study showed that five out

of nine **theo**:(di)hydroxybenzoic acid cocrystals, exhibit binding mode I (*i.e.* cocrystals involving **2HBA**, **3HBA**, **25DBA**, **26DBA**, and **35DBA**) whereas only three cocrystals exhibited binding mode II (*i.e.* cocrystals based on **4HBA**, **23DBA** and **24DBA**). The components in (**theo**)·(**34DBA**), however, do not exhibit either of the two binding modes. Specifically, it was found that the (**theo**)·(**34DBA**) cocrystal exhibits both **theo** and **34DBA** dimers being sustained *via* the $R_2^2(10)$ N-H(imidazole)···O(amide) heterosynthon (Fig. 93a), and the $R_2^2(8)$ O-H(carboxy)···O(carboxy) homosynthon (Fig. 2), respectively. The **theo** and **34DBA** dimers are linked through O-H(hydroxy)···N(imidazole) and O-H(hydroxy)···O(urea) hydrogen bonds. Such formation of a carboxylic acid homosynthons in the presence of an N(aromatic) functional groups is rarely observed in the crystalline solid state. (Fig. 71).[250] However, a recent computational study has indicated that carboxylic acid homodimers can form in the presence of an N(aromatic) moieties to achieve a global minimum in the crystal energy landscape.[259] Notably, the formation of carboxylic-acid homodimers was not experimentally observed in the **caf** cocrystal series involving (di)hydroxybenzoic acids.[240]

The **theo** cocrystal series exhibits another surprising feature: our studies demonstrated the formation of O-H(hydroxy)···N(imidazole) hydrogen bonds (Fig. 1g) being formed between the phenolic groups of **4HBA**, **23DBA, 24DBA**, and **34DBA**, and the imidazole moiety of **theo** (Figure 96a, 97a, 98a, 101a). Conspicuously, O-H(hydroxy)···N(imidazole) heterosynthons were observed in the previously reported **caf** cocrystal series (see section 4.2). The lack of O-H(hydroxy)···N(imidazole) synthons in **caf** cocrystals can be attributed to the deficiency of a second structural moiety that is able to interact with a "strong complementary" hydrogen-bond donor (*i.e.* carboxylic group). The existence of such moiety would allow an interaction between the imidazole(**caf**) unit and a "less complementary" hydrogen-bond donor (*i.e.* hydroxy group) (Fig 103).

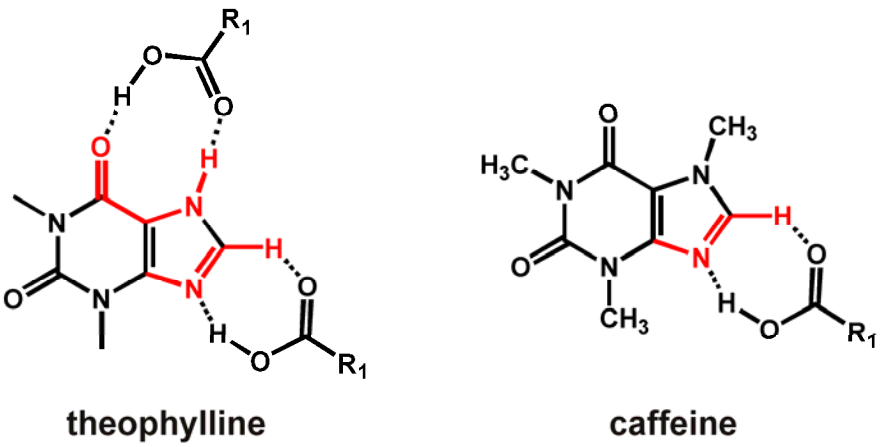

Figure 103 Chemical structures of **theo** and **caf** with highlighted structural moieties (in red) that are most likely to interact with a carboxylic acid.

Overall, the poor persistence of the imidazole:carboxylic acid heterosynthon in **theo**, as compared to analogous **caf** cocrystals, attests to the difficulty of predicting hydrogen-bond patterns in cocrystals held together by multiple homo- and heterosynthos.

Further observed discrepancies between the **theo** and **caf** cocrystal series are associated with the involvement of the C=O(amide) and C=O(urea) moieties in hydrogen bonding. In particular, the **theo** cocrystals showed that the C=O(amide) moiety participates in hydrogen bonding with the in eight instances, whereas the C=O(urea) unit was found to be involved in hydrogen bonding in only five cocrystals (Table 9). The **caf** cocrystal series, on the other hand, revealed an opposite trend. Specifically, the C=O(urea) moiety was found to be more frequently involved in interactions with a CCF than C=O(amide) group: four structurally characterized **caf** cocrystals exhibit the O-H(hydroxy)···O(urea) heterosynthon, two solids reveal the presence of an OH(hydroxy)···O(amide) heterosynthon, and one cocrystal involves both the O-H(hydroxy)···O(urea) and O-H(hydroxy)···O(amide) heterosynthon. The higher occurrence of the O-H(hydroxy)···O(amide) synthon in the **theo** cocrystal series is not surprising at all considering that the C=O(amide) and the N-H(imidazole) moieties define

a structural fragment able to participate in the formation of a robust heterosynthons with either a carboxylic acids or the identical structural fragment from another **theo** molecule. The C=O(urea) unit, on the other hand, stands alone being sterically hindered by two CH_3 groups and is, therefore, less amenable for synthon formation with carboxy(**CCF**), hydroxy(**CCF**) and N-H(**theo**) moieties. The observed deviance in occurrences of the O-H(hydroxy)···O(urea) and O-H(hydroxy)···O(amide) heterosynthons further demonstrates the irregularity of hydrogen patterns in cocrystals involving structurally similar APIs. The results, therefore, further establish the need for systematic studies of synthon hierarchies in molecular cocrystals using crystallographic and computational methods.

Table 9 Overview of structural features in the **theo** cocrystals.

solid	**theo:CCF ratio**	**structure of assembly**	**hydrogen-bond acceptor group of caf**			
			imidazole	urea	amide	total
theo1	1:1	1D infinite	√		√	2
theo2	1:1	1D infinite	√	√	√	3
theo3	1:1	1D infinite	√		√	2
theo4	1:1	1D infinite	√		√	2
theo5	1:1	2D infinite	√	√	√	3
theo6	1:1	2D infinite	√	√	√	3
theo7	2:2	discrete[a]	√		√[b]	2
theo8	1:1	2D infinite	√	√	√	3
theo9	1:1	2D infinite	√	√	√	3

[a] 1D infinite based on included H_2O; [b] hydrogen-bond acceptor interacts with H_2O.

All **theo** cocrystals were found to be mainly based on 1:1 **theo**-to-carboxylic acid ratios and infinite hydrogen-bond patterns. Cocrystals based on **2HBA**, **3HBA**, **4HBA** and **23DBA** form infinite 1D structures, whereas **24DBA**, **25DBA**, **34DBA** and **35DBA** form infinite 2D structures. The preferred formation of infinite structures, as compared to the **caf** cocrystals, is attributed to the presence of larger number hydrogen-bond donors in

theo. The additional donor is assumed to enable and to facilitate the formation of extended hydrogen-bond patterns. Notably, a discrete **theo**-based assembly was only identified in the case of **26DBA**. Specifically, it was found that **theo** and **26DBA** form a discrete assemblies in a 2:2 ratio. Within the assemblies, the carboxylic-acid protons undergo proton transfers to the imidazole units, thus, forming a salt (Fig. 100). The proton transfer is not unexpected having in mind that **theo** and **26DBA** exhibit a negative ΔpK_a value ($\Delta pK_a \sim -0.34$; pK_a(**theo**, base) = 1.64 ± 0.7, pK_a(**26DBA**, acid) = 1.30 ± 0.1). It is generally accepted that two components exhibiting a ΔpK_a value [$\Delta pK_a = pK_a$(conjugated acid of the base) - pK_a(acid)] greater than 3 will undergo a proton transfer to form a salt, whereas a $\Delta pK_a<0$ suggests the formation of a neutral species (*i.e.* cocrystal) (see section 4.5.) Values of ΔpK_a that fall in the range of 0-3 do not allow accurate predictions of a proton transfer and, thus, precluding the prediction of salt *vs.* cocrystal formation.

All **theo** cocrystals were found to be anhydrous, whereas the **26DBA** salt crystallized as monohydrate. In comparison, the analogous **caf** cocrystals series exhibits three cocrystal hydrates. Having in mind that water molecules commonly incorporate themselves into crystal structures of organic molecules to establish a balance of hydrogen-donors and hydrogen acceptors, we attribute the exclusive formation of anhydrous **theo** cocrystals to an equal (or very similar) number of donors and acceptors in both **theo** and **CCF** (hydrogen-bond donor:acceptor (D/H) ratios: D/H=3:3 for hydroxybenzoic acid **CCF**s, D/H=4:3 for dihydroxybenzoic acid **CCF**s).[266] The formation of a hydrate in the case of the (H-**theo**)$^{+}\cdot$(**26DBA**)$^{-}\cdot$(H_2O) salt was ascribed to steric effects, rather than a mismatch in the number of hydrogen-bond donating and accepting functional groups. In particular, water molecules position themselves between two **theo** molecules in the 1D ribbon (Fig. 100b) to minimize repulsive contacts between benzene(**26DBA**) and CH_3(amide,**theo**) moieties that would emerge upon formation of **theo** dimers the *via* $R_2^2(8)$ N-H(imidazole)$\cdots$O(amide) heterosynthons (Fig. 93c).

The *ortho*-hydroxy group of **2HBA**, **24DBA**, **25DBA** and **26DBA** were found to act as bifurcated hydrogen-bond donors in the **theo** solids. Specifically, each *ortho*-hydroxy group participates in both an intramolecular O-H(hydroxy)···O(carboxy) hydrogen bond and an intermolecular O-H(hydroxy)···O(carboxy) or O-H(hydroxy)···N(imidazole) hydrogen bond. Similarly, the *ortho*-hydroxy group of **23DBA** participates in an intramolecular O-H(hydroxy)···O(carboxy) hydrogen bond and an polar intermolecular N(imidazole)···O(hydroxy) interaction. Oppositely, the *ortho*-hydroxy groups of the studied **CCF**s were not found to form intermolecular hydrogen bonds in cocrystals involving **caf**. Origins of the dissimilar behavior of the *ortho*-hydroxy groups in the **theo** and **caf** solids are, at this point, not understood and are currently under investigation.

4.3.5. Conclusion

We have reported the formation of nine **theo** solids based on structural isomers of (di)hydroxybenzoic acids, using **SMPT** as screening method. Structural analyses revealed the formation of crystalline architectures based on intermolecular homo- and heterosynthons, as well as intramolecular heterosynthons. The most prevalent intermolecular interactions were found to be: the O−H(carboxy)···N(imidazole) and O−H(hydroxy)···O(urea) heterosynthons, and the homosynthon comprised of a cyclic array of N–H(imidazole)···O(amide) hydrogen bonds (all synthons occur in 5 out of 9 theo solids). The intermolecular O−H(hydroxy)···N(imidazole) and O−H(hydroxy)···O(carboxy) heterosynthons were found in 4 out of 9 solids, whereas the heterosynton comprised of a cyclic array of N–H(imidazole)···O(carboxy) and O–H(carboxy)···O(amide) hydrogen bonds occurs 3 times. The intermolecular O−H(carboxy)···O(carboxy) homosynthon formed in only one solid. The established synthon hierarchy in **theo** cocrystals is depicted in Fig. 104. The presented study

demonstrates the difficulty to predict outcomes of the self-assembly processes involving two molecules whereby both consist of multiple hydrogen-bonding functional groups. We have also shown that structurally similar PAs (*i.e.* **theo** and **caf**) exhibit distinct supramolecular behavior. In addition, the presented study revealed the unexpected formation of a salt at a negative Δp*K*a value. Altogether, the reported findings impose the need for systematic structural studies of cocrystal based on multiple synthons to establish synthons hierarchies in complex supramolecular systems. The outcomes of these studies are expected to gain further insights into self-assembly processes wherein multiple hydrogen-bonding groups compete for synthon formation.

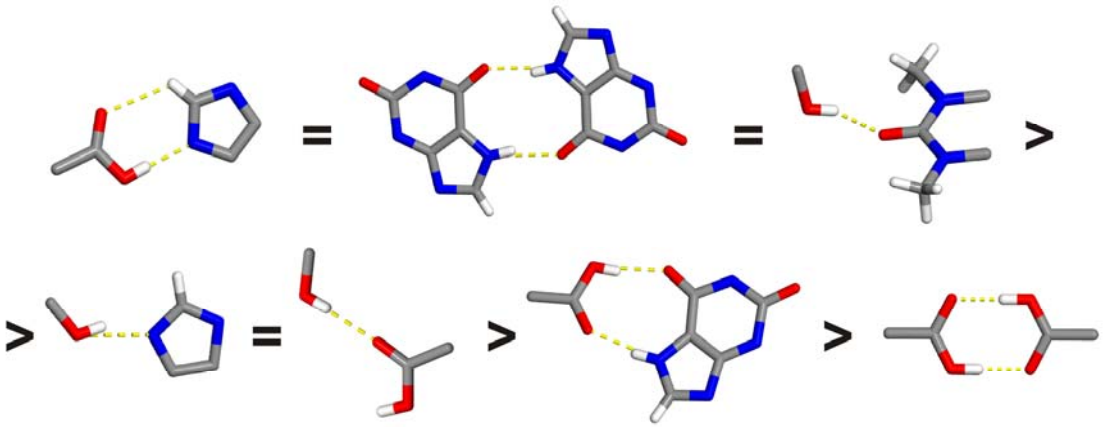

Figure 104 Established synthon hierarchy in **theo** solids based on hydroxybenzoic acids.

4.4. Cocrystals of theobromine and (di)hydroxybenzoic acids: Structural characterization and synthon hierarchies

4.4.1. Introduction

Theobromine (**theb**), a structural isomer of **theo**, naturally occurs in various plant species, such as *theobroma cacao*, *cola acuminta*, and *guarana* (Fig 105). [267] It was in the past used to treat edema, arteriosclerosis, angina pectoris and hypertension.[268] **Theb** is nowadays used as myocardial stimulant, peripheral vasodilator and diuretic. Notably, the alkaloid was just recently discovered to facilitate cancer prevention.[269] In the context of cocrystals and crystal engineering, **theb** has barely been explored. The poor presence of reported **theb** cocrystals in the literature might be attributed to the **theb**'s low solubility in water and common organic solvents, thus complicating the growth of cocrystal single crystals – a form of cocrystals conventionally utilized to retrieve structural data.[270] However, the opportunity of determining crystal structures of (multi-component) organic materials from powder diffraction data was just recently shown to enable structural characterization of cocrystals composed of PAs exhibiting low solubilities.[270]

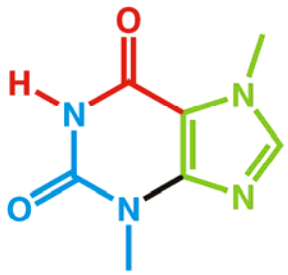

Figure 105 Theobromine and its substructures: imidazole (green), urea (blue) and amide (red) hydrogen-bonding sites.

Theb exhibits three hydrogen-bond acceptor and one hydrogen-bond donating sites: one aromatic N(imidazole) atom acceptor site, both one O(urea) and O(amide)

acceptor sites, and one N-H(amide) donor site (Fig. 106). Each of the four structural moieties is capable of participating in hydrogen-bonding, as evidenced by a CSD search. Although **theb** and **theo** are structurally very similar (*i.e.* they are structural isomers), their supramolecular landscapes exhibit significant differences, as shown in Fig 106.

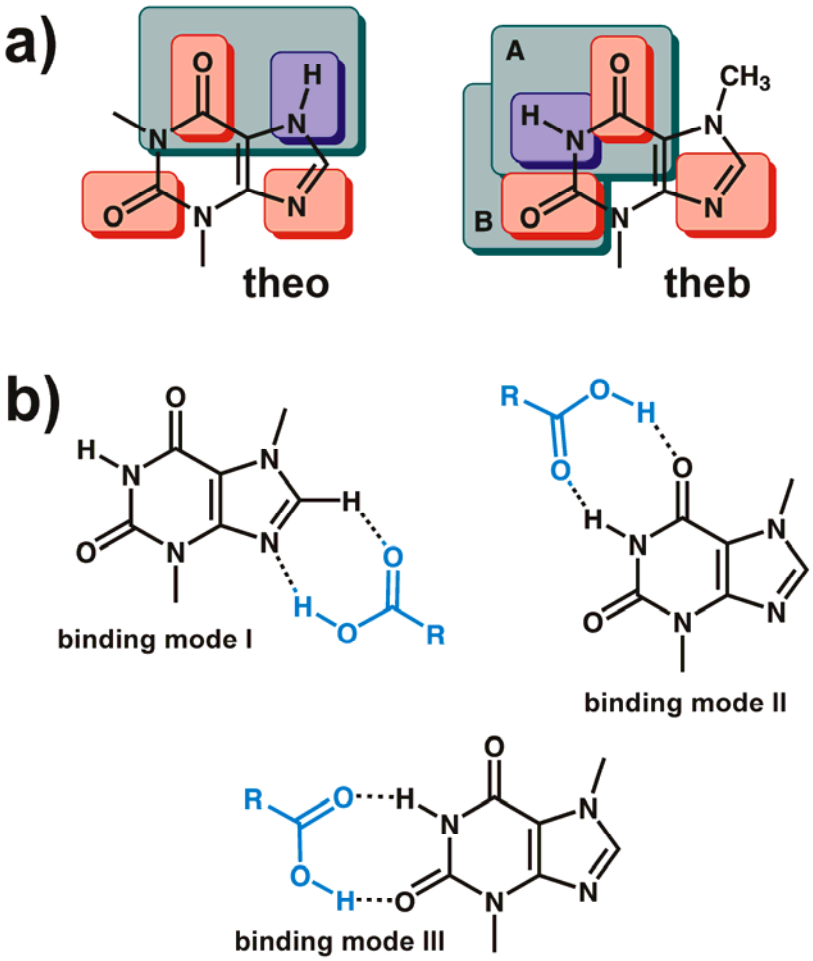

Figure 106 Supramolecular landscapes of **theo** and **theb** (red: hydrogen-bond acceptor, blue: hydrogen-bond donor, green: structural moiety compatible to molecular fragments that act both as donors and acceptors); b) three probable binding modes of **theb** and a carboxylic acid.

Particularly, the N-H(amide) group is positioned in between two carbonyl groups. Such arrangement provides **theb** with three structural fragments that are likely to undergo synthon formation with the carboxylic group of a CCF. In comparison to **theb**, **theo** displays only two moieties of such kind. As shown in Fig. 106, **theb** exhibits the capacity to interact with a carboxy group through the imidazole moiety *via* the O-H(carboxy)···N(imidazole) heterosynthons (*i.e.* binding mode I), or through the amide moieties "A" and "B" *via* cyclic arrays of N–H(amide)···O(carboxy) and O–H(carboxy)···O(amide) hydrogen bonds (*i.e.* binding mode II and III) (Fig 106). Both the imidazole unit and the amide moieties "A" and "B" are expected to form strong interactions with a carboxy group. However, the literature does not report any kind of guidelines that would allow to predict the formation of a **theb**:carboxy interaction *via* binding modes I-III. Furthermore, the scarce structural information on **theb** cocrystals in the CSD also precludes the establishment of synthon hierarchies.

The CSD survey revealed a total of three structures corresponding to neutral **theb**-based molecular complexes (*i.e.* solvates and cocrystals; CCDC reference codes: CSATBR, HIJYAB, HIJYEF). All three structures are based on carboxylic acids wherein the carboxy group interacts with **theb** through one of the binding modes I, II or III (Fig 107). Notably, the inability to predict **theb**:carboxy interactions also affects the predictability of O-H(hydroxy)···**theb** interactions in cocrystals of **theb** and hydroxybenzoic acids.

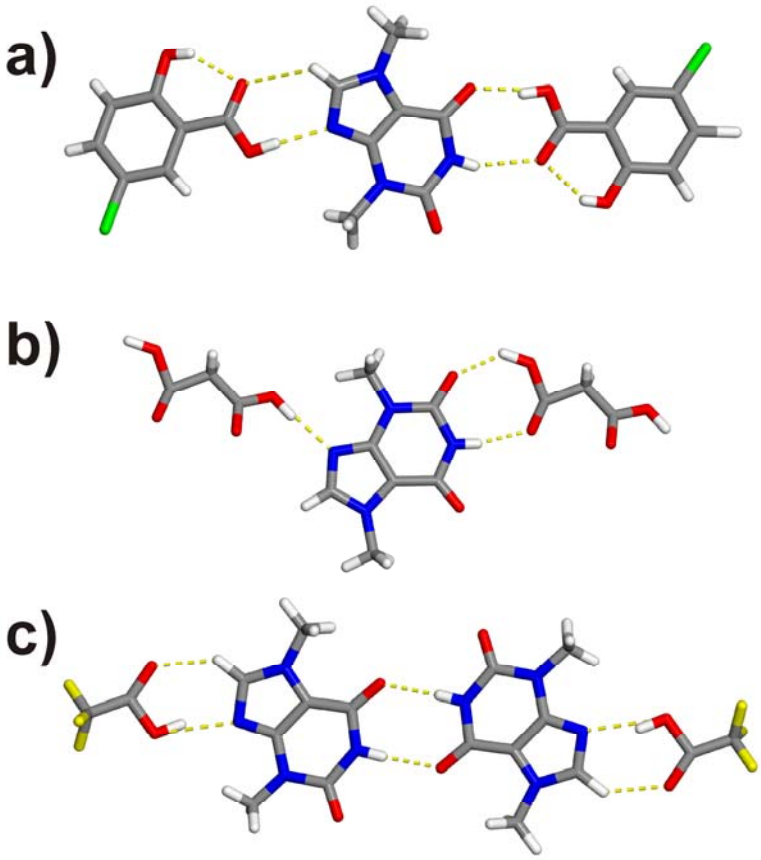

Figure 107 Crystal structures of: a) CSATBR exhibiting binding mode I and II, b) HIJYEF displaying binding mode I and III, and c) HIJYAB exhibiting binding mode I and II.

In addition to the CSD survey, we searched the literature on very recent reports of **theb** cocrystals. The search revealed a study of structure-stability relationships in cocrystal hydrates that reports two **theb** cocrystals, namely (**theb**)·(gallic acid)·2(H_2O) and (**theb**)·(quercitin)·2(H_2O).[271] In contrast to the CSD structures, (**theb**)·(gallic acid)·2(H_2O) was unexpectedly shown to exhibit binding mode III in the absence of binding mode I (Fig. 108). The structure of (**theb**)·(quercetin)·2(H_2O), on the other hand, shows the presence of O-H(hydroxy)···O(amide) and O-H(water)···N(imidazole) synthons in the absence of O-H(hydroxy)···N(imidazole) synthon. Quercetin displays five hydroxy groups able to interact with **theb**. The incorporation of water molecules into

the (**theb**)·(quercetin)·2(H_2O) structure is, therefore, attributed to the tendency of **theb** and gallic acid to self-assemble in low-energy crystal lattices,[259] rather than the maintenance of a hydrogen-bond donor/acceptor balance.[266] Altogether, the surprising synthon formations in the crystal structures of (**theb**)·(gallic acid)·2(H_2O) and (**theb**)·(quercitin)·2(H_2O) provide additional motivation to determine synthon hierarchies in this class of compounds, as well as to elucidate parameters that contribute to such hierarchies.

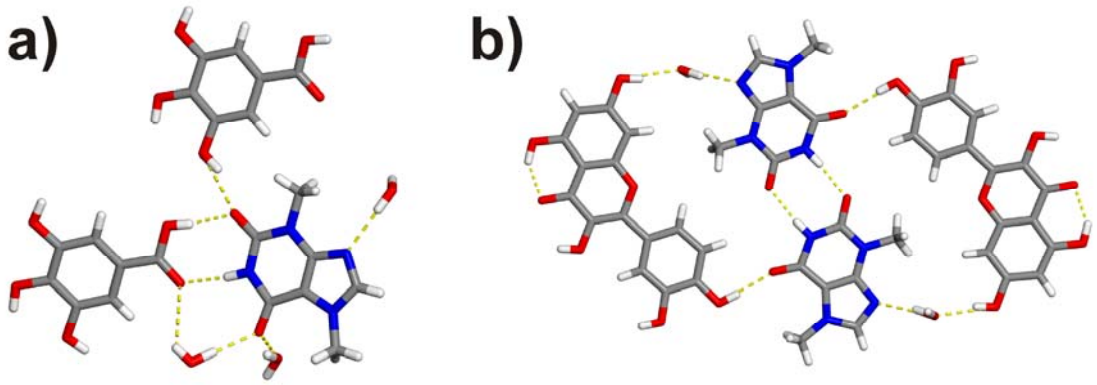

Figure 108 Crystal structures of: a) (**theb**)·(gallic acid)·2(H_2O), and b) (**theb**)·(quercitin)·2(H_2O)

It is also significant that **theb** tends to self-assemble into dimers *via* N-H(amide)···O(amide) hydrogen bonds, as observed in the crystal structures of **theb** and the (**theb**)·(trifluoroacetic acid) cocrystal (CCDC reference cods: SEDNAQ and HIJYAB, respectively) (Fig 109 and 107c). The robustness of the amide homosynthon dimer additionally increases the unpredictability of self-assembly processes and synthon hierarchies in cocrystals comprised of **theb** and hydroxybenzoic acids. Indeed, the results presented in this section will demonstrate the irregularity of synthon formation in such

cocrystals, thus imposing the need for systematic studies of synthon hierarchies in cocrystals involving compounds with multiple functional groups.

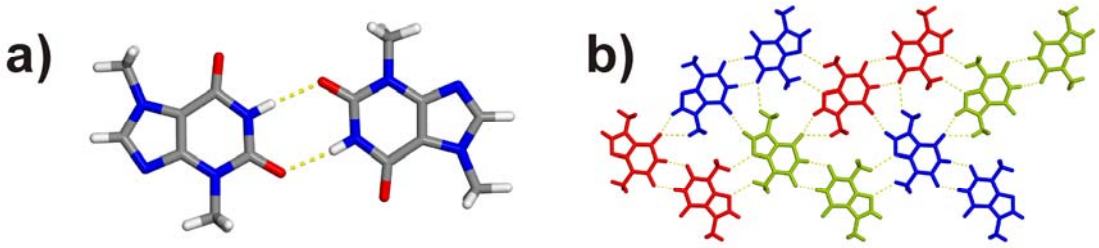

Figure 109 Crystal structure of **theb**: a) a **theb** dimer comprised of two crystallographically independent molecules, b) self-assembled **theb** dimers.

4.4.2. Experimental section

4.4.2.1. Materials

Theobromine (≥99.0%), 2-hydroxybenzoic acid (≥99.0%), 3-hydroxybenzoic acid (99.0%) , 4-hydroxybenzoic acid (≥99.0%), 2,3-dihydroxybenzoic acid (≥97.0%), 2,4-dihydroxybenzoic acid (≥98.0%), 2,5-dihydroxybenzoic acid (≥98.0%), 3,4-dihydroxybenzoic acid (≥97.0%), 3,5-dihydroxybenzoic acid (≥97.0%) and acetonitrile (anhydrous, 99.8%) were purchased from Sigma-Aldrich (St. Louis, MO, USA) and were used as received. Millex syringe filters (PVDF, 0.2 μm, 13mm) were purchased from Millipore (Bedford, MA, USA).

4.4.2.2. Survey of the Cambridge Structural Database

The CSD[48] (version 5.31, update of November 2009) was searched for **theb**-based crystal structures using the following filters: "3D coordinates determined", and "only organics". The search was performed using the ConQuest[251] program (version 1.12), and revealed 8 entries (CCDC reference codes: CSATBR, HIJYAB, HIJYEF, SEDNAQ,

THEBPI01), whereof three entries relate to crystal structures involving **theb** and a carboxylic acid (*i.e.* CSATBR, HIJYAB, HIJYEF).

4.4.2.3. Cocrystal screening

Theb and the selected series of **CCF**s were investigated for cocrystal formation using **SMPT** as screening method.[104, 262] In a typical screening experiment, both **theb** (1 mmol) and an equimolar amount of the **CCF** were suspended in a low volume of acetonitrile (1-4 mL). The obtained suspension was sonicated (Branson 2510R-DTM; frequency: 42 kHz, 6% at 100 W) for 1-2 min to facilitate the **SMPT** process. A phase change was visually evident within two hours. The obtained slurries were equilibrated for a week at ambient conditions to ensure complete conversions of **theo** and the **CCF** into a cocrystal or salt. The slurries were subsequently filtered and the obtained solids were investigated using powder X-ray diffraction (PXRD). The **theb**-based solid phases were further studied *via* IR spectroscopy and single crystal X-ray diffraction (SXRD).

4.4.2.4. Single crystal preparation

Single crystals of (**theb**)·(**2HBA**) (1:1 ratio, **theb1**), (**theb**)·(**3HBA**) (1:1 ratio, **theb2**), (**theb**)·(**4HBA**)·(H_2O) (1:1:1 ratio, **theb3**), (**theb**)·(**23DBA**)·(H_2O) (1:1:1 ratio, **theb4**), (**theb**)·(**24DBA**) (1:1 ratio, **theb5**), (**theb**)·(**25DBA**) (1:1 ratio, **theb6**), $(\mathbf{theb})^{+}\cdot(\mathbf{26DBA})^{-}$ (1:1 ratio, **theb7**), (**theb**)·(**34DBA**) (1:1 ratio, **theb8**), and (**theb**)·(**35DBA**) (1:1 ratio, **theb9**) were obtained by slow evaporation from solution. To obtain single crystals of the **theb** phases, **theb** (0.3 mmol) and the CCF (0.3 mmol) were separately dissolved in a methanol:water solution (1:1, 6-12 ml) at high temperature, the solutions were combined, filtered through a Millex syringe filter (PVDF, 0.2 μm, 13 mm), and left to evaporate at ambient conditions. Single crystals suitable X-ray diffraction measurements were obtained from the filtrate *via* slow evaporation within four weeks after initially a powered substance precipitated. The precipitated powdered solid was not further investigated.

4.4.2.5. Infrared (IR) spectroscopy

Transmission infrared spectra of the **theb**-based solids were obtained using a FT-IR spectrometer (Nicolet Magna 750) equipped with a Nicolet NIC-PLAN microscope. In addition, the utilized microscope was equipped with an MCT-A liquid nitrogen cooled detector. The solids were placed on a BaF_2 sample holder (13 mm × 1 mm), and scanned 64 times at a resolution of 4 cm^{-1}.

4.4.2.6. Powder X-ray diffraction studies

A diffractogram of each **theb**-based solid was obtained using an *Inel G3000* diffractometer being equipped with a curved position sensitive detector, and parallel beam optics. The instrument was operated with a copper-anode tube (1.5 kW, fine focus) at 40 kV and 30 mA. An incident-beam germanium monochrometer was utilized to obtain monochromatic $K_{\alpha 1}$ irradiation. The diffractometer was calibrated using the attenuated direct beam at one-degree intervals using a Si standard reference material (*i.e.* NIST 640c). The diffractometer was operated using the *Symphonix*[254] program, while the data were analyzed using the *Jade*[255] software (version 6.5). The samples were loaded onto an Al sample holder, and leveled with a glass slide.

4.4.2.7. Single crystal X-ray diffraction studies

Single crystal X-ray diffraction measurements of (**theb**)·(**2HBA**), (**theb**)·(**3HBA**), (**theb**)·2(**4HBA**)·(H_2O), (**theb**)·(**23DBA**)·(H_2O), (**theb**)·(**24DBA**), (**theb**)·(**25DBA**), $(\textbf{theb})^{+}\cdot(\textbf{26DBA})^{-}$, (**theb**)·(**34DBA**) and (**theb**)·(**35DBA**) on a *Bruker APEX2* diffractometer. The single crystals were positioned on a *MiYeGen* mount with vacuum grease. All X-ray diffraction data sets were collected using graphite-filtered MoK_α radiation (λ = 0.71069 Å) at temperatures indicated in Table 1, processed using *SAINT-Plus*,[256] and corrected for Lorentz-polarization effects. The data sets were collected with omega scans in 0.5° steps. Structure solution and refinement were accomplished using *XSHELL*.[261] All non-hydrogen atoms were refined anisotropically.

All hydrogen atoms bonded to carbon atoms were located in the Fourier-difference electron density map, fixed in geometrically constrained riding positions, and refined isotropically on the basis of corresponding C-atoms [U(H) = 1.2 U_{eq}(C)]. In the case of (**theb**)·(**2HBA**), (**theb**)·(**3HBA**)·(H_2O), (**theb**)·(**4HBA**)·(H_2O), (**theb**)·(**23DBA**)·(H_2O), (**theb**)·(**25DBA**)·(H_2O), (**theb**)·(**26DBA**), (**theb**)·(**34DBA**) and (**theb**)·(**35DBA**), the hydrogen atoms associated with O- and N-atoms were included in the located positions (*i.e.* coordinates refined) and treated isotropically. In the structures of (**theb**)·(**24HBA**), hydrogen atoms bonded to N- and O-atoms were refined either independently (*i.e.* coordinates and U_{iso} refined) or in a constrained fashion (*i.e.* coordinates constrained and U_{iso} refined). Crystallographic data of the investigated compounds are listed in Table 24-27. Geometry parameters of selected hydrogen-bonds are listed in Table 11.

4.4.2.8 Analysis of hydrogen-bond pattern

The analysis of hydrogen-bond patterns was performed in the same manner as for the **caf** and **theo** cocrystal series. Non-covalent interaction were recognized as hydrogen bond if: 1) the donor (*i.e.* O, N atoms) is covalently bound to at least one hydrogen, 2) the acceptor (*i.e.* O, N atoms) has at least one lone electron pair, 3) the donor-acceptor distance is less than the sum of van der Waals radii of both the hydrogen-bond donor and acceptor, 4) the contact is either intramolecular or intermolecular involving hydrogen-bond donor and acceptor atoms being separated by at least 3 covalent bonds within the molecule, and 5) D-H$\cdots A \geq 100°$, where D = hydrogen-bond donor, A = hydrogen-bond acceptor.[251] The hydrogen-bond parameters were calculated using the CIFTAB routine in WinGX.[253]

4.4.3. Results

We report herein the discovery of nine solids involving **theb** and (di)hydroxybenzoic acids using SMPT[104, 262] as screening method. The formation of a **theb**-based solid was identified using PXRD. All solids were structurally characterized

using both SXRD and FT-IR spectroscopy. The characterized solids were classified as either neutral molecular complexes (*i.e.* cocrystal) or charged complexes (*i.e.* salts) based on the carboxy-group geometries, Fourier difference maps, and FT-IR data. All solids, except (**theb**)$^{+}$·(**26DBA**)$^{-}$, display structures wherein the CCF carboxy group exhibits carbon-oxygen bond distances of distinct lengths being characteristic for protonated carboxylic groups, thus, indicating cocrystal formation. The carboxy group of (**theb**)$^{+}$·(**26DBA**)$^{-}$ exhibits a nearly equal carbon-oxygen distances that are typical for deprotonated carboxylic groups, hence, indicating salt formation (Table 10). Notably, the Fourier difference maps of all solids, except (**theb**)$^{+}$·(**26DBA**)$^{-}$, revealed that the acidic protons are positioned in close proximity to the O-atom of the CCF carboxylic acid group, at distances that correspond to a protonated carboxylic acid group. In the case of (**theb**)$^{+}$·(**26DBA**)$^{-}$, the acidic proton was found to be positioned in close proximity to the imidazole moiety of **theb**.

The described classification of the solids as either a cocrystal or a salts was found to be in agreement with results obtained from IR spectroscopic studies. Specifically, the carbonyl stretching bands of all solids characterized as cocrystals appeared above 1600 cm^{-1} in the IR spectra being consistent with unionized carboxylic acids, while the (**theb**)$^{+}$·(**26DBA**)$^{-}$ salt exhibited a carbonyl stretching band below 1600 cm^{-1}.

Crystallographic data of all **theb**-based solids are given in Appendix A (Tables 24, 25, 26 and 27). Hydrogen bond parameters are provided in Table 11. Structural features of all solids are described in succession, as follows.

Table 10 Carbon-oxygen bond distances of the carboxylic groups of the CCF acids

cocrystal	*d*(C–O) / (Å)	*d*(C=O) / (Å)	*Δd* / (Å) (*)
theb1	1.310(2)	1.230(2)	0.080(3)
theb2	1.331(2)	1.217(2)	0.114(3)
theb3	1.287(3)	1.264(3)	0.023(4)
	1.307(3)	1.243(2)	0.064(4)
	1.293(3)	1.251(2)	0.042(4)
	1.304(3)	1.244(2)	0.060(4)
theb4	1.314(2)	1.234(2)	0.080(3)
theb5	1.326(3)	1.234(3)	0.092(4)
theb6	1.310(2)	1.233(2)	0.077(3)
theb7	1.28(2)	1.27(2)	0.01(3)
	1.36(2)	1.24(2)	0.08(3)
theb8	1.330(3)	1.229(3)	0.101(4)
theb9	1.324(4)	1.228(5)	0.096(6)
	1.322(4)	1.235(5)	0.087(6)

* ***Δd* = [(C–O) - (C=O)]**

4.4.3.1. Cocrystal (**theb**)·(**2HBA**)

Theb and **2HBA** were found to crystallize in the triclinic space group $P\bar{1}$ with both one molecule of **theb** and **2HBA** in the asymmetric unit. Both components form discrete four-component assemblies (Fig. 110a) wherein two **theb** molecules form dimers being held together by two N-H(amide)···O(amide) hydrogen bonds forming $R_2^2(8)$ motif. The imidazole units of both **theb** molecules interact with a **2HBA** molecule *via* a O-H(carboxy)···N(imidazole) hydrogen bond. The *ortho*-hydroxy group of **2HBA** participate in an intramolecular O–H(hydroxy)···O(carboxy) hydrogen bond with the **2HBA** carboxylic group to form a $S_1^1(6)$ ring.[257] The assemblies are stacked in an offset manner by one half of the lengths of a four-component assembly (*i.e.* ~6.8 Å along the (-5 1 1) crystallographic plane), and form a 2D sheet held together by π(**theb**)···π(**2HBA**) interactions (Fig 110b). The layers stack in an offset manner (*i.e.* ~11 Å along the (0 -1 1) crystallographic plane) to assemble a 3D architecture being sustained by a set of C-H···O interactions (Fig. 110c).

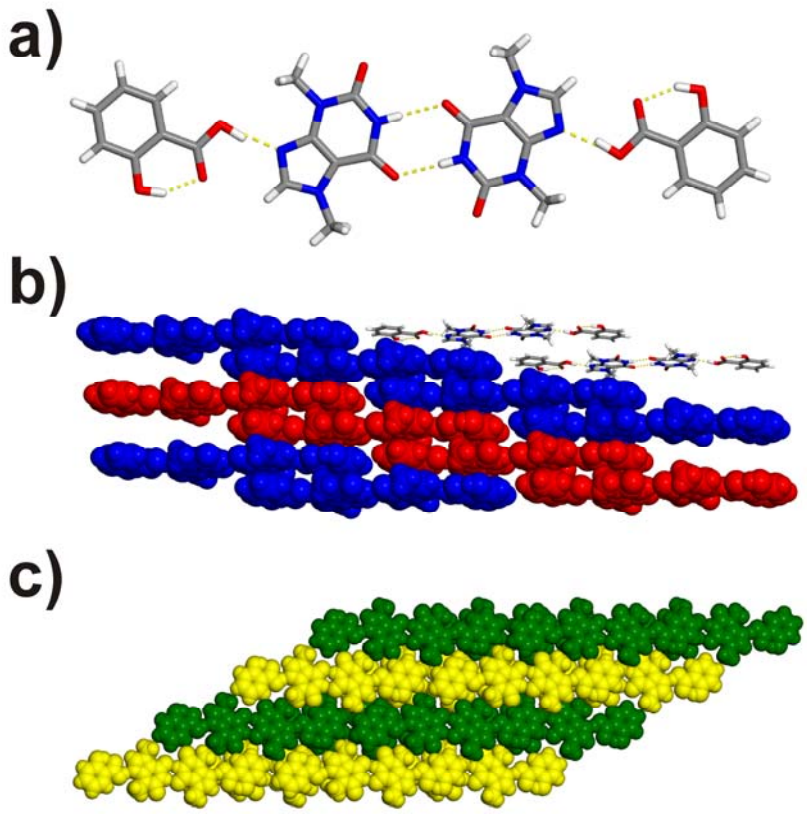

Figure 110 Perspective views: a) a discrete four-component assembly **theb**:**2HBA** assembly held together by O-H(amide)···N(amide), O-H(carboxy)···N(imidazole) and O-H(hydroxy)···O(carboxy) hydrogen bonds, b) a 2D layer composed of **theo**:**2HBA** assemblies being sustained by π(**theb**)···π(**2HBA**) interactions [viewed along the (0 1 10) and (1 0 0) crystallographic plane], and c) stacks of 2D layers held together by C-H···O interactions viewed along the (0 0 1) and (0 1 0) crystallographic planes.

4.4.3.2. Cocrystal (**theb**)·(**3HBA**)

Cocrystal (**theb**)·(**3HBA**) crystallizes in the monoclinic space group $P2_1/c$. **Theb** and **3HBA** form 1D ribbons based on centrosymetric four-component **theb**:**3HBA** assemblies (Fig. 3a). The four-component assemblies are sustained *via* O-H(carboxy)···N(imidazole) [$R_2^2(7)$ motif], and O-H(hydroxy)···O(urea) [*D* motif] heterosynthons, as well as two N-H(amide)···O(amide) hydrogen bonds that facilitate the formation of a $R_2^2(8)$ motif (Fig 111a). The ribbons stack in an offset manner (*i.e.* ~6.5 Å

along the crystallographic *a* axis plane) (Fig 111b). The stacks are sustained by π(**theb**)$\cdots\pi$(**3HBA**) interactions. Neighboring stacks are interacting *via* C-H$\cdots$O and C-H$\cdots\pi$ interactions to assemble into a 3D structures exhibiting a herringbone motif (Fig 111c). **Theb**:**3HBA** ribbons belonging to neighboring stacks are inclined by ~100º.

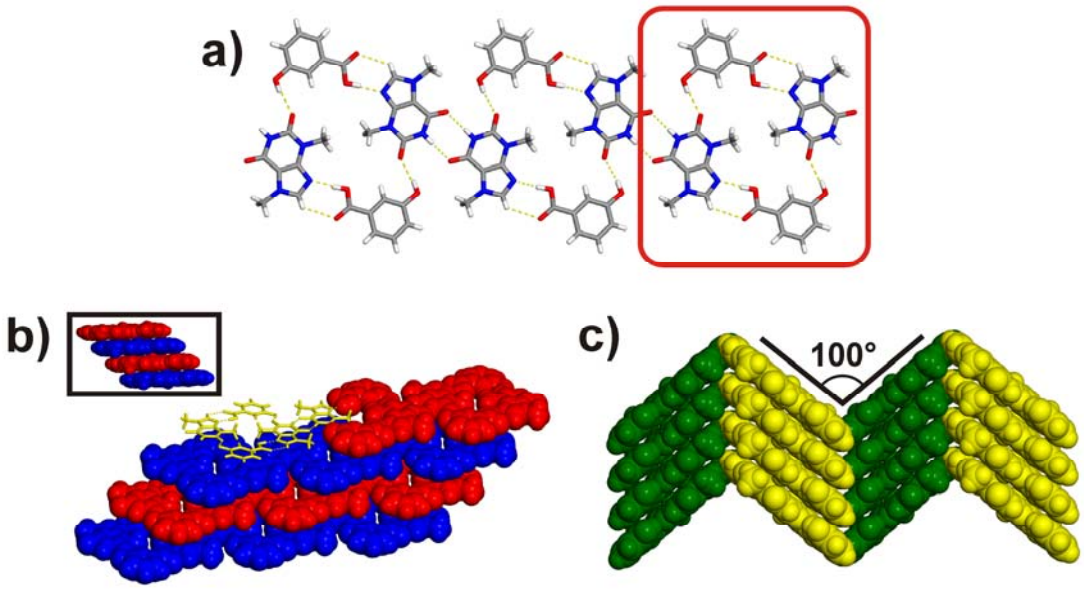

Figure 111 Perspective views: (a) 1D ribbon composed of four-component **theo**:**3HBA** assemblies (highlighted in red), (b) offset stacked **theb**:**3HBA** ribbons being held together by π(**theo**)$\cdots\pi$(**3HBA**) interactions (the displayed ribbons are parallel to the (1 -5 -2) crystallographic plane; inset: viewed along the crystallographic planes (0 1 0) and (-1 0 2)), (c) stacks of **theb**:**3HBA** ribbons self-assembled by C–H$\cdots$O and C–H$\cdots\pi$ interactions exhibiting a herringbone motif (viewed along the crystallographic planes (0 1 0) and (-1 0 2)).

4.4.3.3. Cocrystal (**theb**)·2(**4HBA**)·(H_2O)

The (**theb**)·2(**4HBA**)·(H_2O) cocrystal crystallizes in the triclinic space group $P\bar{1}$ with four molecules of **4HBA** and both two molecules of **theb** and water. **Theb** and **4HBA** were found to form two crystallographically independent and centrosymmetric six-component assemblies (Fig. 112a). The assemblies are composed of two non-centrosymmetric **4HBA** dimers and one centrosymmetric **theb** dimer. The **theb** dimer is

sustained by two N-H(amide)···O(urea) hydrogen bonds forming a $R_2^2(8)$ motif. Both **4HBA** dimers are held together by a $R_2^2(8)$ carboxylic acid homosynthon.

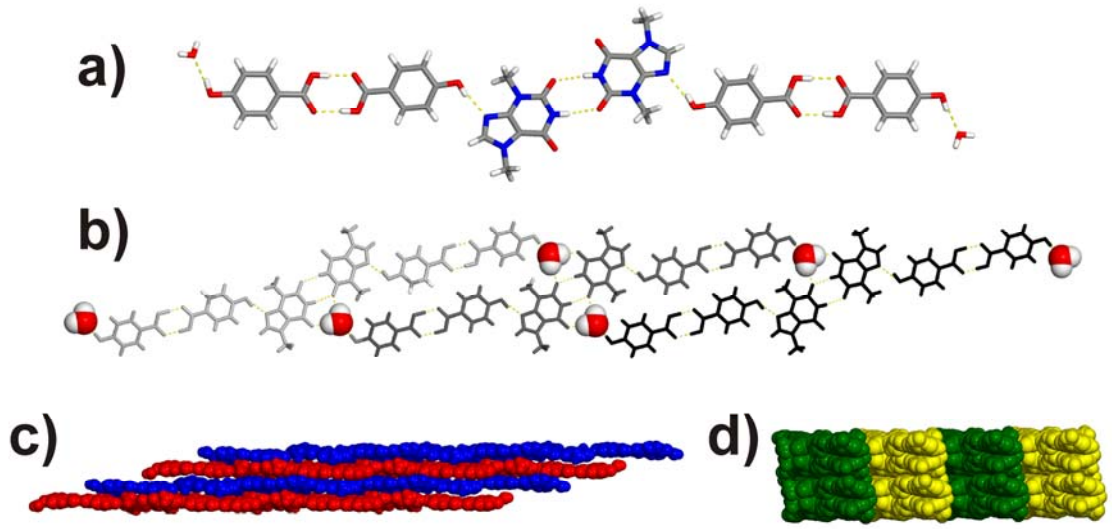

Figure 112 Perspective views: a) six-component **theb**:**4HBA** assemblies hydrogen-bonded to water molecules b) 1D ribbons of six-component **theb**:**4HBA** assemblies held together by water molecules (inset: a lone theb:4HBA assembly), c) stacks of **theb**:**4HBA**:H_2O ribbons viewed along the crystallographic (1 0 0) and (0 0 1) planes, d) neighboring stacks of **theb**:**4HBA** held together by C-H···O interactions (viewed along the crystallographic (-1 0 1) and (0 1 0) planes).

The **4HBA** dimers are linked to the **theb** dimer through a O-H(hydroxy)···N(imidazole) hydrogen bond. Each of the two crystallographically independent **theb**:**4HBA** aggregates further assembles into 1D ribbons being held together by water molecules *via* O-H(hydroxy)···O(water), O-H(water)···O(amide), and O-H(water)···O(urea) hydrogen bonds (Fig. 112b). The two crystallographically independent ribbons stack in an ABAB fashion, and are sustained by weak $\pi\cdots\pi$, C-H···O and other polar interactions (Fig. 112c). Neighboring stacks are held together by C-H···O interactions (Fig. 112d).

4.4.3.4. Cocrystal (**theb**)·(**23HBA**)·(H_2O)

Theb and **23DBA** crystallize in the monoclinic space group *Cc* with one molecule of **theb**, **23DBA** and water in the asymmetric unit. **Theb** and **23DBA** form 1D chains held together by both O–H(carboxy)···N(imidazole) hydrogen bonds, and N–H(amide)···O(hydroxy) bonds supported by a C–H···O interactions, thereby exhibiting $R_2^2(7)$ and $R_2^2(8)$ motifs, respectively (Fig. 113a).

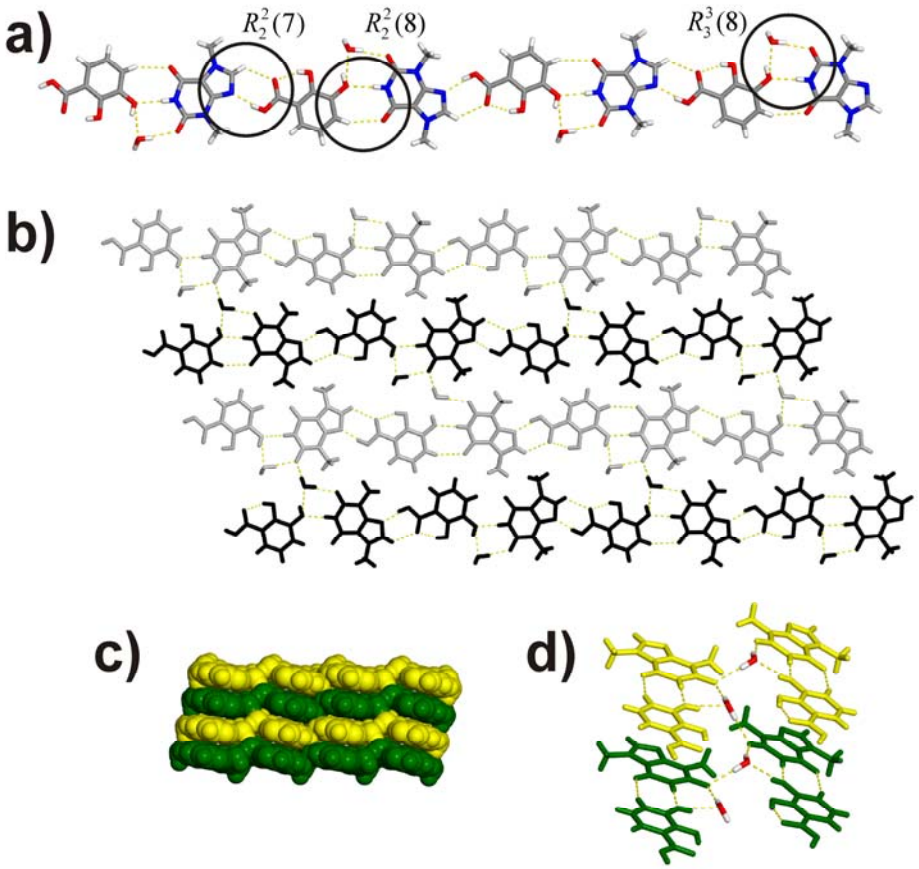

Figure 113 Perspective views: a) 1D chain composed of **theb**, **23DBA** and water molecules, b) hydrogen-bonded 2D sheet composed of **theb**:**23DBA**:H_2O assemblies (viewed along the crystallographic planes (0 1 0) and (1 0 -1)), c) layered 3D structure comprised of **theb**, **23DBA** and water molecules (viewed along the crystallographic planes (0 1 0) and (-3 -1 -1)), and d) fragments of two stacked sheets held together by O–H(water)···O(urea) hydrogen bonds.

Each *otho*-hydroxy(**23DBA**) group is involved in a O–H(hydroxy)···O(caboxy) intramolecular hydrogen bond thereby exhibiting a $S_1^1(6)$ motif.[257] Water molecules are positioned on the periphery of the chain being hydrogen-bonded to the hydroxy group of **23DBA** *via* O–H(hydroxy)···O(water) and O–H(water)···O(urea) hydrogen bonds (Fig. 5a) and, thus, participates in the formation of a $R_3^3(8)$ motif. The water molecules are linking the **theb**:**23DBA** chains into 2D sheets (Fig. 113b) that further self-assemble into a 3D hydrogen-bonded structure (Fig 113c). While the sheets are exclusively sustained by O–H(water)···O(urea) hydrogen bonds, the formation of the 3D structure is facilitated by both O–H(water)···O(urea) hydrogen bonds and π(**theb**)···π(**23DBA**) interactions.

4.4.3.5. Cocrystal (**theb**)·(**24DBA**)

Theb and **24DBA** crystallize in the monoclinic space group $P2_1/n$ with both one molecule of **theb** and **24DBA** in the asymmetric unit. The cocrystal components form a molecular bilayers composed of **theb**:**24DBA** polymers that are held together by O–H(carboxy)···N(imidazole) hydrogen bonds (D motif) and cyclic arrays of N–H(amide)···O(hydroxy) and C–H(aromatic)···O(amide) intermolecular hydrogen bonds ($R_2^2(8)$ motif). The *ortho*-hydroxy(**24DBA**) groups expectedly form $S_1^1(6)$ motifs *via* O–H(hydroxy)···O(carboxy) hydrogen bonds (Fig 114a).[257] The polymers self-assemble into bilayers that resemble 2D rectangular grids (Fig. 114b). The bilayers are sustained by O−H(hydroxy)···O(urea) hydrogen bonds (D motif). Within each of the two layers, the 1D polymers are aligned in parallel and interact *via* π···π and C−H···π forces. Polymers belonging to opposite layers are inclined by φ = 62º (Fig. 6b). The bilayers stack to form a 3D structure being sustained by a set of C−H···O interactions (Fig. 114c).

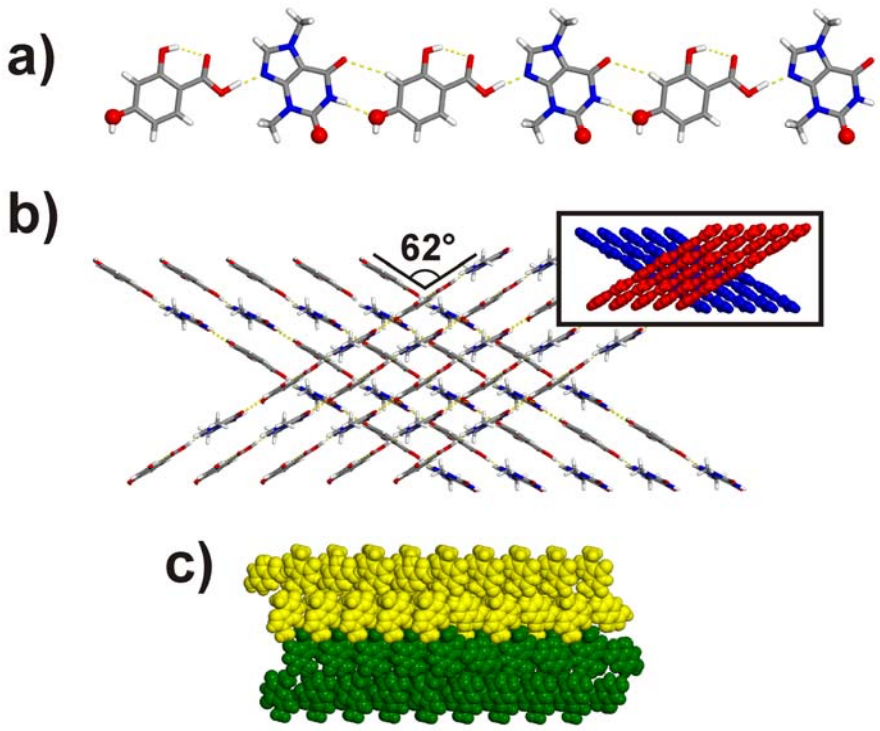

Figure 114 Perspective views of: a) an 1D **theb**:**24DBA** polymer (oxygen atoms depicted using the "ball and stick" model represent atoms participate in hydrogen bonding within two layers of 1D **theb**:**24DBA** polymers, and act as either donors or acceptors), b) a **theb**:**24DBA** bilayer viewed along the (0 1 0) and (1 0 -1) crystallographic planes, c) two stacked bilayers viewed along the crystallographic *a* axis.

4.4.3.6. Cocrystal (**theb**)·(**25DBA**)

Theb and **25DBA** cocrystallize in the triclinic space group *P*$\bar{1}$. The asymmetric unit contains both one molecule of each component. **Theb** and **25DBA** form centrosymetric four-component assemblies (Fig. 115a, highlighted in green) that further assemble into 1D ribbons (Fig 115a). As seen in (**theb**)·(**3HBA**), the four-component assemblies are held together by O-H(carboxy)···N(imidazole) and O-H(hydroxy)···O(urea) hydrogen bonds that exhibit *D* motifs. The *otho*-hydroxy group of 25DBA forms an intramolecular O–H(hydroxy)···O(carboxy) hydrogen bond that forms a $S_1^1(6)$ motif.[257] The assemblies are interlinked through a pair of N-

H(amide)···O(amide) hydrogen bonds that form $R_2^2(8)$ motif. The ribbons stack to form a 3D structure being sustained by π(**theb**)···π(**25DBA**) interactions. The stacks are offset by ~7.9 Å along the crystallographic *b* axis (Fig 115b).

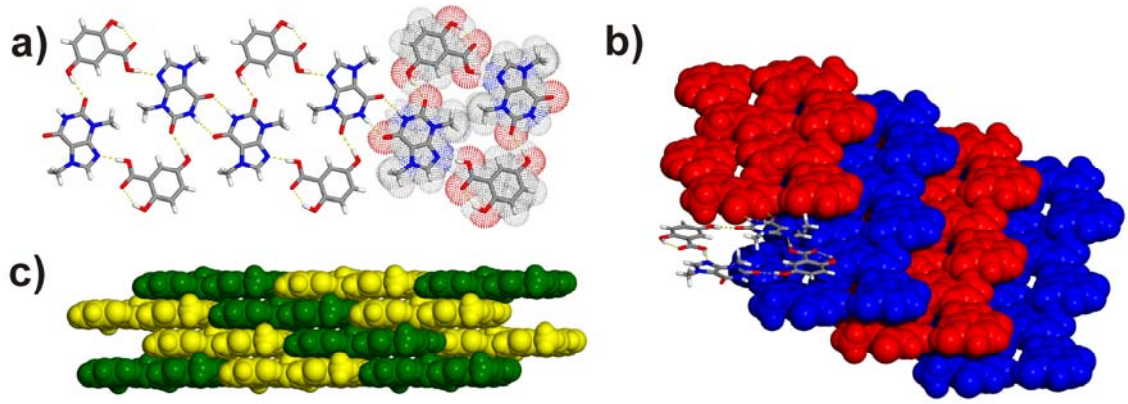

Figure 115 Perspective views: a) 1D ribbons composed of four-component **theb**:**25DBA** assemblies (highlighted using van der Waals surfaces), b) stacked **theb**:**25DBA** ribbons held together by $\pi\cdots\pi$ interactions viewed along the crystallographic (0 1 0) and (1 0 2) planes, and c) stacks of **theb**:**25DBA** ribbons view along the crystallographic (0 1 0) and (1 0 1) planes.

4.4.3.7. (H-**theb**)$^+$·(**26DBA**)$^-$ salt

The diffraction data obtained from single crystals composed of **theb** and **26DBA** were not of satisfying quality and did, hence, *not* suffice to characterize the investigated solid as either salt or cocrystal. However, hydrogen-bond patterns were successfully determined. It was found that **theo** and **26DBA** crystallize in a 1:1 ration in the monoclinic space group *Pc* with both one molecule of **theb** and **26DBA** in the asymmetric unit. The cocrystal components form a discrete four-component assembly held together by intermolecular O-H(carboxy)···N(imidazole) and N-H(amide)···O(amide) hydrogen bonds (forming $R_2^2(7)$ and $R_2^2(8)$ motifs, respectively),

and intramolecular O-H(hydroxy)···O(carboxy) hydrogen bonds (forming $S_1^1(6)$ motifs) (Fig. 116a).

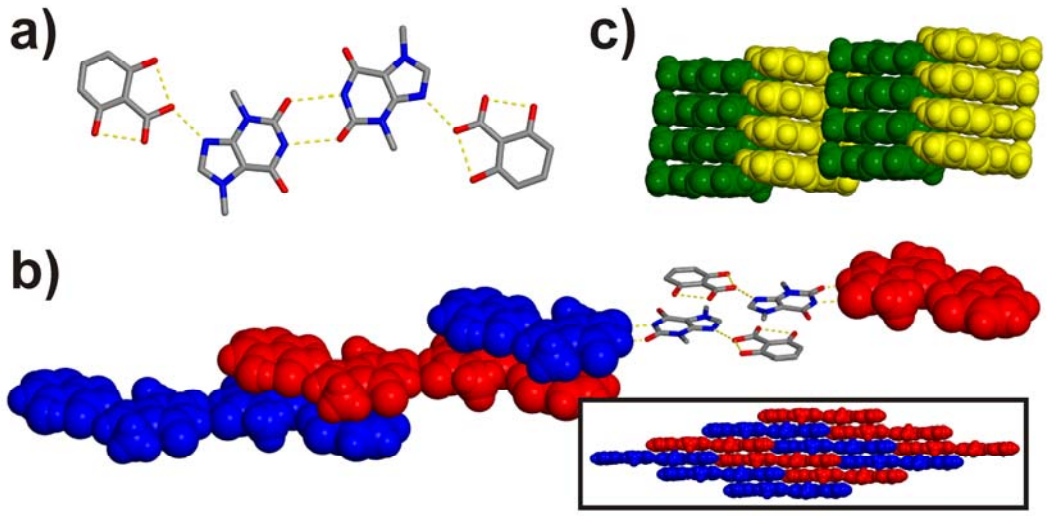

Figure 116 Perspective views: a) discrete four-component **theb**:**26DBA** assembly**,** b) stacked **theb**:**26DBA** assemblies viewed along the crystallographic (-1 1 0) and (0 0 1) planes (inset depicts a view of **theb**:**26DBA** stacks viewed along the crystallographic *b* axis), and c) the 3D structure of the **theb**:**26DBA** solid viewed along the crystallographic (2 0 1) and (0 1 0) planes.

The discrete assemblies are stacked in an offset manner by ~12.5 Å along the crystallographic *c* axis (Fig. 116b). Within the stacks, the assemblies are held together by π(**theb**)···π(**26DBA**) and C-H···O interactions. Neighboring stacks are sustained by C-H···O interactions to form a 3D structure (Fig. 116c).

4.4.3.8. Cocrystal (**theb**)·(**34DBA**)

(**Theo**)·(**34DBA**) crystallizes in the orthorhombic space group *Pbca* with both one molecules of each cocrystal component in the asymmetric unit. The components form a "zig-zag" 2D sheet (Fig 117a) that is held together by O-H(carboxy)···N(imidazole), O-H(hydroxy)···O(urea), N-H(amide)···O(amide) and O-H(hydroxy)···O(carboxy)

hydrogen bonds that participate in the formation of $R_2^2(7)$, $R_2^2(8)$ and D motifs. The sheets exhibit several smaller structural units, namely centrosymmetric four-component **theb**:**34DBA** assemblies and 1D molecular ribbons (Fig 117a). Within the sheets, the tapes are inclined by 57.9º (Fig 117a, inset). Lastly, the sheets stack to form a 3D structure that is sustained by π(**theb**)···π(**34DBA**), C-H···O and π(**theb**)···π(**34DBA**) and polar interactions (Fig 117b).

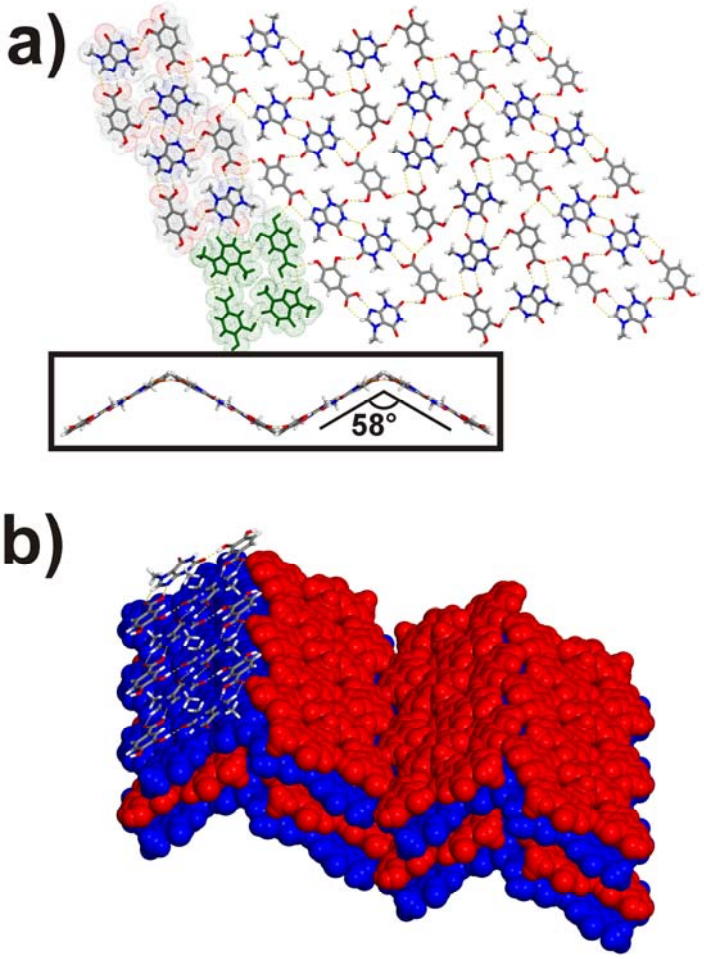

Figure 117 Perspective views: a) molecular sheet composed of **theb** and **34DBA** molecules viewed along the crystallographic *c* axis (the molecular tape is highlighted by using van der Waals surfaces; the four-component assembly is high-lighted in green), and b) stacked sheets viewed along the crystallographic planes (1 0 0) and (0 1 1).

4.4.3.9. Cocrystal (**theb**)·(**35DBA**)

The **theb**:**35DBA** cocrystallizes in crystallizes in the monoclinic space group $P2_1/c$ with both two molecules of each cocrystal component in the asymmetric unit. **Theb** and **35DBA** form planar and porous 2D structures wherein **theb** and **35DBA** molecules are being held together by O-H(carboxy)···N(imidazole) and O-H(hydroxy)···O(urea) hydrogen bonds that form $R_2^2(7)$ and D motifs (Fig. 117a). At the same time, both **theb** and **35DBA** from dimers. While the **theb** molecules are sustained by a pair of N-H(amide)···O(amide) hydrogen bonds, the **35DBA** molecules are hydrogen bonded by O-H(hydroxy)···O(carboxy) interactions. These interactions participate in the formation of hydrogen-bond pattern based on $R_2^2(8)$ and $R_2^2(14)$ motifs. The planar structures form bilayers (Fig 118b) and stack in an offset manner along the crystallographic (0 1 0) plane. The stack are sustained by π(**theb**)···π(**35DBA**) and π(**theb**)···π(**theb**) interactions.

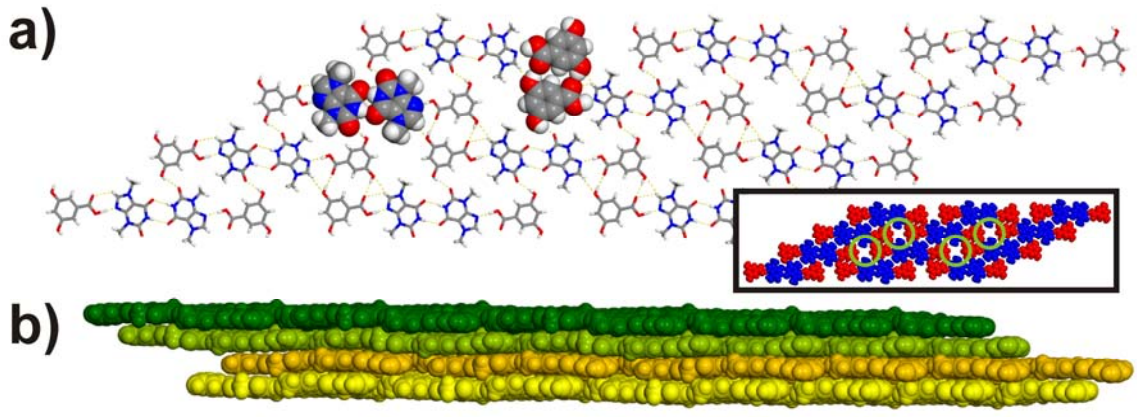

Figure 118 Perspective views: a) 2D sheets viewed along the crystallographic *c* axis (inset depicts pores in the sheet; **theb** and **35DBA** dimers are highlighted using the "space fill" model), and b) stacked planes viewed along the crystallographic *b* axis.

Table 11 Selected hydrogen-bond parameters of the **theb** solids (with estimated standard deviations except for fixed and riding hydrogen atoms).

Compound	*D*–H···*A*	*D*–H	*d*(H···*A*) / Å	*d*(*D*···*A*) / Å	*θ*(*D*–H···*A*)/º
theb1	N3-H3···O1^{i}	0.86	1.98	2.8340(19)	174.7
	O3-H3O···N1	1.01(2)	1.64(3)	2.634(2)	167(2)
	O5-H5O···O4	0.94(2)	1.73(3)	2.5881(19)	151(2)
theb2	N3-H3···O1^{ii}	0.86	1.90	2.7555(14)	174.0
	O4-H4O···N1	0.94(3)	1.78(3)	2.7171(15)	173(2)
	O5-H5O···O2^{iii}	0.82(2)	1.99(3)	2.8037(15)	171(2)
theb3	N3-H3···O2^{iv}	0.86	2.02	2.867(2)	170.2
	N7-H7···O4^{v}	0.86	2.01	2.863(2)	173.1
	O6-H6O···O(12)	0.99(4)	1.67(4)	2.658(2)	173(4)
	O7-H7O···N1	0.92(3)	1.93(3)	2.804(3)	160(3)
	O9-H9O···O14	0.94(4)	1.74(4)	2.683(2)	177(3)
	O10-H10O···N5	0.81(4)	1.94(4)	2.741(3)	167(4)
	O11-H11O···O5	1.07(4)	1.50(4)	2.577(2)	178(4)
	O13-H13O···O18	0.83(3)	1.81(3)	2.634(3)	177(3)
	O15-H15O···O8	0.91(4)	1.66(4)	2.569(2)	175(4)
	O16-H16O···O17	0.88(3)	1.82(3)	2.687(3)	168(3)
	O17-H17A···O3^{vi}	0.78(4)	2.02(4)	2.795(3)	173(4)
	O17-H17B···O4^{vii}	0.81(4)	2.17(4)	2.922(3)	153(3)
	O18-H18A···O1^{vii}	0.90(3)	1.88(3)	2.780(2)	178(3)
	O18-H19B···O2^{viii}	0.86(4)	2.05(4)	2.879(3)	161(3)
theb4	N3-H3···O6^{ix}	0.86	2.03	2.893(2)	176
	O5-H5O···O4	0.80(4)	1.81(4)	2.5675(19)	156(3)
	O6-H6O···O7	0.76(3)	1.99(3)	2.689(2)	153(3)
	O6-H6O···O5	0.76(3)	2.34(3)	2.6977(19)	110(3)
	O7-H7OA···O2^{x}	0.881(9)	1.981(10)	2.8608(18)	176(2)
	O7-H7OB···O2^{xi}	0.891(10)	1.973(10)	2.8543(18)	170(2)
	O3-H3O···N1	0.889(9)	1.784(9)	2.654(2)	166(4)
theb5	N3-H3···O6^{xii}	0.86	2.06	2.907(3)	168.5
	O3-H3O···N1	1.14(4)	1.51(4)	2.644(3)	169(3)
	O5-H5···O4	0.82	1.85	2.579(3)	148.0
	O6-H6O···O2^{xiii}	0.78(4)	1.90(4)	2.672(3)	171(4)
theb6	N3-H3···O1^{xiv}	0.86	1.92	2.7786(14)	172.3
	O3-H3O···N1	0.93(2)	1.69(2)	2.6205(15)	173(2)
	O5-H5O···O4	0.96(2)	1.73(2)	2.6017(14)	150(2)
	O6-H6O···O2^{iv}	0.897(19)	1.857(19)	2.7477(14)	171.9(16)

Table 11 – continued

theb7	N1-H1···O4	0.86	2.06	2.902	167
	N3···O6	N/A	N/A	2.513	N/A
	N5-H5···O2	0.86	2.02	2.854	164
	N7···O10	N/A	N/A	2.526	N/A
	O5-H1X···O6	1.10	1.59	2.626	155
	O8-H2X···O7	0.84	1.71	2.511	158
	O9···O10	N/A	N/A	2.507	N/A
	O12-H4X···O11	1.15	1.80	2.571	120
theb8	N3-H3···O1^{xv}	0.87	1.87	2.735(3)	173.5
	O4-H4O···N1	0.94(4)	1.72(4)	2.659(3)	175(3)
	O5-H5O···O2^{xvi}	1.03(4)	1.75(4)	2.778(3)	177(3)
	O6-H6O···O3^{xvii}	0.93(3)	1.82(3)	2.728(3)	165(3)
theb9	N3-H3···O3	0.86	1.97	2.813	168
	N7-HH7···O1	0.86	1.94	2.793	172
	O5-H4O···O5	1.34	1.36	2.685	148
	O7-H6O···O10^{xviii}	0.84	1.97	2.797	169
	O8-H5O···O4^{xix}	0.67	2.14	2.771	162
	O9-H3O···N5	1.04	1.66	2.689	168
	O11-H1O···O6^{xx}	0.79	2.00	2.790	178
	O12-H2O···O2^{xxi}	0.76	1.99	2.746	173

Symmetry operators: (*i*) -*x*, -*y*+1, -z+1; (*ii*) -*x*, -*y*+1, -*z*; (*iii*) -*x*+2, -*y*+1, -*z*+1; (*iv*) -*x*, -*y*+2, -*z*+1; (*v*) -*x*, -*y*+2, -*z*; (*vi*) *x*+1, *y*, *z*+1; (*vii*) -*x*+1, -*y*+2, -*z*+1; (*viii*) -*x*+1, -*y*+2, -*z*+2; (*ix*) *x*-1/2, -*y*+1/2, *z*+3/2; (*x*) *x*+1/2, *y*-1/2, *z*-1; (*xi*) *x*+1/2, -*y*+1/2, *z*-3/2; (*xii*) *x*-1, *y*-2, *z*; (*xiii*) -*x*+1/2, *y*+3/2, -*z*+1/2; (*xiv*) -*x*+1, -*y*+2, -*z*; (*xv*) -*x*+1, -*y*, -*z*+2; (*xvi*) -*x*+1, -*y*+1, -*z*+2; (*xvii*) -*x*+3/2, *y*+1/2, *z*; (*xviii*) *x*+1, *y*, *z*-1; (*xix*) *x*-1, *y*, *z*; (*xx*) *x*+1, *y*, *z*-1; (*xxi*) *x*+1, *y*, *z*

4.4.4. Discussion

A combined CSD and literature survey revealed five structurally characterized **theb** cocrystals, whereof four involve a carboxylic acid. Three out of the four carboxylic

acid cocrystals (*i.e.* CSATBR, HIJYAB, HIJEF) exhibit binding mode I, whereas two display binding mode III (*i.e.* HIJYEF and the gallic acid cocrystal[271]), and only one binding mode II (*i.e.* CSATBR). Notably, both binding modes II and III generally occur in the presence of binding mode I, and in cocrystals displaying an excess of carboxylic-acid groups (as compared to the number of available imidazole groups). Surprisingly, the occurrence of binding mode II in the absence of binding mode I was observed only in one instance, namely in the gallic acid cocrystal. The herein reported 1:1 **theb**:carboxylic-acid cocrystals, however, exhibit exclusively binding mode I. The persistent formation of such O-H(carboxy)···N(imidazole) interactions is consistent with the high occurrence of the acid:imidazole synthon in the previously discussed **caf** and **theo** cocrystal series (see sections 4.2. and 4.3). The exclusive occurrence of binding mode I in the studied cocrystals suggests that binding mode I is the most stable one. This premise is consistent with the observation that **theb** structures from the CSD display binding modes II and III only along with mode I. It is presumed that **theb** and hydroxybenzoic acids can also exhibit other binding modes when co-crystallized at higher acid-to-**theb** ratios.

Eight out of nine solids cocrystals display an O-H(carboxy)···N(imidazole) interaction (*i.e.* binding mode I). The only solid lacking this interaction, namely (**theb**)·(**4HBA**)·(H_2O), exhibits a carboxylic acid homosynthon in the presence of a phenol-imidazole interaction being realized *via* a O-H(hydroxy)···N(imidazole) hydrogen bond (Fig 112). At the same time, the **theb** molecules were found form dimers sustained by N-H(amide)···O(amide) interactions. In comparison, the **theo** cocrystal series exhibits 4 solids with a O-H(hydroxy)···N(imidazole) interaction. The lower number of phenol-imidazole interactions in **theb** cocrystals might be attributed to the robustness of the amide(**theb**) homosynthon. More specifically, the amide moieties of **theb** tend form a highly robust amide dimer, thus "steering" the carboxy group towards an interaction the with imidazole(**theb**) moiety (Fig. 119). The "xanthine moiety" of **theb**, on the other hand, favors heterosynthon formation with a carboxylic acid rather the formation of a

theb homosynthon, thus enabling phenol:imidazole interactions. Considering the type of interaction that the imidazole(**theb**) unit is participating in, it appears that **theb** behaves during self-assembly processes more similar to **caf**, rather than **theo**.

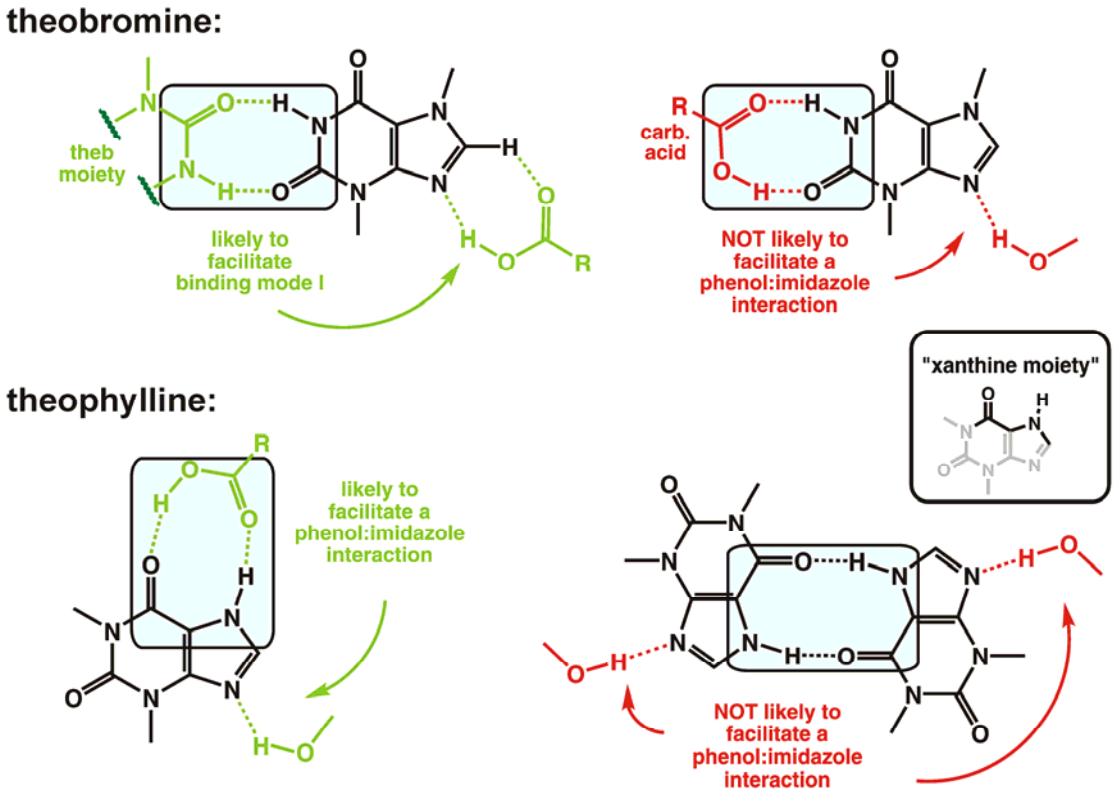

Figure 119 Factors contributing to the lack of phenol:imidazole interactions in **theb** cocrystals.

Notably, (**theb**)·(**4HBA**)·(H_2O) and (**theo**)·(**34DBA**) are the only solids among the investigated xanthine:hydroxybenzoic-acid cocrystals found to display a carboxylic acid $R_2^2(8)$ homosynthon in the presence of an imidazole moiety. The formation of carboxylic acid homosynthons in the presence of available imidazole functional groups is unexpected[250] and may be attributed formation of crystalline lattices of low energies, as determined in the case of the **caf**:**4HBA** cocrystal system.[259]

Additional similarities between the **theb** and **caf** cocrystal series are related to the involvement of the C=O(amide) and C=O(urea) moieties in hydrogen bonding. In both cocrystal series, the C=O(urea) unit is more frequently involved in interactions with phenolic moieties of hydroxybenzoic acids, as compared to the C=(amide) moiety. Specifically, the C=O(amide) was found to be engaged in hydrogen bonding in 6 solids (*i.e.* solids involving **2HBA**, **3HBA**, **4HBA**, **25DBA**, **26DBA**, **34DBA**, and **35DBA**) whereas the C=O(urea) unit participates in hydrogen bonding in 7 solids (i.e. solids involving **3HBA**, **4HBA**, **23DBA**, **24DBA**, **25DBA**, **26DBA**, **34DBA**, and **35DBA**). Five solids (*i.e.* solids based on **3HBA**, **4HBA**, **25DBA**, **34DBA**, and **35DBA**) exhibit hydrogen-bond patterns wherein both the C=O(amide) and C=O(urea) moieties interact with a hydrogen-bond donor. The **2HBA** cocrystal was found to exhibit a C=O(amide) hydrogen bonds in the absence of C=O(urea) hydrogen bonds. In contrast, the **23DBA**, **24DBA** and **26DBA** solids displayed a C=O(urea) interaction in the absence of a C=O(amide) hydrogen bond. An overview if structural features in **theb** cocrystals is given in Table 12.

Table 12 Overview of structural features in the **theb** cocrystals.

solid	**theo:CCF ratio**	**structure of assembly**	**hydrogen-bond acceptor group of caf**			
			imidazole	urea	amide	total
theb1	1:1	discrete	√		√	2
theb2	1:1	1D infinite	√	√	√	3
theb3	1:1	discrete[a]	√	√	√[b]	3
theb4	1:1	2D infinite[c]	√	√[b]		2
theb5	1:1	2D infinite	√	√		2
theb6	1:1	1D infinite	√	√	√	3
theb7	1:1	discrete	√	√		2
theb8	1:1	2D infinite	√	√	√	3
theb9	1:1	2D infinite	√	√	√	3

[a] 1D infinite based on included H_2O; [b] hydrogen-bond acceptor interacts with H_2O; [c] 3D infinite based on included H_2O

We also observed the frequent formation of amide homosynthons based on N-H(amide)···O(amide) interactions. Seven solids were found to display such hydrogen bond. As shown in Figure 106a, **theb** exhibits two structural moieties that can be described as amides – amide "A" and "B". Amide "A" is constituted of the C=O(amide) unit moiety, whereas amide "B" involves C=O(urea), as depicted in Fig. M. Five cocrystals display a **theb** homosynthon comprised of amide "A" moieties, while only two solids participates in the formation of **theb** homosynthons *via* the amide "B" moiety.

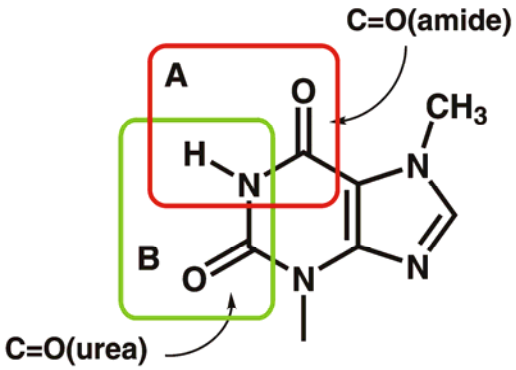

Figure 120 Amides "A" and "B" in the structure of **theb**.

The higher occurrence of homosytnhons of the type "A" is somewhat surprising having in mind that this type of dimer exhibits a higher energy, as compared to the "B" type homodimer. The relative stabilities of both types of dimers were determined using density-functioan-theory (DFT) calculations. The "B" type homodimer was determined to be 0.78 $kJmol^{-1}$ less stable that the "A" dimer (dimer A: -11.67 kcal/mol; dimer B: -12.45 kcal/mol) .

All **theb** solids are based on 1:1 **theb**:CCF ratios. Whereas **2HBA, 4HBA** and **26DBA** form discrete assemblies with **theb**, all other CCFs form infinite structures. More specifically, **3HBA** and **25DBA** form 1D assemblies, while **24DBA**, **23DBA**, **24DBA**

and **35DBA** form 2D assemblies. The discrete **4HBA**:**theb** and the 2D **23DBA**:**theb** assemblies further assemble with water to form 1D and 3D structures, respectively. The higher occurrence of discrete structures in the **theb** solids, as compored to the **theo** solids, is somewhat surprising having in mind that both **theo** and **theb** have the same number of hydrogen-bond donors and acceptors (Fig. 121). In previous section of this chapter, we have attributed the preferred formation of infinite structures in **theo** structures to the presence of a sufficient number hydrogen-bond donors in **theo**. Analogously, it was argued that **caf** tends to form discrete structures owing to a lack of hydrogen-bond donors in its structure**.** The same reasoning can, obviously, not be applied when comparing the **theo** and **theb** solids. However, the lower number of infinite structures in the **theb** solids is possibly caused by the incapacity of **2HBA** and **26DBA** to utilize its *ortho*-hydroxy groups to participate in intermolecular hydrogen-bonding, as seen in the **theo** solids.

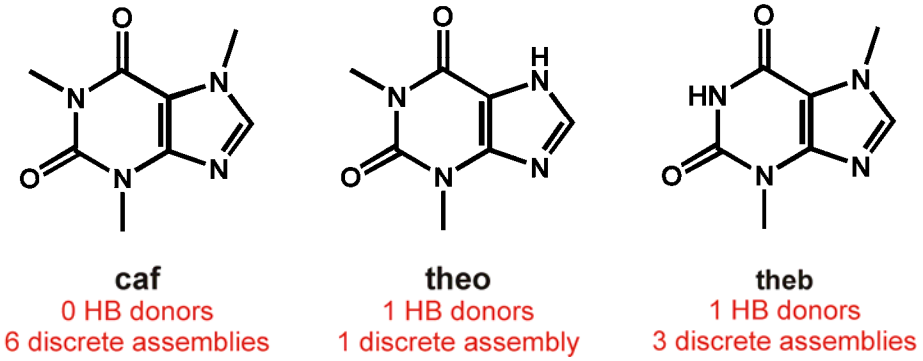

Figure 121 Number of hydrogen-bond donors in the xanthine alkaloid compared to the occurrence of discrete assemblies in xanthine-alkaloid cocrystals (or salts).

Our studies revealed the formation of only one salt, namely (**theb**)$^{+}$·(**26DBA**)$^{-}$. The proton transfer from the carboxylic-acid of the acid to the imidazole moiety of theb was evidenced via single crystal X-ray diffraction and IR spectroscopy. The salt

formation is, as in the case of **caf** and **theo**, unexpected having in mind that the ΔpK_a value is negative ($\Delta pK_a \sim -0.9$; pK_a(**theb**, base) = 0.41 ± 0.70,[272] pK_a(**26DBA**, acid) = 1.30 ± 0.1). The **theb**:**26DBA** complex is therefore not expected to exhibit a proton transfer. Reasons for such unexpected proton transfer are discussed in section 4.5. of this chapter,

Two out of nine **theb** solids were shown to crystallize as monohydrates (*i.e.* **4HBA** and **23DBA** cocrystals). In comparison, the **caf** and **theo** solids formed hydrated structures in 3 and 1 instances, respectively. Water molecules are generally being incorporated into crystal lattices of organic molecules to establish a balance between hydrogen-donors and hydrogen acceptors. With this in mind, we ascribed to the higher number of hydrates in the **caf** series to a lack of hydrogen-bond donors in **caf**. The lower number of hydrates formed in the **theo** series, on the other hand, was ascribed to an (nearly) equal number of donors and acceptors in both components of the solids. Considering that **theo** and **theb** display the same number of hydrogen bond donors, it is not surprising that the **theb** solids display a lower number of hydrates that the **caf** solids. Factors contributing to hydrate formation in **theb** cocrystals are not obvious and remain to be determined.

4.4.5. Conclusion

We have described the preparation and structural characterization of nine **theo** salts and cocrystals involving structural isomers of (di)hydroxybenzoic acids, using **SMPT** as screening method. We have determined the formation of eight cocrystals and one salt. All solids are based on multiple supramolecular synthons. The most prevalent type of interaction is this class of solids was found to be the O−H(carboxy)···N(imidazole) heterosynthons, followed by the N−H(amide)···O(amide) homosynthon and the O−H(hydroxy)···O(urea) heterosynthons (the synthons were found

in 8, 7 and 5 solids, respectively). Both the N−H(amide)···O(hydroxy) and the O−H(hydroxy)···O(carboxy) heterosynthons were identified in 2 solids. The least occurring synthons are the O−H(hydroxy)···N(imidazole) heterosynthon and the O−H(carboxy)···O(carboxy) homosynthon (both found in 1 solid). The deducted synthon hierarchy is shown in Fig 122.

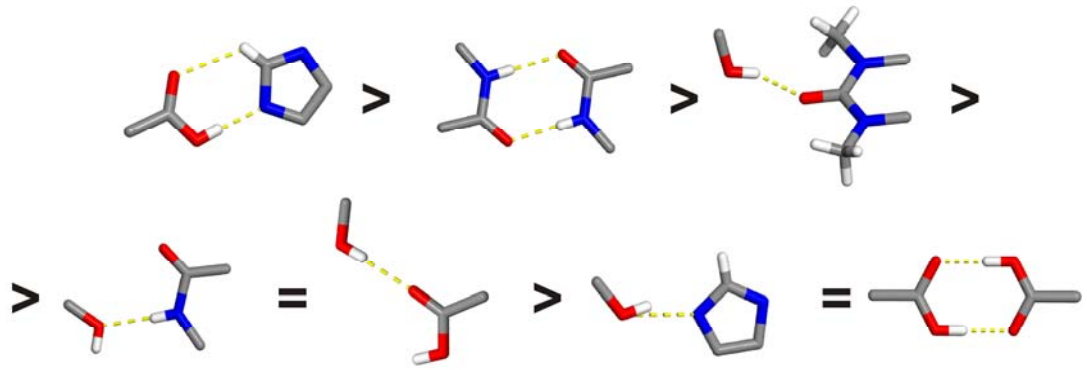

Figure 122 Established synthon hierarchy in **theb** solids based on hydroxybenzoic acids.

The **theb** solids were shown to exhibit a variety of supramolecular synthons that is both comparable to the one observed in **theo** solids, and larger than the one in the **caf** solids. In addition, it was found that the **theb** solids display more structural similarities with the **caf** series, rather than the **theo** series. Such observation seems peculiar having in mind that the chemical structure of **theb** displays more similarities with the one of **theo**, rather than **caf**. Such unanticipated observation imposes the need for further systematic structural studies of cocrystals based on multiple synthons. Our group is currently continuing to investigate cocrystals based on other xanthine alkaloids (*i.e.* xanthine, 8-chlorotheophylline, acephylline and dyphylline) involving the same group of **CCF**s as reported herein. From both the presented and the ongoing studies, we expected to gain an understanding of how multiple functional groups self-assemble into supramolecular

structures. Finally, we identified an unexpected salt formation at a negative Δp*K*a value, just as in the cases of **caf** and **theo**. This finding implies the need to supplement crystallographic studies with quantum chemical solid-state calculation in order to predict and to understand more subtle events (*e.g.* proton transfers) occurring in molecular solids.

4.5. Unexpected salt formation at a negative pK_a value: The case of caffeine 2,6-dihydroxybenzoate

4.5.1 Introduction

PAs with poor physicochemical properties are typically formulated as salts, polymorphs, solvates or amorphous solids. In recent years, pharmaceutical cocrystals have emerged as alternative to these solid forms.[76, 77] This up-and-coming class of solids has been shown to exhibit enhanced physicochemical properties comparable to salts and polymorphs. Notably, cocrystals are also regarded as novel and non-obvious, and hence patentable crystal forms.[88] If a cocrystal is the API form of choice for drug-formulation purposes, considerable attention needs to be paid to the selection of cocrystal former (CCF). A well established and widely used criterion in CCF-selection is the ΔpK_a value of the cocrystal components (*i.e.* PA and CCF),[80] which describes the ionization equilibrium behavior in water:

$$\Delta pK_a = pK_a(\text{conjugated acid of the base}) - pK_a(\text{acid})$$

When the ΔpK_a value is greater than 3, the concentration of the ionized components exceeds the concentration of their unionized counterparts in solution whereby salt formation is favored.[80, 273] Conversely, a ΔpK_a<0 implies that the equilibrated solution exhibits an excess of unionized API and CCF molecules resulting in the formation of a

cocrystal, if exists.[273] The ΔpK_a range of 0-3, however, precludes predictions of salt/cocrystal formation since in this ΔpK_a range both salts and cocrystals are likly to form.[265] Up to date, very few cases of salt formation at $\Delta pK_a<0$ are known and, to our knowledge, no studies are reported to elucidate factors contributing to such event. In this section, we report a case where salt formation occurs unexpectedly at $\Delta pK_a< 0$. We also describe how stereoelectronic properties of the CCF significantly contribute to the observed intermolecular proton transfer.

Our ongoing efforts to establish synthon hierarchies in cocrystals comprised of molecules with multiple functional groups lead to the discovery that discovered **caf** and 2,6-dihydroxybenzoic acid (**26DBA**) (Fig. 123) crystallize to form a salt, namely caffeine 2,6-dihydroxybenzoate, **1**, as opposed to an expected cocrystal. This result is surprising considering that both components exhibit pK_a values that, a priori, would support the formation of a cocrystal ($\Delta pK_a \sim -0.6$; pK_a(**caf**, base) = 0.73 ± 0.7, pK_a(**26DBA**, acid) = 1.30 ± 0.1).

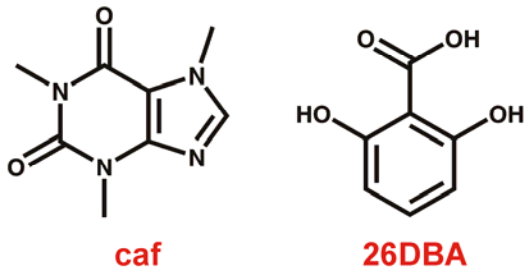

Figure 123 Chemical structures of **caf** and **26DBA**.

To estimate a ΔpK_a value for **caf** and **26DBA** as accurately as possible, we searched the literature for experimentally determined pK_a values for both **caf** and **26DBA**. The literature values are listed in Table 13. Notably, each combination of pK_a(**caf**) and pK_a(**26DBA**) used in the calculation of their ΔpK_a resulted in a negative

value, thus suggesting that the salt formation indeed occurs at a negative ΔpK_a value. In this section, we describe the preparation and structural characterization of the **caf**:**26DBA** salt, as well as quantum-chemical calculations that were performed to elucidate the origins of observed the proton transfer from the carboxylic acid of **26DBA** to the imidazole unit of **caf**.

Table 13 Experimental and calculated pK_a values for **caf** and **26DBA** extracted from the literature.

Ref #	**caf**	**26DBA**	*t* / ºC	Solvent
274	N/A	1.2±0.06	25.0±0.1	H_2O (I=0.1 M)
275	N/A	1.0±0.2	25.0±0.1	H_2O (I=0.2 M)
276	N/A	1.25±0.05	25.0±0.1	H_2O (I=0.1 M)
277	N/A	1.20	25	H_2O (I=0.5 M)
278	N/A	1.08±0.01	25	H_2O (I=0.1 M)
279	N/A	0.91	25	H_2O (I=1.0 M)
280	N/A	1.0	25	H_2O (I=1.0 M)
281	N/A	1.0±0.01	25	H_2O (I=0.2 M)
282	N/A	1.24±0.02	25.0	H_2O (I=0.1 M)
283	N/A	1.29	25.0±0.02	H_2O
283	N/A	1.40	25.0±0.02	1-propanol(aq) (20%)
283	N/A	1.60	25.0±0.02	1-propanol(aq) (30%)
283	N/A	1.63	25.0±0.02	1-propanol(aq) (40%)
283	N/A	1.95	25.0±0.02	1-propanol(aq) (50%)
284	-0.11±0.05	N/A	RT	not reported
245	0.61	N/A	not reported	not reported
285	0.60	N/A	not reported	not reported
272	0.52±0.70	1.30±0.10	not reported	not reported

4.5.2. Experimental section

4.5.2.1. Materials

Caffeine (*ReagentPlus*™), 2,6-dihydroxybenzoic acid (Sigma Aldrich, 98%), acetone (Fluka, >99.5%), acetonitrile (Sigma Aldrich, ACS Reagent, 99.5+%), benzene (Sigma

Aldrich, ACS Reagent, 99%), carbon tetrachloride (Sigma Aldrich, ACS Reagent, 99.9%), cyclohexane (Sigma Aldrich, ACS Reagent, >99%), dimethyl sulfate (Sigma Aldrich, puriss. p.a., ≥99.0% (GC)), 1,4-dioxane (Acros Organics, Spectrophotometric Grade, 99+%), ethanol (Pharmaco-Aaper, ACS/USP Grade, 200 proof), ethyl acetate (Acros Organics, 99.5%), formamide (Sigma Aldrich, ACS Reagent, >99%), glycerol (Sigma Aldrich, 99% (GC)), isopropyl acetate (Sigma Aldrich, 100%), isopropyl alcohol (Sigma Aldrich, ACS Reagent, >99.5%), methanol (Sigma Aldrich, Spectroscopic Grade, >99.9%), methyl ethyl ketone (Sigma Aldrich, spectrophotometric grade, ≥99%), nitromethane (Sigma Aldrich, ACS Reagent, 95+%), succinonitrile (Sigma Aldrich, 99%), tetrahydrofurane (Sigma Aldrich, ACS Reagent, >99.0%), toluene (Acros Organics, ACS Reagent, 99.50%), and water (doubly deionized). All chemicals were used as received.

4.5.2.2. Cocrystal screening

Caf and **26DBA** were investigated for salt/cocrystal formation using the above listed solvents and **SMPT** as screening method.[104] In a typical screening experiment, **caf** (1 mmol) and an equimolar amount of the **255DBA** were suspended in a low volume of a solvent (1-4 mL), and sonicated for 2-5 min to facilitate a phase transformation. The obtained slurries were equilibrated for two weeks at ambient conditions to achieve complete conversions of **caf** and **26DBA** into a cocrystal or salt. The slurries were filtered and the obtained solids were subjected to powder X-ray diffraction (PXRD). The solid were then investigated using IR spectroscopy.

4.5.2.2. Single crystal preparation

Single crystals of the (**caf**)$^{+}$·(**26DBA**)$^{-}$ grown by slow evaporation from solution. Both 0.1 mmol of **caf** and **26DBA** were separately dissolved in acetonitrile (total volume 15 ml), the solutions were combined and filtered through a Millex syringe filter (PVDF,

0.2 μm, 13 mm). The obtained solution was left to evaporate at room temperature until single crystals suitable X-ray diffraction measurements were obtained after one week.

4.5.2.3. Infrared (IR) spectroscopy

Transmission IR spectra of **caf**:**26DBA** salt were retrieved using a Nicolet Magna 750 FT-IR spectrometer. The instrument is equipped with a Nicolet NIC-PLAN microscope and a MCT-A liquid-nitrogen cooled detector. The solids were mounted on a BaF_2 sample holder (13 mm × 1 mm), and scanned 64 times at a resolution of 4 cm^{-1}.

4.5.2.4. Powder X-ray diffraction studies

Diffractograms of all solid were obtained using an *Inel G3000* diffractometer being equipped with a curved position sensitive detector, and parallel beam optics. The instrument was operated with a copper-anode tube (1.5 kW, fine focus) at 40 kV and 30 mA. An incident-beam germanium monochrometer was utilized to obtain monochromatic $K_{\alpha 1}$ irradiation. The instrument was calibrated using a Si standard reference material (*i.e.* NIST 640c) and the attenuated direct beam at one-degree intervals. The instrument was operated using the *Symphonix*[254] program. The data were analyzed using the *Jade*[255] software (version 6.5). All samples were loaded onto Al-sample holder, and leveled with a glass slide.

4.5.2.5. Single crystal X-ray diffraction studies

Single crystal X-ray diffraction measurements of $(\mathbf{caf})^{+}\cdot(\mathbf{26DBA})^{-}$ were performed on a *Bruker APEX2* diffractometer (and a Bruker SMART diffractometer). For data collection s using the SMART system, the single crystals were mounted on a glass pin using epoxy glue. When diffraction data were collected using the APEX2 system, single crystals were positioned on a *MiYeGen* mount with vacuum grease. In both cases, X-ray diffraction data were collected using graphite-filtered MoK_{α} radiation (λ = 0.71069 Å, omega scans, 0.5° steps) at 100, 150, 200 and 298 K. The data were

precessed using *SAINT-Plus* and corrected for Lorentz-polarization effects. Structure solution and refinement were accomplished using *XSHELL*. All non-hydrogen atoms were refined anisotropically. All hydrogen atoms bonded to carbon atoms were located in the Fourier-difference electron density map, fixed in geometrically constrained riding positions, and refined isotropically on the basis of corresponding C-atoms [U(H) = 1.2 U_{eq}(C)]. Hydrogen atoms associated with O- and N-atoms were included in the located positions (*i.e.* coordinates refined) and treated isotropically. Crystallographic data of the investigated compounds are listed in Appendix B (Tables 27, 28). Geometry parameters of selected hydrogen-bonds are listed in Table 14.

4.5.2.6. Quantum-chemical calculations

Ground state geometry optimization of all cluster models were performed in the gas phase using the spin-restricted-resolution-of-identity (RI) MP2 method[286, 287] combined with the TZVP basis set[t288] (and appropriate auxiliary basis sets). Only the valence electrons were correlated (frozen-core approximation). No symmetry constraints were used during the geometry optimization. Geometry optimization convergence was signaled when an energy change between two consecutive optimization iterations was less than 10^{-6} and gradient changes were less than 10^{-3} atomic units. All geometry optimizations were performed using the TURBOMOLE 6.1 program.[289]

Potential energy surface (PES) scans of the **caf**:**26DBA** complex were performed in a simulated dielectric continuum defined by various permittivity values (ε). The dielectric continuum was simulated using a conductor-like screening model COSMO.[290] Solvents used in cocrystal/salt screening methods were simulated by using ε values retrieved from the literature.[245] To simulate an extraordinarily high permittivity medium, we used an epsilon value 200.

Periodic crystal-structure calculations were performed using the CRYSTAL'09 software.[291] Full atom and crystal cell parameter optimizations were performed using the

B3LYP hybrid functional.[292] A shrinking factor of 4 was used to generate a grid of k points in the reciprocal space, whereas tolerances for Coulomb and Exchange sums were set to 7, 7, 7, 7 and 15. SCF convergence threshold on the total energy was 10^{-9}. Basis sets used herein were previously optimized for urea structures, and thus considered as suitable for the performed calculations[293]

4.5.3. Results and discussion

In an attempt to screen **caf** for cocrystal formation using **26DBA** as CCF and acetonitrile as solvent, we discovered the formation of a new phase that was subsequently characterized as a (**caf**)$^{+}$·(**26DBA**)$^{-}$ salt (**cafs**) using single crystal X-ray diffraction and IR spectroscopy.

4.5.3.1. (H-**caf**)$^{+}$·(**26DBA**)$^{-}$ salt

Single crystal X-ray diffraction studies revealed that **1** crystallizes in the monoclinic space group $P2_1/n$ with one 1,3,7-trimethylxanthinium cation, (H-**caf**)$^{+}$, and one 2,6-dihydroxybenzoate (**26DBA**)$^{-}$ anion in the asymmetric unit. Both components form a discrete two-component assembly linked *via* a intermolecular N$^{(+)}$(imidazole)−H···O$^{(-)}$(carboxy) hydrogen bond forming a $R_2^2(7)$ hydrogen-bond pattern (Fig 124a). The *ortho* hydroxyl groups of **26DBA** form a $S_1^1(6)$ hydrogen-bonded pattern that consists of two intramolecular O−H(hydroxy)···O(carboxy) hydrogen bonds (Fig 124a).[257] The (H-**caf**)$^{+}$·(**26DBA**)$^{-}$ complexes are stacked in a "head-to-tail" manner, being held together by π(**caf**)···π(**26DBA**) forces (Fig 124b). The stacks are sustained by weak C−H···O interactions (Fig 124c). All data sets retrieved form the variable-temperature X-ray diffraction studies (100, 150, 200 and 298 K) exhibit the same crystal structure.

Single crystal diffraction data for **cafs** were collected at various temperatures to determine an eventual temperature-dependence of observed proton transfer. Notably, all

retrieved crystal structures exhibit carbon-oxygen bond distances being consistent with the formation of a salt (Table 14).

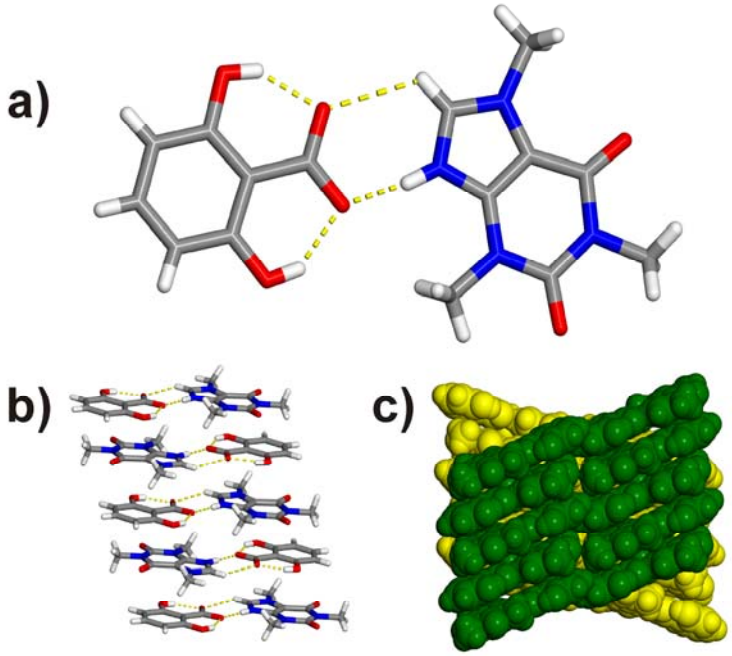

Figure 124 Caffeine 2,6-dihydroxybenzoate: a) caffeine (**caf**) and 2,6-dihydroxybenzoic acid (**26DBA**), X-ray crystal structures of: b) a two-component (H-caf)+·(26DBA)- assembly, c) stacks of (H-**caf**)+·(**26DBA**)$^-$ pairs, and d) stacks (in green and yellow) sustained *via* weak C−H···O interactions.

Table 14 Carbon-oxygen bond distances of the carboxylic groups of the CCF acids

cocrystal	*d*(C–O) / (Å)	*d*(C=O) / (Å)	*Δd* / (Å) (*)
cafs (100 K)	1.293(2)	1.254(3)	0.039(4)
cafs (150 K)	1.292(2)	1.253(3)	0.039(4)
cafs (200 K)	1.292(3)	1.252(3)	0.040(4)
cafs (298 K)	1.288(2)	1.245(3)	0.043(4)

* ***Δd* = [(C–O) - (C=O)]**

The Fourier difference maps also revealed electron densities in close proximity to the imidazole moiety of **caf** that correspond to acidic protons. Moreover, IR-spectra of solid revealed a carbonyl-stretching band below 1600 cm^{-1} being consistent with an ionized carboxylic acids. Based on the location of the acidic protons, the carboxylic group geometry and the IR spectra, the solid of the **caf**:**26DBA** has been shown to exist as salt in the 100-300 K temperature range.

To determine the impact of crystallization conditions on the formation or either a salt or a cocrystal, we performed a series of crystallization experiments wherein **caf** and **26DBA** were allowed to react in 20 solvents with dielectric constants ranging from $\varepsilon = 2.0$ to $\varepsilon = 111.0$ (Fig. 125).

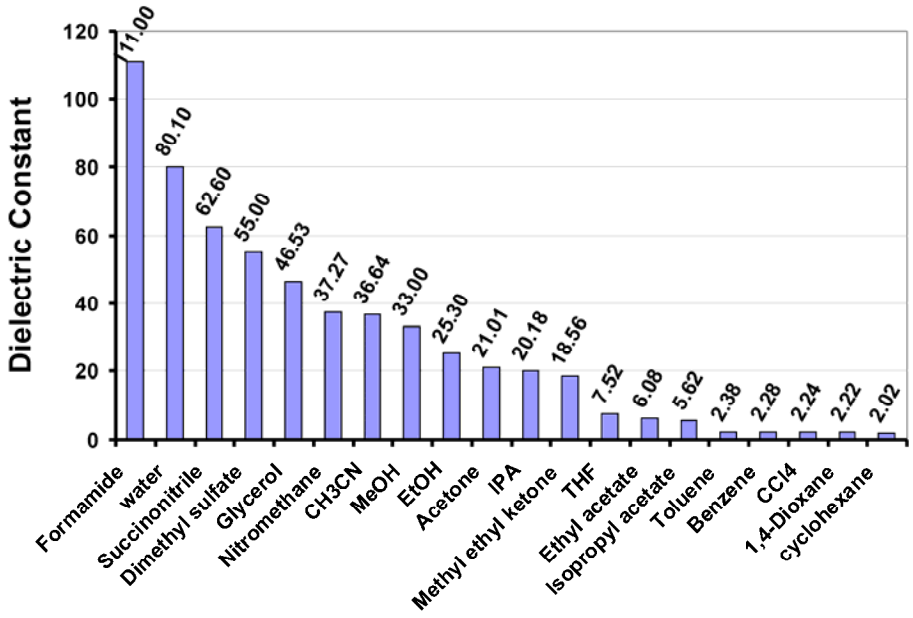

Figure 125 Dielectric constants of solvent used to determine the impact of solvent polarities on the O-H(carboxy, **26DBA**) →N(imidazole, **caf**).

Solvents with high dielectric constants (*e.g.* water, $\varepsilon_r = 80.1$ at 20 ºC) generally have the ability to stabilize charged species and are, thus, expected to support the formation of a salt.[294] On the other hand, solvents with low dielectric constants (*e.g.* cyclohexane, $\varepsilon_r = 2.0$ at 20 ºC), are expected to lack the ability to stabilize charged species and, hence, to facilitate cocrystal formation. Surprisingly, all crystallization trials, except the one wherein formamide was used as solvent, yielded salt **1** as determined *via* PXRD and FT-IR. The screening experiment involving formamide as solvent, however, yielded (**caf**)$^{+}$·(**26DBA**)$^{-}$·(formamide) salt solvate as evidenced by ^{1}H NMR, PXRD and FT-IR. To determine factors responsible for the observed O-H(carboxy, **26DBA**)→N(imidazole, **caf**) proton transfer, we turned to quantum-mechanical calculations. Specifically, calculations involving a conductor-like screening model (COSMO) were utilized to investigate the possibility of a proton transfer in solvents of various dielectric constants (ε). The solvation calculations revealed that no proton transfer is expected to occur in solvents with dielectric constants ranging from 0 to 200. Specifically, **caf**:**26DBA** assemblies optimized in various dielectric-constant environments indicated that the carboxylic acid proton remains bound to the O(carboxy) atom, rather than undergoing a transfer to the imidazole unit of **caf**.

We performed potential energy surface (PES) scans of solvated ($0 \leq \varepsilon \leq 200$) **caf**:**26DBA** assemblies. In the performed PES scans, the H(carboxy,26DBA) atom was moved along the O(carboxy)·····N(imidazole) trajectory and single-point energy calculations were performed for each hydrogen-atom position (Fig. 126). It was determined that, at higher ε values, the PESs exhibits two minima. The minima correspond to **caf**:**26DBA** assemblies wherein the protons occupy positions being consistent with both salt and cocrystal formation (Fig. 126). Although the energy of the "cocrystal" structure was found to be lower than the "salt" structure at each investigated dielectric constant, the energy difference between the relative energies of the salt and the cocrystal was shown to decrease with an increase of solvent polarities (*i.e.* dielectric

constants) (Fig. 126). We therefore conclude that the observed O-H(carboxy, **26DBA**)→N(imidazole, **caf**) proton transfer is most likely not depending on the polarity of the solvent.

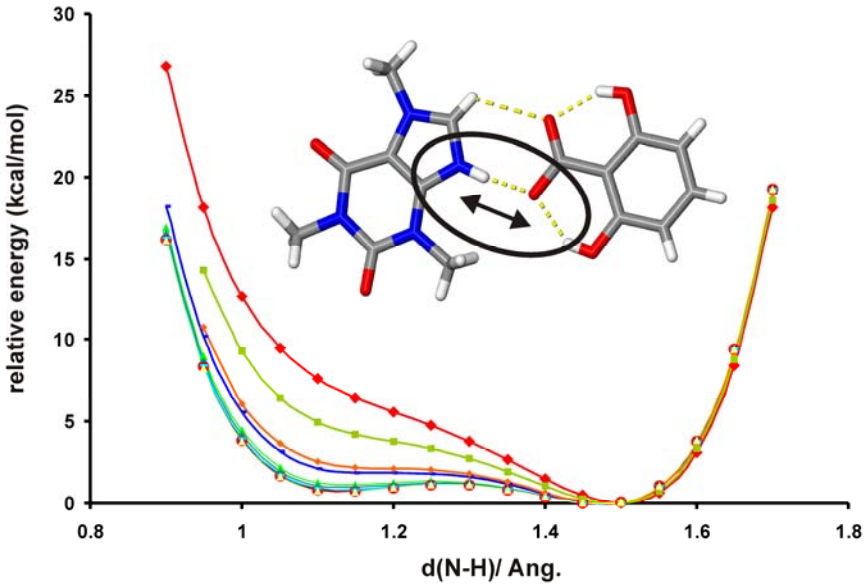

Figure 126 Relative energies of "salt" and "cocrystal" minima, as calculated in various solvents.

Having in mind that **caf** and **2HBA** form a cocrystal rather than a salt (as determined by X-ray diffraction, section 4.2.3.1.), we presumed that the presence of the second *ortho*-hydroxy group play a significant role in the O-H(carboxy, **26DBA**)→N(imidazole, **caf**) proton transfer. Our presumption was also supported by the results of a PES scan of the O(carboxy)···H···N(imidazole) structural fragment belonging to the (**caf**)·(**2HBA**) cocrystal. Specifically, it was determined that solvated complexes (ε = 0, 200) **caf**:**2HBA** complex exhibit only one local minimum that corresponds to a structure wherein the proton sticks to the carboxylic group of **2HBA**, thus demonstrating cocrystal formation (Fig. 127). The existence of a second local

minima in the PES of **caf**:**26DBA** is, therefore, expected to be related to the presence of two *ortho*-hydroxy groups in **26DBA**.

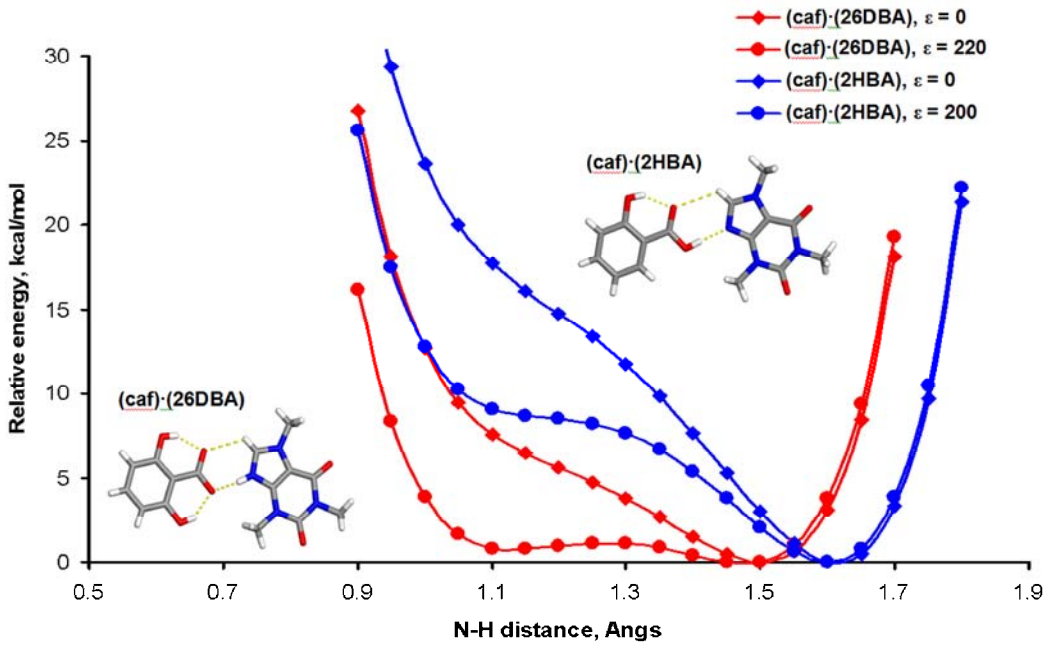

Figure 127 Results of PES scans involving **caf**:**2HBA** and **caf**:**26DBA** complexes.

To determine how the geometry of the second *ortho*-OH(**26DBA**) group simpact the probability of a proton transfer, we have performed a second series of PES scan that involves a second variable, namely the H-atom of the *ortho*-OH(**26DBA**) functional group (Fig. 128). In this series of calculations, the H(carboxy,**26DBA**) atom was moved along the O(carboxy)·····N(imidazole) trajectory to calculate single-point energies for various positions of the H(*ortho*-OH) along the O(COOOH)·····O(OH) trajectory. Remarkably, the calculations revealed that the position of the H(*ortho*-OH) significantly impacts the stability of the ionized **caf**:**26DBA** complex and that a O-H(carboxy, **26DBA**)→N(imidazole, **caf**) proton transfer is triggered once the H(*ortho*-OH) atom is positioned less than 1 Å from the COOH**(26DBA**) group. Notably, the PES

of a complex wherein the H(*ortho*-OH,**26DBA**) atom is positioned 0.974 Å away from O(COOH,**26DBA**) atom reveals only one minimum, rather than two as observed in PES scans involving only one variable (Fig. 128).

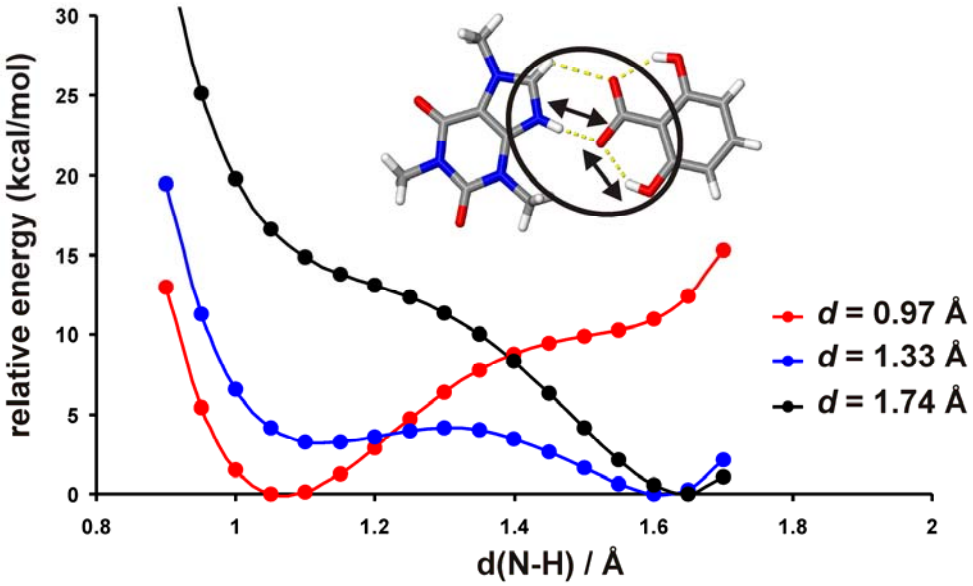

Figure 128 Results of PES scans involving **caf**:**26DBA** complexes wherein the H(*ortho*-OH,**26DBA**) assumes various positions along the O(COOOH) ·····(OH) trajectory.

Having in mind that various physical phenomena (such as intramolecular resonance-assisted hydrogen-bonding, tunneling, or simply thermal motions) can position the H(*ortho*-OH,**26DBA**) atom in close proximity to the O(COOH) group and thereby increase the acidity of the COOH(26DBA group), we conclude that the molecular structure of **26DBA** is responsibly for the proton transfer at $\Delta pK_a<0$.

Finally, periodic crystal structure calculations (*i.e.* full atom and unit-cell parameter optimization) involving **caf**:**26DBA** complexes revealed that the complexes clearly support the O-H(carboxy, **26DBA**)→N(imidazole, **caf**) proton transfer in the solid state. This is not surprising considering that charged (H-**caf**)$^+$ and (**26DBA**)$^-$ species

stabilize each other within molecular stacks (Fig. 129) found the crystal structure of the salt.

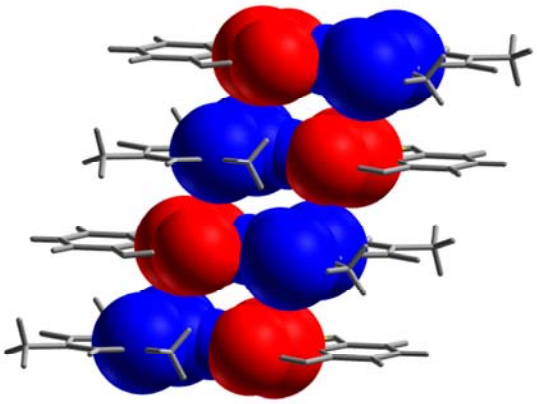

Figure 129 Charged (H-**caf**)$^+$ and (**26DBA**)$^-$ species stabilized within molecular stacks in the solid state (blue: positive charged imidazolium moiety; red – negatively charged benzoate moiety).

Based on results of the presented calculations, we propose that the O-H(carboxy, **26DBA**)→N(imidazole, **caf**) proton transfer occurs as a consequence of resonance-assisted hydrogen-bonding and/or tunneling, and that the charged (H-**caf**)$^+$·(**26DBA**)$^-$ complexes are stabilized in the nucleaction process, thus allowing the growth of a salt, despite a negative ΔpK_a value.

4.5.4. Conclusion

It has been demonstrated that two molecules, namely. **caf** and **26DBA**, can form a salt although their ΔpK_a value strongly suggests the formation of a cocrystal (*i.e.* $\Delta pK_a < 0$). The results presented herein demonstrate that the ΔpK_a value alone is not a conclusive parameter in the CCF-selection process for the design of salts or cocrystals, and that parameters such as molecular structure of CCFs need to be considered in the

drug formulation process. Indeed, that the previously described cocrystallization attempts involving **theo, theb** and **26DBA** yield a salt (see section 4.3.3.7. and 4.4.3.7.), clearly suggests that the molecular structures of "cocrystal" components play a major role in proton transfers.

The ΔpK_a rule of thumb is widely used in drug formulation owing to its facility to reliably predict the occurrence of proton transfers in solid acid-base complexes. However, the results present herein demonstrate the ΔpK_a rule can fail to predict a proton transfer, whereas modern quantum chemical calculations indicated the occurrence of a proton transfer in the crystalline solid state. It is therefore necessary to investigate other solids of PA/CCF systems that exhibit $\Delta pK_a<0$ to potentially elucidate further parameters that account for an eventual salt formation, where cocrystal formation is expected to occur.

Having in mind both the high availability of inexpensive high-performance computer facilities, and the rapid development of powerful (*i.e.* accurate) algorithms for quantum-chemical calculations, it is reasonable to recommend the incorporation of computational studies in drug formulation processes.

4.6. Towards the establishment of synthon hierarchies in related cocrystal systems: Preliminary results and outlook

4.6.1. Introduction

Caf, **theo** and **theb** exhibit functional groups (*e.g.* imidazole, urea, amide, and carbonyl groups) being commonly present in a variety of current drug candidates, and both GRAS and EAFUS compounds. Considering the high occurrence of their functional groups in pharmaceutically relevant compounds, it is reasonable (and important) to develop supramolecular synthons in cocrystals of **caf**, **theo**, **theb** and related xanthine derivatives.

The establishment of synthon hierarchies is expected to lead not only to the knowledge acquisition that will allow to alter physical properties of drug candidates by design – it is also expected to benefit work in related areas of organic solid-state chemistry (*e.g.* organic solid state synthesis, organic electronics). With this in mind we have extended our initial studies to other xanthine alkaloids, namely xanthine (**xan**), 8-chlorotheophylline (**8cth**), acephylline (**ace**) and dyphylline (**dyp**). In addition, we continue our study cocrystals based on xanthine derivatives and other CCFs, namely (di)hydroxynaphthoic acids (shown in Fig 68, section 4.1).

In this section, we *present preliminary results* obtained from cocrystal screening experiments involving **xan**, **ace**, **dyp** and (di)hydroxybenzoic acids, as well as results related to structural analyses of **dyp** cocrystals. Details associated to the performed experiments (*i.e.* materials, cocrystal screening, crystal growth, structural and spectroscopic analyses) and in-depth analyses of the studied crystal structures will be reported elsewhere upon the collection of complete datasets.

The resented results will clearly demonstrate that synthon formation and synthon hierarchies are unexpectedly difficult to predict in cocrystals involving molecules comprised of a larger number of hydrogen-bonding functionalities (as compared to **caf**, **theo** and **theb**).

4.6.2. Preliminary results

We discovered 7 new multi-component phases by subjecting selected purines (*i.e.* **xan**, **ace** and **dyp**) and **CCF**s to **SMPT** (Table 13). Out of the 7 phases, only one has been structurally characterized as cocrystal, namely the 1:1 **dyp**:**23DBA** cocrystal (**dyp1**). The low "hit-rate" might be attributed to the poor solubility of the xanthine derivatives in the utilized solvent (*i.e.* acetonitrile). Specifically, the low solubility of the **PA**s,[245] as compared to **CCF**, is presumed to cause a mismatch in activity values of both cocrystal components, thus providing an insufficient environment for cocrystal

formation.[104] Our efforts are currently focused on the optimization of screening conditions. Specifically, we are utilizing solvents wherein both components exhibit sufficient (*i.e.* similar) solubility.

Table 15 Summary of cocrystal screening results involving xanthine derivatives and (di)hydroxybenzoic acids

	caf	theo	theb	xan	ace	dyp
2HBA						
3HBA						
4HBA						
23DBA						
24DBA						
25DBA						
26DBA						
34DBA						
35DBA						

■ = cocrystal formation, structure determined; ■ = salt formation, structure determined; ■ = new phase detected, structure determination in progress; ■ = no new phase detected, further screening ongoing

Our efforts to structurally characterized the new **xan**, **ace** and **dyp** phases resulted in the determination of the (**dyp**)·(**23DBA**)·(H_2O) cocrystal structure. The (**dyp**)·(**23DBA**)·(H_2O) cocrystal exhibits a very complex hydrogen-bond network based on O-H(hydroxy)···O(hydroxy), O-H(water)···N(imidazole) and O-H(carboxy)···O(hydroxy) hydrogen bonds (Fig. 130). That the carboxy(**23DBA**) group acts as hydrogen-bond donor in an interaction with the hydroxy(**dyp**) group is highly unexpected, and illustrates the sensitivity of the solid-state assembly processes involving molecules with multiple functional groups.

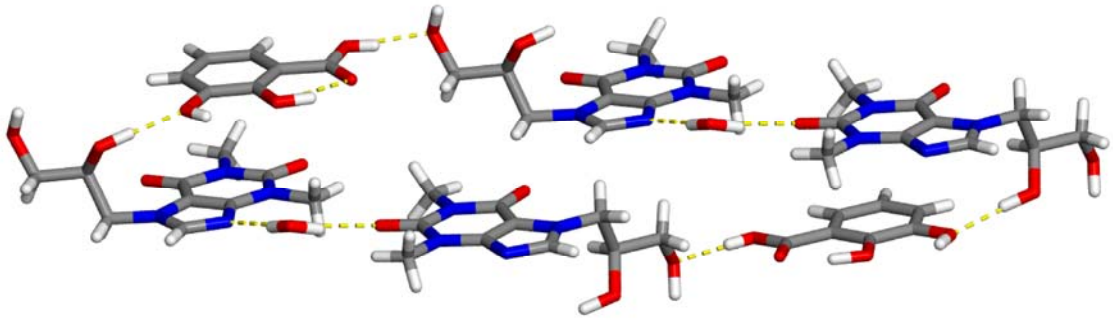

Figure 130 X-ray crystal structure of (**dyp**)·(**23DBA**)·(H_2O) being sustained by O-H(hydroxy)···O(hydroxy), O-H(water)···N(imidazole) and O-H(carboxy)···O(hydroxy) hydrogen bonds.

.

4.6.3 Summary and outlook

The results presented in this chapter demonstrate the complexity of self-assembly processes involving molecules with multiple functional groups. Specifically, it has been shown that *rigid* molecules with *similar molecular* structures, such as **caf**, **theo** and **theb**, exhibit distinct synthon hierarchies in cocrystals based on the same **CCF**s. Furthermore, preliminary results obtained from studies involving structural analogues with flexible functional groups (*i.e.* **dyp**) demonstrate the sensitivity of the solid-state assembly process towards increasing molecular flexibility.

It is the authors believe that the presented results are not carrying great importance as they stand alone. If the field of crystal engineering aims to develop guidelines and principles that grant full control over self-assembly processes in crystalline solids, it is of utmost importance to understand the supramolecular chemistry of functional groups of molecular compounds. Systematic structural studies similar to those presented herein (or as to the reported one by Zaworotko and coworkers[15, 16, 241]) are, therefore, a prerequisite for the development of a base of knowledge that will enable the rational design of cocrystals based on multiple functional groups.

It also the author's opinion that crystallographic studies of molecular cocrystals *alone* are *not sufficient* to gain detailed insights into principles and mechanisms of self-assembly processes involving molecules with multiple functionalities. Quantum-chemical calculations have proven themselves as sufficient tool in both crystal-structure predictions and interpretations of solid-state phenomena and are, thus, anticipated to become a commonly utilized tool in the crystal engineer's "toolbox" in near future. It is expected that such computational methods can also facilitate the understanding of both the nucleation mechanisms of crystals, as well as the role of solvents in such mechanisms.

CHAPTER 5. CONCLUSIONS

The results presented in this thesis demonstrate the utility of synthetic templates (in form of resorcinol derivatives) in controlling solid-state photoreactivity. We have shown that resorcinol can be used at achieve cross-photocycloaddition reaction in cocrystal solid solutions. Specifically, we have shown the photostable solid solutions based on distinct olefins can be activated by the incorporation of synthetic templates into the crystal lattice. By doing so, we achieved a stereospecific [2+2] cross-photocycloaddition in nearly quantitative yields. It is envisioned that templates involving homochiral functional groups could be utilized to construct homochiral molecular targets within chiral crystals. Such opportunity would enable organic synthetic chemists to construct highly complex molecules (*e.g.* natural products) in fewer synthetic steps, with more control and less waste.

We have also shown that products derived form the solid state enable access to materials new materials with intriguing properties. Specifically, we have prepared a thixitropic hydrogel based on amorphous spherical metal-organic nanoparticles. We have used state-or-art analytical methods, namely AFM, STXM and HRTEM to determine their particle size and density. The nanoparticles were shown to transform into films and bundles upon aging. The incorporation of metals into gelators has been recently rocgnized as a significant task since it allows tuning of the gel's properties (*e.g.* magnetic, optical, electronic, rheological).

Our efforts have also resulted in the development of a sonochemical method sufficient for the preparation of nano-dimensional cocrystals. Notably, nano-cocrystals have not been reported in the literature despite their potential technological applicability. It was shown that the small size of such cocrystals supports photoinduced SCSC transformations of olefins into cyclobutanes. We have shown that nano-cocrystals are significantly harder than their macroscopic counterparts. Remarkably, nano-cocrystals

were shown to become harder upon a SCSC [2+2] photodimerization, whereas macrosized cocrystals turn softer. Considering the current ability to design mullti-component organic crystals using principles of crystal engineering, we expect our findings to open possibilities toward tailoring mechanical properties of organic solid-state functional materials.

We have also initiated a systematic study of synthon hierarchies in pharmaceutical cocrystals based on multiple functional groups. For this purpose, we selected a series of xanthine alkaloids (*e.g.* caffeine, theophylline and theobromine) as pharmaceutical model compounds and (di)hydroxybenzoic and (di)hydroxynaphthoic acids as cocrystal formers. Synthon hierarchies for caffeine, theophylline and theobromine were established. We have shown that minor variations in the molecular structure of the pharmaceutical agent seriously impact the self-assembly process and the formation of structural motives within the cocrystal. The great variety of synthon formation and structural motifs observed in the studied cocrystals, as well as the high structural similarity of the studied cocrystal components demonstrates the difficulty of designing molecular cocrystals based on multifunctional molecules. Besides unexpected synthon formation in certain cocrystals, we have also encountered the unanticipated formation of molecular salts at ΔpK_a values. A combined crystallographic and computational study revealed that such unexpected salt formation can be attributed to the molecular structure of the cocrystal former. The gained insights, therefore, clearly suggest that pK_a values alone should not be a conclusive parameter in the cocrystal-former-selection process. Altogether, the presented synthon-hierarchy studies appear to be insignificant as they stand alone considering that more questions can be raised than answered upon analyzing the obtained results. However, the presented studies are significant since they clearly demonstrate the need of more systematic studies on more both related and unrelated cocrystal systems. Notably, our published work on caffeine

cocrystals has triggered several studies concerning solid-state phenomena during our studies (*i.e.* concurrent formation of 1:2 and 2:1 cocrystals).

Since the 1990, tremendous efforts (made by Aakeröy, Bernstein, Desiraju, Etter,, Jones, Resnati, Wuest, Zaworotko and many others lead to the advancement of crystal engineering to a point where one can design and reliably construct two-component molecular crystals wherein the molecules are held together by presumed supramolecular synthons. Such ability has led to the development of functional materials with applications in pharmaceutical sciences, organic synthesis and molecular electronics. Unfortunately, our abilities to design cocrystals based on more than two components, or two components with multiple functional groups are, as shown, very much limited. However, it is the authors strong believe that a large number of systematic synthon-hierarchy studies will eventually lead to a body of knowledge that surely enables the design and construction of cocrystals based on multiple-functional molecules, or even cocrystals comprised of more than three cocrystal formers. It is also expected that computational studies (*e.g.* crystal structure predictions) will greatly support and complement essential X-ray crystallography studies. Having in mind the rapid development of diffractometers and quantum-mechanical algorithms for the prediction of crystal structures and intermolecular interactions in the solid state, it is expected that in near future significant progress will be made in the design of highly complex multi-component molecular solids.

REFERENCES

1. Lehn, J.-M., Supramolecular Chemistry - Scope and Perspectives Molecules - Supermolecules - Molecular Devices. In *Nobel Lectures, Chemistry 1981-1990*, Frängsmyr, T., Ed. World Scientific Publishing Co.: Singapore, 1992.

2. Dunitz, J. D., *Thoughts on Crystals as Supermolecules*. John Wiley & Sons, Ltd.: 2007; p 1-30.

3. Steed, J. W.; Atwood, J. L., *Supramolecular Chemistry*. 2 ed.; John Wiley & Sons, Ltd: Hoboken, New Jersey, 2009.

4. Desiraju, G. R., *Crystal engineering: The design of Organic Solids*. Elsevier: Amsterda, 1989.

5. Pepinsky, R., Crystal engineering: New concept in crystallography. *Phys. Rev.* **1955**, *100*, 971.

6. Pepinsky, R., Determination of crystal structures by means of anomalously scattered X-rays. *Proc Nat Acad Sci USA* **1956**, *42*, 286-92.

7. Schmidt, G. M. J., Photodimerization in the solid state. *Pure Appl. Chem.* **1971**, *27*, 647-678.

8. Aakeröy, C. B.; Seddon, K. R., The hydrogen bond and crystal engineering. *Chemical Society Reviews* **1993**, *22*, 397-407.

9. Desiraju, G. R., Supramolecular synthons in crystal engineering - A new organic synthesis. *Angew. Chem. Int. Ed.* **1995**, *34*, 2311-2327.

10. Corey, E. J., The logic of chemical synthesis: Multistep synthesis of complex carbogenic molecules (Nobel Lecture). *Angew. Chem. Int. Ed.* **1991**, *30*, 455-465.

11. Corey, E. J., Robert Robinson Lecture. Retrosynthetic thinking-essentials and examples. *Chem. Soc. Rev.* **1988,** *17*, 111-133.

12. Doherty, R.; Champness, N., Crystal engineering GRC: Crystal engineering in the mountains. *CrystEngComm* **2010**, *12*, 2644-2645.

13. *SciFinder*, 2007.1; Chemical Abstracts Service: Columbus, OH, 2007.

14. Aakeröy, C. B.; Beatty, A. M.; Helfrich, B. A., "Total synthesis" supramolecular style: Design and hydrogen-bond-directed assembly of ternary supermolecules. *Angew. Chem. Int. Ed.* **2001**, *40*, 3240-3242.

15. Kavuru, P.; Aboarayes, D.; Arora, K. K.; Clarke, H. D.; Kennedy, A.; Marshall, L.; Ong, T. T.; Perman, J.; Pujari, T.; Wojtas, L.; Zaworotko, M. J., Hierarchy of supramolecular synthons: Persistent hydrogen bonds between carboxylates and weakly acidic hydroxyl moieties in cocrystals of zwitterions. *Cryst. Growth Des.* **2010**, *10*, 3568-3584.

16. Shattock, T. R.; Arora, K. K.; Vishweshwar, P.; Zaworotko, M. J., Hierarchy of supramolecular synthons: Persistent carboxylic acid···pyridine hydrogen bonds in cocrystals that also contain a hydroxyl moiety. *Cryst. Growth Des.* **2008**, *8*, 4533-4545.

17. Braga, D., Crystal engineering, Where from? Where to? *Chem. Commun.* **2003**, 2751-2754.

18. Atwood, J. L.; Barbour, L. J.; Jerga, A.; Schottel, B. L., Guest transport in a nonporous organic solid via dynamic van der Waals cooperativity. *Science* **2002**, *298*, 1000-1002.

19. Anastas, P.; Warner, J., *Green Chemistry: Theory and Practice* Oxford University Press: New York, 1998.

20. Riiber, C. N., Synthesis of α-truxillic acid. *Ber. Dtsch. Chem. Ges.* **1902**, *35*, 2411-2415.

21. Riiber, C. N., Polymerization of cinnamylideneacetic acid by light. *Ber. Dtsch. Chem. Ges.* **1913**, *46*, 335-338.

22. de Jong, A. W. K., Action of light on the cinnamic acids and the constitution of the truxillic acids. *Ber. Dtsch. Chem. Ges.Chem. Ges.* **1922**, *56B,* 463-474.

23. Stobbe, H., Light reactions of the cis- and trans-cinnamic acids. *Ber. Dtsch. Chem. Ges.* **1922**, *55B*, 2225-2245.

24. Stobbe, H., Polymerization and depolymerization by light of different wave lengths. II. α- and β-trans-Cinnamic acids, allo-cinnamic acid and their dimers. *Ber. Dtsch. Chem. Ges.* **1925**, *58B*, 2415-2427.

25. de Jong, A. W. K., Constitution of the truxillic and truxinic acids and the action of sunlight on the cinnamic acids and the cinnamic acid salts. *Ber. Dtsch. Chem. Ges.* **1923**, *56B*, 818-8332.

26. Desiraju, G. R., Crystal Engineering: A holistic view. *Angew. Chem. Int. Ed.* **2007**, *46*, 8342-8356.

27. Kohlschütter, V., Über disperses aluminiumhydroxyd. I. *Z. Anorg. Allg. Chem.* **1919**, *105*, 1-25.

28. Schmidt, G. M. J., Topochemistry. III. The crystal chemistry of some trans-cinnamic acids. *J. Chem. Soc.* **1964**, 2014-2021.

29. Fernandes, M. A.; Levendis, D. C.; de Koning, C. B., Solvate and polymorphs of ortho-ethoxy-trans-cinnamic acid: the crystal and molecular structures. *Cryst. Eng.* **2001**, *4*, 215-231.

30. MacGillivray, L. R.; Papaefstathiou, G. S.; Friščić, T.; Hamilton, T. D.; Bučar, D.-K.; Chu, Q.; Varshney, D. B.; Georgiev, I. G., Supramolecular control of reactivity in the solid state: From templates to ladderanes to metal-organic frameworks. *Acc. Chem. Res.* **2008**, *41*, 280-291.

31. Friščić, T.; MacGillivray, L. R., 'Template-switching': a supramolecular strategy for the quantitative, gram-scale construction of a molecular target in the solid state. *Chem. Commun.* **2003**, 1306-1307.

32. Gao, X.; Friščić, T.; MacGillivray, L. R., Supramolecular construction of molecular ladders in the solid state. *Angew. Chem. Int. Ed.* **2004,** *43*, 232-236.

33. Papaefstathiou, G. S.; Hamilton, T. D.; Friščić, T.; MacGillivray, L. R., Self-assembled metal-organic squares derived from linear templates as exemplified by a polydentate ligand that provides access to both a polygon and polyhedron. *Chem. Commun.* **2004**, 270-271.

34. Chu, Q.; Swenson, D. C.; MacGillivray, L. R., A single-crystal-to-single-crystal transformation mediated by argentophilic forces converts a finite metal complex into an infinite coordination network. *Angew. Chem. Int. Ed.* **2005**, *44*, 3569-3572.

35. Papaefstathiou, G. S.; Zhong, Z.; Geng, L.; MacGillivray, L., Coordination-driven self-assembly directs a single-crystal-to-single-crystal transformation that exhibits photocontrolled fluorescence. *J. Am. Chem. Soc.* **2004**, *126*, 9158-9159.

36. Papaefstathiou, G. S.; MacGillivray, L. R., An inverted metal-organic framework with compartmentalized cavities constructed by using an organic bridging unit derived from the solid state. *Angew. Chem. Int. Ed.* **2002**, *41*, 2070-2073.

37. MacGillivray, L. R.; Reid, J. L.; Ripmeester, J. A., Supramolecular control of reactivity in the solid state using linear molecular templates. *J. Am. Chem. Soc.* **2000**, *122*, 7817-7818.

38. Northrop, B. H.; Zheng, Y.-R.; Chi, K.-W.; Stang, P. J., Self-organization in coordination-driven self-assembly. *Acc.Chem. Res.* **2009**, *42*, 1554-1563.

39. Fujita, M.; Tominaga, M.; Hori, A.; Therrien, B., Coordination assemblies from a Pd(II)-cornered square complex. *Acc. Chem. Res.* **2005**, *38*, 369-378.

40. Pluth, M. D.; Bergman, R. G.; Raymond, K. N., Proton-mediated chemistry and catalysis in a self-assembled supramolecular host. *Acc. Chem. Res.* **2009**, *42*, 1650-1659.

41. Horike, S.; Shimomura, S.; Kitagawa, S., Soft porous crystals. *Nat. Chem.* **2009**, *1*, 695-704.

42. Phan, A.; Doonan, C. J.; Uribe-Romo, F. J.; Knobler, C. B.; O'Keeffe, M.; Yaghi, O. M., Synthesis, structure, and carbon dioxide capture properties of zeolitic imidazolate frameworks. *Acc. Chem. Res.* **2009**, *43*, 58-67.

43. Georgiev, I. G.; MacGillivray, L. R., Metal-mediated reactivity in the organic solid state: from self-assembled complexes to metal-organic frameworks. *Chem. Soc. Rev.* **2007**, *36*, 1239-1248.

44. Praetorius, P.; Korn, F., Belichtung ungesättigter Ketone bei Gegenwart von Uranylsalzen. *Ber. Dtsch. Chem. Ges.***1910,** *43*, 2744-2746.

45. Alcock, N. W.; de Meester, P.; Kemp, T. J., Solid-state photochemistry. Part 1. Nature of the stereocontrol in the photodimerisation of dibenzylideneacetone by UO22+ ion: crystal and molecular structure of trans-dichlorobis(trans,trans-dibenzylideneacetone)dioxouranium(VI) and of its acetic acid solvate. *J. Chem. Soc., Perkin Trans. 2* **1979**, 921-926.

46. Lewis, F. D.; Oxman, J. D.; Huffman, J. C., Photodimerization of Lewis acid complexes of cinnamate esters in solution and the solid state. *J. Am. Chem. Soc.* **1984**, *106*, 466-468.

47. Robson, R., Complexes of binucleating ligands I. Two novel binuclear cupric complexes. *Inorg. Nucl. Chem. Lett.* **1970**, *6*, 125-128.

48. Allen, F. H., The Cambridge Structural Database: A quarter of a million crystal structures and rising. *Acta Crystallogr.* **2002**, *B58*, 380-388.

49. Papaefstathiou, G. S.; Georgiev, I. G.; Friščić, T.; MacGillivray, L. R., Directed assembly and reactivity of olefins within a one-dimensional ladder-like coordination polymer based on a dinuclear Zn(ii) platform. *Chem. Commun.* **2005**, 3974-3976.

50. Friščić, T.; MacGillivray, L. R., Single-crystal-to-single-crystal [2+2] photodimerizations: from discovery to design. *Z. Kristallogr.* **2005,** *220*, 351-363.

51. Halasz, I., Single-crystal-to-single-crystal reactivity: Gray, rather than black or white. *Cryst. Growth Des.* **2010**, *10*, 2817-2823.

52. Pyykkö, P., Strong closed-shell interactions in inorganic chemistry. *Chem. Rev.* **1997**, *97*, 597-636.

53. Cheng, K.; Foxman, B. M., Polymerization of dibromobis[tris(2-cyanoethyl)phosphine]nickel: a "triply-specific" solid-state reaction. *J. Am. Chem. Soc.* **1977**, *99*, 8102-8103.

54. J. Blake, A.; R. Champness, N.; S. M. Chung, S.; Li, W.-S.; Schroder, M., In situ ligand synthesis and construction of an unprecedented three-dimensional array with silver(i): A new approach to inorganic crystal engineering. *Chem. Commun.* **1997**, 1675-1676.

55. Simon-Seveyrat, L.; Hajjaji, A.; Emziane, Y.; Guiffard, B.; Guyomar, D., Re-investigation of synthesis of $BaTiO_3$ by conventional solid-state reaction and oxalate coprecipitation route for piezoelectric applications. *Ceram. Int.* **2007**, *33*, 35-40.

56. Lu, J.; Yang, S.; Ng, K. M.; Su, C.-H.; Yeh, C.-S.; Wu, Y.-N.; Shieh, D.-B. Solid-state synthesis of monocrystalline iron oxide nanoparticle based ferrofluid suitable for magnetic resonance imaging contrast application. *Nanotechnology* **2006**, *17*, 5812.

57. Mitzi, D. B.; Feild, C. A.; Harrison, W. T. A.; Guloy, A. M., Conducting tin halides with a layered organic-based perovskite structure. *Nature* **1994**, *369*, 467-469.

58. Kahn, O., Chemistry and physics of supramolecular magnetic materials. *Acc. Chem. Res.* **2000**, *33*, 647-657.

59. Lin, W.; Wang, Z.; Ma, L., A novel octupolar metal-organic NLO material based on a chiral 2D coordination network. *J. Am. Chem. Soc.* **1999**, *121*, 11249-11250.

60. Yoshida, J.-i.; Itami, K., Tag strategy for separation and recovery. *Chem. Rev.* **2002**, *102*, 3693-3716.

61. Lee, S. J.; Lin, W., Chiral Metallocycles: Rational synthesis and novel applications. *Acc. Chem. Res.* **2008**, *41*, 521-537.

62. Papaefstathiou, G. S.; Kipp, A. J.; MacGillivray, L. R., Exploiting modularity in template-controlled synthesis: a new linear template to direct reactivity within discrete hydrogen-bonded molecular assemblies in the solid state. *Chem. Commun.* **2001**, 2462-2463.

63. Hamilton, T. D.; Papaefstathiou, G. S.; MacGillivray, L. R., Discrete and infinite coordination arrays derived from a template-directed, solid-state, organic synthesis. *CrystEngComm* **2002**, *4*, 223-226.

64. Papaefstathiou, G. S.; Milios, C.; MacGillivray, L. R., A 2D metal-organic framework with two different rhombus-shaped cavities: a rare example of a (4,4)-net with alternating metal and organic nodes. *Micropor. Mesopor. Mater.* **2004**, 11-15.

65. Papaefstathiou, G. S.; Friščić, T.; MacGillivray, L. R., Design and construction of a 2D metal-organic framework with multiple cavities: A nonregular net with a paracyclophane that codes for multiply fused nodes. *J. Am. Chem. Soc.* **2005**, *127*, 14160-14161.

66. Yoshizawa, M.; Tamura, M.; Fujita, M., AND/OR bimolecular recognition. *J. Am. Chem. Soc.* **2004**, *126*, 6846-6847.

67. Nishioka, Y.; Yamaguchi, T.; Kawano, M.; Fujita, M., Asymmetric [2 + 2] olefin cross photoaddition in a self-assembled host with remote chiral auxiliaries. *J. Am. Chem. Soc.* **2008**, *130*, 8160-8161.

68. Hamilton, T. D.; Papaefstathiou, G. S.; MacGillivray, L. R., A polyhedral host constructed using a linear template. *J. Am. Chem. Soc.* **2002**, *124*, 11606-11607.

69. Hamilton, T. D.; Papaefstathiou, G. S.; Friščić, T.; Bučar, D.-K.; MacGillivray, L. R., Onion-Shell Metal-Organic Polyhedra (MOPs): A general approach to decorate the exteriors of MOPs using principles of supramolecular chemistry. *J. Am. Chem. Soc.* **2008**, *130*, 14366-14367.

70. Hamilton, T. D.; Bučar, D.-K.; MacGillivray, L. R., Coding a coordination-driven self-assembly via a hydrogen bond-directed solid-state synthesis: An unexpected chiral tetrahedral capsule. *Chem. Commun.* **2007**, 1603-1604.

71. Friščić, T.; Trask, A. V.; Jones, W.; Motherwell, W. D. S., Screening for inclusion compounds and systematic construction of three-component solids by liquid-assisted grinding. *Angew. Chem. Int. Ed.* **2006,** *45*, 7546-7550.

72. Qiu, Y.; Chen, Y.; Zhang, G. G. Z.; Liu, L.; Porter, W., *Developing solid oral dosage forms: Pharmaceutical theory & practice*. 1 ed.; Elsevier: New York, 2009.

73. Bastin, R. J.; Bowker, M. J.; Slater, B. J., Salt selection and optimisation procedures for pharmaceutical new chemical entities. *Org. Process Res. Dev.* **2000,** *4*, 427-435.

74. Morissette, S. L.; Almarsson, Ö.; Peterson, M. L.; Remenar, J. F.; Read, M. J.; Lemmo, A. V.; Ellis, S.; Cima, M. J.; Gardner, C. R., High-throughput crystallization: polymorphs, salts, co-crystals and solvates of pharmaceutical solids. *Adv. Drug Del. Rev.* **2004,** *56*, 275-300.

75. Serajuddin, A. T. M., Salt formation to improve drug solubility. *Adv. Drug Del. Rev.* **2007**, *89*, 603-616.

76. Vishweshwar, P.; McMahon, J. A.; Bis, J. A.; Zaworotko, M. J., Pharmaceutical co-crystals. *J. Pharm. Sci.* **2006**, *95*, 499-516.

77. Jones, W.; Motherwell, W. D. S.; Trask, A. V., Pharmaceutical cocrystals: An emerging approach to physical property enhancement. *MRS Bull.* **2006**, *31*, 875-879.

78. Trask, A. V.; Haynes, D. A.; Motherwell, W. D. S.; Jones, W., Screening for crystalline salts via mechanochemistry. *Chem. Commun.* **2006**, 51-53.

79. Karki, S.; Friščić, T.; Fabian, L.; Jones, W., New solid forms of artemisinin obtained through cocrystallisation. *CrystEngComm* **2010**, *12*, 4038-4041.

80. Stahl, P. H.; Wermuth, C. G., *Handbook of pharmaceutical salts : Properties, selection, and use* Verlag Helvetica Chimica Acta Wiley-VCH Zürich Weinheim, 2002.

81. Berstein, J., *Polymorphism in molecular crystals* Oxford University Press: New York, 2002; Vol. 14.

82. Gavezzotti, A., A Solid-state chemist's view of the crystal polymorphism of organic compounds. *J. Pharm. Sci.* **2007**, *96*, 2232-2241.

83. Day, G. M.; Cooper, T. G.; Cruz-Cabeza, A. J.; Hejczyk, K. E.; Ammon, H. L.; Boerrigter, S. X. M.; Tan, J. S.; Valle, R. G. D.; Venuti, E.; Jose, J.; Gadre, S. R.; Desiraju, G. R.; Thakur, T. S.; Eijck, B. P. v.; Facelli, J. C.; Bazterra, V. E.; Ferraro, M. B.; Hofmann, D. W. M.; Neumann, M. A.; Leusen, F. J. J.; Kendrick, J.; Price, S. L.; Misquitta, A. J.; Karamertzanis, P. G.; Welch, G. W. A.; Scheraga, H. A.; Arnautova, Y. A.; Schmidt, M. U.; Streek, J. v. d.; Wolf, A. K.; Schweizerr, B., Significant progress in predicting the crystal structures of small organic molecules - a report on the fourth blind test. *Acta Crystallogr.***2009**, *B65*, 107-125.

84. Dunitz, J. D.; Bernstein, J., Disappearing polymorphs. *Acc. Chem. Res.* **1995**, *28*, 193-200.

85. Bauer, J.; Spanton, S.; Henry, R.; Quick, J.; Dziki, W.; Porter, W.; Morris, J., Ritonavir: An extraordinary example of conformational polymorphism. *Pharmaceutical Research* **2001**, *18*, 859-866.

86. Chemburkar, S. R.; Bauer, J.; Deming, K.; Spiwek, H.; Patel, K.; Morris, J.; Henry, R.; Spanton, S.; Dziki, W.; Porter, W.; Quick, J.; Bauer, P.; Donaubauer, J.; Narayanan, B. A.; Soldani, M.; Riley, D.; McFarland, K., Dealing with the impact of ritonavir polymorphs on the late stages of bulk drug process development. *Organic Process Research & Development* **2000**, *4*, 413-417.

87. Di Martino, P.; Guyot-Hermann, A. M.; Conflant, P.; Drache, M.; Guyot, J. C., A new pure paracetamol for direct compression: The orthorhombic form. *Int. J. Pharm.* **1996,** *128*, 1-8.

88. Trask, A. V., An Overview of pharmaceutical cocrystals as intellectual property. *Mol. Pharm.* **2007**, *4*, 301-309.

89. Shan, N.; Zaworotko, M. J., The role of cocrystals in pharmaceutical science. *Drug Discov. Today* **2008**, *13*, 440-446.

90. Schultheiss, N.; Newman, A., Pharmaceutical cocrystals and their physicochemical properties. *Cryst. Growth Des.* **2009**, *9*, 2950-2967.

91. Nehm, S. J.; Rodríguez-Spong, B.; Rodríguez-Hornedo, N., Phase solubility diagrams of cocrystals are explained by solubility product and solution complexation. *Cryst. Growth Des.* **2006**, *6*, 592-600.

92. Remenar, J. F.; Morissette, S. L.; Peterson, M. L.; Moulton, B.; MacPhee, J. M.; Guzman, H. R.; Almarsson, O., Crystal engineering of novel cocrystals of a triazole drug with 1,4-dicarboxylic acids. *J. Am. Chem. Soc.* **2003**, *125*, 8456-8457.

93. Childs, S. L.; Chyall, L. J.; Dunlap, J. T.; Smolenskaya, V. N.; Stahly, B. C.; Stahly, G. P., Crystal engineering approach to forming cocrystals of amine hydrochlorides with organic acids. Molecular complexes of fluoxetine hydrochloride with benzoic, succinic, and fumaric acids. *J. Am. Chem. Soc.* **2004**, *126*, 13335-13342.

94. McNamara, D. P.; Childs, S. L.; Giordano, J.; Iarriccio, A.; Cassidy, J.; Shet, M. S.; Mannion, R.; O'Donnell, E.; Park, A., Use of a glutaric acid cocrystal to improve oral bioavailability of a low solubility API. *Pharm. Res.* **2006**, *23*, 1888-1897.

95. Trask, A. V.; Motherwell, W. D. S.; Jones, W., Pharmaceutical cocrystallization: engineering a remedy for caffeine hydration. *Cryst. Growth Des.* **2005**, *5*, 1013-1021.

96. Trask, A. V.; Motherwell, W. D. S.; Jones, W., Physical stability enhancement of theophylline via cocrystallization. *Int. J. Pharm.* **2006,** *320*, 114-123.

97. Sun, C. C.; Hou, H., Improving mechanical properties of caffeine and methyl gallate crystals by cocrystallization. *Cryst. Growth Des.* **2008**, *8*, 1575-1579.

98. Karki, S.; Friščić, T.; László, F.; Peter, R. L.; Graeme, M. D.; William, J., Improving mechanical properties of crystalline solids by cocrystal formation: New compressible forms of paracetamol. *Adv. Mater.* **2009**, *21*, 3905-3909.

99. Chattoraj, S.; Shi, L.; Sun, C. C., Understanding the relationship between crystal structure, plasticity and compaction behaviour of theophylline, methyl gallate, and their 1 : 1 co-crystal. *CrystEngComm* **2010**, *12*, 2466-2472.

100. Datta, S.; Grant, D. J. W., Crystal Structures of Drugs: Advances in determination, prediction and engineering. *Nat. Rev. Drug Discovery* **2004**, *3*, 42-57.

101. Friščić, T.; Jones, W., Recent Advances in understanding the mechanism of cocrystal formation via grinding. *Cryst. Growth Des.* **2009**, *9*, 1621-1637.

102. Friščić, T.; Trask, A. V.; Motherwell, W. D. S.; Jones, W., Guest-directed assembly of caffeine and succinic acid into topologically different heteromolecular host networks upon grinding *Cryst. Growth Des.* **2008**, *8*, 1605-1609.

103. Friščić, T.; Fábián, L.; Burley, J. C.; Jones, W.; Motherwell, W. D. S., Exploring cocrystal–cocrystal reactivity via liquid-assisted grinding: the assembling of racemic and dismantling of enantiomeric cocrystals. *Chem.Commun.* **2006**, 5009-5011.

104. Zhang, G. G. Z.; Henry, R. F.; Borchardt, T. B.; Lou, X., Efficient co-crystal screening using solution-mediated phase transformation. *J. Pharm. Sci.* **2007**, *96*, 990-995.

105. Khankari, R. K.; Grant, D. J. W., Pharmaceutical hydrates. *Thermochimica Acta* **1995**, *248*, 61-79.

106. In an approximation, a_{CCF} equals the ratio of the concentration of the free cocrystal former in solution and the solubility of the cocrystal former in the absence of the drug, or the ratio of vapor pressure and the saturated vapor pressure.

107. Unpublished results.

108. Nishijo, J.; Takenaka, F.; Tanaka, I., The interaction of caffeine with several aliphatic organic dibasic acids in solid State. *J. Pharm. Soc. Jpn.* **1980,** 100, 732-738.

109. Gratton, S. E. A.; Williams, S. S.; Napier, M. E.; Pohlhaus, P. D.; Zhou, Z.; Wiles, K. B.; Maynor, B. W.; Shen, C.; Olafsen, T.; Samulski, E. T.; DeSimone, J. M., The pursuit of a scalable nanofabrication platform for use in material and life science applications. *Acc. Chem. Res.* **2008**, *41*, 1685-1695.

110. Kwon, S. G.; Hyeon, T., Colloidal chemical synthesis and formation kinetics of uniformly sized nanocrystals of metals, oxides, and chalcogenides. *Acc. Chem. Res.* **2008**, *41*, 1696-1709.

111. Murphy, C. J., Spatial control of chemistry on the inside and outside of inorganic nanocrystals. *ACS Nano* **2009**, *3*, 770-774.

112. Rongchao, J., Super robust nanoparticles for biology and biomedicine. *Angew. Chem. Int. Ed.* **2008**, *47*, 6750-6753.

113. Skrabalak, S. E.; Xia, Y., Pushing nanocrystal synthesis toward nanomanufacturing. *ACS Nano* **2009**, *3*, 10-15.

114. Masahura, H.; Nakanishi, H.; Sasaki, K., *Single organic nanoparticles*. Springer Verlag: Berlin, Heidelberg, New York, 2003.

115. Takahashi, S.; Miura, H.; Kasai, H.; Okada, S.; Oikawa, H.; Nakanishi, H., Single-crystal-to-single-crystal transformation of diolefin derivatives in nanocrystals. *J. Am. Chem. Soc.* **2002**, *124*, 10944-10945.

116. Hung, J. D.; Lahav, M.; Luwisch, M.; Schmidt, G. M. J., Topochemistry. XXXV. Formation of mixed dimers from solid solutions of trans-cinnamic acids and trans-cinnamides. *Israel J. Chem.* **1972**, *10*, 585-599.

117. Cohen, M. D.; Cohen, R.; Lahav, M.; Nie, P. L., Topochemistry. Part XXXVI. Relative yields of photodimers from mixed crystals of trans-cinnamic acids and trans-cinnamides. *J. Chem. Soc., Perkin Trans. 2* **1973**, 1095-1100.

118. Elgavi, A.; Green, B. S.; Schmidt, G. M. J., Reactions in chiral crystals. Optically active heterophotodimer formation from chiral single crystals. *J. Am. Chem. Soc.* **1973**, *95*, 2058-2059.

119. Jones, W.; Theocharis, C. R.; Thomas, J. M.; Desiraju, G. R., Structural mimicry and the photoreactivity of organic solids *J. Chem. Soc., Chem. Commun.* **1983**, 23, 1443-1444.

120. Theocharis, C. R.; Desiraju, G. R.; Jones, W., The use of mixed crystals for engineering organic solid-state reactions: application to benzylbenzylidenecyclopentanones. *J. Am. Chem. Soc.* **1984**, *106*, 3606-3609.

121. Kinabara, K.; Adegawa, Y.; Saigo, K.; Hasegawa, M., Formation of a topochemically photoreactive mixed crystal by grinding and its mechanistic interpretation. *Bull. Chem. Soc. Jpn.* **1993**, *66*, 1204-1210.

122. Suzuki, T.; Fukushima, T.; Yamashita, Y.; Miyashi, T., An absolute asymmetric synthesis of the [2 + 2] cycloadduct via single crystal-to-single crystal transformation by charge-transfer excitation of solid-state molecular complexes composed of arylolefins and bis[1,2,5]thiadiazolotetracyanoquinodimethanet. *J. Am. Chem. Soc.* **1994**, *116*, 2793-2803.

123. Sonoda, Y.; Goto, M.; Tsuzuki, S.; Akiyama, H.; Tamaoki, N., [2 + 2] Photodimerization and photopolymerization of diphenylhexatriene crystals utilizing perfluorophenyl-phenyl stacking interactions. *J. Fluorine Chem.* **2009**, *130*, 151-157.

124. Nishioka, Y.; Yamaguchi, T.; Kawano, M.; Fujita, M., Asymmetric [2 + 2] olefin cross photoaddition in a self-assembled host with remote chiral auxiliaries. *J. Am. Chem. Soc.* **2008**, *130*, 8160-8161.

125. Dabros, M.; Emery, P. R.; Thalladi, V. R., A supramolecular approach to organic alloys: Cocrystals and three- and four-component solid solutions of 1,4-diazabicyclo[2.2.2]octane and 4-X-phenols (X=Cl, CH_3, Br). *Angew. Chem. Int. Ed.* **2007**, *46*, 4132-4135.

126. Oliveira, M. A.; Peterson, M. L.; Klein, D., Continuously substituted solid solutions of organic co-crystals. *Cryst. Growth Des.* **2008**, *8*, 4487-4493.

127 Attempts to cocrystallize **ClPE** and **MePE** in a 1:1 ratio resulted in the formation of a solid solution composed of both reactants in a 3:1 ratio. ^{1}H NMR spectroscopy revealed that the solid solution remained photostable upon UV irradiation (broadband medium-pressure Hg-lamp, 450 W) for 25 hours.

128. MacGillivray, L. R.; Reid, J. L.; Ripmeester, J. A.; Papaefstathiou, G. S., Toward a reactant library in template-directed solid-state organic synthesis: Reactivity involving a monofunctional reactant based on a stilbazole. *Ind. Eng. Chem. Res.* **2002**, *41*, 4494-4497.

129. Kitaiigorodskii, A. I., *Molecular crystals and molecules*. Academic Press: London, 1973.

130. Jones, W.; Nakanishi, H.; Theocharis, C. R.; Thomas, J. M., Engineering organic crystals so as to control the photoreactivity of the reactants and the crystallinity of the products. *J. Chem. Soc., Chem. Commun.* **1980**, 610-611.

131. Lee, K. Y.; Mooney, D. J., Hydrogels for Tissue Engineering. *Chem. Rev.* **2001**, *101*, 1869-1880.

132. Xing, B.; Choi, M.-F.; Xu, B., A stable metal coordination polymer gel based on a calix[4]arene and its "uptake" of non-ionic organic molecules from the aqueous phase. *Chem. Commun.* **2002**, 362-363.

133. Tiller, J., C., Increasing the local concentration of drugs by hydrogel formation. *Angew. Chem. Int. Ed.* **2003**, *42*, 3072-3075.

134. Li, J.; Ni, X.; Leong, K., W., Injectable drug-delivery systems based on supramolecular hydrogels formed by poly(ethylene oxide)s and alpha-cyclodextrin. *J. Biomed. Mater. Res. A* **2003**, *65A*, 196-202.

135. Kiyonaka, S.; Sugiyasu, K.; Shinkai, S.; Hamachi, I., First thermally responsive supramolecular polymer based on glycosylated amino acid. *J. Am. Chem. Soc.* **2002**, *124*, 10954-10955.

136. Zhou, S.-L.; Matsumoto, S.; Tian, H.-D.; Yamane, H.; Ojida, A.; Kiyonaka, S.; Hamachi, I., pH-Responsive Shrinkage/Swelling of a Supramolecular Hydrogel Composed of Two Small Amphiphilic Molecules. *Chem. Eur. J.* **2005**, *11*, 1130-1136.

137. Estroff, L. A.; Addadi, L.; Weiner, S.; Hamilton, A. D., An organic hydrogel as a matrix for the growth of calcite crystals. *Org. Biomol. Chem.* **2004**, *2*, 137-141.

138. Bhuniya, S.; Park, S. M.; Kim, B. H., Biotin-amino acid conjugates: An approach toward self-assembled hydrogelation. *Org. Lett.* **2005**, *7*, 1741-1744.

139. Estroff, L. A.; Hamilton, A. D., Water gelation by small organic molecules. *Chem. Rev.* **2004**, *104*, 1201-1218.

140. Oshovsky, G. V.; Reinhoudt, D. N.; Verboom, W., Supramolecular chemistry in water. *Angew. Chem. Int. Ed.* **2007**, *46*, 2366-2393.

141. Swiegers, G. F.; Malefetse, T. J., New self-assembled structural motifs in coordination chemistry. *Chem. Rev.* **2000**, *100*, 3483-3538.

142. Paulusse, J. M. J.; van Beek, D. J. M.; Sijbesma, R. P., Reversible switching of the sol-gel transition with ultrasound in rhodium(I) and iridium(I) coordination networks. *J. Am. Chem. Soc.* **2007**, *129*, 2392-2397.

143. Fages, F., Metal coordination to assist molecular gelation. *Angew. Chem. Int. Ed.* **2006**, *45*, 1680-1682.

144. Beck, J. B.; Rowan, S. J., Multistimuli, multiresponsive metallo-supramolecular polymers. *J. Am. Chem. Soc.* **2003**, *125*, 13922-13923.

145. Weng, W.; Li, Z.; Jamieson, A. M.; Rowan, S. J., Control of gel morphology and properties of a class of metallo-supramolecular polymers by good/poor solvent environments. *Macromolecules* **2009**, *42*, 236-246.

146. Piepenbrock, M.-O. M.; Lloyd, G. O.; Clarke, N.; Steed, J. W., Metal- and anion-binding supramolecular gels. *Chemical Reviews* **2009**, *110*, 1960-2004.

147. Kawano, S.-I.; Fujita, N.; Shinkai, S., A Coordination gelator that shows a reversible chromatic change and sol-gel phase-transition behavior upon oxidative/reductive stimuli. *J. Am. Chem. Soc.* **2004**, *126*, 8592-8593.

148. Grondin, P.; Roubeau, O.; Castro, M.; Saadaoui, H.; Colin, A.; Clérac, R., Multifunctional gels from polymeric spin-crossover metallo-gelators. *Langmuir* **2010**, *26*, 5184-5195.

149. Miravet, J. F.; Escuder, B., Pyridine-functionalised ambidextrous gelators: towards catalytic gels. *Chem. Commun.* **2005**, 5796-5798.

150. Jung, J. H.; John, G.; Masuda, M.; Yoshida, K.; Shinkai, S.; Shimizu, T., Self-Assembly of a Sugar-Based Gelator in Water: Its remarkable diversity in gelation ability and aggregate structure. *Langmuir* **2001**, *17*, 7229-7232.

151. Varshney, D. B.; Papaefstathiou, G. S.; MacGillivray, L. R., Site-directed regiocontrolled synthesis of a 'head-to-head' photodimer via a single-crystal-to-single-crystal transformation involving a linear template. *Chem. Commun.* **2002**, 1964-1965.

152. Hamilton, T. D.; Bučar, D.-K.; MacGillivray, L. R., A metal-organic framework with three cavities based derived from a cyclobutane constructed in the solid state. *New J. Chem.* **2010**, *34,* 2400-2402.

153. Hamilton, T. D. Metal-organic polygons, polyhedra, and extended structures - assemblies arising from products of templatedirected synthesis in the solid state. University of Iowa, Iowa City, **2005**.

154. Oh, M.; Mirkin, C. A., Chemically tailorable colloidal particles from infinite coordination polymers. *Nature* **2005**, *438*, 651-654.

155. Johnson, C. A.; Sharma, S.; Subramaniam, B.; Borovik, A. S., Nanoparticulate metal complexes prepared with compressed carbon dioxide: Correlation of particle morphology with precursor structure. *J. Am. Chem. Soc.* **2005**, *127*, 9698-9699.

156. Champness, Neil R., Coordination Polymers: From metal-organic frameworks to spheres. *Angew. Chem. Int. Ed.* **2009**, *48*, 2274-2275.

157. Maeda, H.; Hasegawa, M.; Hashimoto, T.; Kakimoto, T.; Nishio, S.; Nakanishi, T., Nanoscale spherical architectures fabricated by metal coordination of multiple dipyrrin moieties. *J. Am. Chem. Soc.* **2006**, *128*, 10024-10025.

158. Imaz, I.; Hernando, J.; Ruiz-Molina, D.; Maspoch, D., Metal-organic spheres as functional systems for guest encapsulation. *Angew. Chem. Int. Ed.* **2009**, *48*, 2325-2329.

159. Imaz, I.; Maspoch, D.; Rodríguez-Blanco, C.; Pérez-Falcón, José M.; Campo, J.; Ruiz-Molina, D., Valence-tautomeric metal-organic nanoparticles. *Angew. Chem. Int. Ed.* **2008**, *47*, 1857-1860.

160. Vriezema, D. M.; Hoogboom, J.; Velonia, K.; Takazawa, K.; Christianen, P. C. M.; Maan, J. C.; Rowan, A. E.; Nolte, R. J. M., Vesicles and polymerized vesicles from thiophene-containing rod-coil block copolymers. *Angew. Chem. Int. Ed.* **2003**, *42*, 772-776.

161. Coronado, E.; Galán-Mascarós, J. R.; Monrabal-Capilla, M.; García-Martínez, J.; Pardo-Ibáñez, P., Bistable spin-crossover nanoparticles showing magnetic thermal hysteresis near room temperature. *Adv. Mater.* **2007**, *19*, 1359-1361.

162. Rieter, W. J.; Taylor, K. M. L.; Lin, W., Surface modification and functionalization of nanoscale metal-organic frameworks for controlled release and luminescence sensing. *J. Am. Chem. Soc.* **2007**, *129*, 9852-9853.

163. Wenbin, L.; William , J. R.; Kathryn , M. L. T., Modular Synthesis of Functional Nanoscale Coordination Polymers. *Angew. Chem. Int. Ed.* **2009**, *48*, 650-658.

164. Horcajada, P.; Chalati, T.; Serre, C.; Gillet, B.; Sebrie, C.; Baati, T.; Eubank, J. F.; Heurtaux, D.; Clayette, P.; Kreuz, C.; Chang, J.-S.; Hwang, Y. K.; Marsaud, V.; Bories, P.-N.; Cynober, L.; Gil, S.; Férey, G.; Couvreur, P.; Gref, R., Porous metal-organic-framework nanoscale carriers as a potential platform for drug delivery and imaging. *Nat. Mater.* **2010**, *9*, 172-178.

165. Rieter, W. J.; Pott, K. M.; Taylor, K. M. L.; Lin, W., Nanoscale coordination polymers for platinum-based anticancer drug delivery. *J. Am. Chem. Soc.* **2008**, *130*, 11584-11585.

166. Taylor, K. M. L.; Rieter, W. J.; Lin, W., Manganese-based nanoscale metal-organic frameworks for magnetic resonance imaging. *J. Am. Chem. Soc.* **2008**, *130*, 14358-14359.

167. Weng, W.; Beck, J. B.; Jamieson, A. M.; Rowan, S. J., Understanding the mechanism of gelation and stimuli-responsive nature of a class of metallo-supramolecular gels. *J. Am. Chem. Soc.* **2006**, *128*, 11663-11672.

168. Shirakawa, M.; Fujita, N.; Shinkai, S., A Stable single piece of unimolecularly π-stacked porphyrin aggregate in a thixotropic low molecular weight gel: A one-dimensional molecular template for polydiacetylene wiring up to several tens of micrometers in length. *J. Am. Chem. Soc.* **2005**, *127*, 4164-4165.

169. Lescanne, M.; Grondin, P.; d'Aleo, A.; Fages, F.; Pozzo, J. L.; Monval, O. M.; Reinheimer, P.; Colin, A., Thixotropic organogels based on a simple N-hydroxyalkyl amide: Rheological and aging properties. *Langmuir* **2004**, *20*, 3032-3041.

170. Sun, X.; Tabakman, S., M. ; Seo, W.-S.; Zhang, L.; Zhang, G.; Sherlock, S.; Bai, L.; Dai, H., Separation of nanoparticles in a density gradient: FeCo@C and gold nanocrystals. *Angew. Chem. Int. Ed.* **2009**, *48*, 939-942.

171. Sevonkaev, I.; Halaciuga, I.; Goia, D. V.; Matijević, E., Distribution of density in spherical colloidal particles by transmission electron microscopy. *Colloids Surf., A* **2010**, *354*, 16-21.

172. Godin, M.; Bryan, A. K.; Burg, T. P.; Babcock, K.; Manalis, S. R., Measuring the mass, density, and size of particles and cells using a suspended microchannel resonator. *Appl. Phys. Lett.* **2007**, *91*, 123121-123123.

173. Hooft, R. W. W. *Collect*, Nonius BV: Delft, The Netherlands, **1998**.

174. Otwinowski, Z.; Minor, W., *Processing of X-ray diffraction data collected in oscillation mode*. **1997**; Vol. 276: Macromolecular Crystallography, Part A

175. Sheldrick, G. M., A short history of SHELX. *Acta Cryst.* **2008**, A64, 112-122.

176. Spek, A. L., PLATON - A multipurpose crystallographic tool. *Acta Crystallogr.* **1990**, *A46*, C34.

177. Ma, Y.; Chen, C. T.; Meigs, G.; Randall, K.; Sette, F., High-resolution *K*-shell photoabsorption measurements of simple molecules. *Physical Review A* **1991**, *44*, 1848-1858.

178. Gelator weight based on combined weight of metal and organic components.

179. Snip, E.; Shinkai, S.; Reinhoudt, D. N., Organogels of a nucleobase-bearing gelator and the remarkable effects of nucleoside derivatives and a porphyrin derivative on the gel stability. *Tetrahedron Lett.* **2001**, *42*, 2153-2156.

180. Snip, E.; Koumoto, K.; Shinkai, S., Gel formation properties of a uracil-appended cholesterol gelator and cooperative effects of the complementary nucleobases. *Tetrahedron* **2002**, *58*, 8863-8873.

181. de Loos, M.; van Esch, J.; Stokroos, I.; Kellogg, R. M.; Feringa, B. L., Remarkable stabilization of self-assembled organogels by polymerization. *J. Am. Chem. Soc.* **1997**, *119*, 12675-12676.

182. The blue colour of the gel is consistent with the Cu(II) ions being coordinated by at least four pyridine rings in a triangular bipyramidal coordination geometry.

183. Sun, X.; Dong, S.; Wang, E., Coordination-induced formation of submicrometer-scale, monodisperse, spherical colloids of organic-inorganic hybrid materials at room temperature. *J. Am. Chem. Soc.* **2005**, *127*, 13102-13103.

184. Xu, J.; Liu, X.; Lv, J.; Zhu, M.; Huang, C.; Zhou, W.; Yin, X.; Liu, H.; Li, Y.; Ye, J., Morphology transition and aggregation-induced emission of an intramolecular charge-transfer compound. *Langmuir* **2008**, *24*, 4231-4237.

185. Tivanski, A. V.; Hopkins, R. J.; Tyliszczak, T.; Gilles, M. K., Oxygenated interface on biomass burn tar balls determined by single particle scanning transmission X-ray microscopy. *J. Phys. Chem. A* **2007**, *111*, 5448-5458.

186. Henke, B. L.; Lee, P.; Tanaka, T. J.; Shimabukuro, R. L.; Fujikawa, B. K., Low-energy X-ray interaction coefficients: Photoabsorption, scattering, and reflection : E = 100-2000 eV Z = 1-94. *At. Data Nucl. Data Tables* **1982**, *27*, 1-144.

187. Lee, J.; Farha, O. K.; Roberts, J.; Scheidt, K. A.; Nguyen, S. T.; Hupp, J. T., Metal-organic framework materials as catalysts. *Chem. Soc. Rev.* **2009**, *38*, 1450-1459.

188. Kawano, M.; Fujita, M., Direct observation of crystalline-state guest exchange in coordination networks. *Coord. Chem. Rev.* **2007**, *251*, 2592-2605.

189. Zelenyuk, A.; Cai, Y.; Chieffo, L.; Imre, D., High precision density measurements of single particles: The density of metastable phases. *Aerosol Sci. Technol.* **2005**, *39*, 972-986.

190. Veerman, M.; Resendiz, M. J. E.; Garcia-Garibay, M. A., Large-scale photochemical reactions of nanocrystalline suspensions: A promising green chemistry method. *Org. Lett.* **2006**, *8*, 2615-2617.

191. Ruecroft, G.; Hipkiss, D.; Ly, T.; Maxted, N.; Cains, P. W., Sonocrystallization:The use of ultrasound for improved industrial crystallization. *Org. Proc. Res. Dev.* **2005**, *9*, 923-932.

192. Suslick, K. S., Sonochemistry. *Science* **1990**, *247*, 1439-1445.

193. Dhas, N. A.; Suslick, K. S., Sonochemical preparation of hollow nanospheres and hollow nanocrystals. *J. Am. Chem. Soc.* **2005**, *127*, 2368-2369.

194. Kelly, D. R.; Harrison, S. J.; Jones, S.; Masood, M. A.; Morgan, J. J. G., Rapid crystallisation using ultrasonic irradiation - sonocrystallisation. *Tetrahedron Lett.* **1993**, *34*, 2689-2690.

195. Manish, M.; Harshal, J.; Anant, P., Melt sonocrystallization of ibuprofen: Effect on crystal properties. *Eur. J. Pharm. Sci.* **2005**, *25*, 41-48.

196. Stahly, G. P., A survey of cocrystals reported prior to 2000. *Cryst. Growth Des.* **2009**, *9*, 4212-4229.

197. Wolff, J. J., Crystal packing and molecular geometry. *Angew. Chem. Int. Ed.* **1996**, *35*, 2195-2197.

198. Halasz, I., Single-crystal-to-single-crystal reactivity: Gray, rather than black or white. *Cryst. Growth Des.* **2010**, *10*, 2817-2823.

199. Morimoto, M.; Kobatake, S.; Irie, M., Absolute asymmetric photocyclization in chiral diarylethene co-crystals with octafluoronaphthalene. *Chem. Commun.* **2008**, 335-337.

200. Sokolov, A. N.; Friščić, T.; MacGillivray, L. R., Enforced face-to-face stacking of organic semiconductor building blocks within hydrogen-bonded molecular cocrystals. *J. Am. Chem. Soc.* **2006**, *128*, 2806-2807.

201. Feringa, B. L.; van Delden, R. A.; Koumura, N.; Geertsema, E. M., Chiroptical molecular switches. *Chem. Rev.* **2000**, *100*, 1789-1816.

202. Irie, M., Diarylethenes for memories and switches. *Chem. Rev.* **2000**, *100*, 1685-1716.

203. Garcia-Garibay, M. A., Molecular crystals on the move: From single-crystal-to-single-crystal photoreactions to molecular machinery. *Angew. Chem. Int. Ed.* **2007**, *46*, 8945-8947.

204. Kawata, S.; Kawata, Y., Three-dimensional optical data storage using photochromic materials. *Chem. Rev.* **2000**, *100*, 1777-1788.

205. Al-Kaysi, R. O.; Müller, A. M.; Bardeen, C. J., Photochemically driven shape changes of crystalline organic nanorods. *J. Am. Chem. Soc.* **2006**, *128*, 15938-15939.

206. Turowska-Tyrk, I., Structural transformations in organic crystals during photochemical reactions. *J. Phys. Org. Chem.* **2004**, *17*, 837-847.

207. Bučar, D.-K.; MacGillivray, L. R., Preparation and reactivity of nanocrystalline cocrystals formed via sonocrystallization. *J. Am. Chem. Soc.* **2006**, *129*, 32-33.

208. Reddy, C. M.; Krishna, G. R.; Ghosh, S., Mechanical properties of molecular crystals - applications to crystal engineering. *CrystEngComm* **2010**, 12, 2296-2314.

209. Hutter, J. L.; Bechhoefer, J., Calibration of atomic force microscope tips. *Rev. Sci. Instrum.* **1993**, *64*, 1868-1873.

210. Guo, S.; Akhremitchev, B. B., Investigation of mechanical properties of insulin crystals by atomic force microscopy. *Langmuir* **2008**, *24*, 880-887

211. Guo, J.-G.; Zhao, Y.-P., The size-dependent elastic properties of nanofilms with surface effects. *J. Appl. Phys.* **2005**, 98, 074306(1)-074306(11)

212. Hertz, H. J., Hertzian Model *Reine. Angew. Math.* **1881,** 92, 156-171.

213. Ditzler, L. R.; Karunatilaka, C.; Donuru, V. R.; Liu, H. Y.; Tivanski, A. V., Electromechanical properties of self-assembled monolayers of tetrathiafulvalene derivatives studied by conducting probe atomic force microscopy. *J. Phys. Chem. C* **2010**, *114*, 4429-4435.

214. Tao, N. J.; Lindsay, S. M.; Lees, S., Measuring the microelastic properties of biological material. *Biophys. J.* **1992**, *63*, 1165-1169.

215. A-Hassan, E.; Heinz, W. F.; Antonik, M. D.; D'Costa, N. P.; Nageswaran, S.; Schoenenberger, C.-A.; Hoh, J. H., Relative Microelastic Mapping of Living Cells by Atomic Force Microscopy. *Biophys. J.* **1998**, *74*, 1564-1578.

216. Guo, S.; Akhremitchev, B. B., Packing Density and Structural Heterogeneity of Insulin Amyloid Fibrils Measured by AFM Nanoindentation. *Biomacromolecules* **2006**, *7*, 1630-1636.

217. Domke, J.; Radmacher, M., Measuring the elastic properties of thin polymer films with the atomic force microscope. *Langmuir* **1998**, *14*, 3320-3325.

218. Belikov, S.; Magonov, S.; Erina, N.; Huang, L.; Su, C.; Rice, A.; Meyer, C.; Prater, C.; Ginzburg, V.; Meyers, G.; McIntyre, R.; Lakrout, H., Theoretical modelling and implementation of elastic modulus measurement at the nanoscale using atomic force microscope. *J. Phys. Conf. Ser.* **2007**, *61*, 1303.

219. Perkins, M.; Ebbens, S. J.; Hayes, S.; Roberts, C. J.; Madden, C. E.; Luk, S. Y.; Patel, N., Elastic modulus measurements from individual lactose particles using atomic force microscopy. *Int. J. Pharm.* **2007**, *332*, 168-175.

220. Shulha, H.; Zhai, X.; Tsukruk, V. V., Molecular stiffness of individual hyperbranced macromolecules at solid surfaces. *Macromolecules* **2003**, *36*, 2825-2831.

221. Burnham, N. A.; Colton, R. J., Measuring the nanomechanical properties and surface forces of materials using an atomic force microscope. *J. Vac. Sci. Technol. A.* **1989**, *7*, 2906-2913.

222. Johnson, K. L., *Contact Mechanics.* Cambridge University Press, Cambridge, U.K., **1985**.

223. Bowmen, K., *Mechanical behavior of materials*. 1. ed.; John Wiley & Sons, Inc.: Hoboken, NJ, **2004**.

224. Cook, R. F., Probing the nanoscale. *Science* **2010**, *328*, 183-184.

225. Sahin, O.; Magonov, S.; Su, C.; Quate, C. F.; Solgaard, O., An atomic force microscope tip designed to measure time-varying nanomechanical forces. *Nat. Nano* **2007**, *2*, 507-514.

226. Tranchida, D.; Kiflie, Z.; Acierno, S.; Piccarolo, S., Nanoscale mechanical characterization of polymers by atomic force microscopy (AFM) nanoindentations: viscoelastic characterization of a model material. *Meas. Sci. Technol.* **2009**, *20*, 095702.

227. Wornyo, E.; Gall, K.; Yang, F.; King, W., Nanoindentation of shape memory polymer networks. *Polymer* **2007**, *48*, 3213-3225.

228. Kaupp, G., Photodimerization of anthracenes in the solid state: New results from atomic force microscopy. *Angew. Chem. Int. Ed.* **1992**, *31*, 595-598.

229. Kaupp, G., Photodimerization of cinnamic acid in the solid state: New insights on application of atomic force microscopy. *Angew. Chem. Int. Ed.* **1992**, *31*, 592-595.

230. Dumrul, S.; Bazzana, S.; Warzywoda, J.; Biederman, R. R.; Sacco, A., Imaging of crystal growth-induced fine surface features in zeolite A by atomic force microscopy. *Micropor. Mesopor. Mat.* **2002**, *54*, 79-88.

231. Sun, C. C.; Kiang, Y. H., On the identification of slip planes in organic crystals based on attachment energy calculation. *J. Pharm. Sci.* **2008**, *97*, 3456-3461.

232. Geng, Y. L.; Xu, D.; Wang, X. Q.; Yu, G. W.; Zhang, G. H.; Zhang, H. B., AFM study of surface morphology of {1 0 0} cleavage planes of l-arginine acetate crystals. *J. Cryst. Growth* **2005**, *282*, 208-213.

233. Geng, Y. L.; Xu, D.; Wang, X. Q.; Du, W.; Liu, H. Y.; Zhang, G. H., Growth morphology of {1 1 0} faces of manganese mercury thiocyanate crystals investigated by atomic force microscopy. *Mat. Chem. Phys.* **2006**, *96*, 188-191.

234. Bischel, M. S.; Vanlandingham, M. R.; Eduljee, R. F.; Gillespie, J. W.; Schultz, J. M., On the use of nanoscale indentation with the AFM in the identification of phases in blends of linear low density polyethylene and high density polyethylene. *J. Mater. Sci.* **2000**, *35*, 221-228.

235. Duncan-Hewitt, W. C.; Weatherly, G. C., Evaluating the hardness, Young's modulus and fracture toughness of some pharmaceutical crystals using microindentation techniques. *J. Mater. Sci. Lett.* **1989**, *8*, 1350-1352.

236. Roberts, R. J.; Rowe, R. C.; York, P., The relationship between Young's modulus of elasticity of organic solids and their molecular structure. *Powder Technol.* **1991**, *65*, 139-146.

237. Boudou, T.; Crouzier, T.; Auzély-Velty, R.; Glinel, K.; Picart, C., Internal composition versus the mechanical properties of polyelectrolyte multilayer films: The influence of chemical cross-linking. *Langmuir* **2009**, *25*, 13809-13819.

238. Dal, H.; Kaliske, M., An approach to the modeling of physical ageing in rubbery polymers. *PAMM* **2006**, *6*, 363-364.

239. Kurtz, S. M.; Pruitt, L. A.; Jewett, C. W.; Foulds, J. R.; Edidin, A. A., Radiation and chemical crosslinking promote strain hardening behavior and molecular alignment in ultra high molecular weight polyethylene during multi-axial loading conditions. *Biomaterials* **1999**, *20*, 1449-1462.

240. Bučar, D.-K.; Henry, R. F.; Lou, X.; Duerst, R. W.; MacGillivray, L. R.; Zhang, G. G. Z., Cocrystals of caffeine and hydroxybenzoic acids composed of multiple supramolecular heterosynthons: Screening via solution-mediated phase transformation and structural characterization. *Cryst. Growth Des.* **2009**, *9*, 1932-1943.

241. Bis, J. A.; Vishweshwar, P.; Weyna, D.; Zaworotko, M. J., Hierarchy of supramolecular synthons: Persistent hydroxyl···pyridine hydrogen bonds in cocrystals that contain a cyano acceptor. *Mol. Pharm.* **2007**, *4*, 401-416.

242. Aakeröy, C. B.; Desper, J.; Elisabeth, E.; Helfrich, B. A.; Levin, B.; Urbina, J. F., Making reversible synthesis stick: Competition and cooperation between intermolecular interactions. *Z. Kristallogr.* **2005**, *220*, 325-332.

243. Bhogala, B. R.; Nangia, A., Ternary and quaternary co-crystals of 1,3-cis,5-cis-cyclohexanetricarboxylic acid and 4,4[prime or minute]-bipyridines. *New J. Chem.* **2008**, *32*, 800-807.

244. Scheindlin, S., A new look at the xanthine alkaloids. *Mol. Interv.* **2007**, *3*, 236-242.

245. *The Merck Index*. 14th ed.; Merck & Co., Inc.: Whitehouse Station, NJ, USA, 2001.

246. A survey of the Sci-Finder Scholar database (version 2007) revealed more than 53000 entries referring to the term "caffeine" (as of October 2007).

247. Martin, R.; Lilley, T. H.; Bailey, N. A.; Falshaw, C. P.; Haslam, E.; Magnolato, D.; Begley, M. J., Polyphenol-caffeine complexation. *J. Chem. Soc., Chem. Commun.* **1986**, 105-106.

248. Thuéry, P.; Nierlich, M.; Asfari, Z.; Vicens, J.; Morikawa, O.; Konishi, H., Crystal structure of C-(n-propyl)calix[4]resorcinarene and its complex with caffeine *Supramol. Chem.* **2001**, *13*, 521-527.

249. Karki, S.; Friščić, T.; Jones, W.; Motherwell, W. D. S., Screening for pharmaceutical cocrystal hydrates *via* neat and liquid-assisted grinding. *Mol. Pharm.* **2007**, *4*, 347-354.

250. Bučar, D.-K.; Henry, R. F.; Lou, X.; Duerst, R. W.; Borchardt, T. B.; MacGillivray, L. R.; Zhang, G. G. Z., Co-crystals of caffeine and hydroxy-2-naphthoic acids: Unusual formation of the carboxylic acid dimer in the presence of a heterosynthon. *Mol. Pharm.* **2007**, *4*, 339-346.

251. Bruno, I. J.; Cole, J. C.; Edgington, P. R.; Kessler, M.; Macrae, C. F.; McCabe, P.; Pearson, J.; Taylor, R., New software for searching the Cambridge Structural Database and visualising crystal structures *Acta Crystallogr.* **2002**, *B58*, 389-397.

252. CCDC reference codes of the 12 caffeine-carboxylic acid cocrystals: CESJIU, CESJUG, CESKAN, CESKAN01, DIJVUN, EXUQUJ, EXUQUJ01, GANXUP, GANYAW, GANYEA, NEXWUJ, VAWKIO.

253. Farrugia, L. J., WinGX suite for small-molecule single-crystal crystallography. *J. App. Cryst.* **1999**, *32*, 837-838.

254. *Symphonix*, Inel Corp.: Artenay, France.

255. *Jade* 6.5; Materials Data, Inc.: Livermore, CA, USA.

256. *SaintPlus*, Bruker AXS Inc.: Madision, WI, USA, 1999.

257. Cochran, W., The crystal and molecular structure of salicylic acid. *Acta Crystallogr.* **1953**, *6*, 260-268.

258. *Cerius2*, v4.6 Accelrys Software Inc.: 2001.

259. Habgood, M.; Price, S. L., Isomers, conformers, and cocrystal stoichiometry: Insights from the crystal energy landscapes of caffeine with the hydroxybenzoic Acids. *Cryst. Growth Des.* **2010**, *10*, 3263-3272.

260. He, G.; Chow, P. S.; Tan, R. B. H., Investigating the intermolecular interactions in concentration-dependent solution cocrystallization of caffeine and *p*-hydroxybenzoic acid. *Cryst. Growth Des.* **2010**, *10*, 3763-3769.

261. *XSHELL*, v6.3.1; Bruker AXS Inc.: Madison, WI, USA, 2004.

262. Bučar, D.-K.; Henry, R. F.; Lou, X.; Duerst, R. W.; Borchardt, T. B.; Zhang, G. G. Z., A ‘‘hidden’’ co-crystal of caffeine and adipic acid. *Chem. Commun.* **2007**, 525-527.

263. Bučar, D.-K.; Henry, R.; Duerst, R.; Lou, X.; MacGillivray, L.; Zhang, G., A 1:1 cocrystal of caffeine and 2-hydroxy-1-naphthoic acid obtained via a slurry screening Method. *J. Chem. Crystallogr.* **2010**. in press.

264. Madarasz, J.; Bombicz, P.; Jarmi, K.; Ban, M.; Pokol, G.; Gal, S., Thermal, FTIR and XRD study on some 1 : 1 molecular compounds of theophylline. *J. Therm. Anal. Calorim.* **2002**, 69, 281-290.

265. Childs, S. L.; Stahly, G. P.; Park, A., The salt-cocrystal continuum: The influence of crystal structure on ionization state. *Mol. Pharmaceutics* **2007**, *4*, 323-338.

266. Desiraju, G. R., Hydration in organic crystals: prediction from molecular structure *J. Chem. Soc., Chem. Commun.* **1991**, 426-428.

267. Winston, C., J.,; Thuy, T. N., Caffeine and theobromine levels in cocoa and carob products. *J. Food Sci.* **1984**, *49*, 302–303.

268. Caleb, K. J., Effects of theobromine should be considered in future studies. *Am. J. Clin. Nutr.* **2005**, *82*, 486-488.

269. Joo, L. H.; Won, L. K.; Sun, K. K.; Young, K. D.; Hwan, P. H.; Jong, L. M.; Soo, K. H.; Boo, K. I. Theobromine with an anti-carcinogenic activity. **2003**, US6693104.

270. Karki, S.; Fábián, L.; Friščić, T.; Jones, W., Powder X-ray diffraction as an emerging method to structurally characterize organic solids. *Org. Lett.* **2007**, *9*, 3133-3136.

271. Clarke, H. D.; Arora, K. K.; Bass, H.; Kavuru, P.; Ong, T. T.; Pujari, T.; Wojtas, L.; Zaworotko, M. J., Structure-stability relationships in cocrystal hydrates: Does the promiscuity of water make crystalline hydrates the nemesis of crystal engineering? *Cryst. Growth Des.* **2010**, *10*, 2152-2167.

272. *ACD/Labs software*, 8.14; ACD/Labs **2007**.

273. Bhogala, B. R.; Basavoju, S.; Nangia, A., Tape and layer structures in cocrystals of some di- and tricarboxylic acids with 4,4'-bipyridines and isonicotinamide. From binary to ternary cocrystals. *CrystEngComm* **2005**, *7*, 551-562.

274. Naciye Türkel; Rahmiye Aydin; Özer, U., Scandium(III) and yttrium(III) complexes of hydroxysalicylic acid ligands. *Asian J. Chem.* **2004**, *16*, 1044-1050.

275. Tamás Kiss; Károly Atkári; Jezowska-Bojczuk, M.; Decock, P., Complexes of Al(III) with hydroxyaromatic acids. *J. Coord. Chem.* **1993**, *29*, 81-96.

276. Naciye Türkel; Tabak, E., Dependence on ionic strenght of stability constants, protonation and complexation of 2,X-dihydroxybenzoic acids (X=4, 5 or 6) with aluminium(III). *Main Group Met. Chem.* **2006**, *29*, 175-188.

277. Lauri H. J. Lajunen; Jaakko Saarinen; Parhi, S., The protonation and dimerization of 2,4-, 2,5-, 2,6-and 3,5-dihydroxybenzoic acids in 0.5M sodium perchlorate medium. *Talanta* **1980**, *27*, 71-74.

278. Park, M. V., Complex formation between iron(III) and some substituted salicylic acids. *J. Chem. Soc. A* **1966**, 816-820.

279. Michael Aplincourt; Agnes Debras-Bee; Christian Gerard; Hugel, R. P., Modelling of the interactions of metal cations with soil organic matter. Part 1. Thermadynamic stability of copper(II) complexes with dihydroxybenzoic acids. *J. Chem. Res. (S)* **1986**, 134-135.

280. Edoardo Mentasti; Fernando Secco; Venturini, M., Mechanism of complex formation: Equilibriums and kinetics of iron(3+) and iron hydroxide(2+) interactions with substituted salicylic acids. *Inorg. Chem.* **1982**, *21*, 602-606.

281. Tamas Kiss, H. K., Giovanni Micera, Liliana Strinna Erre, Cupric ion binding by dihydroxybenzoic acids. *Polyhedron* **1989**, *8*, 647-651.

282. M. Suat Aksoy; Özer, U., Potentiometric and spectroscopic studies with chromium(III) complexes of hydroxysalicylic acid derivatives in aqueous solution. *Turk. J. Chem.* **2003**, *27*, 667-673.

283. N. Papadopoulos; Avranas, A., Dissociation of salicylic acid, 2,4-, 2,5- and 2,6-dihydroxybenzoic acids in 1-propanol - water mixtures at 25 °C. *J. Solution Chem.* **1991**, *20*, 293-300.

284. Djokić, A.; Dumanović, D., Spectrophotometric characterization of some analgesics and antipyretics. *Talanta* **1989**, *36*, 931-935.

285. Ali Önen; Sarac, S., Non-aqueous potentiometry of nitrogen containing compounds in chlorobenzene and chlorobenzene-acetic anhydride mixture. *Fresenius Z. Anal. Chem.* **1987**, *328*, 663-664.

286. Weigend, F.; Haser, M., RI-MP2. First derivatives and global consistency. *Theor. Chem. Acc.* **1997**, *97*, 331-340.

287. Weigend, F.; Häser, M.; Patzelt, H.; Ahlrichs, R., RI-MP2: optimized auxiliary basis sets and demonstration of efficiency. *Chem. Phys. Lett.* **1998**, *294*, 143-152.

288. Schäfer, A.; Huber, C.; Ahlrichs, R., Fully optimized contracted Gaussian basis sets of triple zeta valence quality for atoms Li to Kr. *J. Chem. Phys.* **1994**, *100*, 5829-5835.

289. Ahlrichs, R.; Bär, M.; Häser, M.; Horn, H.; Kölmel, C., Electronic structure calculations on workstation computers: The program system turbomole. *Chem. Phys. Lett.* **1989**, *162*, 165-169.

290. Klamt, A.; Schueuermann, G., COSMO: a new approach to dielectric screening in solvents with explicit expressions for the screening energy and its gradient. *J. Chem. Soc., Perkin Trans. 2* **1993**, 799-805.

291. Dovesi, R.; Orlando, R.; Civalleri, B.; Roetti, C.; Saunders, V. R.; Zicovich-Wilson, C. M., CRYSTAL: a computational tool for the ab initio study of the electronic properties of crystals. *Z. Kristallogr.* **2005**, 220, 571-573.

292. Becke, A. D., Density-functional thermochemistry. III The role of exact exchange. *J. Chem. Phys.* **1993**, *98*, 5648-5652.

293. Gatti, C.; Saunders, V. R.; Roetti, C., Crystal-field effects on the topological properties of the electron-density in molecular-crystals - the case of urea. *J. Chem. Phys.* **1994**, *101*, 10686-10696.

294. Rao, N. G.; Murthy, V. L. S. N., Effect od dielectric constant of medium on proton equilibria of L-glutamine and succinic acid. *J. Ind. Chem. Soc.* **2004**, *81*, 424-426.

APPENDIX A.

GENERAL AND CRYSTALLOGRAPHIC DATA RETRIEVED FROM SINGLE-CRYSTAL X-RAY DIFFRACTION STUDIES

Table A1 General and crystallographic for **MePE**, **ClPE**, and solid solution **2** (Chapter 2).

	MePE	**ClPE**	solid solution **2**
empirical formula	$C_{34}H_{32}N_2O_2$	$C_{13}H_{10}ClN$	$C_{33}H_{29}ClN_2O_2$
M_r	500.62	215.67	521.03
crystal system	orthorhombic	triclinic	triclinic
space group	$P2_12_12_1$	$P\bar{1}$	$P\bar{1}$
a, Å	195.25	9.4815(10)	9.9719(10)
b, Å	6.0339(7)	9.6019(12)	10.2525(10)
c, Å	7.6092(9)	14.2885(18)	13.9413(14)
α, °	23.135(3)	71.745(5)	105.546(5)
β, °	90.00	76.746(6)	98.407(5)
γ, °	90.00	62.801(5)	92.507(5)
V, Å^3	90.00	1093.0(2)	1353.3(2)
Z	4	4	2
D_c/gcm^{-3}	1062.2(2)	1.311	1.279
F(000)	416	448	548
μ(Mo K$_\alpha$)/cm^{-1}	0.071	0.312	0.174
T/K	200(2)	298(2)	276(2)
crystal size/mm	0.35 × 0.23 × 0.025	0.22 × 0.18 × 0.08	0.40 × 0.165 × 0.08
range of indices	-7 → 7 -9 → 9 -27 → 27	-11 → 11 -12 → 12 -16 → 16	-11 → 11 -12 → 12 -16 → 16
no. of reflections collected	6496	6854	8431
unique reflections	1860	3859	4715
R_{int}	0.0356	0.0643	0.0249
reflections with $I > 2\sigma(I)$	1502	1775	2902
no. parameters	136	271	368
$R(F)$, $F > 2\sigma$(F)	0.0399	0.1212	0.0604
$wR(F^2)$, $F > 2\sigma$(F)	0.1002	0.3050	0.1600
$R(F)$, all data	0.0547	0.2177	0.1040
$wR(F^2)$, all data	0.1075	0.3747	0.1768
Δ_r (max., min.) eÅ^{-3}	0.146, -0.174	0.457, -0.366	0.507, -0.174

Table A2 General and crystallographic data for solid solution **3** and $[Cu_2(hfac)_4(\mathbf{3,4'\text{-}tpcb})]_\infty \cdot 1.6H_2O \cdot CH_3CN \cdot CHCl_3$ (Chapter 2).

	solid solution **3**	$[Cu_2(hfac)_4(\mathbf{3,4'\text{-}tpcb})]_\infty \cdot 1.6H_2O \cdot CH_3CN \cdot CHCl_3$
empirical formula	$C_{27}H_{26.6}Br_2ClN_2\ O_{0..8}$	$C_{47}H_{31.20}Cl_3Cu_2F_{24}N_5O_{9.60}$
M_r	586.60	1509.00
crystal system	triclinic	monoclinic
space group	$P\bar{1}$	$P2_1/c$
a, Å	18.3233(19)	15.5534(16)
b, Å	9.8023(11)	17.9540(18)
c, Å	14.3984(15)	20.918(2)
α, °	90.00	90.00
β, °	93.253(5)	98.286(5)
γ, °	90.00	90.00
V, Å^3	2581.9(5)	5780.3(10)
Z	4	4
D_c/gcm^{-3}	3.264	1.734
F(000)	1183	3000
μ(Mo K_α)/cm^{-1}	1.509	1.010
T/K	200(2)	190(2)
crystal size/mm	0.30 × 0.26 × 0.055	0.30 × 0.11 × 0.08
range of indices	-21 → 20 -11 → 9 -17 → 17	-18 → 18 -21 → 21 -15 → 24
no. of reflections collected	11967	24831
unique reflections	4489	9166
R_{int}	0.0385	0.0552
reflections with $I > 2\sigma(I)$	3339	6017
no. parameters	308	779
$R(F)$, $F > 2\sigma$(F)	0.0479	0.0920
$wR(F^2)$, $F > 2\sigma$(F)	0.1014	0.1247
$R(F)$, all data	0.0728	0.2511
$wR(F^2)$, all data	0.1087	0.2763
Δ_r (max., min.) eÅ^{-3}	0.521, -0.506	0.970, -0.560

Table A3 General and crystallographica data for 2(**5-CN-res**)·2(**4,4'-bpe**) and 2(**5-CN-res**)·(**4,4'-tpcb**) (Chapter 3).

	2(**5-CN-res**)·2(**4,4'-bpe**)	2(**5-CN-res**)·(**4,4'-tpcb**)
molecular formula	$(C_7H_5NO_2)\cdot (C_{12}H_{10}N_2)$	$2(C_7H_5NO_2)\cdot (C_{24}H_{20}N_4)$
M_r	317.34	634.68
crystal system	triclinic	triclinic
space group	$P\bar{1}$	$P\bar{1}$
a, Å	7.6903(9)	7.7709(9)
b, Å	9.4154(11)	9.8124(11)
c, Å	24.120(3)	23.620(3)
α, °	86.888(5)	86.635(5)
β, °	89.295(5)	89.850(5)
γ, °	71.235(5)	66.617(5)
V, Å^3	1651.2(3)	1649.9(3)
Z	4	2
D_c/gcm^{-3}	1.277	1.278
$F(000)$	664	664
μ(Mo K$_\alpha$)/cm^{-1}	0.085	0.085
T/K	298(2)	298(2)
crystal size/mm	0.30 × 0.26 × 0.19	0.21 × 0.17 × 0.16
range of indices	-10 → 10 -9 → 9 -37 → 36	-10 → 10 -9 → 9 -37 → 36
no. of reflections collected	9857	8534
unique reflections	5778	5798
R_{int}	0.0304	0.0222
reflections with $I > 2\sigma(I)$	3549	3261
no. parameters	437	445
$R(F)$, $F > 2\sigma$(F)	0.0511	0.0517
$wR(F^2)$, $F > 2\sigma$(F)	0.0889	0.1114
$R(F)$, all data	0.1341	0.1232
$wR(F^2)$, all data	0.1522	0.1421
Δ_r (max., min.) eÅ^{-3}	0.161, -0.183	0.146, -0.153

Table A4 General and crystallographic data for **caf1**, **caf2** and **caf3** (Chapter 4)

	caf1	**caf2**	**caf3**
molecular formula	$(C_8H_{10}O_2N_4)\cdot(C_7H_6O_4)$	$(C_8H_{10}O_2N_4)\cdot(C_7H_6O_4)$	$(C_8H_{10}O_2N_4)\cdot 2(C_7H_6O_4)$
M_r	332.32	332.32	470.44
crystal system	monoclinic	monoclinic	monoclinic
space group	$P2_1/c$	$P2_1/c$	$P2_1/c$
a, Å	14.771(3)	7.687(3)	7.421(5)
b, Å	7.021(1)	6.948(3)	22.494(15)
c, Å	16.209(3)	28.098(11)	12.939(9)
α, °	90.00	90.00	90.00
β, °	117.194(3)	95.029(7)	92.242(12)
γ, °	90.00	90.00	90.00
V, Å^3	1495.2(5)	1494.8(10)	2158(3)
Z	4	4	4
D_c/gcm^{-3}	1.476	1.477	1.448
F(000)	696	696	984
μ(Mo K_α)/cm^{-1}	0.113	0.113	0.112
T/K	173(2)	173(2)	173(2)
crystal size/mm	0.40 × 0.15 × 0.05	0.30 × 0.10 × 0.10	0.30 × 0.05 × 0.05
range of indices	-19 → 19 -9 → 9 -21 → 21	-10 → 10 -9 → 9 -37 → 36	-9 → 9 -29 → 29 -17 → 17
no. of reflections collected	17081	16727	25368
unique reflections	3658	3647	5271
R_{int}	0.129	0.066	0.223
reflections with $I > 2\sigma(I)$	3114	3227	4343
no. parameters	223	228	326
$R(F)$, $F > 2\sigma$(F)	0.059	0.061	0.102
$wR(F^2)$, $F > 2\sigma$(F)	0.148	0.142	0.178
$R(F)$, all data	0.069	0.068	0.129
$wR(F^2)$, all data	0.155	0.146	0.185
Δ_r (max., min.) eÅ^{-3}	0.384, -0.341	0.405, -0.261	0.426, -0.411

Table A5 General and crystallographic data for **caf4**, **caf5** and **caf6** (Chapter 4).

	caf4	**caf5**	**caf6**
molecular formula	$2(C_8H_{10}O_2N_4)\cdot(C_7H_6O_4)$	$(C_8H_{10}O_2N_4)\cdot(C_7H_6O_4)\cdot(H_2O)$	$(C_8H_{10}O_2N_4)\cdot(C_7H_6O_4)\cdot(H_2O)$
M_r	526.52	366.33	366.33
crystal system	monoclinic	triclinic	triclinic
space group	$P2_1/n$	$P\bar{1}$	$P\bar{1}$
a, Å	9.938(4)	6.657(4)	7.201(3)
b, Å	16.537(6)	8.796(5)	8.620(4)
c, Å	14.758(6)	15.670(9)	13.822(6)
α, °	90.00	77.832(9)	90.258(7)
β, °	101.096(6)	83.426(9)	101.078(7)
γ, °	90.00	71.568(9)	106.517(7)
V, Å^3	2379.8(15)	849.8(8)	805.6(6)
Z	4	2	2
D_c/gcm^{-3}	1.470	1.432	1.510
$F(000)$	1104	384	384
μ(Mo K_α)/cm^{-1}	0.112	0.115	0.122
T/K	173(2)	173(2)	173(2)
crystal size/mm	0.40 × 0.30 × 0.30	0.40 × 0.30 × 0.10	0.40 × 0.05 × 0.05
range of indices	-13 → 13 -21 → 21 -19 → 19	-8 → 8 -11 → 11 -20 → 20	-9 → 9 -11 → 11 -18 → 18
no. of reflections collected	28063	9783	9416
unique reflections	5872	4039	3843
R_{int}	0.1203	0.1696	0.1490
reflections with $I > 2\sigma(I)$	4662	2590	2621
no. parameters	404	238	247
$R(F)$, $F > 2\sigma$(F)	0.045	0.109	0.092
$wR(F^2)$, $F > 2\sigma$(F)	0.129	0.137	0.192
$R(F)$, all data	0.056	0.298	0.140
$wR(F^2)$, all data	0.135	0.324	0.216
Δ_r (max., min.) eÅ^{-3}	0.317, -0.273	0.649, -0.415	0.386, -0.486

Table A6 General and crystallographic data for **caf7** and **caf8** (Chapter 4).

	caf7	**caf8**
molecular formula	$(C_8H_{10}O_2N_4)\cdot(C_7H_6O_4)$	$(C_8H_{10}O_2N_4)\cdot(C_7H_6O_4)\cdot(H_2O)$
M_r	348.32	366.33
crystal system	monoclinic	monoclinic
space group	$P2_1/c$	$P2_1/c$
a, Å	15.703(6)	7.015(2)
b, Å	6.818(3)	7.693(2)
c, Å	16.215(6)	30.319(9)
α, °	90.00	90.00
β, °	117.349(5)	90.594(5)
γ, °	90.00	90.00
V, Å^3	1542.0(10)	1636.1(8)
Z	4	4
D_c/gcm^{-3}	1.500	1.487
F(000)	728	768
μ(Mo K_α)/cm^{-1}	0.118	0.120
T/K	173(2)	173(2)
crystal size/mm	0.40 × 0.10 × 0.10	0.40 × 0.40 × 0.10
range of indices	-20 → 20 -9 → 9 -21 → 21	-9 → 9 -10 → 10 -40 → 40
no. of reflections collected	17504	18295
unique reflections	3782	4001
R_{int}	0.1408	0.1163
reflections with $I > 2\sigma(I)$	2948	3412
no. parameters	229	249
$R(F)$, $F > 2\sigma$(F)	0.090	0.056
$wR(F^2)$, $F > 2\sigma$(F)	0.122	0.147
$R(F)$, all data	0.189	0.065
$wR(F^2)$, all data	0.205	0.152
Δ_r (max., min.) eÅ^{-3}	0.392, -0.464	0.391, -0.275

Table A7 General and crystallographic data for **theo2**, **theo3** and **theo4** (Chapter 4).

	theo2	**theo3**	**theo4**
molecular formula	$(C_7H_8N_4O_2)\cdot(C_7H_6O_3)$	$(C_7H_8N_4O_2)\cdot(C_7H_6O_3)$	$(C_7H_8N_4O_2)\cdot(C_7H_6O_4)$
M_r	318.29	318.29	334.29
crystal system	triclinic	monoclinic	monoclinic
space group	$P\bar{1}$	$P2_1/c$	$P2_1/c$
a, Å	7.683(2)	7.0444(11)	15.327(7)
b, Å	8.191(2)	7.8993(12)	6.792(3)
c, Å	23.307(6)	24.731(4)	14.041(6)
α, °	98.202(5)	90.00	90.00
β, °	92.589(5)	92.042(2)	106.297(4)
γ, °	103.123(4)	90.00	90.00
V, Å^3	1409.2(7)	1375.3(4)	1403.1(10)
Z	4	4	4
D_c/gcm^{-3}	1.500	1.992	1.583
F(000)	664	864	696
μ(Mo K_α)/cm^{-1}	0.117	0.150	0.126
T/K	170(2)	100(2)	100(2)
crystal size/mm	0.40 × 0.30 × 0.05	0.40 x 0.10 x 0.05	0.40 × 0.10 × 0.10
range of indices	-9 → 9 -10 → 10 -30 → 30	-6 → 6 -7 → 7 -22 → 22	-13 → 13 -4 → 6 -12 → 12
no. of reflections collected	15917	4535	4373
unique reflections	6377	1078	1057
R_{int}	0.034	0.0280	0.055
reflections with $I > 2\sigma(I)$	5210	917	798
no. parameters	435	210	219
$R(F)$, $F > 2\sigma$(F)	0.054	0.0329	0.037
$wR(F^2)$, $F > 2\sigma$(F)	0.067	0.0422	0.059
$R(F)$, all data	0.130	0.0984	0.099
$wR(F^2)$, all data	0.138	0.1172	0.133
Δ_r (max., min.) eÅ^{-3}	0.391, -0.325	0.175, -0.187	0.177, -0.193,

Table A8 General and crystallographic data for **theo5**, **theo6** and **theo7** (Chapter 4).

	theo5	**theo6**	**theo7**
molecular formula	$(C_7H_8N_4O_2)\cdot(C_7H_6O_4)$	$(C_7H_8N_4O_2)\cdot(C_7H_6O_4)$	$(C_7H_8N_4O_2)\cdot(C_7H_6O_4)\cdot(H_2O)$
M_r	334.29	334.29	352.31
crystal system	monoclinic	triclinic	monoclinic
space group	$P2_1/c$	$P\bar{1}$	$P2_1/c$
a, Å	12.565(4)	7.106(4)	14.6593(19)
b, Å	7.894(3)	8.068(5)	6.5583(8)
c, Å	14.528(5)	13.045(7)	15.727(2)
α, °	90.00	86.052(12)	90.00
β, °	98.840(6)	81.363(18)	94.0430(10)
γ, °	90.00	73.956(11)	90.00
V, Å^3	1423.8(9)	710.4(7)	1508.2(3)
Z	4	2	4
D_c/gcm^{-3}	1.560	1.563	1.552
F(000)	696	348	736
μ(Mo K$_\alpha$)/cm^{-1}	0.124	0.125	0.126
T/K	170(2)	100(2)	100(2)
crystal size/mm	0.40 × 0.40 × 0.25	0.25 × 0.10 × 0.10	0.30 × 0.15 × 0.15
Range of indices	-16 → 16 -10 → 10 -19 → 19	-9 → 9 -10 → 10 -16 → 16	-18 → 19 -8 → 8 -20 → 20
no. of reflections collected	16002	8137	16040
Unique reflections	3478	3207	3436
R_{int}	0.063	0.035	0.037
reflections with $I > 2\sigma(I)$	3244	2499	2225
no. parameters	219	231	252
$R(F)$, $F > 2\sigma$(F)	0.043	0.035	0.039
$wR(F^2)$, $F > 2\sigma$(F)	0.045	0.047	0.081
$R(F)$, all data	0.1207	0.099	0.113
$wR(F^2)$, all data	0.1234	0.116	0.164
Δ_r (max., min.) eÅ^{-3}	0.282, -0.353	0.278, -0.272	0.293, -0.259

Table A9 General and crystallographic data for **theo8**, **theo9** and **theb1** (Chapter 4).

	theo8	**theo9**	**theb1**
molecular formula	$(C_7H_8N_4O_2)\cdot(C_7H_6O_4)$	$(C_7H_8N_4O_2)\cdot(C_7H_6O_4)$	$(C_7H_8N_4O_2)\cdot(C_7H_6O_3)$
M_r	334.29	334.29	318.29
crystal system	triclinic	triclinic	triclinic
space group	$P\bar{1}$	$P\bar{1}$	$P\bar{1}$
a, Å	8.0694(12)	7.2253(17)	6.780(4)
b, Å	8.5782(13)	7.9998(19)	7.915(4)
c, Å	11.5578(17)	12.650(3)	14.072(8)
α, °	103.147(2)	81.240(4)	94.057(9)
β, °	104.970(2)	85.071(4)	103.273(9)
γ, °	105.358(2)	82.509(4)	103.355
V, Å^3	706.70(18)	714.9(3)	709.0(7)
Z	2	2	2
D_c/gcm^{-3}	1.571	1.553	1.491
F(000)	348	348	332
μ(Mo K$_\alpha$)/cm^{-1}	0.125	0.124	0.116
T/K	100(2)	170(2)	100(2)
crystal size/mm	0.40 × 0.40 × 0.10	0.40 × 0.40 × 0.05	0.40 × 0.10 × 0.05
range of indices	-10 → 10 -11 → 11 -15 → 15	-9 → 9 -10 → 10 -16 → 16	-8 → 8 -10 → 10 -18 → 16
no. of reflections collected	8226	8422	8154
unique reflections	3287	3399	3167
R_{int}	0.027	0.075	0.0365
reflections with $I > 2\sigma(I)$	2609	2629	2540
no. parameters	231	223	218
$R(F)$, $F > 2\sigma$(F)	0.035	0.059	0.0367
$wR(F^2)$, $F > 2\sigma$(F)	0.046	0.072	0.1161
$R(F)$, all data	0.103	0.154	0.0478
$wR(F^2)$, all data	0.120	0.167	0.1305
Δ_r (max., min.) eÅ^{-3}	0.328, -0.288	0.334, -0.359	-0.237, 0.272

Table A10 General and crystallographic data for **theb2**, **theb3** and **theb4** (Chapter 4).

	theb2	**theb3**	**theb4**
molecular formula	$(C_7H_8N_4O_2)\cdot(C_7H_6O_3)$	$(C_7H_8N_4O_2)\cdot 2(C_7H_6O_3)\cdot(H_2O)$	$(C_7H_8N_4O_2)\cdot 2(C_7H_6O_4)\cdot(H_2O)$
M_r	318.29	474.43	352.31
crystal system	monoclinic	triclinic	monoclinic
space group	$P2_1/c$	$P\bar{1}$	Cc
a, Å	6.4672(9)	6.9917(19)	13.207(3)
b, Å	23.694(3)	12.473(3)	15.273(3)
c, Å	9.3029(13)	24.657(7)	7.8026(16)
α, °	90.00	99.670(3)	90.00
β, °	101.602(2)	91.704(4)	106.275(2)
γ, °	90.00	99.439(4)	90.00
V, Å^3	1396.4(3)	2087.3(10)	1510.8(5)
Z	4	4	4
D_c/gcm^{-3}	1.514	1.510	1.549
F(000)	664	992	736
μ(Mo K$_\alpha$)/cm^{-1}	0.118	0.120	0.126
T/K	100(2)	100(2)	100(2)
crystal size/mm	0.30 × 0.20 × 0.20	0.40 × 0.10 × 0.05	0.40 × 0.40 × 0.20
Range of indices	-8 → 8 -30 → 30 -12 → 12	-8 → 9 -16 → 16 -31 → 31	-17 → 17 -19 → 19 -10 → 10
no. of reflections collected	15986	23921	8502
Unique reflections	3184	9277	3399
R_{int}	0.0349	0.0412	0.0509
reflections with $I > 2\sigma(I)$	2736	5912	3274
no. parameters	218	665	248
$R(F)$, $F > 2\sigma$(F)	0.0364	0.0451	0.0345
$wR(F^2)$, $F > 2\sigma$(F)	0.1099	0.1222	0.0899
$R(F)$, all data	0.0447	0.0869	0.0362
$wR(F^2)$, all data	0.1221	0.1590	0.1011
Δ_r (max., min.) eÅ^{-3}	-0.313, 0.404	-0.329, 0.282	-0.268, 0.247

Table A11 General and crystallographic data for **theb5**, **theb6** and **theb7** (Chapter 4).

	theb5	**theb6**	**theb7**
molecular formula	$(C_7H_8N_4O_2)\cdot(C_7H_6O_4)$	$(C_7H_8N_4O_2)\cdot(C_7H_6O_4)$	$(C_7H_8N_4O_2)\cdot(C_7H_6O_4)$
M_r	334.29	334.29	363.31
crystal system	monoclinic	triclinic	monoclinic
space group	$P2_1/n$	$P\bar{1}$	Pc
a, Å	7.9086(17)	6.822(2)	6.937(4)
b, Å	6.3756(14)	7.941(3)	16.619(10)
c, Å	28.683(6)	14.015(4)	12.458(8)
α, °	90.00	79.511(4)	90.00
β, °	95.768(3)	78.531(9)	95.607(8)
γ, °	90.00	77.403(5)	90.00
V, Å^3	1438.9(5)	718.5(4)	1429.5(15)
Z	4	2	4
D_c/gcm^{-3}	1.543	1.545	1.688
F(000)	696	348	756
μ(Mo K$_\alpha$)/cm^{-1}	0.123	0.123	0.136
T/K	100(2)	100(2)	100(2)
crystal size/mm	0.40 × 0.10 × 0.05	0.40 × 0.10 × 0.10	0.20 × 0.10 × 0.10
Range of indices	-8 → 8 -30 → 30 -12 → 12	-8 → 8 -10 → 10 -18 → 18	-8 → 8 -21 → 21 -16 → 16
no. of reflections collected	15736	8427	16322
Unique reflections	3273	3247	6381
R_{int}	0.0601	0.0633	0.1301
reflections with $I > 2\sigma(I)$	2209	2703	2083
no. parameters	227	231	306
$R(F)$, $F > 2\sigma$(F)	0.0526	0.0367	0.0532
$wR(F^2)$, $F > 2\sigma$(F)	0.1503	0.1053	0.0913
$R(F)$, all data	0.0810	0.0434	0.1893
$wR(F^2)$, all data	0.1673	0.1148	0.1191
Δ_r (max., min.) eÅ^{-3}	0.487, -0.261	0.276, -0.300	0.331, -0.289

Table A12 General and crystallographic data for **theb8**, **theb9** and **cafs**(RT) (Chapter 4).

	theb8	**theb9**	**cafs**(RT)
molecular formula	$(C_7H_8N_4O_2)\cdot(C_7H_6O_4)$	$(C_7H_8N_4O_2)\cdot(C_7H_6O_4)$	$(C_8H_{10}N_4O_2)\cdot(C_7H_6O_4)$
M_r	334.29	334.29	348.32
crystal system	orthorhombic	monoclinic	monoclinic
space group	*Pbca*	$P2_1/c$	$P2_1/n$
a, Å	26.782(7)	14.469(7)	14.8895(18)
b, Å	14.184(4)	12.759(6)	7.0850(9)
c, Å	7.2355(19)	15.803(8)	15.9692(19)
α, °	90.00	90.00	90.00
β, °	90.00	92.449(9)	115.6670(10)
γ, °	90.00	90.00	90.00
V, Å^3	2748.6(12)	2915(2)	1518.4(3)
Z	8	8	4
D_c/gcm^{-3}	1.616	1.524	1.524
F(000)	1392	1392	728
μ(Mo K_α)/cm^{-1}	0.129	0.122	0.120
T/K	100(2)	100(2)	296(2)
crystal size/mm	0.30 × 0.10 × 0.05	0.20 × 0.20 × 0.20	0.30 × 0.10 × 0.20
range of indices	-34 → 34 -18 → 18 -9 → 9	-13 → 18 -15 → 16 -20 → 20	-16 → 16 -7 → 7 -17 → 17
no. of reflections collected	29157	19745	11898
unique reflections	3173	6597	2170
R_{int}	0.0906	0.0931	0.0276
reflections with $I > 2\sigma(I)$	2127	3204	3204
no. parameters	231	461	241
$R(F)$, $F > 2\sigma$(F)	0.0477	0.0708	0.0352
$wR(F^2)$, $F > 2\sigma$(F)	0.1325	0.1768	0.1048
$R(F)$, all data	0.0796	0.1458	0.0532
$wR(F^2)$, all data	0.1613	0.2120	0.1373
Δ_r (max., min.) eÅ^{-3}	0.670, -0.393	0.584, -0.419	0.251, -0.213

Table A13 General and crystallographic data for **cafs** (100 K, 150 K, 200 K) (Chapter 4).

	cafs(100 K)	**cafs**(150 K)	**cafs**(200 K)
molecular formula	$(C_8H_{10}N_4O_2)\cdot(C_7H_6O_4)$	$(C_8H_{10}N_4O_2)\cdot(C_7H_6O_4)$	$(C_8H_{10}N_4O_2)\cdot(C_7H_6O_4)$
M_r	348.32	348.32	348.32
Crystal system	monoclinic	monoclinic	monoclinic
Space group	$P2_1/n$	$P2_1/n$	$P2_1/n$
a, Å	14.831(4)	14.847(2)	14.867(2)
b, Å	6.9381(17)	6.9664(11)	7.0043(10)
c, Å	15.867(4)	15.895(3)	15.927(2)
α, °	90.00	90.00	90.00
β, °	115.387(3)	115.484(2)	115.5640(10)
γ, °	90.00	90.00	90.00
V, Å^3	1475.0(6)	1484.1(4)	1496.1(4)
Z	4	4	4
D_c/gcm^{-3}	1.569	1.559	1.546
F(000)	728	728	728
μ(Mo K$_\alpha$)/cm^{-1}	0.124	0.123	0.122
T/K	100(2)		
crystal size/mm	0.30 × 0.20 × 0.20	0.30 × 0.20 × 0.20	0.30 × 0.20 × 0.20
range of indices	-16 → 16 -7 → 7 -17 → 17	-16 → 16 -7 → 7 -17 → 17	-16 → 16 -7 → 7 -17 → 17
no. of reflections collected	11253	11459	11642
unique reflections	2141	2139	2149
R_{int}	0.0305	0.0273	0.0250
reflections with $I > 2\sigma(I)$	1771	1765	1752
no. parameters	241	241	241
$R(F)$, $F > 2\sigma$(F)	0.0337	0.0321	0.0328
$wR(F^2)$, $F > 2\sigma$(F)	0.1061	0.0996	0.1034
$R(F)$, all data	0.0483	0.0456	0.0484
$wR(F^2)$, all data	0.1314	0.1248	0.1319
Δ_r (max., min.) eÅ^{-3}	0.230, -0.262	0.270, -0.234	0.251, -0.247

Table A14 General and crystallographic data related to Chapter 4: **dyp1** (Chapter 4).

	dyp1
molecular formula	$(C_9H_{16}N_4O_2)\cdot(C_7H_6O_4)\cdot(H_2O)$
M_r	348.32
crystal system	monoclinic
space group	$P2_1/c$
a, Å	12.790(4)
b, Å	11.280(4)
c, Å	13.718(5)
α, °	90.00
β, °	108.230(7)
γ, °	90.00
V, Å^3	1879.8(11)
Z	4
D_c/gcm^{-3}	1.344
F(000)	800
μ(Mo K$_\alpha$)/cm^{-1}	0.107
T/K	293(2)
crystal size/mm	0.10 × 0.30 × 0.20
range of indices	-14 → 16 -14→ 5 -18 → 17
no. of reflections collected	5465
unique reflections	3272
R_{int}	0.0636
reflections with $I > 2\sigma(I)$	1984
no. parameters	300
$R(F)$, $F > 2\sigma$(F)	0.0531
$wR(F^2)$, $F > 2\sigma$(F)	0.1087
$R(F)$, all data	0.0936
$wR(F^2)$, all data	0.1263
Δ_r (max., min.) eÅ^{-3}	0.274, -0.246

APPENDIX B. ^{1}H NMR SPECTRA

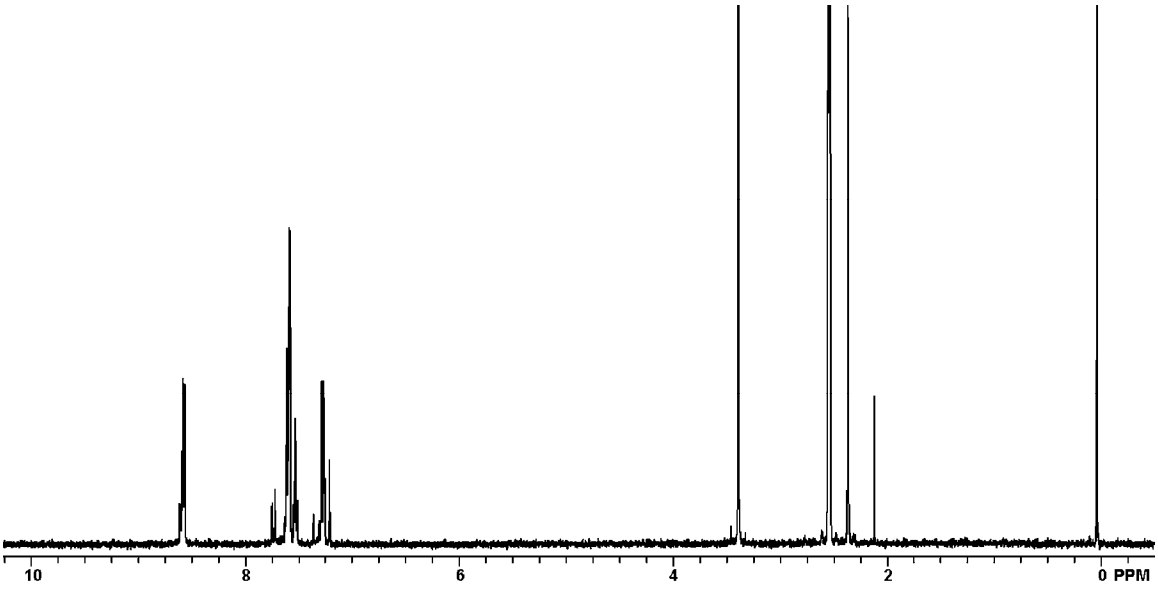

Figure B1 ^{1}H-NMR spectrum of solid solution **1** before UV irradiation.

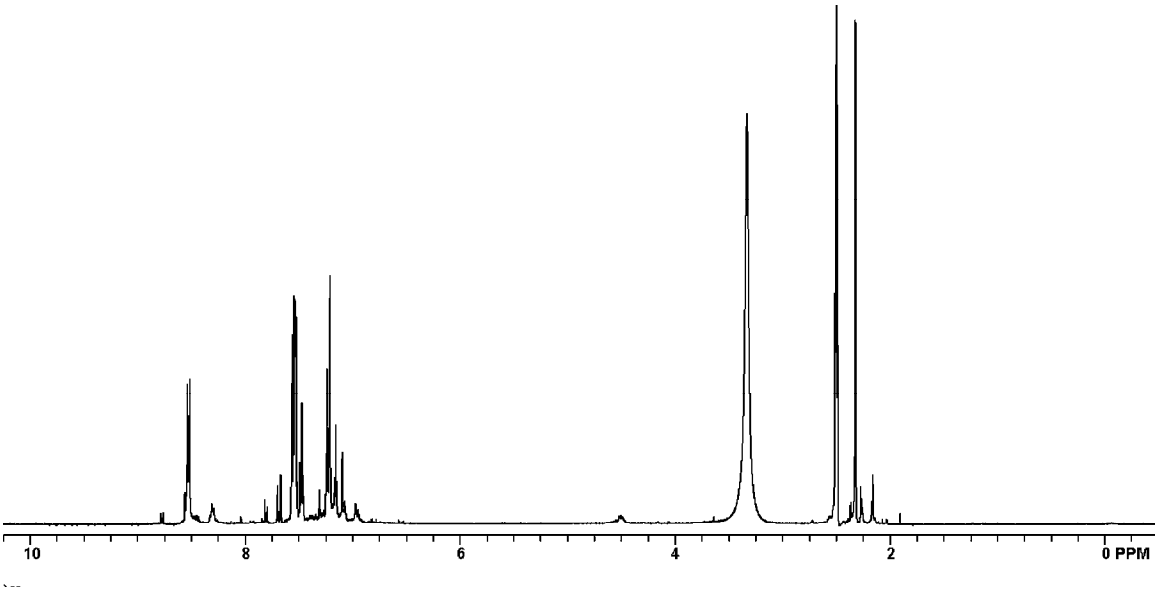

Figure B2 ^{1}H-NMR spectrum of solid solution **1** after UV irradiation.

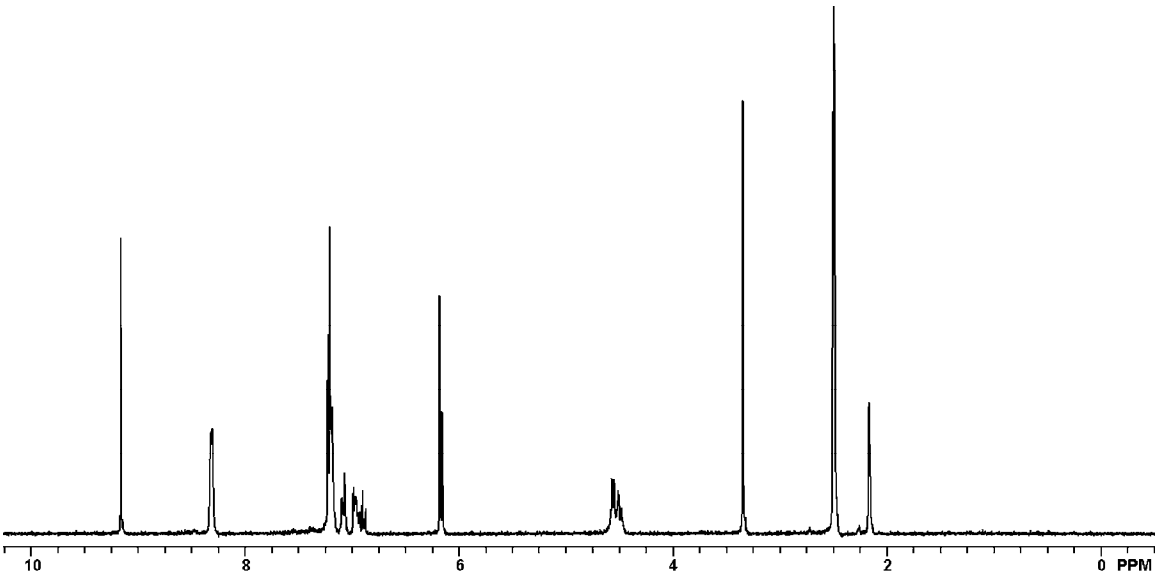

Figure B3 ^{1}H-NMR spectrum of solid solution **2** before UV irradiation.

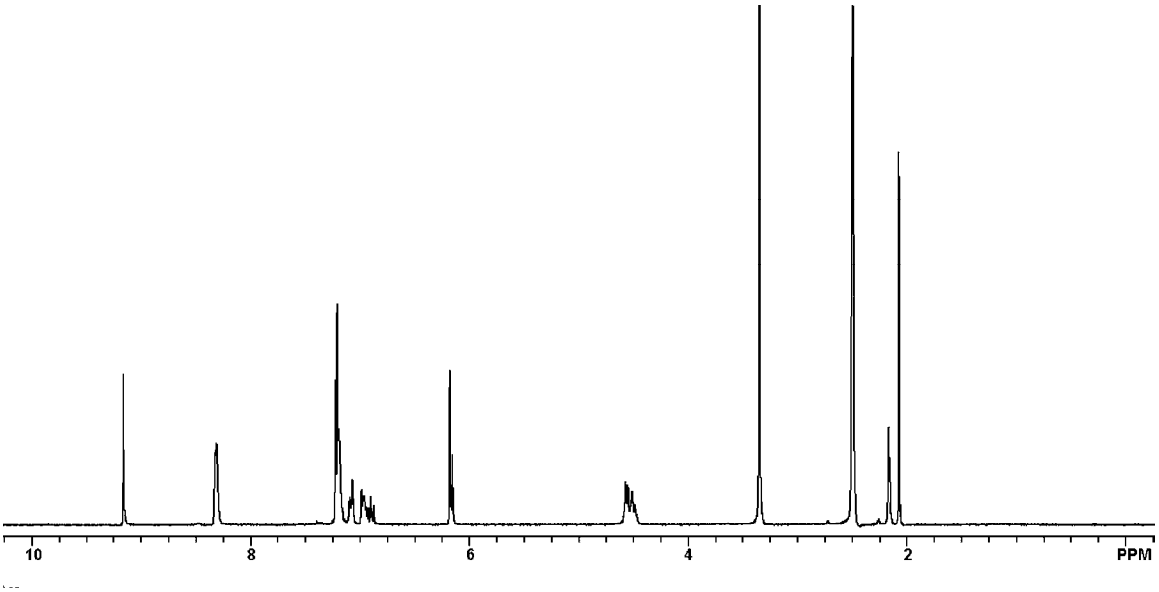

Figure B4 ^{1}H-NMR spectrum of solid solution **2** after UV irradiation.

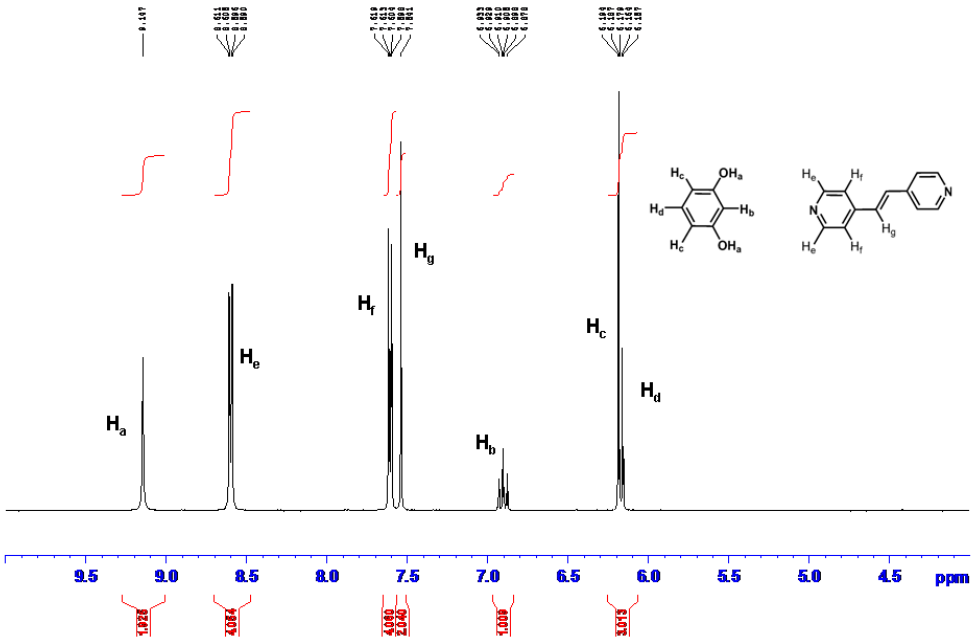

Figure B5 ^{1}H-NMR spectrum of 2(**res**)·2(**4,4'-bpe**) (macro cocrystals before UV-irradiation).

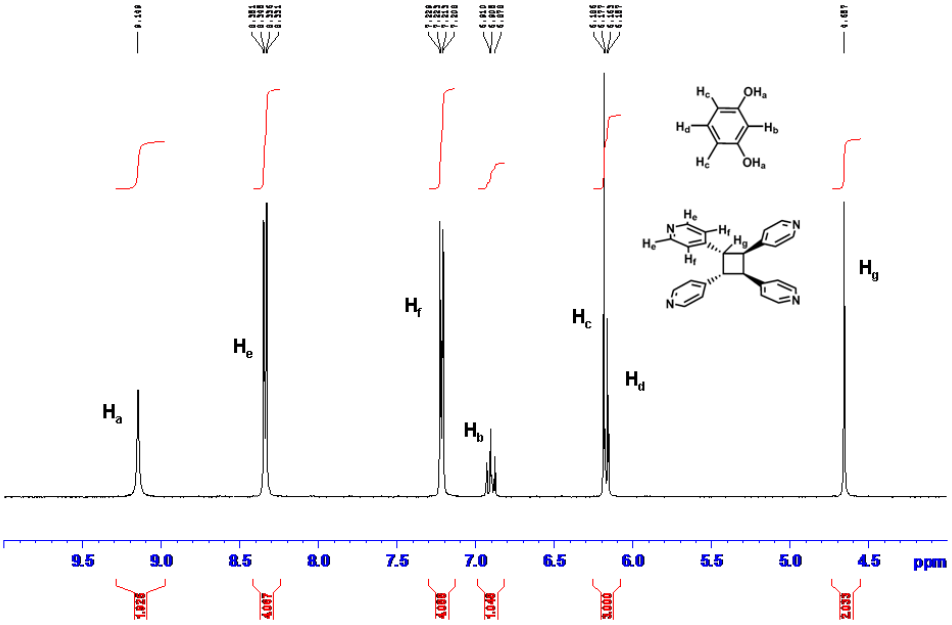

Figure B6 ^{1}H-NMR spectrum of 2(**res**)·2(**4,4'-bpe**) (macro cocrystals after UV-irradiation).

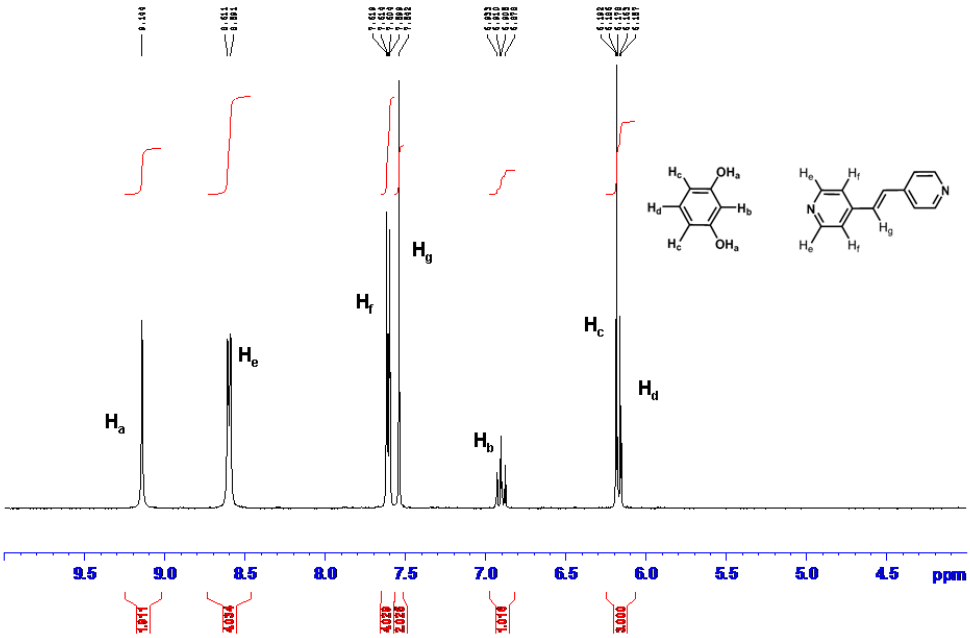

Figure B7 ^{1}H-NMR spectrum of 2(**res**)·2(**4,4'-bpe**) (nanostructured cocrystals before UV-irradiation).

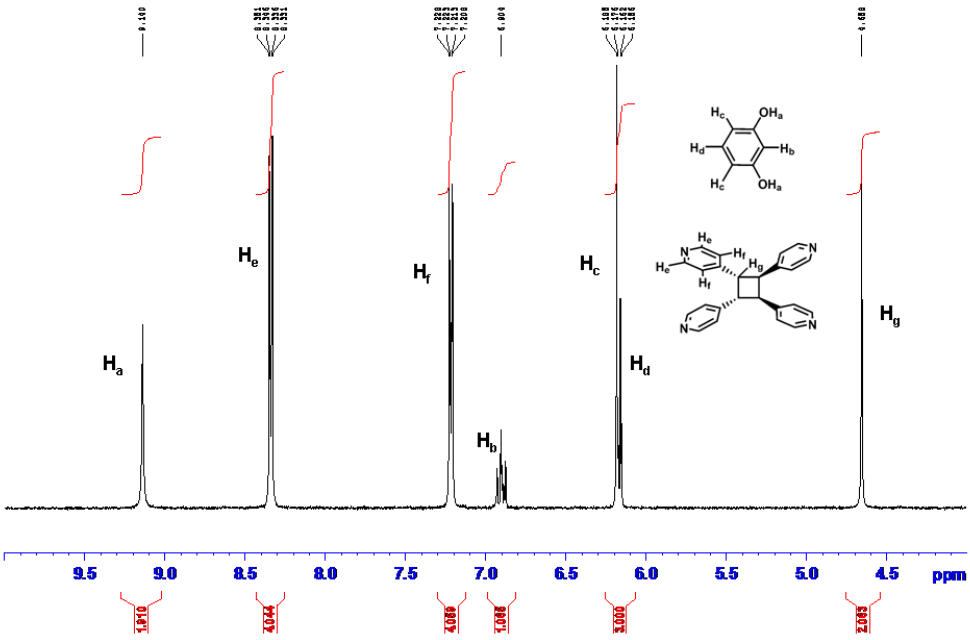

Figure B8 ^{1}H-NMR spectrum of 2(**res**)·2(**4,4'-bpe**) (nanostructured cocrystals after UV-irradiation).

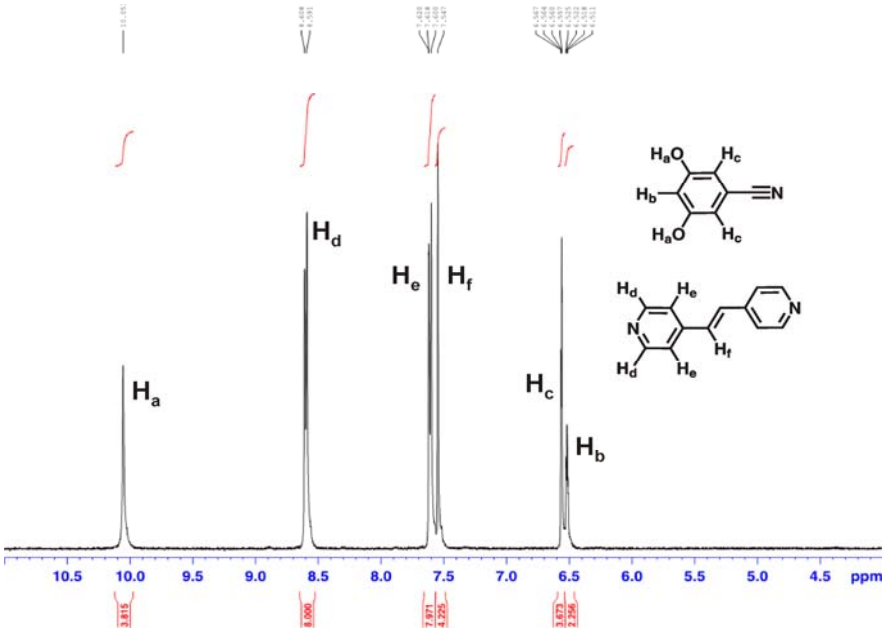

Figure B9 ^{1}H-NMR spectrum of nanodimensional 2(**5-CN-res**)·(**4,4'-bpe**) cocrystals before UV irradiation.

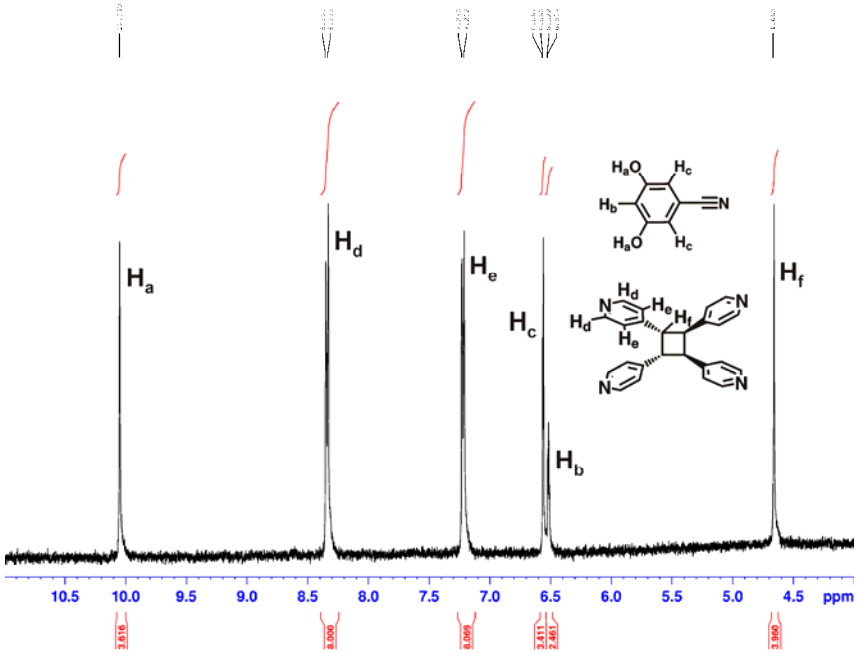

Figure B10 ^{1}H-NMR spectrum of nanodimensional 2(**5-CN-res**)·(**4,4'-bpe**) cocrystals after UV irradiation.

APPENDIX C. ESI-MASS SPECTRA AND HPLC CHROMATOGRAMS

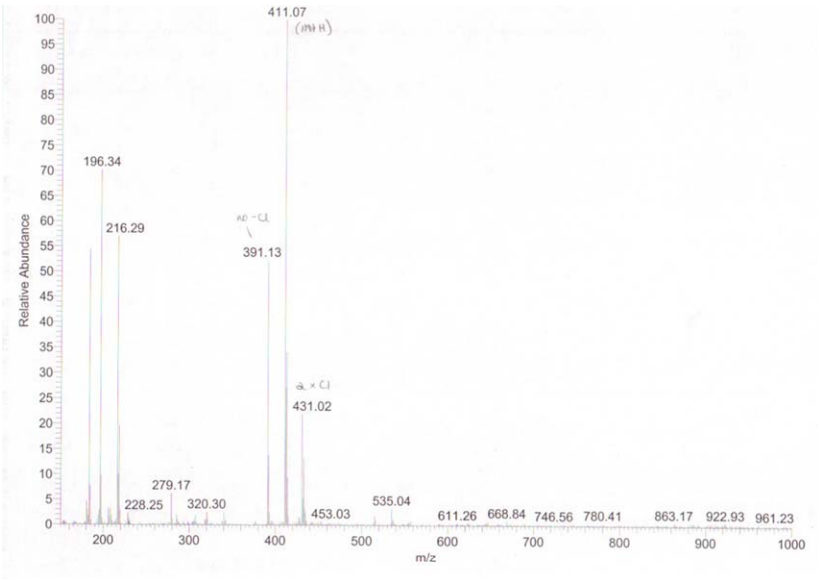

Figure C1 ESI-mass spectrum of the UV irradiated solid solution **2**.

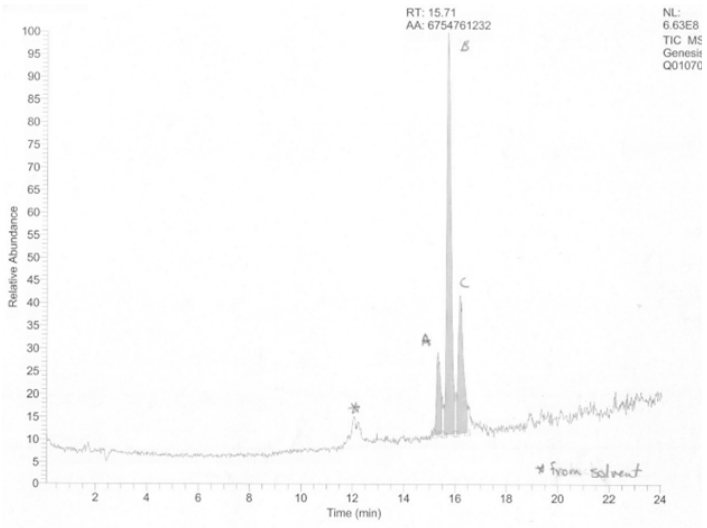

Figure C2 Chromatogram of the physical mixture of photoproducts used to quantitatively analyze the products obtained from solid solution **2**.

APPENDIX D. A COPY OF AN ARTICLE PUBLISHED IN MOLECULAR PHARMACEUTICS IN 2007

molecular pharmaceutics

articles

Co-Crystals of Caffeine and Hydroxy-2-naphthoic Acids: Unusual Formation of the Carboxylic Acid Dimer in the Presence of a Heterosynthon

Dejan-Krešimir Bučar,[†,‡] Rodger F. Henry,[§] Xiaochun Lou,[†] Richard W. Duerst,[∥] Thomas B. Borchardt,[⊥] Leonard R. MacGillivray,[‡] and Geoff G. Z. Zhang*[,†]

Solid State Sciences, Global Pharmaceutical R&D, Abbott Laboratories, North Chicago, Illinois 60064, Department of Chemistry, University of Iowa, Iowa City, Iowa 52242, Structural Chemistry, Global Pharmaceutical R&D, Abbott Laboratories, Abbott Park, Illinois 60064, Microscopy Group, Global Pharmaceutical R&D, Abbott Laboratories, Abbott Park, Illinois 60064, and Solid State Chemistry, Global Pharmaceutical R&D, Abbott Laboratories, North Chicago, Illinois 60064

Received January 5, 2007; Revised Manuscript Received April 16, 2007; Accepted April 20, 2007

Abstract: A group of caffeine-containing co-crystals of hydroxy-2-naphthoic acids were synthesized and analyzed *via* single-crystal X-ray diffraction and IR analysis. The imidazole−carboxylic acid synthon was observed in co-crystals involving 1-hydroxy-2-naphthoic and 3-hydroxy-2-naphthoic acid. In the case of 6-hydroxy-2-naphthoic acid, the co-crystal exhibits a hydrogen-bonded carboxylic acid dimer in the presence of a hydroxyl−caffeine heterosynthon.

Keywords: Pharmaceutical co-crystals; co-crystal screening; hydrogen bond; caffeine; naphthoic acid; supramolecular synthon; crystal engineering; 1-hydroxy-2-naphthoic acid; 3-hydroxy-2-naphthoic acid; 6-hydroxy-2-naphthoic acid

Introduction

Although the term "crystal engineering" was introduced in 1955 by Pepinsky[1] as a new concept in crystallography, it was first applied much later in 1971 by Schmidt in the context of synthetic and mechanistic photochemistry.[2] Two decades later, in the early 1990s, crystal engineering began to evolve from a concept to a scientific discipline focused on the design of organic solids with desired structures and properties engineered at the molecular level and derived from molecular building blocks associated by intermolecular forces (i.e., supramolecular synthons).[3−5]

Crystal engineering can be considered as the design and synthesis of crystalline solids based on supramolecular synthons, which are utilized as robust structural units (*cf.* "reactants" in conventional organic chemistry) to control the structures of single- and multicomponent solids. Co-crystals, one of the synthetic targets in crystal engineering, are a long known class of compounds, but they were not extensively studied until the late 1990s when they became recognized as valuable materials.[6−9] Even now, more than one hundred

* Author to whom correspondence should be addressed. Mailing address: Solid State Sciences, Global Pharmaceutical R&D, Abbott Laboratories, 1401 Sheridan Rd, North Chicago, IL 60064. E-mail: Geoff.GZ.Zhang@abbott.com. Tel: 1-847-937-4702. Fax: 1- 847-937-2417.

† Solid State Sciences, Global Pharmaceutical R&D, Abbott Laboratories.

‡ Department of Chemistry, University of Iowa.

§ Structural Chemistry, Global Pharmaceutical R&D, Abbott Laboratories.

∥ Microscopy Group, Global Pharmaceutical R&D, Abbott Laboratories.

⊥ Solid State Chemistry, Global Pharmaceutical R&D, Abbott Laboratories.

(1) Pepinsky, R. Crystal Engineering: New Concepts in Crystallography. *Phys. Rev.* **1955**, *100*, 971−971.

(2) Schmidt, G. M. Photodimerization in the Solid State. *J. Pure Appl. Chem.* **1971**, *27*, 647−678.

(3) Braga, D. Crystal engineering, Where from? Where to? *Chem. Commun.* **2003**, 2751−2754.

(4) Desiraju, G. R. Supramolecular Synthons in Crystal Engineering—A New Organic Synthesis. *Angew. Chem., Int. Ed. Engl.* **1995**, *34*, 2311−2327.

(5) Nangia, A.; Desiraju, G. R. Supramolecular Synthons and Pattern Recognition. *Top. Curr. Chem.* **1998**, *198*, 57−95.

10.1021/mp070004b CCC: $37.00 © 2007 American Chemical Society
Published on Web 05/10/2007

years after the first co-crystals were reported,[10,11] the definition of the term co-crystal is a current theme and a topic for discussion.[12,13] The most recent definition of co-crystals has been given by Aakeröy and co-workers.[14] They defined co-crystals as (1) compounds constructed from neutral molecules; (2) made from reactants that are solids at ambient conditions; and (3) structurally homogeneous crystalline materials that contains at least two neutral building blocks with a well-defined stoichiometry.

In recent years, concepts of crystal engineering have been successfully applied in the template-directed solid-state synthesis of molecular targets,[15−17] development of organic semiconductors,[18] and development of other functional materials.[19−23] In the field of pharmaceutical sciences, however, crystal engineering has emerged only recently.[24−32] Despite such recent emergence, however, several attempts to design new pharmaceutical solids to improve properties of pharmaceutical agents (PAs) (e.g., solubility, dissolution rate, bioavailability, stability) have already been reported. Studies show that PA-containing co-crystals may have a significant impact on pharmaceutical formulations. These studies have focused primarily on the improvement of solubility/dissolution[33,34] and hygroscopicity[35] by co-crystallization of the PA with appropriate co-crystal formers.

In this contribution, we focus on the syntheses and structural characterizations of co-crystals of caffeine and three hydroxy-2-naphthoic acids; namely, 1-hydroxy-2-naphthoic acid (1HNA), 3-hydroxy-2-naphthoic acid (3HNA), and 6-hydroxy-2-naphthoic acid (6HNA) (Scheme 1). Recently, co-crystals of caffeine and various carboxylic acids

(6) Panunto, T. W.; Urbanczyk-Lipkowska, Z.; Johnson, R.; Etter, M. C. Hydrogen-Bond Formation in Nitroanilines: The First Step in Designing Acentric Materials. *J. Am. Chem. Soc.* **1987**, *109*, 7786−7797.

(7) Etter, M. C. Hydrogen Bonds as Design Elements in Organic Chemistry. *J. Phys. Chem.* **1991**, *95*, 4601−4610.

(8) Etter, M. C.; Urbakzyk-Lipkowska, Z.; Mohammad Zia-Ebrahimi, S.; Panunto, T. W. Hydrogen Bond Directed Cocrystallization and Molecular Recognition Properties of Diarylureas. *J. Am. Chem. Soc.* **1990**, *112*, 8415−8426.

(9) Etter, M. C.; Reutzel, S. M.; Choo, C. G. Self-organization of Adenine and Thymine in the Solid State. *J. Am. Chem. Soc.* **1993**, *115*, 4411−4412.

(10) Wöhler, F. Untersuchungen über das Chinon. *Annalen* **1844**, *51*, 153−153.

(11) Ling, A. R.; Baker, J. L. Derivatives of Quinhydrone. *J. Chem. Soc.* **1893**, *63*, 1314−1327.

(12) Desiraju, G. R. Crystal and Co-crystal. *CrystEngComm* **2003**, *5*, 466−467.

(13) Dunitz, J. D. Crystal and Co-crystal: A Second Opinion. *CrystEngComm* **2003**, *5*, 506−506.

(14) Aakeröy, C. B.; Salmon, D. J. Building Co-crystals with Molecular Sense and Supramolecular Sensibility. *CrystEngComm* **2005**, *7*, 439−448.

(15) Friščić, T.; MacGillivray, L. R. "Template-switching": A Supramolecular Strategy for the Quantitative, Gram-scale Construction of a Molecular Target in the Solid State. *Chem. Commun.* **2003**, 1306−1307.

(16) Gao, X.; Friščić, T.; MacGillivray, L. R. Supramolecular Construction of Molecular Ladders in the Solid State. *Angew. Chem., Int. Ed.* **2004**, *43*, 232−236.

(17) Hamilton, T. D.; Papaefstathiou, G. S.; MacGillivray, L. R. A Polyhedral Host Constructed Using a Linear Template. *J. Am. Chem. Soc.* **2002**, *124*, 11606−11607.

(18) Sokolov, A. N.; Friščić, T.; MacGillivray, L. R. Enforced Face-to-Face Stacking of Organic Semiconductor Building Blocks within Hydrogen-Bonded Molecular Cocrystals. *J. Am. Chem. Soc.* **2006**, *128*, 2806.

(19) Thallapally, P. K.; Wirsig, T. B.; Barbour, L. J.; Atwood, J. L. Crystal Engineering of Nonporous Organic Solids for Methane Sorption. *Chem. Commun.* **2005**, 4420−4422.

(20) Eddaoudi, M.; Moler, D. B.; Li, H. L.; Chen, B. L.; Reineke, T. M.; O' Keeffe, M.; Yaghi, O. M. Modular Chemistry: Secondary Building Units as a Basis for the Design of Highly Porous and Robust Metal-Organic Carboxylate Frameworks. *Acc. Chem. Res.* **2001**, *34*, 319−330.

(21) Kitagawa, S.; Kitaura, R.; Noro, S. Functional Porous Coordination Polymers. *Angew. Chem., Int. Ed.* **2004**, *43*, 2334−2375.

(22) Moulton, B.; Zaworotko, M. J. From Molecules to Crystal Engineering: Supramolecular Isomerism and Polymorphism in Network Solids. *Chem. Rev.* **2001**, *101*, 1629−1658.

(23) Rowsell, J. L. S.; Spencer, E. C.; Eckert, J.; Howard, J. A. K.; Yaghi, O. M. Gas Adsorption Sites in a Large-Pore Metal-Organic Framework. *Science* **2005**, *309*, 1350−1354.

(24) Walsh, R. D. B.; Bradner, M. W.; Fleischman, S. G.; Morales, L. A.; Moulton, B.; Rodriguez-Hornedo, N.; Zaworotko, M. J. Crystal Engineering of the Composition of Pharmaceutical Phases. *Chem. Commun.* **2003**, 186−187.

(25) Fleischman, S. G.; Kuduva, S. S.; McMahon, J. A.; Moulton, B.; Walsh, R. D. B.; Rodriguez-Hornedo, N.; Zaworotko, M. J. Crystal Engineering of the Composition of Pharmaceutical Phases: Multiple-Component Crystalline Solids Involving Carbamazepine. *Cryst. Growth Des.* **2003**, *3*, 909−919.

(26) McMahon, J. A.; Bis, J. A.; Vishweshwar, P.; Shattock, T. R.; McLaughlin, O. L.; Zaworotko, M. J. Crystal Engineering of the Composition of Pharmaceutical Phases 3. Primary Amide Supramolecular Heterosynthons and Their Role in the Design of Pharmaceutical Co-crystals. *Z. Kristallogr.* **2005**, *220*, 340−350.

(27) Almarsson, Ö.; Zaworotko, M. J. Crystal Engineering of the Composition of Pharmaceutical Phases. Do Pharmaceutical Co-crystals Represent a New Path to Improved Medicines? *Chem. Commun.* **2004**, 1889−1896.

(28) Vishweshwar, P.; McMahon, J. F.; Peterson, M. L.; Hickey, M. B.; Zaworotko, M. J. Crystal Engineering of Pharmaceutical Co-crystals from Polymorphic Active Pharmaceutical Ingredients. *Chem. Commun.* **2005**, 4601−4603.

(29) Morissette, S. L.; Almarsson, Ö.; Peterson, M. L.; Remenar, J. F.; Read, M. J.; Lemmo, A. V.; Ellis, S.; Cima, M. J.; Gardner, C. R. High-throughput Crystallization: Polymorphs, Salts, Co-crystals and Solvates of Pharmaceutical Solids. *Adv. Drug Del. Rev.* **2004**, *56*, 275−300.

(30) Childs, S. L.; Chyall, L. J.; Dunlap, J. T.; Smolenskaya, V. N.; Stahly, B. C.; Stahly, G. P. Crystal Engineering Approach To Forming Cocrystals of Amine Hydrochlorides with Organic Acids. Molecular Complexes of Fluoxetine Hydrochloride with Benzoic, Succinic, and Fumaric Acids. *J. Am. Chem. Soc.* **2004**, *126*, 13335−13342.

(31) Reddy, L. S.; Babu, N. J.; Nangia, A. Carboxamide−pyridine N-oxide Heterosynthon for Crystal Engineering and Pharmaceutical cocrystals. *Chem. Commun.* **2006**, 1369−1371.

(32) Trask, A. V.; Motherwell, W. D. S.; Jones, W. Solvent-drop Grinding: Green Polymorph Control of Cocrystallization. *Chem. Commun.* **2004**, 890−891.

Scheme 1. The Chemical Structure of (a) Caffeine, (b) 1-Hydroxy-2-naphthoic Acid, (c) 3-Hydroxy-2-naphthoic Acid, and (d) 6-Hydroxy-2-naphthoic Acid

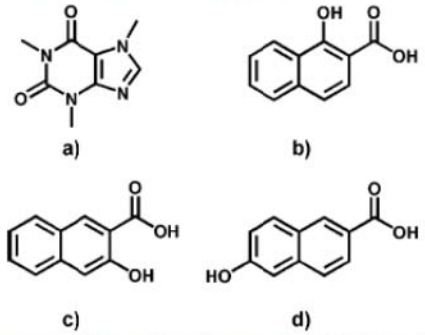

have emerged as materials to improve the physical properties of caffeine (e.g., physical stability against hydration), as well as model compounds for studying preparation methods (e.g., solvent-free grinding)[35] and structural effects associated with pharmaceutical co-crystals in general. In these solids, caffeine invariably forms molecular complexes in which the carboxylic acid group interacts with the N atom of the imidazole ring *via* an O−H···N hydrogen bond.[36] A literature search of the Cambridge Structural Database (CSD)[37] has revealed 21 complexes in which the caffeine and carboxylic acid components are held together by one of two heterosynthons: (1) an $R_2^2(7)$ heterosynthon and (2) an $R_3^3(11)$ network based on $R_2^2(7)$ and $R_2^2(6)$ heterosynthons (Figure 1).[35,38−40,44c] A general goal of this study is to begin to examine the structural effects of adding a hydrogen-bond-donating functional group (i.e., hydroxyl group) along the periphery of a carboxylic acid in a caffeine−carboxylic acid co-crystal. Indeed, studies to introduce additional synthons to co-crystals are emerging as useful means to refine crystal engineering strategies of organic solids. Upon further searching the CSD, we noticed that the carbonyl group of caffeine, in a molecular complex of caffeine with methyl 3,4,5-trihydroxybenzoate,[41] served as a hydrogen-bond acceptor group in an O−H···O hydrogen bond with the benzoate component. Moreover, this observation suggested to us that the incorporation of an additional heterosynthon to a caffeine−carboxylic acid co-crystal was possible. To our surprise, although we have found that the O−H···O=C heterosynthon can be introduced within the co-crystal of caffeine and 6HNA, we have discovered that the introduction of the heterosynthon disrupts the COOH···N interaction and, in addition to the new heterosynthon, yields the well-known hydrogen-bond carboxylic acid dimer. To our knowledge, the co-crystal of caffeine and 6HNA represents a rare case in which the carboxylic acid dimer coexists with a heterosynthon.

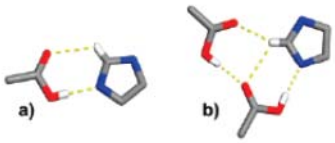

Figure 1. The most common acid−imidazole heterosynthons present in caffeine:carboxylic acid co-crystals.

Experimental Section

Materials. Caffeine (ReagentPlus), 1HNA (99%), 3HNA (98%), 6HNA (98%), and acetonitrile (anhydrous, 99.8%)

(33) Nehm, J. S.; Rodríguez-Spong, B.; Rodríguez-Hornedo, N. Phase Solubility Diagrams of Cocrystals Are Explained by Solubility Product and Solution Complexation. *Cryst. Growth Des.* **2006**, *6*, 592−600.

(34) Remenar, J. F.; Morissette, S. L.; Peterson, M. L.; Moulton, B.; MacPhee, J. M.; Guzmán, H. R.; Almarsson, Ö. Crystal Engineering of Novel Cocrystals of a Triazole Drug with 1,4-Dicarboxylic Acids. *J. Am. Chem. Soc.* **2003**, *125*, 8456−8457.

(35) Trask, A. V.; Motherwell, W. D. S.; Jones, W. Pharmaceutical Cocrystallization: Engineering a Remedy for Caffeine Hydration. *Cryst. Growth Des.* **2005**, *5*, 1013−1021.

(36) CSD refcodes: CAFSAL, DIJVUN, EXUQUJ, EXUQUJ03, GANXUP, GANYAW, GANYEA, GANYIE, VAWKIO, VAWOU, VAWKUA, VAWKU01.

(37) Allen, F. H.; Motherwell, W. D. S. The Cambridge Structural Database: A Quarter of a Million Crystal Structures and Rising. *Acta Crystallogr.* **2002**, *B58*, 380−388.

(38) Trask, A. V.; van de Streek, J.; Motherwell, W. D. S.; Jones, W. Achieving Polymorphic and Stoichiometric Diversity in Cocrystal Formation: Importance of Solid-State Grinding, Powder X-ray Structure Determination, and Seeding. *Cryst. Growth Des.* **2005**, *5*, 2233−2241.

(39) Fričšić, T.; Fábián, L; Burley, J. C.; Jones, W.; Motherwell, W. D. S. Exploring Cocrystal-Cocrystal Reactivity *via* Liquid-assisted Grinding: The Assembling of Racemic and Dismantling of Enantiomeric Cocrystals. *Chem. Commun.* **2006**, 5009−5011.

(40) Bučar, D.-K.; Henry, R. F.; Lou, X.; Borchardt, T. B.; Zhang, G. G. Z. A "Hidden" Co-crystal of Caffeine and Adipic Acid. *Chem. Commun.* **2007**, 525−527.

(41) Martin, R.; Lilley, T. H.; Bailey, N. A.; Falshaw, C. P.; Haslam, E.; Magnolato, D.; Begley, M. J. Polyphenol−caffeine Complexation. *Chem. Commun.* **1986**, 105−106.

(42) Bruno, I. J.; Cole, J. C.; Edgington, P. R.; Kessler, M.; Macrae, C. F.; McCabe, P.; Pearson, J.; Taylor, R. New Software for Searching the Cambridge Structural Database and Visualizing Crystal Structures. *Acta Crystallogr.* **2002**, *B58*, 389−397.

(43) Zhang, G. G. Z.; Henry, R. F.; Borchardt, T. B., Lou, X. Efficient Co-Crystal Screening Using Solution-Mediated Phase Transformation. *J. Pharm Sci.* **2007**, *96*, 990−995.

(44) For recent publications on co-crystal formation, see: (a) Bučar, D.-K.; MacGillivray, L. R. Preparation and Reactivity of Nanocrystalline Cocrystals Formed *via* Sonocrystallization. *J. Am. Chem. Soc.* **2007**, *129*, 32−33. (b) Rodríguez-Hornedo, N.; Nehm, S. J.; Seefeldt, K. F.; Pagán-Torres, Y.; Falkiewicz, C. J. Reaction Crystallization of Pharmaceutical Molecular Complexes. *Mol. Pharmaceutics* **2006**, *3*, 362−367. (c) Fričšić, T.; Trask, A. V; Jones, W.; Motherwell, W. D. S. Screening for Inclusion Compounds and Systematic Construction of Three-Component Solids by Liquid-Assisted Grinding. *Angew. Chem., Int. Ed.* **2006**, *45*, 7546−7550.

Table 1. Crystallographic Data for A, B and C

	A	B	C
molecular formula	$(C_8H_{10}N_4O_2)(C_{11}H_8O_3)$	$(C_8H_{10}N_4O_2)(C_{11}H_8O_3)$	$(C_8H_{10}N_4O_2)(C_{11}H_8O_3)$
M_r	382.37	382.37	382.37
crystal system	monoclinic	monoclinic	triclinic
space group	$P2_1/n$	$P2_1/c$	$P\bar{1}$
a, Å	7.606(2)	9.040(9)	8.029(3)
b, Å	14.042(3)	24.42(2)	8.592(3)
c, Å	16.327(4)	8.654(8)	13.996(5)
α, deg	90.000	90.000	106.475(5)
β, deg	94.030(4)	117.2(1)	98.162(5)
γ, deg	90.000	90.000	104.904(6)
V, Å^3	1739.6(7)	1702(3)	870.3(5)
Z	4	4	2
D_c/g cm^{-3}	1.460	1.492	1.459
$F(000)$	800	800	400
μ(Mo Kα)/cm^{-1}	0.108	0.111	0.108
crystal size/mm	0.5 × 0.25 × 0.10	0.3 × 0.2 × 0.1	0.4 × 0.2 × 0.15
range of indices	−10, 9; −18, 18; −21, 21	−11, 12; −32, 32; −11, 11	−10, 10; −11, 11; −18, 18
no. of reflections collected	20038	19094	10422
unique reflections	4246	4167	4196
R_{int}	0.1294	0.1024	0.0804
reflections with $I > 2\sigma(I)$	3374	4167	3270
no. of parameters	265	264	303
$R(F)$, $F > 2\sigma(F)$	0.0926	0.0631	0.0605
$wR(F^2)$, $F > 2\sigma(F)$	0.1198	0.1038	0.0757
$wR(F^2)$, all data	0.2166	0.1011	0.1187
Δ_r (max, min) e Å^{-3}	0.346, −0.319	0.270, −0.199	0.371, −0.198

Table 2. Carbon−Oxygen Bond Distances in the Caffeine−Hydroxy-2-naphthoic Acid Co-Crystals

co-crystal	d(C−O)/(Å)	d(C=O)/(Å)
A	1.318(4)	1.236(4)
B	1.320(3)	1.217(3)
C	1.312(2)	1.240(2)

were purchased from Sigma-Aldrich (St. Louis, MO) and were used as received.

Cambridge Crystallographic Database Search. The CSD database survey was accomplished on version 5.27 (including Update 3, August 2006) using ConQuest[42] (version 1.8). The CSD was searched with respect to fragments with a single filter in place: hits are organic compounds and with 3-D coordinates.

Co-Crystal Screening. A recently developed co-crystal screening method that utilizes the thermodynamically driven solution-mediated phase transformation[43] was used to screen the hydroxy-2-naphthoic acids for co-crystal formation[44] with caffeine. Caffeine (1 mmol) was mixed with 1 molar equiv of 1HNA, 3HNA, and 6HNA, respectively. Acetonitrile (2 mL) was added to the physical mixture. The suspension was briefly sonicated and equilibrated overnight at ambient conditions. The residual solid was filtered and examined by powder X-ray diffractometry. In all cases, a new solid phase was formed from the suspension, indicating a potential co-crystal formation. Single crystals were then grown and structures were determined as described below to confirm the co-crystal formation.

Single-Crystal Preparation. Single crystals of compounds **A** (caffeine:1HNA co-crystal), **B** (caffeine:3HNA co-crystal), and **C** (caffeine:6HNA co-crystal) were obtained by slow evaporation from solution. Caffeine (0.1 mmol) was individually mixed with 1HNA, 3HNA, and 6HNA, respectively (0.1 mmol). Acetonitrile (2 mL) was added to the solid mixtures. The suspension was heated until the caffeine: hydroxy-2-naphthoic acid mixture was completely dissolved. The resulting mixture was kept at 348 K for 10 min and filtered. The filtrate was left to evaporate slowly at 298 K. Single crystals of **A** suitable for X-ray diffraction study were obtained after 1 day, while those of **B** and **C** were obtained after 2 days.

Infrared (IR) Spectroscopy. Transmission infrared spectra of the solids were obtained using a Fourier-transform infrared spectrometer (Nicolet Magna 750 FT-IR spectrometer) equipped with a Nicolet NIC-PLAN microscope. The microscope has an MCT-A liquid nitrogen cooled detector. The samples were rolled on a 13 mm x 1 mm BaF_2 disk sample holder; 64 scans were collected at 4 cm^{-1} resolution.

Powder X-ray Diffractometry (PXRD). PXRD data were collected using a G3000 diffractometer (Inel Corp., Artenay, France) equipped with a curved position sensitive detector and parallel beam optics. The diffractometer was operated with a copper anode tube (1.5 kW fine focus) at 40 kV and 30 mA. An incident beam germanium monochromator provided monochromatic $K\alpha_1$ radiation. The diffractometer was calibrated using the attenuated direct beam at 1° intervals. Calibration was checked using a silicon powder

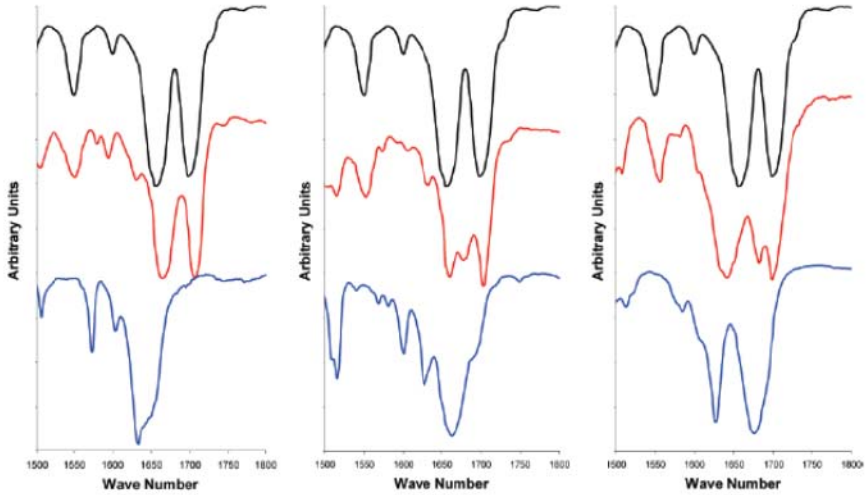

Figure 2. Infrared spectra of the carbonyl stretching region for caffeine (top, black), co-crystal (middle, red), and co-crystal former (bottom, blue). Left: caffeine−1HNA. Middle: caffeine−3HNA. Right: caffeine−6HNA.

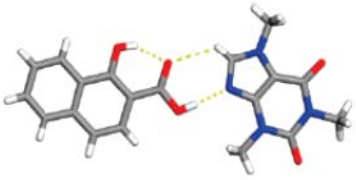

Figure 3. A perspective view of the two-component complex of caffeine and 1-hydroxy-2-naphthoic acid with an $R_2^2(7)$ hydrogen-bond pattern.

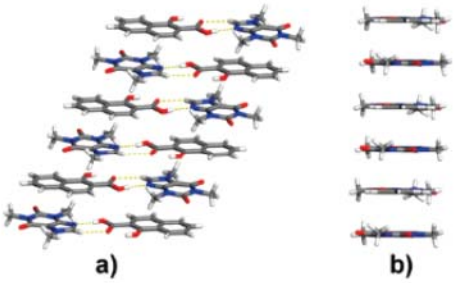

Figure 4. Perspective views of caffeine:1-hydroxy-2-naphthoic acid assemblies in the solid state, stacked in a "head-to-tail" manner.

line position reference standard (NIST 640c). The instrument was computer controlled using the Symphonix software,[45] and the data was analyzed using the Jade 6.5 software.[46] The sample was loaded onto an aluminum sample holder and leveled with a glass slide.

Crystallography. Single crystals of **A**, **B**, and **C** were individually mounted on glass fibers. Intensity data were collected on a Bruker SMART system equipped with an APEX CD camera. Data were collected at 173 K with graphite-monochromated Mo Kα radiation ($\lambda = 0.71073$ Å). Data were collected in four sets using $\omega-\phi$ scans with ω steps of 0.3° and ϕ steps of 90°. A total of 2350 frames were collected with 20 s frame exposures. Data were processed using Saint*Plus*.[47] Corrections for Lorentz−polarization effects were applied. Absorption was negligible. All structures were solved using direct methods that yielded the non-hydrogen atoms. All presented hydrogen atoms were located in Fourier-difference electron density maps. All non-hydrogen atoms were refined anisotropically. Hydrogen atoms associated with carbon atoms were refined in geometrically constrained riding positions. Hydrogen atoms associated with oxygen atoms were included in the located positions. Refinement was achieved with the use of SHELX-97.[48]

Results

The crystal structure analyses reveal a 1:1 stoichiometry of caffeine:acid in each solid. The asymmetric units of **A**, **B**, and **C** contain one molecule of caffeine and one molecule of hydroxy-2-naphthoic acid. To classify the new caffeine

(45) Symphonix, Inel Corp., Artenay, France.

(46) Jade, version 6.5, Materials Data, Inc., Livermore, CA.
(47) Saint*Plus*, version 6.02, Bruker AXS Inc., Madision, WI, 1999.
(48) Sheldrick, G. M., University of Göttingen, Germany, 1998.

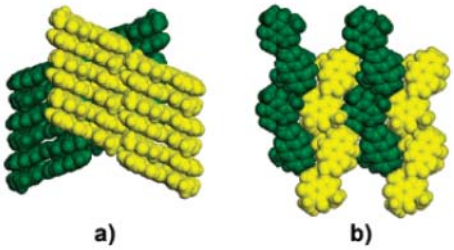

Figure 5. A space-filling model of the crystal packing of stacked caffeine:1-hydroxy-2-naphthoic acid assemblies viewed along the crystallographic planes: (a) (1 1 0) and (0 1 0); (b) (1 1 0) and (0 0 1).

Table 3. Selected Hydrogen-Bond Parameters of Co-Crystals **A**, **B**, and **C**

co-crystal	D−H···A	d(H···A)/Å	d(D···A)/Å	θ(D−H···A)/deg
A	O5−H2o···O4	1.71(4)	2.545(3)	156(4)
	O3−H1o···N3	1.78(5)	2.669(3)	173(4)
B	O5−H2o···O4	1.81(3)	2.576(3)	150(3)
	O3−H1o···N3	1.75(3)	2.692(3)	170(2)
C	O5−H2o···O2	1.84(2)	2.742(2)	170(2)
	O3−H1o···O4	1.66(2)	2.642(2)	177(2)

phases **A**, **B**, and **C** as either a neutral (i.e., co-crystal) or ionic (i.e., salt) complex, it was necessary to analyze the geometry of the carboxyl group and locate the acidic proton. The carbon−oxygen bond distances were consistent with the formation of a co-crystal in each case (Table 2). Moreover, an analysis of the Fourier difference map revealed that the acidic proton was located 0.887−0.983 Å from the O atom of the carboxylic acid. Thus, compounds **A**, **B**, and **C** were classified as co-crystals. Additionally, analyses of the carbonyl stretching bands in the infrared spectra, which are all above 1600 cm^{-1} (Figure 2), confirmed un-ionized carboxylic acids and thus co-crystal formation for these new phases. A typical ionized carboxylic acid salt band would be expected to occur below 1600 cm^{-1}.

1. Co-Crystal A. Co-crystal **A** crystallizes in the monoclinic $P2_1/n$ space group. Caffeine and 1HNA form a two-component assembly based on an $R_2^2(7)$ hydrogen-bond pattern that involves the carbonyl and imidazole moieties. The hydroxy group of 1HNA is involved in an intramolecular O−H···O hydrogen bond[49] with the carboxylic group to form an $S_1^1(6)$ ring (Figure 3). The two-component assemblies stack in a "head-to-tail" manner (Figure 4), being held together by weak van der Waals interactions. The stacks are sustained by C−H···O hydrogen bonds (Figure 5). Selected hydrogen-bond parameters are listed in Table 3.

2. Co-Crystal B. Co-crystal **B** crystallizes in the monoclinic $P2_1/c$ space group. Similar to **A**, the caffeine and acid components form a two-component assembly involving

(49) Cochran, W. The Crystal and Molecular Structure of Salicylic Acid. *Acta Crystallogr.* **1953**, *6*, 260−268.

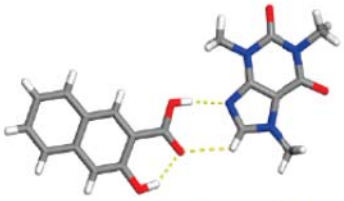

Figure 6. A perspective view of the neutral 1:1 caffeine:3-hydroxy-2-naphthoic acid assembly.

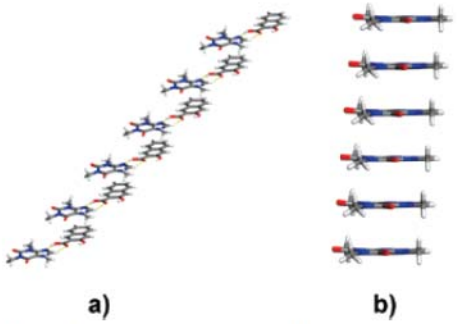

Figure 7. Perspective views of caffeine:3-hydroxy-2-naphthoic acid assemblies in the solid state, stacked in a "head-to-head" manner.

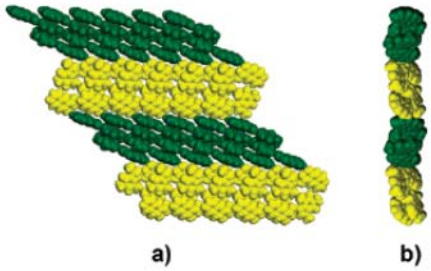

Figure 8. A space-filling model of the crystal packing of stacked caffeine:3-hydroxy-2-naphthoic acid assemblies viewed along the crystallographic planes: (a) (1 0 1) and (0 1 0); (b) (1 0 −1) and (0 1 0).

both an intramolecular O−H···O and an intermolecular O−H···N hydrogen bond (Figure 6). The acid−base pairs interact in a parallel and offset manner *via* weak van der Waals forces to form stacks. The stacks are sustained by C−H···O hydrogen bonds (Figures 7 and 8). The pairs within the stacks are offset by one caffeine molecule. Selected hydrogen bond parameters are shown in Table 3.

3. Co-Crystal C. Co-crystal **C** crystallizes in the triclinic $P\bar{1}$ space group. Similar to **A** and **B**, an intermolecular hydrogen bond has formed between the caffeine and hy-

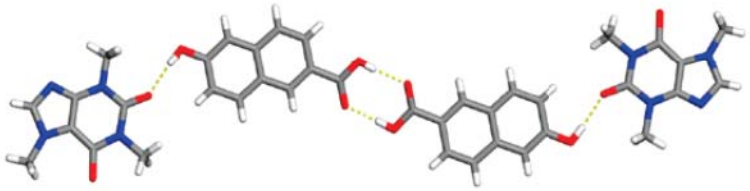

Figure 9. A perspective view of the 1:1 caffeine:6-hydroxy-2-naphthoic acid (the second position of the disordered caffeine is omitted for clarity).

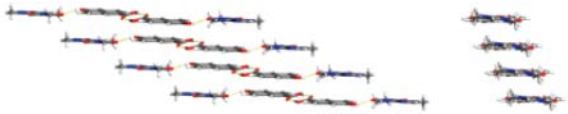

Figure 10. Perspective views of caffeine:6-hydroxy-2-naphthoic acid assemblies in the solid state, stacked in a "head-to-head" manner.

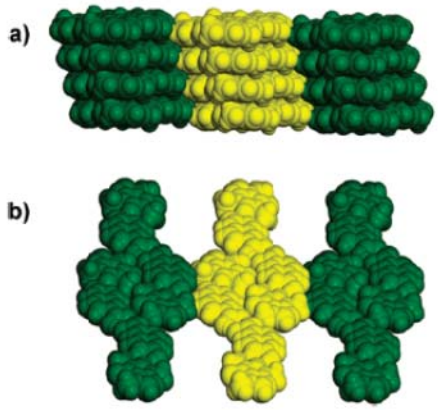

Figure 11. A space-filling model of the crystal packing of stacked assemblies of caffeine:6-hydroxy-2-naphthoic acid viewed along the crystallographic planes: (a) (1 2 0) and (0 0 1); (b) (0 1 0) and (0 0 1).

droxy-2-naphthoic acid molecule. In contrast to **A** and **B**, however, yet can be as expected, the intermolecular hydrogen bond involves the free hydroxy group of 6HNA. The free hydroxyl group participates in an O−H···O interaction with the carbonyl group of caffeine. Surprisingly, the carboxylic acid groups of the two acids interact with each other, forming a dimer that is based on the well-known $R_2^2(8)$ homosynthon. Consequently, the N atom of the imidazole ring, which lies disordered over two positions (site occupancies: 0.662: 0.338), does not participate in a hydrogen bond. The assembly process has, thus, produced a discrete four-component array that is held together by two intermolecular O−H(carboxyl)···O(carboxyl) and two intermolecular O−H(hydroxyl)···O(carbonyl) hydrogen bonds (Figure 9). The assemblies stack in a parallel and offset manner (Figure 10), being held together *via* weak van der Waals interactions. The stacks are sustained by C−H···O hydrogen bonds (Figure 11). Selected hydrogen bond parameters are listed in Table 3.

Discussion

Co-crystals **A** and **B** form two-component assemblies based on the well-established caffeine(imidazole)−carboxylic acid synthon. As in the case of 1HNA and 3HNA, ortho hydroxy groups of carboxylic acids are known to form intramolecular O−H···O hydrogen-bonds.[49] It was, therefore, expected that an intermolecular O−H(hydroxyl)···O(caffeine) heterosynthon would not likely form in those co-crystals involving 1HNA and 3HNA.

The introduction of a free (i.e., incapable of intramolecular hydrogen bonding) hydroxyl group of 6HNA resulted in the formation of an O−H···O hydrogen bond between the hydroxy group of 6HNA and the caffeine carbonyl group in **C**. To the best of our knowledge, this is the first reported case in which the imidazole(caffeine)−carboxylic acid synthon is absent in a caffeine−carboxylic acid co-crystal. Moreover, the coexistence of a carboxylic acid dimer in the presence of such a supramolecular heterosynthon[50,51] is rare.

(50) Aakeröy, C. B.; Desper, J.; Helfrich, B. A. Heteromeric Intermolecular Interactions as Synthetic Tools for the Formation of Binary Co-crystals. *CrystEngComm* **2004**, *6*, 19−24.

(51) Sharma, C. V. K.; Panneerselvam, K.; Pilati, T.; Desiraju, G. R. Molecular Recognition Involving an Interplay of O−H···O, C−H···O and π−π Interactions. The Anomalous Crystal Structure of the 1:1 Complex 3,5-Dinitrobenzoic Acid−4-(*N*,*N*-dimethylamino)benzoic acid. *J. Chem. Soc., Perkin Trans. 2* **1993**, 2209−2016.

Indeed, to date, there are only few reported cases of a carboxylic acid dimer homosynthon in the presence of a heterosynthon.[52−58] We are currently working to increase the number of co-crystals in this family of solids to determine those factors responsible for the coexistence of the O−H···O heterosynthon and carboxylic acid dimer.

Conclusion

In this contribution, three co-crystals of caffeine with hydroxy-2-naphthoic acids were structurally characterized. In addition to the known imidazole−acid synthon, structural analyses of these solids have revealed an unusual case in which a carboxylic acid dimer forms in the presence of a rationally introduced heterosynthon. Efforts are underway to further increase the structural diversity of co-crystals that can be achieved through the deliberate addition of functional groups into self-assembly processes involving organic co-crystals.

Supporting Information Available: Crystallographic information (.cif) for **A**, **B**, and **C**. This material is available free of charge via the Internet at http://pubs.acs.org.

MP070004B

(52) Papaefstathiou, G. S.; Kipp, A. J.; MacGillivray, L. R. Exploiting Modularity in Template-controlled Synthesis: A New Linear Template to Direct Reactivity Within Discrete Hydrogen-bonded Molecular Assemblies in the Solid State. *Chem. Commun.* **2001**, 2462−2463.

(53) Hosomi, H.; Ohba, S.; Ito, Y. Benzene-1,2,4,5-tetracarboxylic Acid-*trans*-cinnamamide (1/2). *Acta Crystallogr.* **2000**, *C56*, e511−e511.

(54) Zeng, Q.; Wu, D.; Ma, H.; Shu, C.; Lia, Y.; Wang, C. Polymeric Hydrogen-bonded Supramolecules by Self-assembling of Adamantane Derivatives with Bipyridines. *CrystEngComm* **2006**, *8*, 189−201.

(55) Aakeröy, C. B.; Desper, J.; Urbina, J. F. Is Conformational Flexibility in a Supramolecular Reagent Advantageous for High-yielding Co-crystallization Reactions? *CrystEngComm* **2005**, *7*, 193−201.

(56) Lee, T. W.; Lau, J. P. K.; Szeto, L. Diphenic Acid-4,4′-bipyridine (2/1). *Acta Crystallogr.* **2003**, *E59*, o942−944.

(57) Vinodu, M.; Goldberg, I. Supramolecular self-assembly of porphyrinic materials by design. Non-centrosymmetric architectures of the 5-(3′-pyridyl)-10,15,20-tris(4′-carboxyphenyl) and 5-(2′-quinolyl)-10,15,20-tris(4′-hydroxyphenyl) porphyrins. *CrystEngComm* **2005**, *7*, 133−138.

(58) Moreno-Fuquen, R.; Valderramanaranjo, J; Montaño, A. M. 1-(*tert*-Butyl)-3-(2-pyridyl)thiourea. *Acta Crystallogr.* **1999**, *C55*, 218−220.

APPENDIX E. A COPY OF A COMMUNICATION PUBLISHED IN NEW JOURNAL OF CHEMISTRY IN 2008.

LETTER www.rsc.org/njc | New Journal of Chemistry

A lanthanide-based helicate coordination polymer derived from a rigid monodentate organic bridge synthesized in the solid state†‡

Dejan-Krešimir Bučar,[a] Giannis S. Papaefstathiou,[b] Tamara D. Hamilton[a] and Leonard R. MacGillivray*[a]

Received (in Durham, UK) 18th January 2008, Accepted 3rd March 2008
First published as an Advance Article on the web 25th March 2008
DOI: 10.1039/b800878g

Tetratopic *rctt*-tetrakis(4-pyridyl)cyclobutane acts as an angular bifunctional ligand that yields a single-stranded helicate coordination polymer based on a Ln(III) ion.

The design and construction of helicates[1] (*i.e.* metal-containing helices) is of great interest in metallosupramolecular chemistry owing to their potential applications in areas such as optics,[2–6] catalysis,[7,8] and medicine.[9–11] Helicity in such a metallosupramolecular architecture is a result of the geometric and stereoelectronic preferences of the organic ligand and metal center.[12,13] Whereas the synthesis of helicates has been typically achieved using angular ditopic bridging ligands based on either flexible monodentate or rigid chelating units (*e.g.* quarterpyridine),[14] helicates based on angular rigid monodentate bridges (*e.g.* 1,3-benzenetricarboxylic acid) have been rare.[15] The fact that such constructions have been rare can be ascribed to subtle structure effects of the self-assembly process. Generally, the curvature of a helix is achieved by organic and metal components that, collectively, produce an angle between 0 and 180°. Whereas a flexible bridge can, *de facto*, afford a relatively wide range of angles to support a helix, rigid bridges are more restrictive (Scheme 1). This means that a self-assembly designed to afford a helix based on a rigid organic bridge will most likely succeed using a metal with a flexible coordination sphere. Chelating groups have been useful in this regard since the multiple binding sites of a chelator saturate the coordination sphere of a metal, and thus prohibit ancillary components (*e.g.* anions or solvent) from disrupting the assembly process.

In recent years, we have described a method to control [2 + 2] photodimerizations in organic solids using hydrogen bond-mediated self-assembly involving small molecules as linear templates.[16] Resorcinol and derivatives have been used to stack *trans*-1,2-bis(4-pyridyl)ethylene to react and form *rctt*-tetrakis(4-pyridyl)cyclobutane (4,4′-tpcb). We have shown that the tetrapyridine invariably acts as a 4-connected node in a series of 2D metal-organic frameworks (MOFs), with topologies that conform to grids and are based on *d*-block transition metal ions [*e.g.* Cu(II)]. Each pyridyl group of each solid was coordinated to a metal.[17,18] Metal–organic polygons and polyhedra have also been obtained using other tetrapyridines obtained using our solid-state strategy. Similar to the MOFs, each pyridine was coordinated to a metal.[19]

Herein, we wish to report the synthesis and structural characterization of a single-stranded helicate coordination polymer based on 4,4′-tpcb. We show that only two of the four 4-pyridyl units of 4,4′-tpcb coordinate to metals of the helicate, which, in turn, enables the tetrapyridine to function as a rare rigid monodentate bridge of a helix (Scheme 2). The helicate is based on a Ln(III) cation in $\{[Pr(4,4'\text{-tpcb})(Cl)_3(CH_3OH)(H_2O)]\cdot 2(CH_3OH)\cdot(H_2O)\}_\infty$ (**1**). Our use of Ln(III) ions stem from the fact that such metals can afford coordination materials, with applications as luminescent materials, radiopharmaceuticals and MRI contrast agents. We also show that the self-assembly process based on 4,4′-tpcb and Pr(III) is sensitive to the nature of the counterion, with a 3D hydrogen-bonded network being realized in $\{[Pr(NO_3)_3(MeOH)_{1.58}(H_2O)_{2.42}]\cdot 2(4,4'\text{-tpcb})\cdot 0.84H_2O\}_\infty$ (**2**).

Compound **1** was prepared by the addition of a methanol solution of 4,4′-tpcb (36.4 mg, 0.1 mmol) to a methanol solution of $PrCl_3{\cdot}6H_2O$ (35.9 mg, 0.1 mmol; 8 ml methanol). The green solution was left to evaporate at room temperature. Green prismatic crystals of **1** suitable for single-crystal X-ray diffraction were obtained after 12 d (yield: 55%).§

A view of the crystal structure of **1** is shown in Fig. 1. The Pr(III) cation is heptacoordinated, with a coordination geometry that conforms to a pentagonal bipyramid. Two chlorine atoms occupy the apical sites of the bipyramid (Pr–Cl(1) 2.717(1), Pr–Cl(2) 2.723(1) Å), while the remaining chlorine atom (Pr–Cl(3) 2.743(1) Å), along with two 4-pyridyl groups (Pr–N(1) 2.661(3), Pr–N(2) 2.671(3) Å), occupy the base of the bipyramid. The latter chlorine atom lies between the 4-pyridyl groups. In this arrangement, the two pyridyl groups, which are from two different cyclobutane molecules, bridge two metal

Scheme 1 General roles of flexible monodentate and rigid chelating ligands in helicates.

[a] *University of Iowa, Department of Chemistry, Iowa City, IA, USA. E-mail: len-macgillivray@uiowa.edu; Fax: +1 319-335-1270; Tel: +1 319-335-3504*
[b] *Laboratory of Inorganic Chemistry, Department of Chemistry, National and Kapodistrian University of Athens, Panepostimiopolis, Zografou 15771, Greece*

† Dedicated to Professor Jerry Atwood on the occasion of his 65th birthday. We gratefully acknowledge him for his inspirational work over the years.

‡ CCDC reference numbers 674103 and 674104. For crystallographic data in CIF or other electronic format see DOI: 10.1039/b800878g

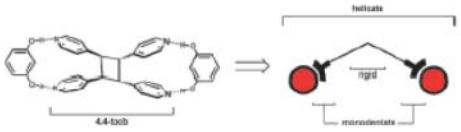

Scheme 2 Templated synthesis of 4,4′-tpcb, and 4,4′-tpcb as a rigid ditopic monodentate ligand in a helicate.

centers. The bridging arises from two pyridyl groups that are *transoid* to each other. As a result, the cyclobutane acts as a bis-monodentate angular bridge, exhibiting a N–cyclobutane–N angle of 102.9°. As a consequence of these arrangements, the self-assembly of the ligands and the metal ions produces a single-stranded helical coordination polymer along a 2_1 screw axis. The pitch of the helix is 20.1 Å, and it contains two Pr(III) ions per turn, which are separated by 11.8 Å. Helices of both hands are present in the solid, being related by a center of inversion. **1** is a rare example of a helicate coordination polymer based upon a rigid organic bridge with monodentate units.

The fact that the tetrapyridine acts as a ditopic ligand means that two of the four pyridyl groups are not coordinated. These pyridyl groups participate in O–H···Ni (O(1)···N(3) 2.708(4) Å; i: $-x + 1, -y + 2, -z + 1$) hydrogen bonds with the coordinated water molecules to form hydrogen-bonded dinuclear rhomboids. The rhomboids link helices of opposite handedness (*i.e.* left and right handed) in the solid (Fig. 2). The cavity of each rhomboid accommodates two coordinated methanol molecules. The edges of the rhomboids are defined by the pyridyl groups, while the corners are defined by two cyclobutane rings and two $[Pr(MeOH)]^{3+}$ units located at opposite corners (approximate corner distances: cyclobutane···cyclobutane 15.0 Å, Pr(III)···Pr(III) 8.8 Å). The solid also exhibits small voids occupied by highly disordered H_2O and methanol molecules.

Compound **2** was obtained by dissolving $PrNO_3{\cdot}6H_2O$ (4.35 mg, 0.1 mmol) and 4,4′-tpcb (3.64 mg, 0.1 mmol) in methanol (8 ml), which produced a light green solution. Large green block crystals suitable for X-ray diffraction formed within 14 d upon solvent evaporation (yield: 68%).§

The structure of **2** reveals that the self-assembly of the helicate of **1** depends on the nature of the anion. In particular, the components of **2** have assembled to produce a 3D hydrogen-bonded network. As shown in Fig. 3, each metal is coordinated by three bidentate chelating NO_3^- ions

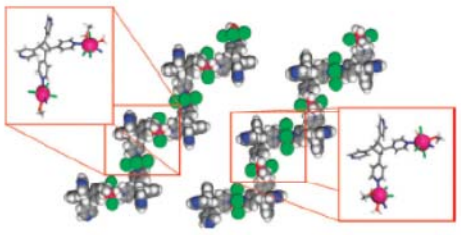

Fig. 1 Space-filling models of left- and right-handed helicates of **1**.

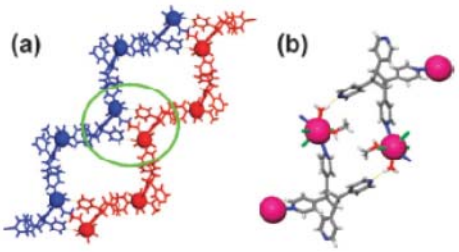

Fig. 2 Perspective view of: (a) left- and right-handed helicates (blue and red) that form a (b) hydrogen-bonded polygon.

(Pr–O(1) 2.597(2), Pr–O(2) 2.593(2), Pr–O(4), 2.662(2) Å), as well as two water molecules (Pr–O(6) 2.453(2) Å) (Fig. 2b). The remaining two sites are partially occupied by disordered methanol (Pr–O(7) 2.529(2); occupancy 79%) and water (Pr–O(8) 2.529(2); occupancy 21%) molecules. The metal ion is effectively decacoordinated. Indeed, it is likely that the chelating behavior of the NO_3^- ions, as opposed to the chloride ion of **1**, precludes two molecules of 4,4′-tpcb from coordinating to the Pr(III) cation to support the formation of a helix. The structure of the 3D network is based on molecules of 4,4′-tpcb, which act as a 3-connected node, and complexes of $[Pr(NO_3)_4(MeOH)_{1.58}(H_2O)_{2.42}]$, which act as a 6-connected node, that interact *via* $O–H\cdots N_{pyridyl}$ hydrogen bonds (O7(8)···N6 2.819(4), O6···N5^{i} 2.759(4), O6···N3^{ii} 2.750(3) Å; i: $-x + \frac{3}{2}, y + \frac{1}{2}, -z + \frac{3}{2}$, ii: $x, y, z + 1$). As a result of these arrangements, the 3D hydrogen-bonded structure constitutes a two-fold interpenetrated binodal net, with a $(4.6^2)_2(4^2.6^{10}.8^3)$ topology (Fig. 3b).[20,21] To our knowledge, **2** is the first example of a self-assembled framework that conforms to this topology.[21–23] Channels are present in the solid, occupied by disordered water molecules, that run along both the crystallographic *c*-axis and [0 0 1]-plane. Collectively, the structure of **2** attests to the sensitivity of the self-assembly process; specifically, how the nature of the counterion can influence helix formation.

In conclusion, we have presented a helical coordination polymer based on a tetratopic molecule that acts as an angular and rigid monodentate bridging ligand. We have also shown that the self-assembly process is sensitive to the nature of the anion. The coordination polymer was achieved *via* a template-controlled solid-state organic synthesis, and using a metal center based upon a Ln(III) ion. Efforts are under way to

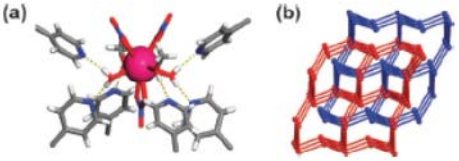

Fig. 3 Perspective view of (a) the coordination and hydrogen bonds around the metal of **2**, and (b) the two-fold interpenetration of the 3D network.

further determine the factors that influence the self-assembly of the ligands obtained from the solid state into metal–organic frameworks and discrete structures.

We thank the National Science Foundation (CAREER Award, L. R. M., DMR-0133138) and the Special Account for Research Grants (SARG) of the National and Kapodistrian University of Athens (G. S. P. 70/4/9316) for financial support.

References

§ Crystal data for **1**: $C_{27}H_{36}Cl_3N_4O_4Pr$, orthorhombic, space group *Pbcn*, a = 23.061(2), b = 13.596(1), c = 20.094(2) Å, V = 6300.3(1) Å^3, D_c = 1.57 g cm^{-3}, Z = 8, $F(000)$ = 3008, μ = 1.84 mm^{-1}, Mo-K_α radiation (λ = 0.71070 Å), T = 190(1) K, 31701 collected reflections, 5528 unique reflections (R_{int} = 0.046), 3227 observed reflections [$I > 2\sigma(I)$], θ_{max} = 25.0°, R_1(obs) = 0.025, wR_2(obs) = 0.049, R_2(all) = 0.044, wR_2(all) = 0.046. The Fourier difference map revealed peaks that were identified as highly disordered water and methanol molecules. Despite the extensive use of restraints, attempts to resolve the disorder were unsuccessful, since the resulting model included unreasonably short intermolecular contacts. The electron contribution of the solvent molecules was therefore subtracted from the diffraction data using the SQUEEZE[24] procedure. The solvent molecules were determined to occupy 870.9 Å^3 or 13.8% of the unit cell. The total electron count of 211 electrons per unit cell corresponds to approximately one water and one methanol molecule. CCDC 674103.
Crystal data for **2**: $C_{49.59}H_{52.85}N_{11}O_{13.84}Pr$, monoclinic, space group $C2/c$, a = 23.020(3), b = 16.869(2), c = 13.834(2) Å, β = 96.593(2), V = 5336.6(1) Å^3, D_c = 1.45 g cm^{-3}, Z = 4, $F(000)$ = 2388, μ = 0.987 mm^{-1}, Mo-K_α radiation (λ = 0.71070 Å), T = 200(1) K, 17468 collected reflections, 4637 unique reflections (R_{int} = 0.052), 4081 observed reflections [$I > 2\sigma(I)$], θ_{max} = 25.0°, R_1(obs) = 0.033, wR_2(obs) = 0.043, R_2(all) = 0.070, wR_2(all) = 0.072. CCDC 674104.
For crystallographic data in CIF or other electronic format see DOI: 10.1039/b800878g

1 J.-M. Lehn, A. Rigault, J. Siegel, J. Harrowfield, B. Chevrier and D. Moras, *Proc. Natl. Acad. Sci. U. S. A.*, 1987, **84**, 2565–2569.
2 M. Albrecht, O. Osetska, R. Fröhlich, J.-C. G. Bünzli, A. Aebischer, F. Gumy and J. Hamacek, *J. Am. Chem. Soc.*, 2007, **129**, 14178–14179.
3 H. Katagiri, T. Miyagawa, Y. Furusho and E. Yashima, *Angew. Chem., Int. Ed.*, 2006, **45**, 1741–1744.
4 S. Torelli, D. Imbert, M. Cantuel, G. Bernardinelli, S. Delahaye, A. Hauser, J.-C. G. Bünzli and C. Piguet, *Chem.–Eur. J.*, 2005, **11**, 3228.
5 V. Amendola, L. Fabbrizzi, F. Foti, M. Licchelli, C. Mangano, P. Pallavicini, A. Poggi, D. Sacchi and A. Taglietti, *Coord. Chem. Rev.*, 2006, **250**, 273–299.
6 S. Zang, Y. Su, Y. Li, Z. Ni and Q. Meng, *Inorg. Chem. Commun.*, 2006, **45**, 174–180.
7 H.-L. Kwong, H.-L. Yeung, W.-S. Lee and W.-T. Wong, *Chem. Commun.*, 2006, 4841–4843.
8 C.-T. Yeung, H.-L. Yeung, C.-S. Tsang, W.-Y. Wong and H.-L. Kwong, *Chem. Commun.*, 2007, 5203–5205.
9 A.-S. Chauvin, S. Comby, B. Song, C. D. B. Vandevyver, F. Thomas and J.-C. G. Bünzli, *Chem.–Eur. J.*, 2007, **13**, 9515–9526.
10 G. I. Pascu, A. C. G. Hotze, C. Sanchez-Cano, B. M. Kariuki and M. J. Hannon, *Angew. Chem., Int. Ed.*, 2007, **46**, 4374–4378.
11 C. D. B. Vandevyver, A.-S. Chauvin, S. Comby and J.-C. G. Bünzli, *Chem. Commun.*, 2007, 1716–1718.
12 L. P. Harding, J. C. Jeffery, T. Riis-Johannessen, C. R. Rice and Z. Zenga, *Chem. Commun.*, 2004, 654–655.
13 R. Vilar, *Angew. Chem., Int. Ed.*, 2003, **42**, 1460–1477.
14 M. Albrecht, *Chem. Rev.*, 2001, **101**, 3457–3497.
15 L. Han and M. Hong, *Inorg. Chem. Commun.*, 2005, **8**, 406–419.
16 L. R. MacGillivray, J. L. Reid and J. A. Ripmeester, *J. Am. Chem. Soc.*, 2000, **122**, 7817–7818.
17 G. S. Papaefstathiou and L. R. MacGillivray, *Angew. Chem., Int. Ed.*, 2002, **41**, 2070–2073.
18 G. S. Papaefstathiou, C. Milios and L. R. MacGillivray, *Microporous Mesoporous Mater.*, 2004, 11–15.
19 G. S. Papaefstathiou, T. D. Hamilton, T. Friščić and L. R. MacGillivray, *Chem. Commun.*, 2004, 270–271.
20 Topological analysis was performed using the TOPOS program package: http://www.topos.ssu.samara.ru
21 V. A. Blatov, *IUCr CompComm Newsletter*, 2006, No. 7, pp. 4–38.
22 RCSR (Reticular Chemistry Structure Resource) a source of crystalline networks: http://rcsr.anu.edu.au/.
23 Network was constructed with Systre: http://gavrog.sourceforge.net/.
24 A. L. Spek, *Acta Crystallogr., Sect. A: Found. Crystallogr.*, 1990, **46**, C34.

APPENDIX F. A COPY OF A COMMUNICATION PUBLISHED IN NEW JOURNAL OF CHEMISTRY IN 2010 (JOINT FIRST AUTHOR).

LETTER www.rsc.org/njc | New Journal of Chemistry

A metal–organic framework with three cavities based on three-coloured square tiling derived from a cyclobutane constructed in the solid state†

Tamara D. Hamilton,‡ Dejan-Krešimir Bučar‡ and Leonard R. MacGillivray*

Received (in Victoria, Australia) 14th May 2010, Accepted 29th June 2010
DOI: 10.1039/c0nj00367k

The unsymmetrical tetratopic ligand *rctt*-1,2-bis(3-pyridyl)-3,4-bis(4-pyridyl)cyclobutane self-assembles with zinc(II) nitrate to form a 2D metal–organic framework with three distinct cavities.

Metal–organic frameworks (MOFs) are one of the most studied class of compounds in the area of materials science and supramolecular chemistry.[1] Tremendous interests in MOFs are attributed to scientific and technological applicability (*e.g.* gas storage,[2–4] catalysis,[5] anion[6] and guest[7] exchange, drug delivery).[8–10] Recent studies have reported biporous MOFs (*i.e.* MOFs with two distinct pores) being able to accommodate different guest molecules in different channels.[11–18] A very rare example of a triporous MOF supported by calix[4]arenes has just been reported.[19] Indeed, MOFs with more than one type of cavity can be considered to represent an entry to a new generation of MOF-based materials with applications in areas such as separation processes that, in principle, allow the recognition and storage of compounds unable to coexist (*e.g.* acid/base, oxidizers/reducers).[11] Understanding how to design molecular building units that self-assemble to form MOFs with more than one cavity type can, thus, be considered to represent an important area of development in the advancing field.

In recent years, we have demonstrated how [2 + 2] photodimerisations can be engineered in the organic solid state.[20] Specifically, we have shown that molecular cocrystals can be utilized as reaction media wherein synthetic templates arrange olefins for intermolecular [2 + 2] photodimerisations using principles of hydrogen-bond-driven self-assembly. The cocrystals react to form cyclobutanes lined with pyridyl groups that form stereospecifically, in quantitative yield, and in gram amounts. We have also shown that the resulting cyclobutanes can be utilised as polytopic ligands[21] to form MOFs with up to two different cavities,[15] helical coordination polymers,[22] MOFs with functionalized pores,[23] as well as related metal–organic polygons[24] and polyhedra.[25–27]

Herein, we report a MOF with three different cavities;[28] namely, $[Zn_2(\mathbf{3,4'\text{-}tpcb})_2(NO_3)_4(H_2O)_4]_\infty$ (**1**) (where **3,4'-tpcb** = *rctt*-1,2-bis(3-pyridyl)-3,4-bis(4-pyridyl)cyclobutane). The ligand **3,4'-tpcb** has been prepared in a templated solid-state synthesis stereospecifically and in quantitative yield (Scheme 1).[29] In the MOF, the cyclobutane, which is unsymmetrical, binds four metal atoms *via* the two different pyridyl groups to give a 2D MOF based exclusively on 4-connected nodes. The formation of three different cavities arises from an ability of the different pyridyl groups to sustain tiling of square cavities wherein the walls of the cavities consist of combinations of 3- and 4-pyridyl groups. The resulting 2D framework exhibits a topology that corresponds to uniform 3-coloured tiling of squares wherein each colour, *de facto*, represents a chemically distinct cavity. Although square tiling is a well-documented target in MOF chemistry, the framework **1** represents, to our knowledge, the first example of a 2D MOF based on 3-coloured uniform tiling. Uniform *n*-coloured tilings (where $n > 1$) are Archimedian tilings that involve *n*-coloured polygons surrounding each identical vertex (Fig. 1).[30,31] MOFs with topologies that correspond to *n*-coloured tilings have, to our knowledge, not been addressed yet, and as we will demonstrate, are attractive models to develop 2D frameworks based on multiple cavities.

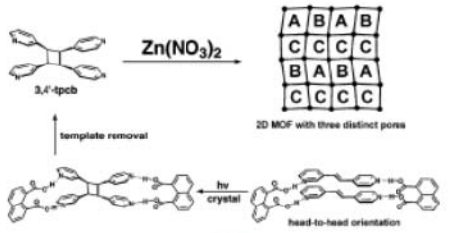

Scheme 1

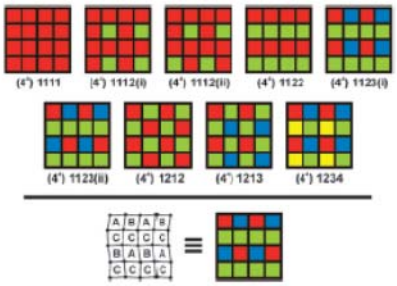

Fig. 1 Uniform colourings of square tiling [(4^4) indicates the vertex configuration,[30,31] whereas each of the four subsequent numbers symbolizes a tile of a distinct colour surrounding a vertex; (i) indicates a simple reflection symmetry, (ii) indicates a glide reflection symmetry].

Department of Chemistry, University of Iowa, Iowa City, IA, USA. E-mail: len-macgillivray@uiowa.edu; Fax: +1 319-335-1270; Tel: +1 319-335-0563

† CCDC 776968. For crystallographic data in CIF or other electronic format see DOI: 10.1039/c0nj00367k

‡ Authors contributed equally to the manuscript.

Compound **1** was prepared by combining acetonitrile solutions of **3,4′-tpcb** (0.025 g, 0.068 mmol) and $Zn(NO_3)_2{\cdot}H_2O$ (0.014 g, 0.068 mmol) (25 mL total). A 5 mL aliquot of the colourless solution was layered with 10 mL diethyl ether in a test tube and allowed to sit for approximately one week, which resulted in the formation of colourless single crystals of $\mathbf{1}{\cdot}4(H_2O){\cdot}(CH_3CN){\cdot}[(CH_3CH_2)_2O]$ (**1a**) suitable for X-ray diffraction (yield: 0.030 g, 77%).

X-Ray diffraction studies§ revealed that **1a** crystallises in the monoclinic space group $P2_1/n$. The asymmetric unit contains two **3,4′-tpcb** ligands, two Zn(II) cations, four NO_3^- anions, eight H_2O molecules, one acetonitrile molecule, and one diethyl ether molecule. The components self-assemble into a 2D MOF wherein each ligand and metal ion act as a 4-connected node (Fig. 2). Each Zn(II) ion lies in an octahedral coordination environment, with two 3-pyridyl groups and two 4-pyridyl groups in equatorial positions and water molecules in the axial positions [Zn(II)–N bond distances: 2.124(7)–2.238(7) Å; Zn(II)–O bond distances: 2.113(6)–2.176(6) Å]. As a consequence of the self-assembly process, the components form a 2D MOF based on tiling of approximate square cavities. The opposite corners of each cavity are defined by two Zn(II) ions and two cyclobutane rings, with the walls being composed of the 3- and 4-pyridyl groups. Importantly, that the cyclobutane possesses two different pyridyl groups means that the grid consists of three chemically distinct cavities. In particular, the walls of Cavity A are defined by four 4-pyridyl units, the walls of Cavity B are defined by two 4-pyridyl and two 3-pyridyl units at opposite walls, and the walls of Cavity C are defined by one 4-pyridyl and three 3-pyridyl units. Cavity A is, thus, defined by two acute angles provided by **3,4′-tpcb**, Cavity B is defined by two obtuse angles, and Cavity C is defined by combinations of acute and obtuse angles. The cavities alternate along the crystallographic *b* axis in an ACBC manner and through a 2-fold roto-inversion axis in an ABAB manner. Each vertex is, thus, identical being surrounded by one Cavity A, one Cavity B, and two Cavities C's. As a result of the arrangement, the 2D framework constitutes a 4-connected uninodal net with a ($4^4 \times 6^2$) topology (*i.e.* Shubnikov tetragonal plane net).[32,33]

The framework **1** self-assembles as stacked layers that are held together by a network of hydrogen bonds. The network involves 16 water molecules, eight NO_3^- ions, and two molecules of diethyl ether (Fig. 3a). The solvent water and ether molecules, as well as included acetonitrile, occupy lacunae between the stacked layers. The hydrogen bonding involving the components can be considered to be composed of one major and two minor subunits. The major subunit lies on a center of inversion and is composed of four NO_3^- ion and six water molecules sustained by 12 hydrogen bonds (Fig. 3b). Four of the water molecules belong to (H_2O)–Zn moieties of adjacent frameworks. The two minor subunits consist of one NO_3^- ion, five water molecules, and one diethyl ether molecule held together by eight hydrogen bonds, with two of the five water molecules belonging to a (H_2O)–Zn moiety (Fig. 3c). The hydrogen bonding serves to link stacked layers (Fig. 3d and e).

An analysis of the structure of **1** using SOLVE subroutine in PLATON[34] revealed that each of the three different cavities do not exhibit solvent-accessible voids. Despite a lack of sizable pores, however, **1** exhibits intriguing structural features that require further comment. Specifically, the MOF **1** is a unique example of a 2D framework with three chemically distinct cavities, or in the mathematical language, a uniform 3-coloured (4^4) 1123(ii) tiling of squares (where (ii) is glide reflection symmetry).[30] More specifically, the different coloured tiles correspond to the three different cavities of **1**

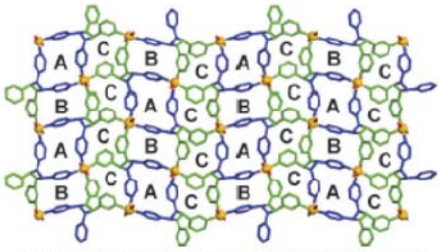

A = 4py, 4py, 4py, 4py; B = 4py, 3py, 4py, 3py; C = 4py, 3py, 3py, 3py
(3py = 3-pyridyl; 4py = 4-pyridyl)

Fig. 2 Crystal structure of 1 showing three different cavities (A, B, C) along the crystallographic *c*-axis (colour scheme: Zn, orange; O, red; 3-pyridyl, green; 4-pyridyl, blue). Cavity dimensions (corner-to-corner distances) and angles: Cavity A: 7.2 × 6.9 Å, 99° and 80°; Cavity B: 7.2 × 6.2 Å, 94° and 85°; Cavity C: (a) 6.9 × 6.6 × 6.2 × 6.6 Å, 92°, 87°, 99° and 82° and (b) 6.9 × 6.6 × 6.1 × 6.6 Å, 85°, 94°, 92° and 88°.

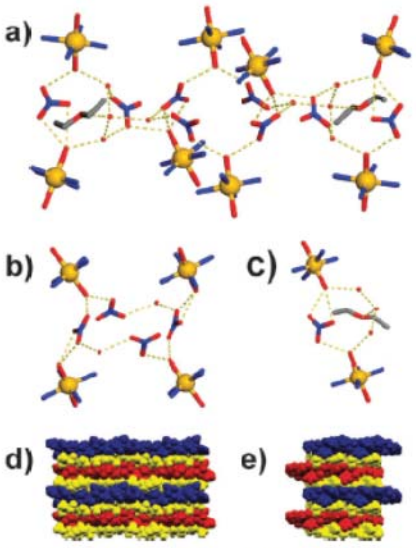

Fig. 3 Crystal structure of (a) hydrogen-bonding involving the NO_3^- ions, H_2O, and ether molecules, (b) major subunit, (c) minor subunit, stacked layers of 1 along the crystallographic axis *c* (d), and *b* (e).

Scheme 2

(Cavity A = red; Cavity B = blue, Cavity C = green) with metal ions and cyclobutane rings as vertices. From a mathematical standpoint, there are only three ways to form uniform square tiling with three distinct colours (Scheme 1). That the components of **1** afford (4^4) 1123(ii) tiling of squares can be attributed to both the presence of the two different pyridyl groups attached to the cyclobutane ring, which defined a total of three different angles, and the flexibility of cavity formation (*e.g.* coordination geometry of Zn(II) ion) to support combinations of acute and obtuse corners (Scheme 2). Moreover, it is likely that other *n*-uniform coloured tilings can be accessible using similar unsymmetrically substituted ligands, which suggests that such coloured tilings can serve as models to develop 2D MOFs based on more than one cavity type.[35]

In summary, we have presented a 2D MOF with three chemically distinct cavities based on an unsymmetrical and rigid tetratopic ligand derived from a solid-state synthesis. The structure of the 2D MOF is based on uniform three-coloured square tiling. Studies are underway to prepare unsymmetrical ligands in the solid state involving pyridyl functionalities that exhibit longer bridge lengths, which would be expected to support MOFs that accommodate different guest species and take advantage of the unusual topologies that can be achieved by stereocontrolled solid-state syntheses.

Notes and references

§ Crystal data for **1a**: $C_{54}H_{69}N_{13}O_{21}Zn_2$, M_r = 1366.96, monoclinic, a = 13.0139(13) Å, b = 27.361(3) Å, c = 17.7274(18) Å, α = 90.00°, β = 90.687(5)°, γ = 90.00°, V = 6311.8(11) Å^3, T = 183(2) K, space group $P2_1/n$, Z = 4, μ(MoKα) = 0.844 mm^{-1}, 40 470 reflections measured, 11 091 independent reflections (R_{int} = 0.1121). The final R_1 values were 0.0901 ($I > 2\sigma(I)$). The final w$R(F^2)$ values were 0.2344 ($I > 2\sigma(I)$). The final R_1 values were 0.1438 (all data). The final w$R(F^2)$ values were 0.2624 (all data). The goodness of fit on F^2 was 1.079. The investigated crystal exhibited pseudo-merohedral twinning that precluded the modeling of the hydrogen atoms belonging to water molecules.

1 S. Horike, S. Shimomura and S. Kitagawa, *Nat. Chem.*, 2009, **1**, 695–704.
2 R. Matsuda, R. Kitaura, S. Kitagawa, Y. Kubota, R. V. Belosludov, T. C. Kobayashi, H. Sakamoto, T. Chiba, M. Takata, Y. Kawazoe and Y. Mita, *Nature*, 2005, **436**, 238–241.
3 A. Phan, C. J. Doonan, F. J. Uribe-Romo, C. B. Knobler, M. O'Keeffe and O. M. Yaghi, *Acc. Chem. Res.*, 2009, **43**, 58–67.
4 J. L. C. Rowsell and O. M. Yaghi, *Angew. Chem., Int. Ed.*, 2005, **44**, 4670–4679.
5 J. Lee, O. K. Farha, J. Roberts, K. A. Scheidt, S. T. Nguyen and J. T. Hupp, *Chem. Soc. Rev.*, 2009, **38**, 1450–1459.
6 S. R. Halper, L. Do, J. R. Stork and S. M. Cohen, *J. Am. Chem. Soc.*, 2006, **128**, 15255–15268.
7 M. Kawano and M. Fujita, *Coord. Chem. Rev.*, 2007, **251**, 2592–2605.
8 P. Horcajada, T. Chalati, C. Serre, B. Gillet, C. Sebrie, T. Baati, J. F. Eubank, D. Heurtaux, P. Clayette, C. Kreuz, J.-S. Chang, Y. K. Hwang, V. Marsaud, P.-N. Bories, L. Cynober, S. Gil, G. Férey, P. Couvreur and R. Gref, *Nat. Mater.*, 2010, **9**, 172–178.
9 P. Horcajada, C. Serre, G. Maurin, N. A. Ramsahye, F. Balas, M. Vallet-Regí, M. Sebban, F. Taulelle and G. Férey, *J. Am. Chem. Soc.*, 2008, **130**, 6774–6780.
10 R. Zou, A. I. Abdel-Fattah, H. Xu, Y. Zhao and D. D. Hickmott, *CrystEngComm*, 2010, **12**, 1337–1353.
11 O. Ohmori, M. Kawano and M. Fujita, *Angew. Chem., Int. Ed.*, 2005, **44**, 1962–1964.
12 O. Ohmori, M. Kawano and M. Fujita, *CrystEngComm*, 2005, **7**, 255–259.
13 M. Kawano, T. Kawamichi, T. Haneda, T. Kojima and M. Fujita, *J. Am. Chem. Soc.*, 2007, **129**, 15418–15419.
14 A. Comotti, S. Bracco, P. Sozzani, S. Horike, R. Matsuda, J. Chen, M. Takata, Y. Kubota and S. Kitagawa, *J. Am. Chem. Soc.*, 2008, **130**, 13664–13672.
15 G. S. Papaefstathiou, T. Friščić and L. R. MacGillivray, *J. Am. Chem. Soc.*, 2005, **127**, 14160–14161.
16 P. Kanoo, K. L. Gurunatha and T. K. Maji, *J. Mater. Chem.*, 2010, **20**, 1322–1331.
17 W. Yang, X. Lin, J. Jia, A. J. Blake, C. Wilson, P. Hubberstey, N. R. Champness and M. Schroder, *Chem. Commun.*, 2008, 359–361.
18 J. Seo, H. Sakamoto, R. Matsuda and S. Kitagawa, *J. Nanosci. Nanotechnol.*, 2010, **10**, 3–20.
19 S. Kennedy, G. Karotsis, C. M. Beavers, S. J. Teat, E. K. Brechin and S. J. Dalgarno, *Angew. Chem., Int. Ed.*, 2010, **49**, 4205–4208.
20 L. R. MacGillivray, G. S. Papaefstathiou, T. Friščić, T. D. Hamilton, D.-K. Bučar, Q. Chu, D. B. Varshney and I. G. Georgiev, *Acc. Chem. Res.*, 2008, **41**, 280–291.
21 D.-K. Bučar, G. S. P. Papaefstathiou, T. D. H. Hamilton, Q. L. C. Chu, I. G. G. Georgiev and L. R. MacGillivray, *Eur. J. Inorg. Chem.*, 2007, 4559–4568.
22 D.-K. Bučar, G. S. Papaefstathiou, T. D. Hamilton and L. R. MacGillivray, *New J. Chem.*, 2008, **32**, 797–799.
23 T. D. Hamilton, D.-K. Bučar, M. B. J. Atkinson, G. S. Papaefstathiou and L. R. MacGillivray, *J. Mol. Struct.*, 2006, **796**, 58–62.
24 G. S. Papaefstathiou, T. D. Hamilton, T. Friščić and L. R. MacGillivray, *Chem. Commun.*, 2004, 270–271.
25 T. D. Hamilton, D.-K. Bučar and L. R. MacGillivray, *Chem. Commun.*, 2007, 1603–1604.
26 T. D. Hamilton, G. S. Papaefstathiou, T. Friščić, D.-K. Bučar and L. R. MacGillivray, *J. Am. Chem. Soc.*, 2008, **130**, 14366–14367.
27 T. D. Hamilton, G. S. Papaefstathiou and L. R. MacGillivray, *J. Am. Chem. Soc.*, 2002, **124**, 11606–11607.
28 The term "cavity" is generally used to describe the space within a chemical entity that exhibits the capacity to accommodate a guest species. In this contribution the term is being used to describe a void space within a MOF, regardless of size or capacity to accommodate a guest since the parts of structure **1** described as Cavity A, B and C exhibit small voids and since the findings are directly translatable into guidelines for the design and synthesis of MOFs with larger voids.
29 D. B. Varshney, G. S. Papaefstathiou and L. R. MacGillivray, *Chem. Commun.*, 2002, 1964–1965.
30 B. Grünbaum and G. C. Shephard, *Tilings and Patterns*, W. H. Freeman, New York, 1987.
31 M. d. Graef and M. E. McHenry, *Structure of Materials: An Introduction to Crystallography, Diffraction, and Symmetry*, Cambridge University Press, Cambridge, 2007.
32 Topological analysis was performed using the TOPOS program.
33 V. A. Blatov, *IUCr Compcomm Newsletter*, 2006, **7**, 4–38.
34 A. L. Spek, *Acta Crystallogr., Sect. A: Fundam. Crystallogr.*, 1990, **46**, C34.
35 We expect that 3,4′-tpcb, for example, can support 2D tiling of other *n*-uniform coloured tilings.

APPENDIX G. A COPY OF A COMMUNICATION PUBLISHED IN CHEMICAL COMMUNICATIONS IN 2010 (JOINT FIRST AUTHOR).

COMMUNICATION www.rsc.org/chemcomm | ChemComm

Stereospecific and quantitative photodimerisation of terminal olefins in the solid state†

Ivan G. Georgiev,‡ Dejan-Krešimir Bučar and Leonard R. MacGillivray*

Received 29th April 2010, Accepted 5th May 2010
First published as an Advance Article on the web 1st June 2010
DOI: 10.1039/c0cc01184c

Reaction of 4-vinylpyridine with $AgClO_3$ yields a crystalline solid that supports a stereospecific and quantitative [2+2] photodimerisation of two terminal olefins. Structural dynamics of the $-CH=CH_2$ group, nature of the counterion, and extended packing influence the photoreactivity.

Terminal olefins (*e.g.* styrene) are important reagents in synthetic chemistry and precursors of commercial products (*e.g.* polystyrene).[1] Terminal olefins are also becoming important in the field of supramolecular chemistry, with interactions between end $-CH=CH_2$ groups recently implicated in host–guest chemistry and cooperative recognition.[2] The hydrocarbon functionality that results from the cycloaddition of two $-CH=CH_2$ groups is also a structural element in molecules of synthetic (*e.g.* cyclophanes)[3] and biological (*e.g.* ladderanes)[4] importance.

Whereas photocycloadditions of terminal olefins proceed well in solution,[5] a long-standing restriction of the reactivity of olefins in the organic solid state has been the photocycloaddition of two end $-CH=CH_2$ groups. Although the solid state can afford stereocontrolled, solvent-free, and quantitative access to molecules that result from the C–C forming transformation, undesirable effects of crystal packing have hindered efforts to reliably direct the photoreaction—particularly in the presence *or absence* of various functional groups—in solids.[6] To the best of our knowledge, the photocycloaddition of two terminal $-CH=CH_2$ groups in the solid state has not been reported.[7] This lack of reactivity may be attributed to the fact that efforts to engineer solids that undergo the photoreaction have required internal olefins with groups that steer a –C=C– bond in the appropriate position for the reaction.[6]

Here, we report the first photodimerisation of terminal olefins in the solid state. Recently, we described an approach to direct [2+2] photodimerisations in solids that exploits argentophilic forces of Ag(I) ions (*i.e.* Ag···Ag interactions) (Scheme 1).[8] The approach employs the ability of two Ag(I) ions to self-assemble on the order of 3.5 Å and stack coordinated ligands into close proximity. We herein demonstrate successful application of the method to couple two $-C=CH_2$ groups. We show that UV-irradiation of crystalline $[Ag_2(\mathbf{4\text{-}vpy})_4][ClO_3]_2$

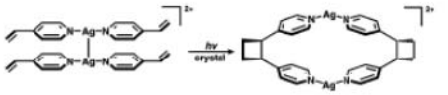

Scheme 1

(where: **4-vpy** = 4-vinylpyridine) (**1**) results in the stereospecific generation of *cis*-1,2-bis(4-pyridyl)cyclobutane (**1,2-bpcb**) in quantitative yield. Scope of the reaction in terms of the counterion is also presented.[9,10] We demonstrate that the bite angle of the anion, along with secondary packing effects, dictate the reactivity of the end $-CH=CH_2$ unit, which adopt different orientations owing to its small size and flexibility.

Solid **1** was prepared *via* slow evaporation of a solution of $AgClO_3$ (0.091 g, 0.5 mmol) and a freshly distilled 4-vinylpyridine (0.105 g, 1 mmol) in CH_3CN (10.0 mL) (1 : 2 ratio). Single crystals of **1** formed within two days. The solid was characterized *via* ^1H NMR spectroscopy§ and single-crystal X-ray crystallography.¶

A perspective view of the X-ray structure of **1** based on data collected at room temperature is shown in Fig. 1. The Ag(I) ions and **4-vpy** form a dinuclear complex sustained by argentophilic forces, with Ag···Ag distances in the lower range (Ag···Ag distances: 3.204(1), 3.210(1) Å). The asymmetric unit consists of two one-half complexes, each of which sits around a center of inversion. Each Ag(I) ion is coordinated by two *trans* **4-vpy** molecules in a linear geometry (Fig. 1a). The ClO_3^- anions lie in close proximity to the Ag(I) ions yet are non-coordinating.

The terminal $-CH=CH_2$ groups lie disordered over two positions, being organized in a crisscross manner. One C-atom of the $-CH=CH_2$ unit of the minor occupied site also interacts with the Ag(I) ion *via* Ag···C(vinyl) forces (Ag···C distance: 3.26 Å). Diffraction data collected at a lower temperature (150 K) reveal the $-CH=CH_2$ groups to be ordered, which is consistent with the $-CH=CH_2$ groups being

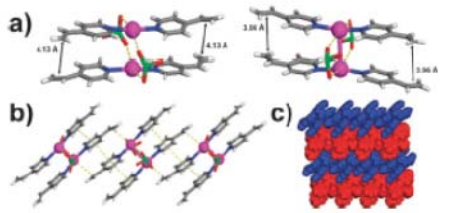

Fig. 1 Structure of **1**: (a) major sites of independent Ag-complexes, (b) quadruple π-stacks, and (c) space-filling view of sheets.

Department of Chemistry, University of Iowa, Iowa City, IA, USA. E-mail: len-macgillivray@uiowa.edu; Fax: +1 319-335-1270; Tel: +1 319-335-0563

† Electronic supplementary information (ESI) available: synthetic procedures (*i.e.* single-crystal growth, photoreactivity studies) and ^1H NMR spectra. CCDC 766415–766422. For ESI and crystallographic data in CIF or other electronic format see DOI: 10.1039/c0cc01184c.

‡ Authors contributed equally to the manuscript.

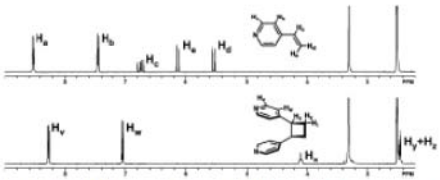

Fig. 2 ^{1}H NMR spectra (solvent: DMSO-d_6) of **1** before (above) and after (below) UV irradiation for a period of 28 hours.

dynamically disordered in the solid. The Ag···C(vinyl) force of the minor occupied site collected at room temperature is not present at the lower temperature. The atoms of the C=C bonds are separated by distances that range from 3.85 to 4.34 Å. The complexes self-assemble to form 1D quadruple π-stacked arrays held together by a combination of face-to-face π···π and Ag···π(C=C) forces (Fig. 1b). The 1D strands are organized as 2D sheets *via* C–H(pyridyl)···O(chlorate) interactions. The sheets stack in an ABAB manner.

To determine the reactivity of **1**, a powdered crystalline sample was exposed to broadband UV irradiation (450 W medium-pressure Hg-lamp) for a period of 28 h. ^{1}H NMR spectroscopy demonstrated that the –CH=CH$_2$ groups underwent a [2+2] photodimerization in quantitative yield. The formation of a cyclobutane ring was evidenced by the disappearance of the three olefinic protons at 6.76 ppm, 6.17 ppm, and 5.57 ppm and appearance of cyclobutane ring protons at 4.09 ppm and 2.48 ppm (Fig. 2).

To determine the stereochemistry of the photoproduct, the cyclobutane was isolated *via* a liquid phase extraction using $CHCl_3$ and NaOH. Extraction and subsequent distillation afforded the cyclobutane product as a colorless, viscous liquid (0.20 g). Given that the product is a liquid, the cyclobutane was reacted with a fresh equivalent of $AgClO_3$. We expected that reaction of the cyclobutane and Ag(I) would afford a solid that would enable the stereochemistry of the cyclobutane to be determined *via* single-crystal X-ray diffraction. Thus, the photoproduct (0.210 g, 1 mmol) was added to a solution of $AgClO_3$ (0.191 g, 1 mmol) in CH_3CN (10.0 mL) and left for a period of approximately two days to evaporate. Yellow single crystals of composition [Ag(**1,2-bpcb**)ClO_3]$_\infty$ (**2**) formed after a period of approximately four days.

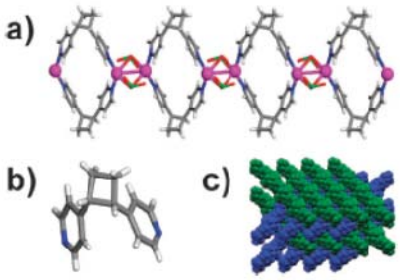

Fig. 3 Structure of the 1D polymer **2**: (a) 1D strands, (b) **1,2-bpcb**, and (c) space-filling of adjacent 2D sheets.

As shown in Fig. 3a, a single-crystal X-ray analysis of **2** enabled us to structurally authenticate the stereochemistry of the photoproduct. The X-ray analysis revealed the cyclobutane to adopt a head-to-head stereochemistry in **1,2-bpcb**, which is consistent with the crystal structure of **1** (Fig. 3b). The cyclobutane and Ag(I) ions assemble to form a 1D coordination polymer sustained, similar to **1**, by Ag–N bonds and Ag···Ag forces. Each 1D polymer is composed of Ag-metallomacrocycles linked by argentophilic forces (Fig. 3c). In contrast to **1**, the ClO_3^- ions lie coordinated to the Ag(I) ions, with the terminal C–H groups of **1,2-bpcb** being directed along the periphery of the polymer. The 1D polymers are connected *via* C–H(pyridyl)···O(chlorate) interactions as 2D sheets stacked in a ABAB manner (Fig. 3c).

That **4-vpy** reacted in the solid **1** encouraged us to study the effects of related polyatomic oxoanions on the assembly and reactivity of the terminal olefin. The olefin was, thus, reacted in the presence of ClO_4^-, $CF_3CO_2^-$, and NO_3^- ions, which support the $[Ag\cdots Ag]^{2+}$ unit.[9,10]

In general, reactions of **4-vpy** with the Ag(I) salts of ClO_4^-, $CF_3CO_2^-$, and NO_3^- ions afforded both photoactive and photostable solids (Fig. 4). The $[Ag\cdots Ag]^{2+}$ unit was maintained in [Ag(**4-vpy**)$_4$][ClO_4] (**3a**) (3.458(1) Å) and [Ag(**4-vpy**)$_4$][CF_3CO_2] (**3b**) (3.042(1) Å), with the olefins being aligned, similar to **1**, in head-to-head geometries (Fig. 4). The –CH=CH$_2$ groups of both **3a** and **3b** exhibited less disorder than **1**. In particular, **3a** exhibited disorder of only a single –CH=CH$_2$ group at both low (*i.e.* 190 K) and room temperature, while the terminal groups of **3b** were not disordered (*i.e.* 150 K). Whereas the complexes of **3a** packed to form quadruple arrays, the complexes of **3b** exhibited a more canted geometry. The olefins of both solids, however, reacted upon UV irradiation to generate **1,2-bpcb** stereospecifically in up to approximately 75% and 55% yields, respectively. In [Ag(**4-vpy**)$_2$][NO_3] (**3c**), the $[Ag\cdots Ag]^{2+}$ was not maintained. Each Ag(I) ion participated in a Ag···C interaction with one of two disordered terminal –CH=CH$_2$ groups. The interaction involving the terminal group afforded a dimer with adjacent complexes oriented approximately orthogonal and with nearest-neighbour C=C bonds separated >4.34 Å. In line with the structure of **3c**, the solid was photostable.

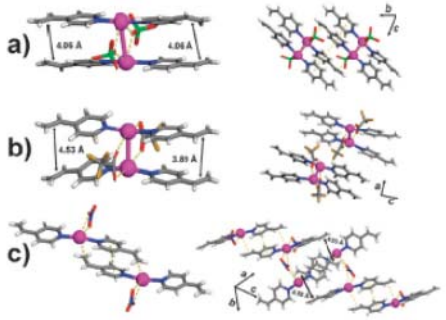

Fig. 4 Complexes and packing: (a) **3a**, (b) **3b**, and (c) **3c**.

Table 1 Solid-state reactivity of **1** and **3a–c**

X^-	d(Ag···Ag)/Å	C=C (centroid) separation/Å	–CH=CH_2 alignment	Yield (%)
ClO_3^-	3.20, 3.21	3.85, 4.34	Crisscross	100
ClO_4^-	3.46	4.06, 4.20	Crisscross, parallel	75
$CF_3CO_2^-$	3.04	3.88, 4.53	Parallel	55
NO_3^-	N/A	4.34, 4.64	N/A	0

The Ag–Ag separation in **3b** is remarkably small[9,10] and can be attributed to the small and narrow bite size of the oxoanion (O–O bite ranges: ClO_3^- 2.30–2.36 Å, ClO_4^- 2.17–2.33 Å, $CF_3CO_2^-$ 2.18–2.19 Å). Notwithstanding **3c**, the small bite size corresponds to the solid that exhibits the lowest reactivity, as well as an appreciably large C···C separation (4.53 Å, Table 1). Collectively, these observations suggest that the reactivity of the terminal –CH=CH_2 group is influenced by the Ag–Ag separation and bite size of the anion. A short Ag–Ag separation 'squeezes' the pyridyl groups[11] in a proximity that makes the –CH=CH_2 group more prone, owing to the free rotation and small size of the –CH=CH_2 unit, to be separated at a larger distance. We note that **1** and **3a**, which display the highest reactivities, both pack to form π-stacked arrays. The mode of stacking likely supports the photoreactivity by 'nestling' the –CH=CH_2 units in a planar geometry. The reactivity of the terminal olefins is, thus, influenced by a combination of argentophilic forces, long-range packing, and conformational freedom of the –CH=CH_2 unit. Complexes with appropriately lengthened Ag–Ag separations minimize repulsion, with the π-stacking providing a secondary means to promote the reaction. We also suggest that the structural flexibility of the –CH=CH_2 in a solid likely accounts for a current lack of examples of terminal olefins reacting in the solid state.

To conclude, we have achieved a stereospecific and quantitative [2+2] photodimerization of terminal olefins in the solid state. The solid-state photoreaction was mediated by Ag(I) ions, which organize **4-vpy** in a position suitable for reaction. We have revealed that the photoreactivity is influenced by the nature of the counterion and long-range packing, as well as the flexibility of the –CH=CH_2 unit. We expect efforts to integrate the reactions of terminal olefins into products rationally designed in the solid state can lead to the rapid development of products of enhanced structural complexity.

Notes and references

§ ^{1}H NMR data for **1** before UV irradiation (DMSO-d_6, δ/ppm): 8.53 (dd, 8H), 7.46 (dd, 8H), 6.79–6.70 (dd, 4H), 6.16–5.52 (dd, 8H); ^{1}H NMR data for **1** after UV irradiation (DMSO-d_6, δ/ppm): 8.27 (dd, 8H), 7.04 (dd, 8H), 4.13–4.08 (m, 4H), 2.47–2.44 (m, 8H); ^{1}H NMR data for **3a** before UV irradiation (DMSO-d_6, δ/ppm): 8.54 (dd, 8H), 7.48 (dd, 8H), 6.80–6.70 (dd, 4H), 6.17–5.53 (dd, 8H); ^{1}H NMR data for **3a** after UV irradiation (DMSO-d_6, δ/ppm): 8.54 (dd, 1.9H), 8.27 (dd, 6.1H), 7.48 (dd, 1.9H), 7.04 (dd, 6.1H), 6.80–6.70 (dd, 0.95H), 6.17–5.53 (dd, 1.9H), 4.13–4.08 (m, 3.05H), 2.47–2.44 (m, 6.1H); ^{1}H NMR data for **3b** before UV irradiation (DMSO-d_6, δ/ppm): 8.54 (dd, 8H), 7.49 (dd, 8H), 6.80–6.71 (dd, 4H), 6.18–5.54 (dd, 8H); ^{1}H NMR data for **3b** after UV irradiation (DMSO-d_6, δ/ppm): 8.54 (dd, 3.6H), 8.28 (dd, 4.4H), 7.49 (dd, 3.6H), 7.06 (dd, 4.4H), 6.80–6.71 (dd, 1.8H), 6.18–5.54 (dd, 3.6H), 4.14–4.09 (m, 2.2H), 2.47–2.44 (m, 4.4H); ^{1}H NMR data for **3c** before UV irradiation (DMSO-d_6, δ/ppm): 8.53 (dd, 8H), 7.46 (dd, 8H), 6.80–6.70 (dd, 4H), 6.16–5.52 (dd, 8H); ^{1}H NMR data for **3c** before UV irradiation (DMSO-d_6, δ/ppm): 8.53 (dd, 8H), 7.46 (dd, 8H), 6.80–6.70 (dd, 4H), 6.16–5.52 (dd, 8H).

¶ Crystal data for **1**: $C_{14}H_{14}AgClN_2O_3$, M = 401.59, monoclinic, a = 16.5837(18) Å, b = 11.4570(12) Å, c = 17.1283(18) Å, α = 90°, β = 101.558(5)°, γ = 90°, V = 3188.4(6) Å^3, T = 290(2) K, space group $P2_1/n$, Z = 8, R_{int} = 0.0739. The final R_1 values were 0.0527 ($I > 2\sigma(I)$). Crystal data for **1** (low temp): $C_{56}H_{56}Ag_4Cl_4N_8O_{12}$, M = 1606.37, monoclinic, a = 16.0786(17) Å, b = 11.3557(12) Å, c = 17.0932(18) Å, α = 90°, β = 100.711(5)°, γ = 90°, V = 3066.6(6) Å^3, T = 150(2) K, space group $P2_1/n$, Z = 2, R_{int} = 0.0336. The final R_1 values were 0.0298 ($I > 2\sigma(I)$). Crystal data for **2**: $C_{14}H_{14}AgClN_2O_3$, M = 401.59, monoclinic, a = 18.3059(19) Å, b = 10.9939(12) Å, c = 14.6045(16) Å, α = 90°, β = 90.896(5)°, γ = 90°, V = 2938.8(5) Å^3, T = 150(2) K, space group $C2/c$, Z = 8, R_{int} = 0.0371. The final R_1 values were 0.0357 ($I > 2\sigma(I)$). Crystal data for **3a**: $C_{14}H_{14}AgClN_2O_4$, M = 417.59, triclinic, a = 8.5247(10) Å, b = 9.5750(11) Å, c = 11.3228(12) Å, α = 70.075(5)°, β = 88.600(5)°, γ = 68.447(5)°, V = 802.75(16) Å^3, T = 290(2) K, space group $P\bar{1}$, Z = 2, R_{int} = 0.0127. The final R_1 values were 0.0434 ($I > 2\sigma(I)$). Crystal data for **3a** (low temp): $C_{14}H_{14}AgClN_2O_4$, M = 417.59, triclinic, a = 8.2375(9) Å, b = 9.2898(10) Å, c = 11.4161(12) Å, α = 71.026(5)°, β = 89.128(5)°, γ = 71.020(5)°, V = 777.22(14) Å^3, T = 190(2) K, space group $P\bar{1}$, Z = 2, R_{int} = 0.0108. The final R_1 values were 0.0281 ($I > 2\sigma(I)$). Crystal data for **3b**: $C_{32}H_{28}Ag_2F_6N_4O_4$, M = 862.32, orthorhombic, a = 13.4624(14) Å, b = 15.2237(16) Å, c = 16.9018(18) Å, α = 90°, β = 90°, γ = 90°, V = 3464.0(6) Å^3, T = 290(2) K, space group $P2_12_12_1$, Z = 4, R_{int} = 0.0279. The final R_1 values were 0.0475 ($I > 2\sigma(I)$). Crystal data for **3b** (low temp): $C_{32}H_{28}Ag_2F_6N_4O_4$, M = 862.32, orthorhombic, a = 12.8602(14) Å, b = 15.1102(16) Å, c = 17.0170(18) Å, α = 90°, β = 90°, γ = 90°, V = 3306.7(6) Å^3, T = 150(2) K, space group $P2_12_12_1$, Z = 4, R_{int} = 0.0232. The final R_1 values were 0.0277 ($I > 2\sigma(I)$). Crystal data for **3c**: $C_{14}H_{14}AgN_3O_3$, M = 380.15, monoclinic, a = 11.0503(12) Å, b = 10.9201(12) Å, c = 12.8477(14) Å, α = 90°, β = 94.835(5)°, γ = 90°, V = 1544.8(3) Å^3, T = 290(2) K, space group $P2_1/n$, Z = 4, R_{int} = 0.0308. The final R_1 values were 0.0418 ($I > 2\sigma(I)$).

1 T. J. Donohoe, T. J. C. O'Riordan and C. P. Rosa, *Angew. Chem., Int. Ed.*, 2009, **48**, 1014–1017.

2 W. Rie, I. Tomohiro, K. Yohei, S. Seiji and T. Masayuki. *Angew. Chem., Int. Ed.*, 2009, **48**, 6667–6670.

3 J. Nishimura, Y. Nakamura, Y. Hayashida and T. Kudo, *Acc. Chem. Res.*, 2000, **33**, 679–686.

4 (*a*) D. H. Nouri and D. J. Tantillo, *Curr. Org. Chem.*, 2006, **10**, 2055–2074; (*b*) H. Hopf, *Angew. Chem., Int. Ed.*, 2003, **42**, 2822–2825; (*c*) J. S. Sinninghe Damste, M. M. Strous, W. I. C. Rijpstra, E. C. Hopmans, J. A. J. Geenevasen, A. C. T. van Duin, L. A. van Niftrik and M. S. M. Jetten, *Nature*, 2002, **419**, 708–712.

5 T. Nakano, A. Marin, C. Rivas and C. Pérez, *J. Heterocycl. Chem.*, 1977, **14**, 921–924.

6 (*a*) L. R. MacGillivray, G. S. Papaefstathiou, T. Friščić, T. D. Hamilton, D.-K. Bučar, Q. Chu, D. B. Varshney and I. G. Georgiev, *Acc. Chem. Res.*, 2008, **41**, 280–291; (*b*) M. Nagarathinam, A. M. P. Peedikakkal and J. J. Vittal, *Chem. Commun.*, 2008, 5277–5288.

7 For reaction of a single terminal double bond in a mixed crystal, see: T. Suzuki, T. Fukushima, Y. Yamashita and T. Miyashi, *J. Am. Chem. Soc.*, 1994, **116**, 2793–2803.

8 Q. Chu, D. C. Swenson and L. R. MacGillivray, *Angew. Chem., Int. Ed.*, 2005, **44**, 3569–3572.

9 N. Schultheiss, D. R. Powell and E. Bosch, *Inorg. Chem.*, 2003, **42**, 8886–8890.

10 O.-S. Jung, Y. J. Kim, Y.-A. Lee, S. W. Kang and S. N. Choi, *Cryst. Growth Des.*, 2003, **4**, 23–24.

11 M. Nagarathinam and J. J. Vittal Jagadese, *Angew. Chem., Int. Ed.*, 2006, **45**, 4337–4341.

Supplementary Material (ESI) for Chemical Communications

Electronic Supplementary Information (ESI)

Stereospecific and quantitative photodimerization of terminal olefins in the solid state

Ivan G. Georgiev, Dejan-Krešimir Bučar, and Leonard R. MacGillivray

Materials. Silver(I) chlorate (≥99.9%), silver(I) perchlorate (99.9%), silver(I) triflouroacetate (≥99%), and silver(I) nitrate (≥99.0%), 4-vinylpyridine (95%), acetonitrile (anhydrous, 99.8%) and diethyl ether (anhydrous, ACS reagent, ≥99.0%) were purchased from Sigma-Aldrich (St. Louis, MO). 4-Vinylpyridine was distilled prior to use, whereas all other materials were used as received.

Crystal growth. Solids **1** and **3a-c** were prepared as follows. The silver salt (0.5 mmol) and 4-vinylpyridine (1.0 mmol) were separately dissolved in acetonitrile (10 ml). The solutions were combined, subsequently filtered through a Millex syringe filter (PVDF, 0.2 μm, 13mm) and left to evaporate at room temperature. Solid **2** was prepared in the same manner using equimolar amounts of the silver salt and **1,2-bpcb** (1.0 mmol). The single crystals were filtered upon formation, washed with diethyl ether and dried at room temperature with exposure to UV light (*i.e.* dark place)

Photoreactivity studies. In a typical photoreaction experiment, 100 mg of the silver complex were gently ground using a mortar and pestle. The obtained powder was placed between two Pyrex glass plates. The plates were transferred in a plastic bag, filled up with N_2(g) and sealed. The sealed bag was placed in a photoreactor cabinet equipped with a broad-band 450 W medium-pressure Hg-lamp. The powder distributed between the plates was mixed every 10 hours. Importantly, the photoreactive powder should be exposed to air *as less as possible* since the both the photoreactive solids and the photoproducts are air sensitive (*i.e.* they are oxidizing)

Supplementary Material (ESI) for Chemical Communications
This journal is (c) The Royal Society of Chemistry 2010

Crystallographic studies. The diffraction data were measured on a Nonius Kappa CCD single-crystal X-ray diffractometer at both room and low temperatures using MoK_α radiation (λ = 0.71073 Å). Data collection, cell refinement and data reduction were performed using *Collect*[1] and *HKL Scalepack*/*Denzo*,[2] respectively. Structure solution and refinement were accomplished using SHELXS-97 and SHELXL-97,[3] respectively. The heavy-atom sites were in all structures identified using the Patterson method, whereas all other non-hydrogen atoms were indentified from the difference Fourier map within several refinement steps. All non-hydrogen atoms were refined anisotropically. Hydrogen atoms associated with carbon atoms were refined in geometrically constrained positions. Hydrogen atoms associated with oxygen atoms were calculated in an optimal hydrogen bonding geometry. The details of the structural analysis of all solids are summarized in Table S1.

Table S1 Crystallographic data for **1**, **2** and **3a-e**.

Compound reference	**1**	**1** (low temperature)	**2**	**3a**
Chemical formula	$C_{14}H_{14}AgClN_2O_3$	$C_{56}H_{56}Ag_4Cl_4N_8O_{12}$	$C_{14}H_{14}AgClN_2O_3$	$C_{16}H_{16}AgClN_2O_4$
Formula Mass	401.59	1606.37	401.59	417.59
Crystal system	Monoclinic	Monoclinic	Monoclinic	Triclinic
a/Å	16.5837(18)	16.0786(17)	18.3059(19)	8.5247(10)
b/Å	11.4570(12)	11.3557(12)	10.9939(12)	9.5750(11)
c/Å	17.1283(18)	17.0932(18)	14.6045(16)	11.3228(12)
α/°	90	90	90	70.075(5)
β/°	101.558(5)	100.711(5)	90.896(5)	88.600(5)
γ/°	90	90	90	68.447(5)
Unit cell volume/Å^3	3188.4(6)	3066.6(6)	2938.8(5)	802.75(16)
Temperature/K	290(2)	150(2)	150(2)	290(2)
Space group	$P2_1/n$	$P2_1/n$	$C2/c$	$P\bar{1}$
No. of formula units per unit cell, *Z*	8	2	8	2
Radiation type	MoKα	MoKα	MoKα	MoKα
Absorption coefficient, μ/mm^{-1}	1.441	1.499	1.564	1.439
No. of reflections measured	19347	17790	9500	5289
No. of independent reflections	5590	5372	2603	2814
R_{int}	0.0739	0.0336	0.0371	0.0127
Final R_1 values ($I > 2\sigma(I)$)	0.0527	0.0298	0.0357	0.0434
Final $wR(F^2)$ values ($I > 2\sigma(I)$)	0.1293	0.0837	0.0729	0.1252
Final R_1 values (all data)	0.1291	0.0457	0.0484	0.0604
Final $wR(F^2)$ values (all data)	0.1546	0.1159	0.0784	0.1355
Goodness of fit on F^2	0.908	1.168	1.062	1.092
CCDC number	766415	766416	766417	766418

Table S1 (continued) Crystallographic data for **1**, **2** and **3a-c**.

Compound reference	**3a** (low temperature)	**3b**	**3b** (low temperature)	**3c**
Chemical formula	$C_{14}H_{14}AgClN_2O_4$	$C_{32}H_{28}Ag_2F_6N_4O_4$	$C_{32}H_{28}Ag_2F_6N_4O_4$	$C_{14}H_{14}AgN_3O_3$
Formula Mass	417.59	862.32	862.32	380.15
Crystal system	Triclinic	Orthorhombic	Orthorhombic	Monoclinic
a/Å	8.2375(9)	13.4624(14)	12.8602(14)	11.0503(12)
b/Å	9.2898(10)	15.2237(16)	15.1102(16)	10.9201(12)
c/Å	11.4161(12)	16.9018(18)	17.0170(18)	12.8477(14)
α/°	71.026(5)	90	90	90
β/°	89.128(5)	90	90	94.835(5)
γ/°	71.020(5)	90	90	90
Unit cell volume/Å^3	777.22(14)	3464.0(6)	3306.7(6)	1544.8(3)
Temperature/K	190(2)	290(2)	150(2)	290(2)
Space group	$P\bar{1}$	$P2_12_12_1$	$P2_12_12_1$	$P2_1/n$
No. of formula units per unit cell, Z	2	4	4	4
Radiation type	MoKα	MoKα	MoKα	MoKα
Absorption coefficient, μ/mm^{-1}	1.487	1.204	1.261	1.317
No. of reflections measured	5256	21109	28524	8702
No. of independent reflections	2702	6079	7569	2697
R_{int}	0.0108	0.0279	0.0232	0.0308
Final R_1 values ($I > 2\sigma(I)$)	0.0281	0.0475	0.0277	0.0418
Final $wR(F^2)$ values ($I > 2\sigma(I)$)	0.0734	0.1352	0.0862	0.1186
Final R_1 values (all data)	0.0297	0.0755	0.0358	0.053
Final $wR(F^2)$ values (all data)	0.0743	0.1476	0.1051	0.1261
Goodness of fit on F^2	1.064	1.103	1.012	1.068
CCDC number	766419	766420	766421	766422

^{1}H NMR studies. ^{1}H NMR data were collected on an AVANCE Bruker NMR spectrometer operating at 300 MHz using DMSO-d_6 as solvent. Figures S1-S4 depict the ^{1}H NMR spectra of **1** and **3a-c** before and after UV irradiation, respectively.

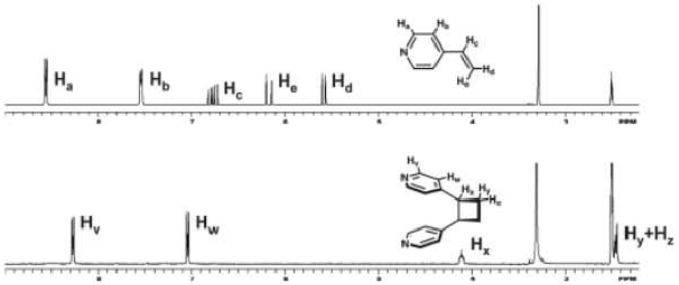

Figure S1. ^{1}H NMR spectra of **1** before UV irradiation (above) [DMSO-d_6, δ/ppm: 8.56 (dd, 8H), 7.54 (dd, 8H), 6.82-6.72 (dd, 4H), 6.20-5.56 (dd, 8H)], and ^{1}H NMR spectra of **1** after UV irradiation (below) [DMSO-d_6, δ/ppm: 8.27 (dd, 8H), 7.06 (dd, 8H), 4.13-4.08 (m, 4H), 2.47-2.44 (m, 8H)].

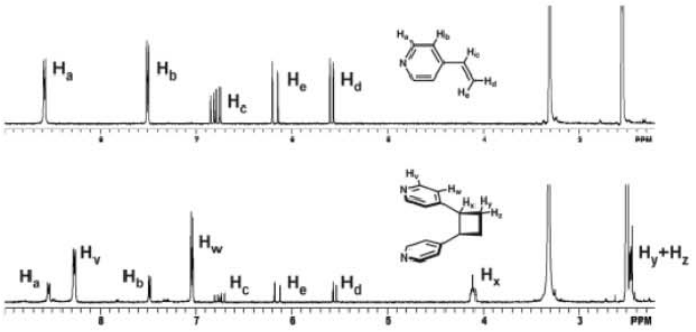

Figure S2. ^{1}H NMR spectra of **3a** before UV irradiation (above) [DMSO-d_6, δ/ppm: 8.54 (dd, 8H), 7.46 (dd, 8H), 6.80-6.70 (dd, 4H), 6.16-5.52 (dd, 8H)], and ^{1}H NMR spectra of **3a** after UV irradiation (below) [DMSO-d_6, δ/ppm: 8.54 (dd, 1.9H), 8.27 (dd, 6.1H), 7.48 (dd, 1.9H), 7.05 (dd, 6.1H), 6.80-6.71 (dd, 0.95H), 6.17-5.53 (dd, 1.9H), 4.13-4.08 (m, 3.05H), 2.47-2.44 (m, 6.1H)]. The small peaks at 8.8 ppm and 7.8 ppm are corresponding to oxidized pyridyl functional groups that start to form once the photoreaction in the solid state stops proceeding.

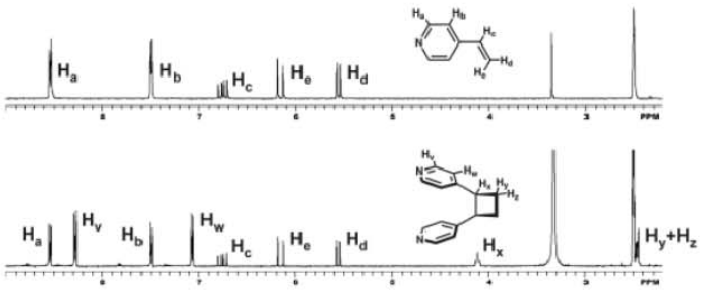

Figure S3. ^{1}H NMR spectra of **3b** before UV irradiation (above) [DMSO-d_6, δ/ppm: 8.54 (dd, 8H), 7.50 (dd, 8H), 6.80-6.71 (dd, 4H), 6.19-5.54 (dd, 8H)], and ^{1}H NMR spectra of **3b** after UV irradiation (below) [DMSO-d_6, δ/ppm: 8.54 (dd, 3.6H), 8.28 (dd, 4.4H), 7.50 (dd, 3.6H), 7.06 (dd, 4.4H), 6.81-6.71 (dd, 1.8H), 6.18-5.54 (dd, 3.6H), 4.14-4.09 (m, 2.2H), 2.47-2.44 (m, 4.4H)]. The small peaks at 8.8 ppm and 7.8 ppm are corresponding to oxidized pyridyl functional groups that start to form once the photoreaction in the solid state stops proceeding.

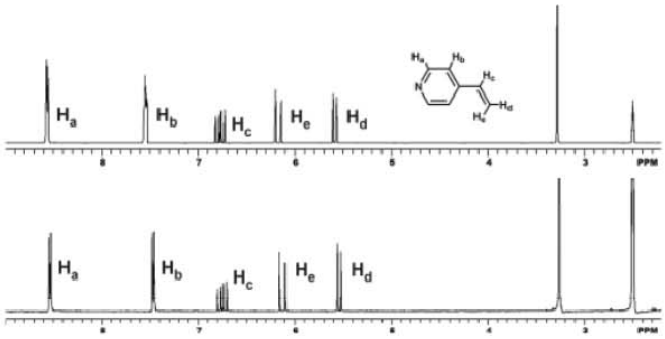

Figure S4. ^{1}H NMR spectra of **3c** before UV irradiation (above) [DMSO-d_6, δ/ppm: 8.56 (dd, 8H), 7.54 (dd, 8H), 6.82-6.73 (dd, 4H), 6.20-5.57 (dd, 8H)], and ^{1}H NMR spectra of **3c** after UV irradiation (below) [DMSO-d_6, δ/ppm: 8.54 (dd, 8H), 7.46 (dd, 8H), 6.80-6.70 (dd, 4H), 6.16-5.52 (dd, 8H)].

References

[1] R. W. W. Hooft, Nonius BV, Delft, The Netherlands, 1998.
[2] Z. Otwinowski, W. Minor in *Methods in Enzymology*, ed. C. W. Carter Jr and R. M. Sweet , 1997, Vol. 276 (*Macromolecular Crystallography*, Part A), pp. 307-326.
[3] G. M. Sheldrick, *Acta Cryst.*, 2008, **A64**, 112-122.